Computation and Measurement of Wind Induced Ventilation

by

Matthew Peter Straw, BEng, MRes

Thesis submitted to the University of Nottingham for the degree of Doctor of Philosophy

March 2000

Contents

List of Figures

List of Tables

Notation

A	area of ventilation opening
A_W	effective area of ventilation opening
B	coefficient in ventilation spectrum
C	concentration of tracer gas
$\overline{C}$	mean concentration of tracer gas
C_d	orifice discharge coefficient
C_p	pressure coefficient
$\overline{C_p}$	mean pressure coefficient
C_p'	fluctuating pressure coefficient
K	coefficient of linearisation
L	orifice depth in direction of flow
${}^xL_u$	streamwise turbulent length scale
N	number of ventilation openings
$P_k(t)$	modal pressure field
Q	instantaneous ventilation rate
$\overline{Q}$	mean ventilation rate
Q_B	broad banded and mean ventilation rates
Q_{pulse}	pulsating ventilation rate
Q_T	total ventilation rate
R	covariance of fluctuating pressure coefficients
R_e	Reynolds number
S_{Cpi}	spectral density of internal pressure coefficient
S_{QQ}	spectral density of ventilation rate
S_{Tk}	spectral density of mode k
S_{uu}	spectrum of windspeed
$T_k(t)$	modal time function
U	magnitude of wind speed
U_{ref}	reference wind speed
$U(z)$	windspeed at height z
c	damping of turbulent ventilation system
d	zero plane displacement
k	turbulent kinetic energy
k_b	effective bulk modulus
$\dot{m}$	mass flow rate of tracer gas
n, ω	frequency
p	pressure
p'	fluctuating pressure
p_e	external surface pressure

p_i	internal pressure
q	fluctuation ventilation rate
t	time
u	streamwise component of wind speed
$\overline{u}$	mean streamwise component of wind speed
u'	turbulent streamwise component of wind speed
u^+	non-dimensional velocity parameter
u_*	friction velocity
x	streamwise distance
x_r, x_s	spatial coordinates on building surface
v	transverse/lateral component of wind speed
$\overline{v}$	mean transverse component of wind speed
v'	turbulent transverse component of wind speed
w	vertical component of wind speed
$\overline{w}$	mean vertical component of wind speed
w'	turbulent vertical component of wind speed
x_{cube}	streamwise dimension of cubic test structure
y	transverse/lateral distance
y_{cube}	transverse/lateral dimension of cubic test structure
y^+	non-dimensional distance parameter
z	vertical distance
z_{abl}	height of atmospheric boundary layer
z_{cube}	vertical dimension of cubic test structure
z_{ref}	reference height
z_o	ground surface roughness
i , j , k	subscripts denoting individual mode number
Π_i	modal transform function
α	power law exponent
ε	dissipation of turbulent kinetic energy
μ	dynamic viscosity of fluid
μ_t	eddy viscosity
ϕ	arbitrary scalar quantity
ν_t	kinematic eddy viscosity
ρ	density of air
σ	standard deviation (rms)
σ_Q	rms of ventilation
σ_u	rms of streamwise velocity
σ_v	rms of transverse velocity
σ_w	rms of vertical velocity
τ	shear stress

Published Papers

The following are papers published and submitted as a direct result of this research.

Straw, M.P., Baker, C.J., Robertson, A.P. (1998), Modelling wind induced ventilation of structures, *Proceedings of the 4th UK Conference on Wind Engineering*, pp. 105-110.

Straw, M.P., Baker, C.J., Robertson, A.P. (1999), Experimental measurements and computations of the wind induced ventilation of a cubic structure, *Proceedings of the 10th International Conference on Wind Engineering*, pp. 1951-1958.

Straw, M.P., Baker, C.J., Robertson, A.P. (1999), Experimental measurements and computations of the wind driven ventilation of a cubic structure, *Journal of Wind Engineering and Industrial Aerodynamics* (Submitted).

Acknowledgements

There are numerous organisations and individuals to whom I owe a great deal of gratitude for their help and assistance throughout the period of my research and in the production of this thesis.

Firstly, I would like to thank the University of Nottingham and Silsoe Research Institute. Without the financial assistance and funding this research would not have been undertaken.

I would like to show my appreciation to Rev. Prof. Chris Baker for his commitment and continued inspiration throughout. His enthusiasm for this work and incredible rate of proof reading really are second to none.

For providing the encouragement and assistance in the full-scale experiments I would like to thank Dr. Adam Robertson. It was always good to know that on a cold and wet Monday morning, when a week of sub-zero experiments lay ahead, there was always someone to discuss the fortunes of Nottingham Forest with over coffee.

I would also like to thank Dr. Roger Hoxey, Dr. Andrew Quinn, Lynne Short and Theo Demmers along with all of the staff at Silsoe Research Institute for their assistance during my time there. For teaching me that there is a solution to every problem my thanks go to Len Burgess.

With their magical computer fingers for curing crashed computers and for the hours of help with diverging CFD simulations my thanks go to Dr. Nigel Wright and Dr. Dave Hargreaves.

For their financial and moral support throughout my education (that went on longer than either they, or myself, could ever have imagined) I would like to thank my parents.

Finally, I would like to thank Louise. Not only for your eternal optimism and hours spent reading this thesis but also for the years of just being there.

1. INTRODUCTION

Ventilation is an extremely important stage in many building design procedures. In structures for human occupation it is important to provide a habitable, comfortable and adequately ventilated environment. In agricultural glass houses it is often necessary to quantify the amount of carbon dioxide (used to enhance crop growth) lost through leakage and ventilation processes. When housing livestock, predicting ventilating airflow patterns would be advantageous for providing a suitable environment and the controlled removal of gaseous pollutants. Through improved understanding of ventilation mechanisms and prediction techniques, the control of temperature and relevant environmental parameters can be optimised.

Ventilation can be categorised as forced or natural. Forced ventilation is driven through the use of mechanical fans, for example, in air conditioning systems. This form of ventilation is capable of providing the required ventilation flow for which the system is designed and can be controlled with relative ease. Natural ventilation employs no fans, or mechanical systems, instead relying upon air flow induced by thermal gradients (buoyant flows), the action of the wind or a combination of the two mechanisms.

Where the ventilating flow rate must be strictly managed and conditions maintained within close limits it is necessary to employ forced systems. If however the conditions are acceptable within wider limits (in terms of airflow and temperature control) natural ventilation becomes a viable option. Concerns over the efficiency and cost of forced ventilation systems have lead to an increase in the number of architects turning their attention to natural ventilation techniques. For example, the Inland Revenue office in Nottingham is just one modern structure to rely on natural ventilation to control the indoor climate.

This thesis is concerned only with ventilation driven by the action of the wind. The effects of thermal gradients on natural ventilation have been found to be negligible above reasonably low wind speeds (approximately $2ms^{-1}$). Wind induced ventilation occurs due to pressure differences between openings in a building envelope and by momentum of the incoming air if the ventilation openings are large. If natural ventilation, more specifically wind induced ventilation, is to be utilised in a greater number of applications, control and confidence that the system can perform within the required limits is of prime importance. Consequently, it is necessary for a design

procedure to incorporate reliable methods and techniques for predicting the expected ventilation rates within reasonable limits of accuracy.
The most common technique currently used for predicting wind driven ventilation utilises mean pressures measured in the positions of ventilation openings measured on sealed buildings (no openings present) and assuming a steady-state process (BS 5925 (1991)). The prediction of wind induced ventilation through the use of mean pressure data alone has however, lead to significant discrepancies with measurements (e.g. Choiniere et al (1992)). Discrepancies become more prominent as the pressure difference between ventilation openings reduces. If the mean pressure difference across openings was zero, steady-state methods predict zero ventilation. In reality, significant air exchange has been found to take place in such cases as a result of the action of turbulent flow mechanisms.

This thesis aims to predict wind induced ventilation of a structure through the application of current analytical techniques, computational fluid dynamics simulations and novel techniques for ventilation flows induced by turbulent mechanisms. Validation of the predictions was carried out through full-scale measurements undertaken on a purpose built test structure. The structure was of cubic design with an external dimension of 6m. The construction of this full-scale research structure at Silsoe Research Institute, Bedfordshire, England, provided a unique opportunity for undertaking full-scale experimentation on a fundamental wind engineering test case which, prior to this thesis, had only been investigated using scale models in wind tunnels and computational simulations.

Extensive background theory into areas of wind engineering that are relevant to this study is provided in Chapter 2. The nature of airflow structure within the atmospheric boundary layer is discussed along with methods available for its simulation. The external flow fields and surface pressure distributions induced by the wind around a structure are described. The fundamentals of wind induced ventilation are also introduced. After the important concepts have been discussed, a literature review of the relevant fields of study is presented.

Chapter 3 explores the novel full-scale investigations initially focussing on the test structure and its location, this is proceeded by details of the experimental techniques adopted and the results gained. Experiments were undertaken on the structure with and without ventilation openings to provide the relevant data for assessing wind induced ventilation rates through predictive techniques and direct measurement. Reference velocity data was recorded from which it was possible to describe the characteristics of the atmospheric boundary layer. Pressure measurements around the surface of the structure were utilised to investigate the external pressure distributions and in the prediction of ventilation rates.

By incorporating removable panels over ventilation openings it was possible to measure directly the wind driven ventilation rate by monitoring air speeds in the openings and through the application of tracer gas techniques. Internal velocity profiles were made in order to gain an indication of internal air flow structure induced by the wind. For all of the ventilation work within this thesis, a simple configuration of two $1m^2$ openings located on opposing faces at a height of 3m above the ground was used. The effect of incident wind angle on ventilation was assessed for the wind normal to the openings (0° case), wind parallel to the openings (90° case) and a number of wind directions in between.

The application of computational fluid dynamics (CFD) is assessed in Chapter 4. The theoretical basis and techniques employed in CFD is discussed prior to the introduction of the investigations. Simulations were developed to assess the effectiveness of CFD predictions of wind induced ventilation. Testing involved simulation of the atmospheric boundary layer to provide the correct boundary conditions before introducing the cubic test structure and modelling the external flow and pressure fields. The external environment was simulated before any attempt was made to directly model wind induced ventilation. This was necessary due to the fact that the external conditions drive the internal flow. Through the comparison of experimentally measured surface pressures, it was possible to identify the most appropriate techniques and numerical methods to apply to the full simulation of the wind driven ventilation.

Chapter 5 concentrates on the development of novel techniques for predicting the contribution of turbulent ventilation mechanisms to the overall wind induced ventilation. Two techniques are introduced. A frequency domain technique developed utilises the proper orthogonal decomposition of a time series of measured external pressure data. The power spectra of the external pressures in the locations of ventilation openings are derived. By transforming these pressure spectra it is possible to predict the unsteady pulsating ventilation flow that would occur. A time domain method is also introduced and involved an expansion of a steady state method to account for fluctuations in ventilation.

The individual investigations described in Chapters 3, 4 and 5 are reconciled in Chapter 6 where comparison between experimental measurements and computational and analytical predictions of wind driven ventilation are made. This chapter attempts to assess the success of the modelling techniques applied by rigorous validation with the experimental data gathered from full-scale investigations.

Finally, the conclusions of the research are given in Chapter 7. These include summaries of the findings of this study and suggestions for areas of improvement and opportunities for further study.

2. BACKGROUND

2.1Introduction

The aim of this background chapter is to introduce the necessary information with regard to wind induced ventilation. In order to understand the physical mechanisms involved in wind induced ventilation it is necessary to consider the nature of the wind itself and methods available for its simulation. The theoretical background relating to the structure of airflow and pressure distributions around low rise, surface mounted structures is also presented.

Proceeding the introduction to the physical characteristics of the wind and external building aerodynamics, the fundamentals of wind induced ventilation are discussed. Modelling techniques and assessment methods are examined, as are the effects of turbulence, and conclusions deduced from a literature review of previous research.

2.2The Atmospheric Boundary Layer

When undertaking wind engineering research it is important to have a thorough understanding of the region of the Earth's atmosphere under consideration. It is necessary to develop methods that are capable of quantifying wind speeds and characteristics of the wind with respect to mean quantities and turbulent fluctuations.

The majority of wind engineering is concerned with the lowest few hundred metres of the atmosphere, since it is often surface features that are of interest i.e. structures. The region of interest in this work is termed the *atmospheric boundary layer* (ABL). The ABL can be defined as 'the region of the Earth's atmosphere where the effects of the surface (friction, heating and cooling) are felt directly on a time scale of less than a day, and in which significant fluxes of momentum, heat or matter are carried by turbulent motions on a scale of the order of the depth of the boundary layer or less' (Garrat (1992)).

The ABL can be divided into two distinct regions:

- Interfacial layer
- Ekman layer

These two layers can be defined in terms of the variation of a turbulent shear stress termed 'Reynolds stress' with respect to height through the ABL as shown in Figure 2.1. Reynolds stress is defined by equation 2.1.

$$\tau_{xy} = -\rho\overline{uw} \tag{2.1}$$

where ρ is the density of air and $\overline{uw}$ is the time averaged value of *u.w* (*u* and *w* are the velocity components in *x* and *z* directions respectively, and can be substituted by other velocity components) i.e. covariances of turbulent velocities.

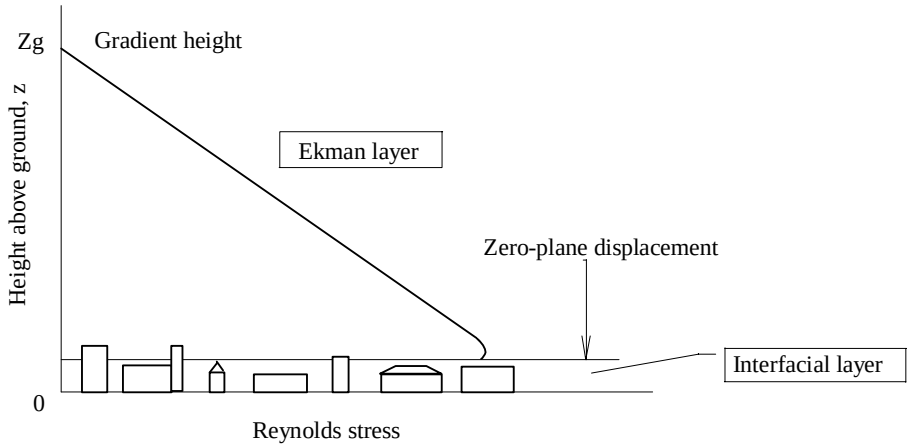

Figure 2.1. Reynolds stress through the atmospheric boundary layer

Source: Cook, N. J. (1985), *The designers guide to wind loading on structures: Part 1*, Butterworths.

2.2.1 Interfacial Layer

The interfacial layer is the lowest region of the ABL and is usually occupied by surface features. The predominant Reynolds stress reduces from a maximum value to zero at the surface as momentum is given up as pressure forces on individual roughness elements. The interfacial layer thickness is defined as the *zero-plane displacement*.

The size of the zero-plane displacement is a function of the nature of the surface in the region concerned. In an urban area, where surface roughness is large, the zero-plane displacement corresponds to approximately four fifths of the average building height. In rural regions, roughness is very small hence the zero-plane displacement is very shallow (e.g. depth of vegetation) and can often be considered negligible.

2.2.2 Ekman Layer

Above the interfacial layer the Ekman layer begins and makes up the remainder of the ABL. Within the Ekman layer momentum is obtained from the *gradient wind* (constant free stream wind unaffected by the Earths surface) to form the Reynolds stress. Reynolds stress increases from zero at the top of the ABL (gradient height) to

a maximum at the boundary with the zero-plane displacement. With respect to this research, where ground roughness is very low, it is the Ekman layer that is of importance in terms of wind speed profiles and turbulence.

2.2.3 Mean Windspeed Profile in the ABL

The mean windspeed profile through the ABL is discussed with respect to the Ekman layer with a negligible interface layer i.e. rural environment. Winds within the interfacial layer are more significant in regions of greater surface roughness, such as urban areas, since the interfacial layer would have significant depth.

The mean windspeed profile through the Ekman layer is sensitive to surface roughness which controls the surface shear stress, τ_0. For equilibrium conditions to be present in the ABL (i.e. the mean vertical velocity profile remains constant with streamwise distance), the free wind must travel a significant distance over a constant surface roughness. When equilibrium is reached, the momentum required to overcome the surface shear stress exactly balances the supplied momentum (Cook (1992a)).

The nature of the Earths surface defines the supply of momentum required for equilibrium, with less being required for smoother surfaces. This implies that different surface roughness' lead to different mean windspeed profiles being produced as demonstrated in Figure 2.2.

Figure 2.2 shows how wind speeds close to ground level are faster for smoother surfaces than at the same height for rougher surfaces (however, the depth of the ABL remains constant).

Air passing from an area of lower roughness to one of greater roughness undergoes changes in the mean windspeed profile (as shown in Figure 2.2). This transition is not instantaneous and requires a significant distance before the state of equilibrium is regained. As air reaches the surface of altered roughness surface shear stress is increased, slowing the wind near ground level. This change requires time to work up through the ABL by the action of Reynolds stresses. Further downstream, when the changes in the profile reach the gradient height, z_g, equilibrium is again reached in the altered profile.

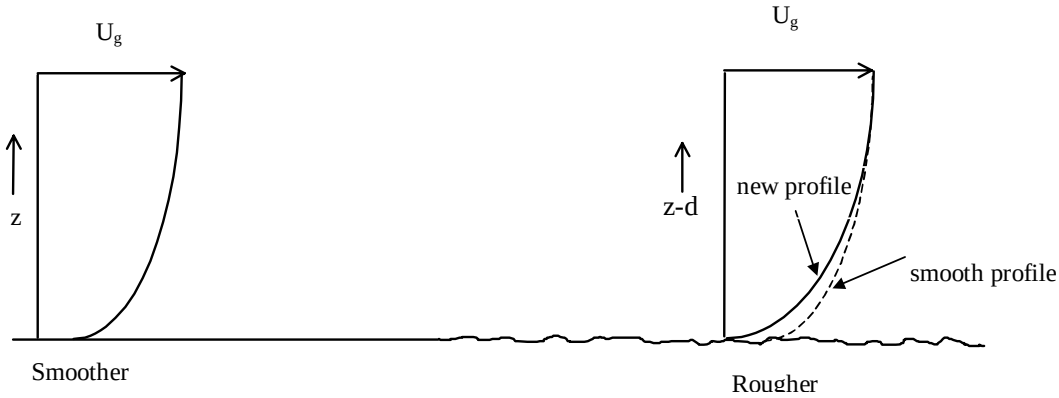

Figure 2.2 Change in mean windspeed profiles over smooth and rougher terrain

2.2.4 Models of Mean Windspeed Profiles

In 1958 Jensen showed that, in wind engineering models, it is equally as important to correctly model the wind as it is to model the building under consideration. Although this was written in the context of wind tunnel testing, the same must also apply for numerical models. The implications of such a statement are that any modelling will be useless if the simulated wind profile is incorrect. A number of methods have been devised utilising mathematical expressions that describe the region of the ABL under consideration.

From the examination of experimental data a *power law* relationship can be produced as shown in equation (2.2).

$$\frac{U(z)}{U_{ref}} = \left[\frac{(z-d)}{Z_{ref}} \right]^{\alpha} \tag{2.2}$$

where $U(z)$ is the windspeed at height z, U_{ref} is the velocity at some reference height z_{ref} (usually 10m or building roof height) and d is the zero-plane displacement height. The exponential function, α, is a characteristic of the underlying roughness of the surface which increases in value for increased roughness. The exponential, α, has typical values of 0.17 in open country terrain and 0.24 for an average urban environment.

The power law model provides adequate correlation with experimental data for the upper region of the ABL (Cook 1992). However agreement is poor within the lower areas. This presents a major limitation of the power law method if studying wind induced phenomena with respect to surface features. It is the lower regions of the ABL that are of interest in building studies and the power law proves inadequate for modelling wind speeds for such applications.

An alternative modelling technique capable of predicting wind speeds within the lower regions of the Ekman layer more accurately would be desirable in the terms of this research. One such method is available in the form of the *log-law model*.

$$U(z) = \frac{1}{\kappa} u_* \ln\left[\frac{z}{z_0}\right] \tag{2.3}$$

where κ is von Karmans constant (equal to 0.4), u_* is the surface friction velocity ($\tau = \rho u_*^2$, where ρ is the density of air and τ is the surface shear stress) and z_0 is the aerodynamic surface roughness. The other components were defined previously.

The value of z_0 is analogous to the exponential function, α, in the power law model and has values in the order of tens of millimetres for smooth rural landscapes. Wieringa (1993) provided one of the latest classifications for roughness of differing surface types shown in Table 2.1. Eight roughness classes were identified ranging from an extremely smooth '*sea*' surface to extremely rough '*chaotic*' surface (characteristic of typical city centres).

The advantages of the log law method for describing mean windspeed profiles in the ABL are (Cook (1992a)):

- It is scale dependant through the use of z_0 as a scaling parameter;
- It is derived from theory;
- It fits well near the surface.

All of the above advantages of the log law model make it well suited to wind engineering modelling especially when studying structures at ground level.

Table 2.1 Davenport Roughness Classification

z_o (m)	Surface	Landscape description
(1) 0.0002	Sea	Open sea or lake, tidal flat, snow covered plain, featureless desert, tarmac and concrete, with a free fetch of several kilometres.
(2) 0.005	Smooth	Featureless land surface without any noticeable obstacles and ridges, morass and snow covered or fallow open country.
(3) 0.03	Open	Level country with low vegetation and isolated obstacles with separations of at least 50 obstacle heights.
(4) 0.10	Roughly open	Cultivated area with regular cover of low crops, or moderately open country with occasional obstacles at relative horizontal distances of at least 20 obstacle heights.
(5) 0.25	Rough	Recently developed "young" landscape with high crops or crops of varying height and scattered obstacles at relative distances of about 15 obstacle heights.

(6) 0.50	Very rough	Old cultivated landscape with many rather large obstacle groups separated by open spaces of about 10 obstacle heights. Also low large vegetation with small interspaces.
(7) 1.0	Closed	Landscape totally and quite regularly covered with similar size obstacles with open spaces comparable to the obstacle heights e.g. homogeneous cities or villages.
(8) ≥ 2	Chaotic	Centres of large towns with mixture of low-rise and high-rise buildings. Also large irregular forests with many clearings.

Source: Wieringa, J. (1993), Representative roughness parameters for homogeneous terrain, *Boundary Layer Meteorology*, Vol. 63, No. 4, pp. 323-364.

2.3Atmospheric Turbulence

This chapter has, prior to this point, been involved in describing time averaged wind parameters within the ABL. However the wind is by no means steady. The presence of turbulence gives rise to more complicated conditions than mean values indicate. This section provides information of the driving mechanisms for turbulence and its nature, followed by the methods available for quantifying atmospheric turbulence.

Turbulence is a feature in many engineering fluid flows. Visualisation of turbulent flows show rotational flow structures in the form of *turbulent eddies*. These eddies exist over a wide spectrum of *length scales* (or sizes), the largest having length scales comparable to that of the flow boundaries and others of intermediate and small sizes. This implies, in the case of atmospheric turbulence, a vast range in eddy length scales effecting airflow.

The state of a fluid flow (in terms of turbulence) is often characterised through the non-dimensional Reynolds number (*Re*). The *Re* provides a measure of the ratio of inertial forces to the viscous forces in a flow regime. The *Re* is defined as

$$\frac{\rho l \bar{u}}{\mu} \tag{2.4}$$

where ρ is the density of the fluid, l is a characteristic length scale of the flow, $\bar{u}$ is the mean velocity of the flow and μ is the viscosity of the fluid.

The largest turbulent eddies in a flow interact with the mean flow and extract energy by a process termed *vortex stretching* (Veersteeg and Malalasekera (1995)). In a sheared flow (as in the ABL) the rotational turbulent eddies are distorted by this vortex stretching. The stretching is due to the velocity profile, as the upper end of a vortex is forced to move faster than the lower end.

Larger eddies tend to have characteristic length scales and velocities that are of the same order as those of the mean flow. This implies that the large eddies must have

high Reynolds numbers as they are dominated by inertia forces with viscous forces being negligible. Angular momentum of the inviscid large eddies is conserved during vortex stretching, leading to an increase in rotation rate and a decrease in radius. This infers that the process creates motions at smaller length and time scales. It is the stretching work done by the mean flow on the large eddies that maintains the turbulent flow. The structure of large eddies is highly anisotropic (directional) and flow dependant due to strong interaction with the mean flow whilst the diffusive action of viscosity tends to cancel out directionality at small scales making the smallest eddies isotropic (non-directional).

The large eddies continue the stretching process on smaller eddies (as does the mean flow to some degree), passing kinetic energy down through eddies of smaller sizes forming what is termed the *energy cascade*. Cook (1992) describes turbulence production and dissipation in terms of frequency. Low frequency fluctuation implies the convection of a large eddy and higher frequencies implying smaller eddies. The assessment of turbulence in terms of frequency is discussed in greater length in section 2.3.2 below.

2.3.1 Statistical Representation of Turbulence

The atmosphere is highly turbulent hence if velocity at a point in space was plotted over a time period, Δt, the subsequent plot would show random fluctuations as shown in Figure 2.3. The oscillations in Figure 2.3 represent the fluctuating gust velocities in different directions.

In order to produce a quantitative assessment of the randomly fluctuating wind, a decision must be made whether to take an instantaneous value (for example the maximum in a sample) or attempt to define the whole sample by means of statistical quantities.

It is convenient to take into account the fluctuations in velocity by defining the time-varying total windspeed U as having both mean and fluctuating components for each direction as in equation (2.5).

$$U = (u(t)^2 + v(t)^2 + w(t)^2)^{1/2} \qquad (2.5)$$

where

$$u(t) = \bar{u} + u', \quad v(t) = \bar{v} + v' \text{ and } w(t) = \bar{w} + w'$$

and $u(t)$, $v(t)$ and $w(t)$ are the time varying components of velocity, $\bar{u}, \bar{v}$ and $\bar{w}$ are the mean components of velocity and u', v' and w' represent the fluctuating components of velocity. It should be noted that the mean quantities denote average values over a time interval, say, T, where $T >> t$.

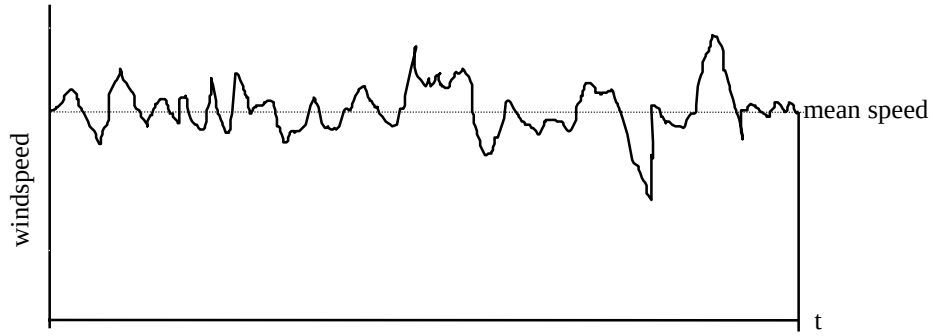

Figure 2.3 Windspeed measured through time

By this definition, the mean of the turbulent component of windspeed is zero

$$\overline{u'} = \overline{v'} = \overline{w'} = 0$$

Turbulence tends to be quantitatively described with respect to the root mean square (rms) value or standard deviation, σ, of the instantaneous velocity about the mean from a set of windspeed data. For example, for the streamwise, u, component of turbulence

$$\sigma_u = \frac{1}{n}\sum_0^n \overline{(u')^2} \tag{2.6}$$

where n is the number of measurements in a data set. There would, of course, be a rms value for each component of velocity.

Turbulence characteristics of the ABL are often represented in the form of turbulence intensities, σ/U_{ref}, which are a normalised form of the rms value defined above. Turbulence intensity is a measure of the magnitude of the fluctuating velocity component relative to the mean reference wind speed.

The covariance provides basic statistical information about the magnitude of fluctuations (of a variable) at a point, or the relationship with fluctuations (of a variable) at other points in the flow.

Covariance is defined by the following equation

$$COV(X,Y) = \overline{[(X-\mu_x)(Y-\mu_Y)]} \tag{2.7}$$

where X and Y are two variables, the overbar signifies the mean of the values in square brackets whilst μ_x and μ_Y are mean values of X and Y respectively.

Holmes (1990) discusses covariance with respect to pressures induced by the wind over the surface of a structure. He states that it is a fundamental quantity containing basic statistical information, both on the magnitude of the pressure fluctuations at a point, or on a discrete area, of a bluff body, as well as the relationship with the pressure fluctuations at other points on the body. The covariance of two pressures, c_{ij}, is defined as

$$c_{ij} = \overline{p_i'(t).p_j'(t)} \tag{2.8}$$

where $p_i'(t), p_j'(t)$ represent the fluctuating parts of the pressures at points *i* and *j* on the surface of the structure and the overbar indicates a time average. Pressures are often normalised and written in their coefficient form by dividing by the reference dynamic or velocity pressure of the wind ($0.5\rho U_{ref}^2$, where U_{ref}^2 is a mean reference wind speed).

2.3.2 Spectral Analysis

In basic terms, spectral analysis of a time series transforms data from the time domain into the frequency domain and provides an indication of how much power is associated with different frequencies.

Spectra are produced by the technique of Fourier analysis in which data is split into an infinite number of sine waves of differing frequencies and amplitudes that represent the data series when combined.

The Fourier series are represented by the following equation

$$\begin{aligned} f(x) &= a_0 + \sum_{n=1}^{\infty}\left(a_n \cos nx + b_n \sin nx\right) \\ &= a_0 + \frac{1}{2}\sum_{n=1}^{\infty}\left(c_n e^{inx} + k_n e^{inx}\right) \end{aligned} \tag{2.9}$$

where a_0, a_n and b_n are constants, $c_n = \frac{1}{2}(a_n - ib_n)$; $k_n = \frac{1}{2}(a_n + ib_n)$; *n=1,2….*

The Fourier Transform of a function, *f(x)*, is denoted by $\hat{f}(\omega)$ where $\omega = 2\pi f$ and *f* is a frequency. The transform can be made by the integration

$$\hat{f}(\omega) = \frac{1}{\sqrt{2\pi}}\int_{-\infty}^{\infty} f(x)e^{-i\omega x}dx \tag{2.10}$$

The Fourier Transform physically represents the distribution of strength of a time series or signal with frequency. In order to calculate a Fourier Transform a technique termed a Fast Fourier Transform (FFT) is utilised. For this research the FFT calculations for any spectra found were undertaken using Adaptec Scientific MathCad Version 8 software.

The Fourier series and transforms defined above assume that the series can be summed or integrated to infinity and that the data is continuous. In most practical

situations however, data is sampled over discrete intervals therefore the analysis is constrained by the data set analysed.

Production of a spectra over a discrete frequency band of *n* samples, equally spaced by a time interval of Δt, has a record length, *T*, where

$$T = n\Delta t \tag{2.11}$$

The time interval, Δt, is also termed the time resolution interval. The reciprocal of Δt is the sampling frequency, *f*, and the frequency resolution (minimum frequency in the FFT) is defined as

$$\textit{frequency resolution} = \frac{n}{T} = \pm\frac{1}{N\Delta t} \tag{2.12}$$

where *N* is the number of samples in the FFT used to calculate the spectrum. The frequency axis of the power spectrum is plotted with an interval as specified by the resolution i.e. sampling frequency/number of points in the FFT. The number of data points in the FFT is termed the order of the FFT. The higher the order of the FFT, the closer it becomes to the continuous spectrum.

At least two points per cycle of a sine wave are required if it is to be recognised. This implies that the sampling frequency must be at least twice the highest spectral frequency of interest. From this, a critical frequency, f_c, or the Nyquist critical frequency is defined as being equal to half the sampling frequency, *f*,

$$f_c = \frac{f}{2} = \frac{1}{2\Delta t} \tag{2.13}$$

A test for the presence of so called aliasing in a spectrum is to see if the Fourier Transform is approaching zero as the frequency enters the critical range $\pm f_c$. If the spectrum is approaching a finite value, then aliasing is likely.

2.3.2.1 The van der Hoven Spectrum

The van der Hoven spectrum was the first comprehensive spectrum compiled that showed the components and characteristics of the wind and weather systems in the atmospheric boundary layer in terms of frequency. Figure 2.4 shows the spectrum of the wind after van der Hoven.

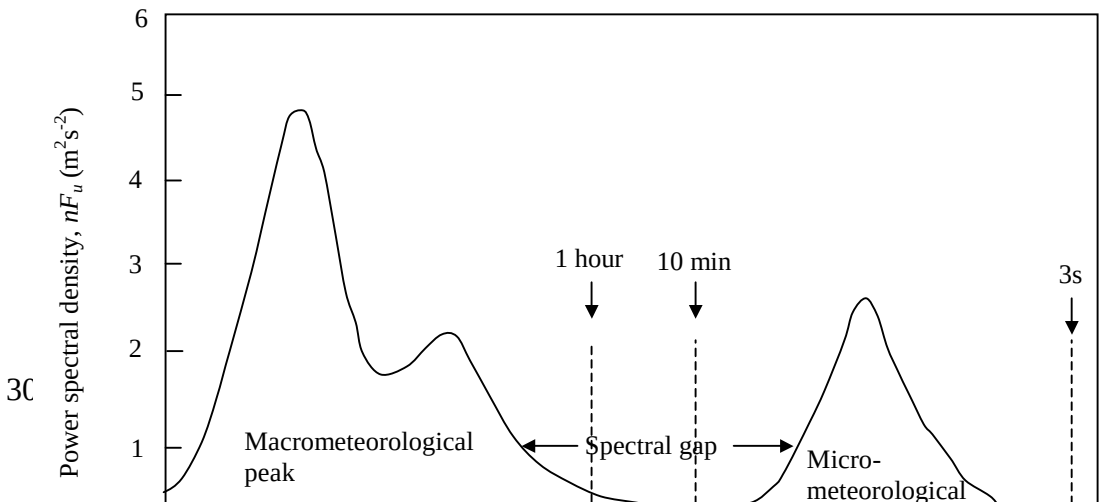

Figure 2.4 The van der Hoven spectrum
Source: Cook, N. J. (1985), ***The designers guide to wind loading on structures: Part 1*****, Butterworths.**

The van der Hoven spectrum shows fluctuations in the wind with three distinct features (Cook (1992a));

- A major peak at a frequency of 0.01 cycles/hour, corresponding to the typical 4-day transit period of fully developed weather systems, usually called the macrometeorological peak.

- A second peak comprising a range of higher frequencies which are associated with the turbulence of the boundary layer and that range in period from about 10 minutes to less than 3 seconds. This is termed the micrometeorological peak.

- The well defined gap between these two peaks is called the spectral gap in which there is little fluctuation over a range of frequency of about one order of magnitude.

The spectral gap is an important feature as it enables analysis of the macrometeorological and micrometeorological fluctuations without interference from the other influences.

2.3.2.2 Micrometeorological Power Spectrum

In many wind engineering applications it is normal to examine only the micrometeorological conditions (higher frequency region of the van der Hoven spectrum). If energy in the form of the power spectral density, $S(n)$, is plotted against frequency, n, the wind power spectrum shown in Figure 2.5 (a) is produced. The low frequency region corresponds to large eddies and high frequencies to smaller eddies.

It is obvious from Figure 2.5 (a) that there is less energy in the wind at higher frequencies.

It is common to plot the atmospheric power spectrum in the form $nS(n)/\sigma^2$,(absisca) against nL/V ,(ordinate) where $L={}^{x}L_u$, the characteristic streamwise turbulent length scale and σ^2 is the variance of the turbulence. This produces the form of power spectrum shown in Figure 2.5(b) that can be described analytically by the von Karman equation (2.14).

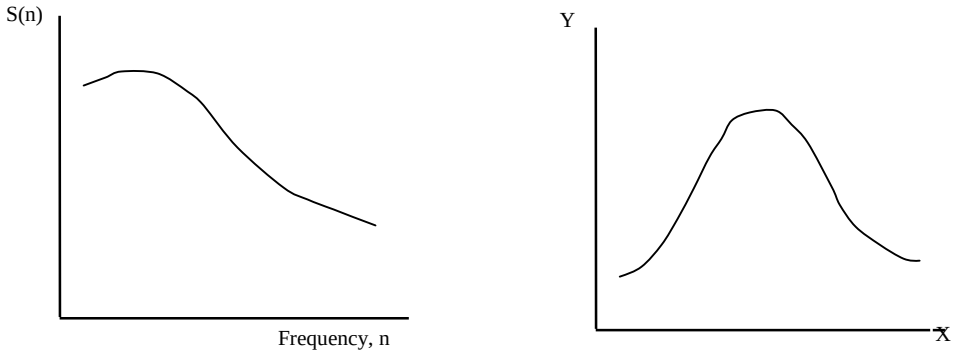

(a) Power spectrum **(b) Von Karman form of Spectrum**

Figure 2.5 Typical power (turbulence) spectra

The turbulent length scale, ${}^{x}L_u$, is a representation of the size of eddy containing the peak power in the spectrum and is a critical parameter when describing wind characteristics. Characteristic values of the length scale are in the order of tens to 1000m depending upon the mean wind speed and the height at which measurements are taken. By curve fitting using the von Karman equation (2.14), it is possible to find the turbulent length scale for a measured data set of wind velocities.

$$Y = \frac{4X}{\left(1+70.8X^2\right)^{5/6}} \qquad (2.14)$$

At lower frequencies (*the production range*) turbulence is generated by instabilities in the flow in the form of large eddies. The middle range of frequencies is termed the *inertial range* where large eddies break up transferring their momentum to smaller eddies down through the energy cascade discussed in the previous section (4.3). In the *dissipation range* (at very high frequencies) eddies within the flow become so small that viscosity becomes significant and their energy is dissipated as heat.

2.4Building Aerodynamics

Internal airflow through a structure is a function of the momentum of the air entering ventilation openings and the pressure differential between openings in the building envelope. The pressure differences between openings are controlled by the pressure distribution around the structure that is, in turn, controlled by the pattern of air flow around the structure.

Buildings can usually be described as '*bluff bodies*'. A body is defined as aerodynamically '*bluff*' when the flow streamlines do not follow the surface of the body, but detach from it leaving regions of separated flow and a wide trailing wake. Such flows are far more complex than those around aerodynamically '*smooth*' bodies, such as wings, and provide a significant challenge to the wind engineer.

This section provides information of the airflow patterns and resulting pressure distributions around a cubic structure with the incident wind (wind meeting the building face) normal and skewed to the front face (referred to as the windward face). Pressures are discussed in terms of pressure coefficients defined by equation 2.15.

$$C_p = \frac{p}{\frac{1}{2}\rho U_{ref}^2} \tag{2.15}$$

where p is the static pressure on the building surface relative to the pressure at a reference point, ρ is the density of air and U_{ref} is the reference wind velocity (taken at building roof height).

2.4.1 Incident Wind Normal to Building

When the mean windspeed of the ABL meets the windward face of the structure the velocity gradient leads to increased wind speeds higher up the face. In this case, air is brought to rest approximately two-thirds of the way up the windward face, termed the 'stagnation point'. Above the stagnation point, air flows up and over the roof of the building .

Below the stagnation point air is forced to move down the face until reaching the ground. Air moving towards the ground possesses greater kinetic energy than the slower moving incident wind at the same height. This greater kinetic energy allows the flow to move against the wind when it reaches the ground, in doing so, losing its kinetic energy until it is brought to rest. The air is then forced to reverse itself and travel with the incident wind forming a vortex close to the ground in front of the windward face as shown in Figure 2.6(a).

The presence of the vortex on the front face and the position of the stagnation point lead to a very different pressure distribution compared to that exhibited in a uniform incident wind (no shear). In a uniform flow, the point of maximum pressure is located on the centre-line of the face close to ground level. The value of this maximum is equal to the incident dynamic pressure producing a maximum pressure coefficient of unity. However, in a sheared boundary layer, the maximum pressure is

located at the stagnation point. The corresponding pressure coefficient at this point would be in the range of 0.7 to 0.9 (Cook (1992)).

In a sheared boundary layer, only flow above the stagnation point is directed over the roof. This flow possesses less kinetic energy than the unconstrained flow (due to the velocity profile). Together these factors act to reduce the separation height of flow over the roof of the cube. This, coupled with the Reynolds stress in a sheared flow lead to re-attachment of the separated flow as shown in Figure 2.6(a). The pressure distribution across the roof in a sheared layer shows high negative values at the upwind edge becoming less negative towards the downwind edge.

Air deflected laterally across the windward face separates along the line of the corner with each of the side faces of the cube. Lower down the face, flow moving around the sides originates from the vortex in-front of the windward face as shown in Figure 2.6 (b). Flow in this region is significantly faster than the incident wind at the same height. Pressure at the upwind edge of the building sides is highly negative due to the separation of flow and becomes less negative with downwind distance.

In the lee of the structure, a large separation of flow occurs and a recirculating wake forms downstream of the leeward face as shown in Figure 2.6(b). Recirculations at each corner of the leeward face are driven by the horseshoe vortex at the front face through shear layers along each side of the building. A larger recirculation can also be seen in Figure 2.6(b) that is driven through the shear layer over the roof, this vortex also tends to draw the corner vortices vertically upwards. The flow in the lee of bluff structures are very unsteady with the vortices described in the wake of a building being periodically shed.

The wake flow produced in the lee of a structure often affects the flow for large distances downstream. It is a significant distance downstream before the wind profile becomes completely independent of the upwind obstruction. The distance required for flow to return to its undisrupted profile is approximately nine times the height of the obstruction encountered (Oke (1987)).

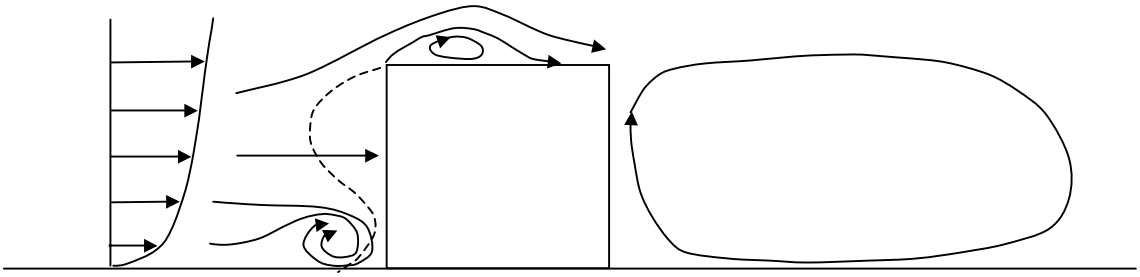

(a) Side elevation (at centre section) flow field

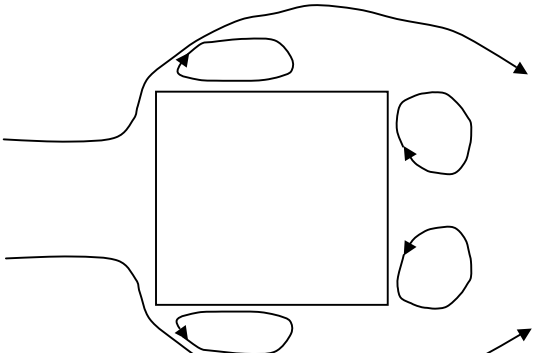

(b) Plan elevation

Figure 2.6 Airflow around cubic structure in sheared flow

Source: Cook (1992), The designer's guide to wind loading of building structures: Part 1, Butterworths, London.

2.4.2 Flow Skewed to Building

When the incident wind direction is not normal to the leading face of the structure, flow patterns and pressure distributions are altered in relation to the incident wind direction. In this case the flow separating from the upwind edge of the roof possesses a component of velocity along the line of separation. Figure 2.7 shows the formation of delta wing vortices on each of the leading (windward) edges. These vortices form as flow A (in Figure 2.7) separates near the windward corner of the roof and is displaced beneath flow B separating immediately downwind. The vorticity of flow A adds to that of B and the vortices continue to form a conical vortex along the edge of the roof as shown in Figure 2.7. The two vortices will usually have different strengths unless the wind angle relative to the recirculations is the same (at an angle of 45 degrees to the front corner).

The flow over the region of the roof between the two delta-wing vortices is attached. Pressures at the centres of the two vortices are highly negative leading to uplifting forces acting along the peripheral roof edges.

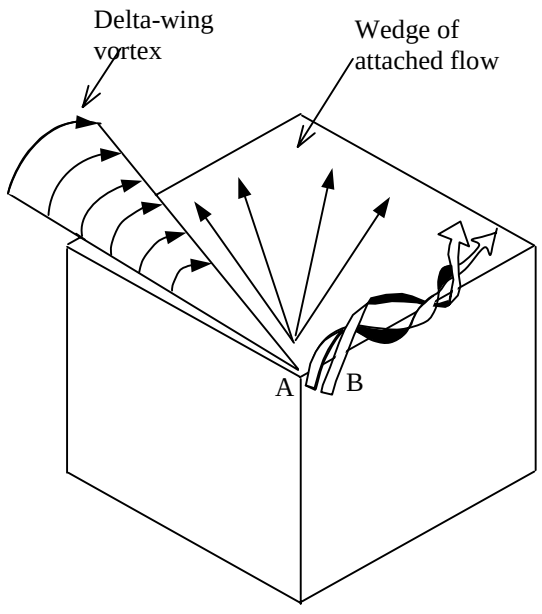

Figure 2.7 Formation of delta-wing vortices over roof with flow skewed to orientation of structure

2.4.3 Physical Modelling of Building Aerodynamics

Full-scale testing involves monitoring the required parameters on or around an actual building whether this is a purpose built structure (e.g. Silsoe structures building) or an existing building. Such experimentation can often prove very expensive in terms of time and equipment as well as manpower. If undertaken correctly, the results obtained from full-scale tests are very useful.

Some of the problems and difficulties present in full-scale modelling can be solved through the testing of a model at an arbitrary smaller scale. Many scale tests are undertaken at very small scales such as 1:100 in wind tunnels (e.g. Jozwick (1995)). Scale modelling can often significantly reduce costs relative to full-scale work and also has the advantage of control in terms of wind speed and direction. Again, time can become a major factor in wind tunnel work.

By modelling at scales smaller than full-scale, scaling effects may occur. Utilising reduced length scales, important scaling parameters such as the Reynolds number may be very different when compared to the full-scale situation and such effects can lead to discrepancies in results obtained. Although such problems are a contentious issue within the field of wind engineering, the wind tunnel provides a popular and practical research and industrial design tool. Castro and Robins (1977) undertook a comprehensive scale wind tunnel study into the flow field and pressure distributions around a cube. This research has provided much of the knowledge that is now available in many building aerodynamics text e.g. Cook (1992).

2.4.4 Computational Modelling of Building Aerodynamics

Modelling in the form of computational fluid dynamics (CFD) provides a convenient method of simulating airflow. However the highly turbulent flows in the external environment around a structure are often poorly represented through CFD models utilising common grid spacing, numerical models and domain (model) extents (Peterka et al (1996)).

Murakami (1997) states a number of complexities that make the application of CFD to wind engineering difficult in comparison with the simulation of flows within other engineering disciplines:

- Difficulty related to high Reynolds numbers
- Difficulty related to complexity of flow field with impingment
- Difficulty related to sharp edges of bluff body
- Difficulty related to inflow and outflow conditions

The problems related to high Reynolds number flows are due to the resolution of the computational grid required in the region close to the walls of bluff bodies. In wind engineering we are often concerned with small-scale flow phenomena within a large solution domain (the ABL). In order to accurately reproduce the correct conditions of zero velocity at the surface of a solid wall, Murakami discusses the need for a very fine computational grid in the near wall region.

The flowfield around a bluff body is very complicated with phenomena such as impinging, separation and vortex shedding defining the flow. Such flows are highly complex to model and are also highly three-dimensional in nature. Many of the popular methods for simulating turbulence within CFD assume isotropic turbulence which leads to problems in wind engineering where the turbulence is very much anisotropic. It is not practical to model highly 3-dimensional flow fields in two dimensions which has in the past been undertaken in studies such as Basara and Younis (1992) when modelling the flow around a surface mounted structure.

High gradients of variables associated with the flow and separation around sharp edges provide another problem associated with the computational simulation of wind engineering flowfields. The presence of many sharp edges can lead to non-physical solutions in these regions that require great care and experience to ensure problems are overcome.

The complex boundary conditions associated with velocity and turbulence profiles in the ABL must be modelled in any reliable computational simulation. This can present a non-trivial problem, a fact that Ferziger (1993) discusses. Ferziger states that the complexity of the approaching flow is almost unique to wind engineering. Richards and Hoxey (1993) attempted to develop appropriate boundary conditions for the simulation of ABL velocity and turbulence properties from experimental measurements for the lower 200m of the ABL. They made alterations to model constants in the k-ε turbulence model in order for computational profiles to match experimental data better. Such changes must be made with great care as the constants used in many of the common turbulence models are the result of detailed validation and experimentation over a wide range of engineering flow problems. The alterations made by Richards and Hoxey are not widely applicable to many flow situations but do highlight the problem of accurately simulating inflow boundary conditions in wind engineering.

The effects of an obstruction in the flow must be minimal when flow exits the computational domain (equivalent to air leaving the test area of a wind tunnel). This leads to the requirement of large computational domain sizes when modelling flows around relatively small structures. This again leads to the problems of modelling small-scale flow phenomena in large flow domains.

Zhang et al (1993) undertook a CFD study in order to investigate how incident wind profile and turbulence effected the flow patterns produced around a cube using the k-ε turbulence model. Four cases were investigated in this study:

- Case A; sheared boundary layer profile with turbulence;
- Case B; sheared boundary layer profile with no turbulence;
- Case C; uniform boundary layer profile with turbulence;
- Case D; uniform boundary layer profile with no turbulence.

The equations that are utilised in the k-ε turbulence model and the general theory of this approach are discussed in detail in Chapter 4. Each case studied was identical except for the differences mentioned.

In cases C and D, when the inlet windspeed had a uniform vertical profile, the small vortex expected in front of the windward face was absent and the stagnation point was located very close to the ground. Such results would be expected as discussed in the general theory of building aerodynamics in section 2.2. When a sheared boundary layer was introduced (cases A and B) the front vortex was simulated.

Although the results produced by Zhang et al reproduced the small vortex in front of the cube, a major discrepancy between their computational model and experimental measurements was found over the cube roof. In case D, when the incident wind had a uniform profile, flow separated at the leading edge of the roof and did not reattach until downstream of the cube. A recirculation formed within the separated region. Upon the introduction of a sheared boundary layer, the height of the separation decreased (since less air would rise over the roof possessing less kinetic energy than the free flow) however, no recirculation formed within the separation bubble. The authors stated that the failure to simulate the recirculating flow over the roof was due to the grid utilised. It was argued that the reduced separation height would produce a recirculation that was too small to be reproduced with the grid utilised. Such a statement infers that a finer grid would have improved the simulation of the roof vortex.

When undertaking CFD simulations, it is important to ensure that the grid (into which the computational domain is divided) does not effect the results obtained. This involves running a model numerous times, each time increasing the density of the grid until the results obtained do not change. Zhang et al (1993) discussed their grid independence study that involved testing two grids and resulted in ‘the difference between the mean velocity fields in the two cases being virtually identical’. This statement conflicts with the reason for the failure to reproduce the roof vortex being the grid density in this region.

Murakami et al (1996), Selvam (1996), Strathpoulos and Baskaran (1996) and Abe et al (1993) have undertaken studies similar to those of Zhang et al. All of the investigations aimed to reproduce airflows around a surface mounted cube in an ABL using the k-ε turbulence model and all failed to simulate the recirculation over the roof using this turbulence model. Reasons given for the absence of the vortex did not however, include the grids used. Murakami et al (1996) state that it is the failure of the standard k-ε turbulence model to correctly reproduce the distribution of turbulent

kinetic energy, k, around the leading edge of the building which causes the discrepancy. It was noted that the value of k is much larger at the front of the cube using the k-ε model than was found in physical experimentation.

The overestimation of turbulent kinetic energy near the frontal corner (when using the k-ε model) gives rise to a large eddy viscosity (used to model turbulence properties). This in turn leads to a large mixing effect and the elimination of the reverse flow over the roof. The overestimation of k is due to the term responsible for turbulence production, P_k that is also over-predicted.

Deficiencies in the standard k-ε turbulence model are not only found in the flow over the roof. Murakami et al (1992) discovered that the recirculating flow in the building wake was predicted to be greater than measured in wind tunnel experiments. This problem was caused by an over-estimation of the dissipation of turbulent kinetic energy, ε, in the building wake. Consequently very low values of turbulent kinetic energy were produced, leading to a reduced eddy viscosity and lesser mixing effect (and too large value of velocity) within the reverse flow. Numerous attempts to improve the k-ε model modifications have been undertaken, these include the MMK k-ε, RNG k-ε and the Kato-Launder k-ε turbulence models.

Selvam (1996) compared the Kato-Launder k-ε model (described in detail in Kato and Launder (1993)) to the standard model. The comparison involved modelling airflow patterns around the Texas Tech building (a purpose built structure for this form of test). The Kato-Launder model differed from the standard k-ε model by the modification of the term responsible for calculating the production of turbulent kinetic energy, P_k. The aim of the modified model (with respect to bluff body aerodynamics) was to improve the accuracy of flows over the leading edge of the roof and in the wake of the building. However, in the case of Selvam (1996) very little improvement was found through the use of the modifications. The distribution of k was almost unaffected and the author stated that 'if one is interested in velocity or pressure around a building, it seems that it is immaterial which procedure is used'.

The application of numerous other turbulence models to flows around bluff bodies was undertaken by Murakami et al (1992) and (1996). Comparisons of four turbulence models for the prediction of flows around a cube were presented. The turbulence models tested were:

- Standard k-ε;
- Algebraic stress model (ASM);
- Differential stress model (DSM);
- Large eddy simulation (LES).

The LES model produced results that agreed well with experimental data in terms of distributions of mean velocity, mean surface pressure and turbulent kinetic energy. The other three models did not however, perform as well as the LES with the standard k-ε model, as previously stated, producing several serious discrepancies.

The ASM was found to improve on the k-ε model although inaccuracies were still present. The recirculation over the roof of the cube was present although it extended

all of the way over the roof length. This is much further than was found from experimental data where the recirculation occupied approximately half of the roof. No improvements were found when the DSM was utilised since separation over the roof rose to a height greater than would be expected. The separated flow showed no re-attachment on the roof at all, leading to a poor pressure distribution prediction when compared to experimental data. Figure 2.8 shows the flows over the cube roof produced by each of the four turbulence models tested by Murakami along with the experimental results.

Although many turbulence models have been investigated for application to bluff body aerodynamics and the standard k-ε model widely criticised for its inadequacies within this field, it is still very popular. The ease of implementation and the scope for modification (which can help improve results) make k-ε one of the most viable models to use within CFD. However, it is always important to take great care and to validate computational results against some form of experimental data.

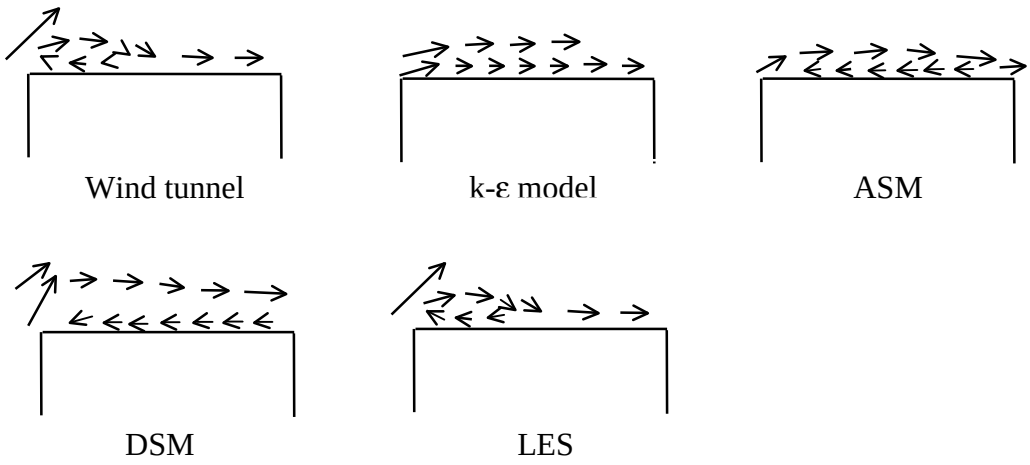

Figure 2.8 Flows over roofs predicted by numerous turbulence models

Source: Murakami et al (1996) Numerical prediction of flow around a building with various turbulence models, *ASHRAE Transactions*, vol.102, no.1, pp 741-753.

Richards and Hoxey (1992) compare the computational and wind tunnel model mean wind load predictions on the Silsoe structures building (SSB), a full-scale purpose built test structure. The wind tunnel experiments were undertaken by three separate institutions; BRE (UK), UWO (Canada) and the University of Auckland (NZ). The SSB is a purpose built portal-framed structure with 10-degree duo-pitched roof. The wind tunnel tests were conducted at 100th scale and the computational investigations made use of the standard k-ε turbulence model. The main outcome of this study was the adequacy of the computational investigations in predicting surface pressure distributions with respect to wind direction whilst the differences in results between the three sets of experimental data were surprising. The data obtained by University of Aukland were found to be closest to full-scale measured data. This paper

highlighted the care that must be taken in any wind engineering investigation and any validation of computational simulations with experimental data must be comparable.

2.5Natural Ventilation

Ventilation can be undertaken by two methods:

1. mechanical or forced ventilation;
2. natural ventilation.

Mechanical or forced ventilation requires the use of a system that employs fans in some way to drive a movement of air throughout a building. This research project however, is related to systems that utilise natural ventilation, where fans and mechanical systems are entirely absent.

Initially, the primary ventilation mechanisms are described followed by a more detailed description of the theory and mathematical descriptions of air exchange due to wind induced ventilation only. Finally a more in-depth discussion of the methods available for assessing ventilation and studying the phenomena involved is provided. Whilst ventilation due to thermal effects are described, details are provided in a qualitative sense only. This work is related to wind induced processes where thermal effects are negligible.

2.5.1 Definition of Natural Ventilation

Natural ventilation can be defined as 'the movement of air through openings in a buildings fabric, due to wind or to static pressures created by the differences in temperature between the interior and exterior of the building (generally known as the stack effect), or to a combination of these acting together' (BS:5925:1991).

Natural ventilation is subject to the variability of wind speed, wind direction, air temperature and opening configuration. Not only do these factors affect the rate of fresh air supply but also determine whether openings will act as an inlet or outlet for the air in any space within a building.

2.5.2 Natural Ventilation Mechanisms

There are three forms of natural ventilation that must be considered. The three forms are:

- Wind induced only;
- Temperature difference only;
- Wind and temperature difference.

The following descriptions of the different processes refer to a simple cubic structure with ventilation openings located on opposing faces as shown in Figure 2.9.

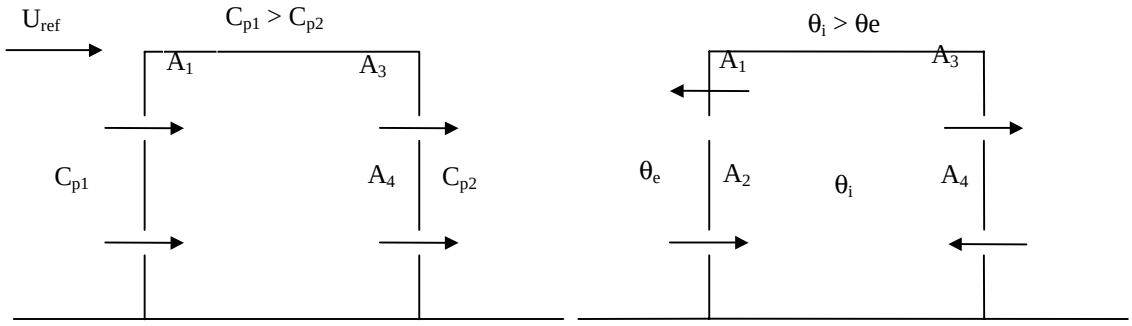

a) Natural ventilation due to wind only.

b) Natural ventilation due to temperature difference only

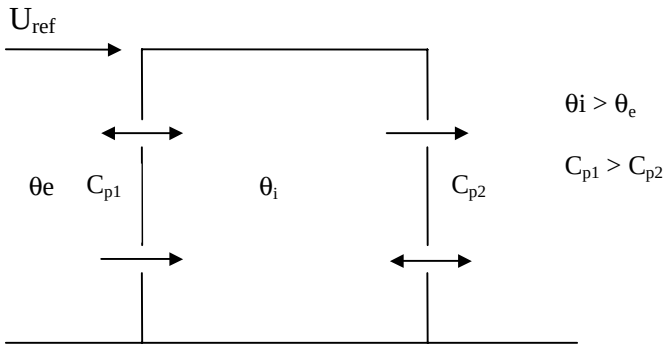

c) Natural ventilation due to wind and temperature difference.

Figure 2.9 Natural ventilation of a building by the three dominant mechanisms

Source: BS 5925:1991, *Ventilation principles and designing for natural ventilation*, BSI, England.

2.5.2.1 Wind-Induced Ventilation

Ventilation can be induced solely by the action of the wind on the surface of the building, around the location of any openings in the building envelope. The nature of the pressure distribution and the momentum of the incoming wind around the structure drive this form of ventilation.

Assuming no fluctuations in the incoming wind, flow is induced as a result of the difference in mean pressures between the building faces containing openings. From the pressure distributions discussed previously in section 2.5.1 for a simple cubic structure, air flows in through the openings located on the windward face and out of those on the leeward face as shown in Figure 2.9(a).

Papadakis et al (1996) state that for free wind speeds exceeding (approximately) 1.8 ms^{-1}, thermal buoyancy can be neglected. Hence the assumption that temperature effects are negligible here is valid in many cases (this may exclude greenhouses located in hot climates). Techniques available for modelling and assessing wind induced ventilation are discussed in detail below.

2.5.2.2 Thermally-Induced Ventilation

Air density varies approximately as the inverse of absolute temperature (BSI 1991). Two vertical columns of air maintained at different temperatures, separated by a vertical surface have different weights hence a pressure difference across the surface results. If the internal region of a building is at a higher temperature than the external environment the pressure difference leads to a flow of air through openings in the building envelope. In the case of Figure 2.9(b), warm air rises vertically and exits through the upper openings (A_1 and A_3) with this air being replaced by air entering through the lower openings (A_2 and A_4). Ventilation rate is proportional to both temperature difference and height between openings.

2.5.2.3 Wind and Thermally Induced Ventilation

When both wind and thermal effects are present, different ventilation flow patterns are produced depending upon the relative contributions of each. At low temperature differences, flow patterns are similar to those of wind acting alone. If however, temperatures are increased and wind speed is maintained at a constant (low) level a combined effect enhances the air flow through the lower windward and upper leeward openings and inhibits flow through the upper windward and lower leeward openings. In the case shown in Figure 2.9(c), a point is reached where flow in the upper windward and lower leeward openings would reduce to zero. If the temperature difference is increased further flow would reverse, approaching a flow pattern typical of temperature difference alone.

Accurate calculation for this case is difficult. Approximations can be made by calculating flow rates expected for the two separate conditions and taking the larger to apply in the combined case (BSI 1991).

2.5.3 Steady-State Ventilation Modelling

For ventilation to occur, there must be a difference between the internal and external pressures of an opening. The mean ventilation discharge, $\overline{Q}$, through any opening (with typical dimensions larger than approximately 10 mm (BSI (1991)) is a result of this difference in pressure and is described by equation 2.16.

$$\overline{Q} = {}^{+}_{-} C_d A_w \sqrt{\frac{2 \cdot |\Delta P|}{\rho}} \tag{2.16}$$

where C_d is the orifice discharge coefficient, A_w is the effective area of the ventilation opening (equation 2.17), ΔP is the pressure difference across the opening and ρ is the density of air.

Equation (2.16) assumes a turbulent flow regime is present where the effects of viscous forces are not explicitly considered but are accounted for in the discharge coefficient that relates pressure losses due to flow resistance in the opening. It is conventional to assign a value to the discharge coefficient as that of a sharp edged orifice (BSI (1991)). The total ventilation area A, consequently becomes the equivalent area associated with that particular opening i.e. the area of the equivalent sharp-edged orifice which would give the same flow rate as the opening concerned at the same applied pressure. BS:5925:1991 states that for openings such as open windows (or openings of the same scale), whose depths in the direction of flow is much smaller than the typical lateral dimensions, the equivalent area can be taken as the geometrical area.

In the case where ventilation is purely wind induced (as shown in Figure 2.9(a)) the effective equivalent ventilation opening area is found by adding the area of openings in parallel arithmetically and those in series by summing the reciprocal of the squares. Equation (2.17) demonstrates this for Figure 2.9(a).

$$\frac{1}{A_w^2} = \frac{1}{\left(A_1 + A_2\right)^2} + \frac{1}{\left(A_3 + A_4\right)^2} \tag{2.17}$$

where A_w is the effective equivalent area, A_1 and A_2 are the geometrical areas of the inlets and A_3 and A_4 are the geometrical areas of the outlets (as in Figure 2.9).

The internal and external aerodynamic pressures at an opening may be written as a coefficient, Cp_i and Cp_e respectively, the ratio of internal and external pressure to the dynamic pressure of the free wind

$$Cp_i = \frac{\left(p_i - p_{ref}\right)}{\frac{1}{2}\rho U_{ref}^2} \tag{2.18}$$

$$Cp_e = \frac{\left(p_e - p_{ref}\right)}{\frac{1}{2}\rho U_{ref}^2} \tag{2.19}$$

where, U_{ref} is the free wind speed reference velocity (usually taken at building roof height), p_{ref} is a reference pressure (usually atmospheric), ρ is the density of air, p_i and p_e are the internal and external pressures respectively.

Although external pressure coefficients will vary with position around a building, internal pressure coefficients are considered to be constant throughout the volume of the building in many cases (Harris (1990)).

If conservation of mass is introduced i.e. total inflow equals total outflow, it is possible for the ventilation to be found from the pressure data for a building. The pressure difference across any opening is found from equation (2.20).

$$\Delta p = p_e - p_i = \frac{1}{2}\rho U_{ref}^2 \left(Cp_e - Cp_i\right) \tag{2.20}$$

where Δp is the difference in pressure across the opening and the other terms are described above.

By combining equations (2.16) and (2.20), it is possible to obtain the mean ventilation discharge in terms of pressure coefficients

$$\overline{Q} = \pm C_d U_{ref} A_w \sqrt{\left|Cp_e - Cp_i\right|} \tag{2.21}$$

where the positive or negative solution is chosen to preserve flow direction.

The equations described within this chapter form a technique of assessing wind induced ventilation termed the *steady-state pressure difference method* and has been utilised in numerous ventilation studies including Choiniere (1992) and Matthews and Rousseau (1994). The method requires the measurement of pressure coefficients around the surface of sealed models or structures in the positions of ventilation openings and the subsequent application of the pressure difference equations (2.16) to (2.21) to predict ventilation rates.

2.5.3.1 Inadequacies of the Steady-State Model

There are limitations involved in using the pressure difference method and numerous assumptions are required, these were provided by Choiniere et al (1992):

- There is no stack effect (thermal effects)
- There is no pressure drop inside the building due to partitions;
- Perfect mixing is achieved;
- Airflow due to mean pressure differences with fluctuating pressure effects ignored.

The primary inadequacy of the pressure difference method derives from the assumption that ventilation rates are calculated from mean pressure differences alone.

Thus the method disregards the dynamics and spatially variable nature of the pressure field generated by the wind. The effect of this assumption on calculations will be greatest where the mean pressure difference between ventilation openings is low and turbulence is highest. Such cases may occur when ventilation openings are located close together as Cermak (1984) points out. In such situations, the root mean square (rms) pressure fluctuations are large in comparison to mean values, thus questioning the validity of applying mean values to such cases. Bruce (1975) stated that in a turbulent flow, ventilation can take place as pulses in and out of an opening. This will be unaccounted for when time-averaged pressure coefficient data is used.

Even when applying the pressure difference method to situations that are most suited to the technique can be problematic for a number of reasons. Vickery and Karakatsanis (1985) stated that for tangential wind angles, the external flow caused changes to the orifice loss coefficient (the reciprocal of the discharge coefficient squared) to occur, this was most apparent for lower velocity flows. Potter (1979) was another who found discrepancies between ventilation rates calculated from the pressure difference method and measured values found through tracer gas experiments. Tracer gas experiments involve the controlled release of a gas (in this case nitrous oxide, N_2O) and measurement of its subsequent concentration, from which the ventilation rate can be found (tracer gas tests are discussed in greater detail in Chapter 3). Potter measured ventilation rates in a room where ventilation only occurred through air leakage around the windows i.e. a low porosity enclosure that was highly suited to the pressure difference method. Potter found that ventilation rates found from the time-averaged pressures under-predicted the measured ventilation rates by 25% up to 80% at low flow rates. From the pressure time histories around the windows he found that they exhibited sign changes indicating periods of flow reversal for the openings something that would not be obvious from the use of mean pressures alone.

Potter (1979) found that flow reversal across the openings was greatest when the wind angles was parallel to the plane of the openings when the mean pressure difference would be very low. Turbulence induced fluctuations in the pressures led to ventilation flow in the form of pulsation in and out of individual openings. Harris-Bass et al (1974) observed a similar effect to Potter and for winds parallel to ventilation openings ventilation rates were found to be only just below half those measured for winds normal to the opening planes.

Ernest et al (1992) attempted to compare predicted ventilation rates using external surface pressures measured on a sealed model to those induced if openings were introduced. The two methods showed satisfactory correlation when small ventilation openings were used with wind directions normal to the openings. Predicted ventilation rates were found to deteriorate for non-normal wind directions and increased ventilation opening area.

In the case of modelling large openings (wall porosity around 10% and above) it has been found by Snyckers (1970) that the pressure distribution is affected in the near opening region when compared to sealed pressures. This may suggest that the application of sealed pressures when assessing wind induced ventilation by the pressure difference method for large openings is not practical without understanding

the effects of the openings on local pressures. Vickery and Karakatsanis (1987) also found that errors become apparent in the application of external pressure distributions measured on sealed models when attempting to determine ventilation rates for enclosures with large openings. This problem was re-iterated by Aynsley (1988) when attempted to include the internal flow resistance effects in a revised model.

2.5.4 Turbulent Ventilation Mechanisms

Prior to this point, ventilation has only been discussed with respect to mean, steady airflows. However, turbulence causes variations in wind velocity that will have an effect on the efficiency of wind induced ventilation. The following section aims to highlight the mechanisms involved in relation to turbulent ventilation processes as well as provide some details of work carried out within relevant fields.

Turbulent air exchange can occur through four physical phenomena:

- Continuous (but variable) airflow through an opening;
- Pulsating flow;
- Penetration of eddies;
- Static or molecular diffusion.

Static (or molecular) diffusion is not discussed within this report. However further information is provided by Malinowski (1971). The first three forms of turbulent ventilation are due to *spatial* and *temporal* pressure variations and will be detailed in the following sections.

The scale to which each of the different forms of turbulent ventilation is responsible for air exchange is dependent on factors associated with the building envelope and turbulence structure of the wind inducing the ventilation.

2.5.4.1 Continuous Airflow

Continuous airflow is not strictly a single flow mechanism but refers to the bulk unsteadiness of a ventilating flow due the effects of turbulence. Continuous airflow through a ventilated space occurs when openings are located at points of different pressure. Although any airflow that takes place is continuous, it is not steady since small flow fluctuations occur due to variations in external conditions i.e. due to turbulent fluctuations around the building. This case is analogous to the steady state ventilation described in section 2.6.4 except that in the former case no fluctuations were assumed to occur. Figure 2.10 shows this continuous airflow diagramatically.

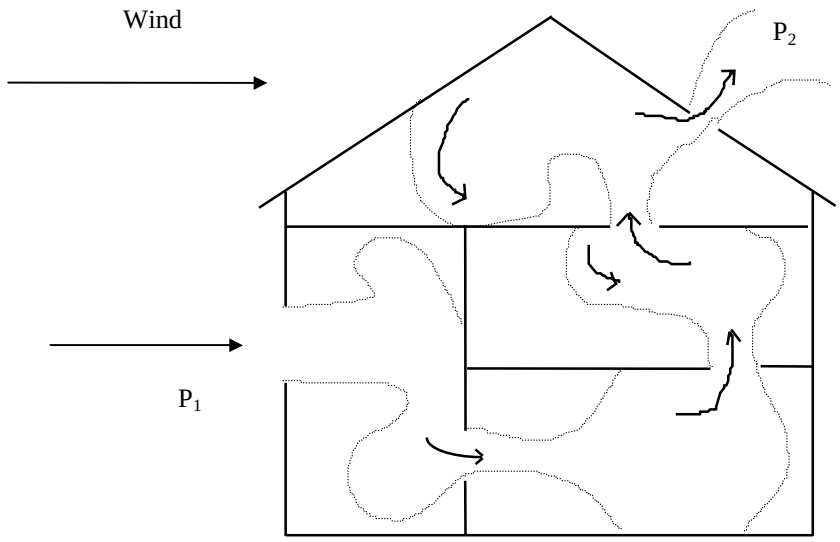

Figure 2.10. Continuous turbulent ventilating flow

Malinowski, H. K., (1971), Wind effect on the air movement inside buildings, *Proc. 3rd International Conference on Wind on Buildings and Structures,* Tokyo, pp.125-134.

2.5.4.2 Pulsating Flow

Pulsating flow can take one of two forms, both of which will be discussed. The different forms of pulsating flow are dependent upon the position or number of ventilation openings. When all openings are located in areas of equal external pressure (as is the case for a small single opening), changes in external pressures with time can cause an opening to act as an inlet or an outlet at different times. Figure 2.11 (a) demonstrates this pulsating mechanism diagramatically.

The second form of pulsating flow across an opening occurs when external pressure changes between two or more openings, leading to flows periodically changing direction. In such a case, the spatial pressure difference between openings is no longer negligible as with the first case, which was dependent only on temporal pressure differences. Figure 2.11 (b) shows this second pulsating flow case.

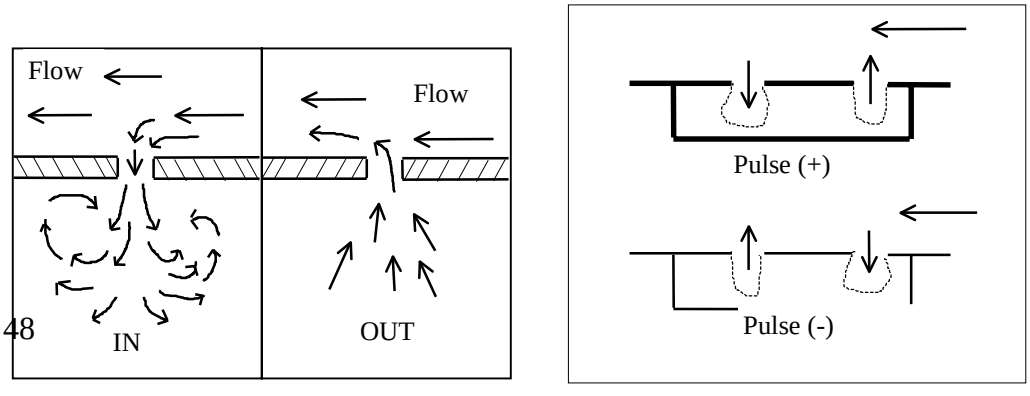

(a) Pulsating flow-single opening **(b) Pulsating flow-multiple openings**

Figure 2.11 Two forms of pulsating flow

Source: Malinowski, H. K., (1971), Wind effect on the air movement inside buildings, *Proc. 3rd International Conference on Wind on Buildings and Structures,* Tokyo, pp.125-134.

2.5.4.3 Eddy Penetration

The previous mechanisms of turbulent air exchange relied on the assumption that pressure difference across individual openings was uniform. An opening located within a turbulent region of air flow will undergo air exchange due to penetration of eddy flows with length scales in the order of, or smaller than, the opening (Figure 2.12). In this case there is both spatial and temporal pressure fluctuations within the plane of a *single* opening. This case is more likely to apply to larger openings where significant variations in pressure occur along the length of the opening.

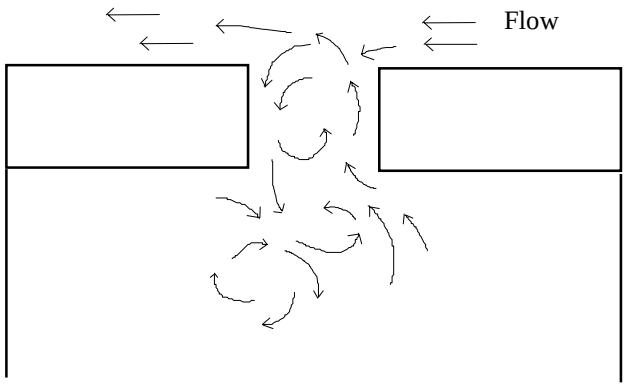

Figure 2.12 Eddy penetration

Malinowski, H. K., (1971), Wind effect on the air movement inside buildings, *Proc. 3rd International Conference on Wind on Buildings and Structures,* Tokyo, pp.125-134.

2.5.4.4 Analytical Modelling of Turbulent Ventilation

The mechanisms involved in turbulent ventilation have been discussed in the previous sections. Although the phenomena involved are understood, very little research has been carried out to quantify the processes. Haghighat et al (1991) present an approach utilising the analysis of pressure spectra in order to model the pulsating flows through the openings of a building. Power spectra analysis was discussed with respect to turbulence within the atmosphere in section 2.3.1

The effect of fluctuating infiltration is of greatest significance when the mean pressure difference across an opening is low while the turbulent components are large. This can occur in a number of situations including; single opening enclosures, enclosures with two parallel openings when thermal effects neutralise wind induced motion and when flow reversal occurs (Haghighat et al (1991)). It was demonstrated that the wind pressure spectra and the co-spectra, that describe the characteristics of turbulence in wind induced pressures on building surfaces, can be utilised directly as input to a fluctuating airflow infiltration model.

Baker (1998) outlined the application of proper orthogonal modal decomposition in the understanding of unsteady wind driven ventilation through buildings. This method was based on that used by Haghighat et al (1991). Here, fluctuating pressure data from the Silsoe structures building was utilised. By carrying out an orthogonal decomposition of the fluctuating pressures it was hypothesised that the pressures could be considered as a sum of a series of products of dimensionless spatial and time functions. By calculating the modal pressure spectra of the pressures it was described how these could be transformed in order to assess the pulsating ventilation flow that would be induced by these modal pressures. Although the calculations were based upon experimentally measured pressure data, no validation was undertaken in order to compare the calculated results. The author aimed to highlight the possible implications of the method in assessing turbulent pulsating flows.

2.5.5 Full-Scale Ventilation Experimentation

Many studies have been undertaken with respect to the full-scale modelling and investigation of airflows both within and around buildings as well as ventilation rates, pressure distributions and fluctuations. A whole variety of building types have been tested for numerous reasons including:

- Livestock buildings: to ensure efficient removal of gaseous pollutants and a suitable environment for livestock (Lynch and Brennock (1987));
- Greenhouses: to predict losses of gases (CO_2) used to enhance plant growth and/or to provide a suitable environment (Boulard and Draoui (1995));
- Buildings for human use: to provide a comfortable environment (Dutt et al (1992)).

When undertaking any modelling the identification of the processes to be studied is paramount i.e. define exactly what parameters are to be measured. The parameters to be monitored will differ depending upon the nature of the testing and can include:

- Ventilation rates;
- Leakage rates;
- Airflow patterns;
- Discharge coefficients of ventilation openings;

Ventilation rates and leakage rates are very much linked to each other. Ventilation rate tends to refer to air exchange that is designed to occur whereas leakage rate is the air exchange due to cracks and failures in a building envelope. Often, the leakage rates of a building must be known in order to find the air exchange occurring purely due to ventilation.

There have been many full-scale studies carried out with respect to the natural ventilation of greenhouses. Natural ventilation plays an important role in affecting greenhouse climate that is defined by temperature, humidity and CO_2 concentration (Boulard and Draoui (1995)).

Fernandez and Bailey (1992) aimed to quantify the natural ventilation and leakage rates in a multi-span greenhouse and to analyse the influence of wind speed, wind direction and inside-outside temperature differences. Tracer gas experiments were conducted by injecting nitrous oxide (N_2O) into the greenhouse. By the measurement of the rate of decay of concentration, the ventilation rate could be found. When studying the influence of wind speed, wind direction and temperature difference on the overall ventilation rate, only the effects of wind speed produced any discernible difference on the ventilation rate.

Papadakis et al (1996) undertook natural ventilation studies with respect to commercial greenhouses. The study involved the investigation of the ventilation efficiency with respect to positions of the ventilation openings. Here, continuous ventilation openings were utilised, which is common in greenhouses situated in hot and humid climates. As with many of the other ventilation studies the use of a tracer gas, the concentration of which was monitored, produced the results of ventilation efficiency. The major finding from this work was the negligible effect of thermal processes on the ventilation when the wind speed exceeded approximately 1.8 ms^{-1}. The effects of windspeed and total opening area were found to be far more dominant factors in the control of ventilation than temperature gradients.

When carrying out a comprehensive investigation into fluctuating airflow through large openings, Haghighat et al (1992) made use of the Bouin test house at CSTB in France. The test house had a volume of 93 m^2. Figure 2.13 shows the dimensions of the structure.

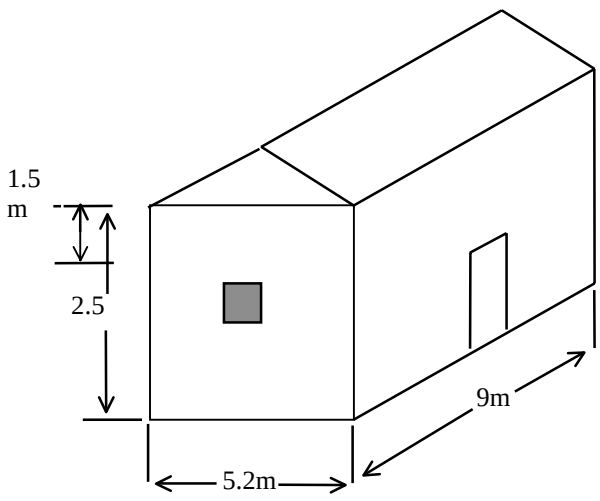

Figure 2.13 Bouin Test House, CSTB, France

Numerous parameters were measured simultaneously at a rate of 10 Hz, these were:

- Wind induced external pressures;
- Wind induced internal pressures;
- Wind speed;
- Wind direction;
- Tracer gas concentration.

Wind pressure was monitored close to the openings shown in Figure 2.13 and was equal to the difference between the total pressure and the external static pressure. Pressures were also measured at eight points within the openings both inside and outside the building. This allowed the direction of airflow to be known locally. The research aimed to produce a computer model capable of reliably reproducing the results obtained from the physical testing. Information of the results obtained from the full-scale results was scant. However the technique was relevant to the work to be undertaken in this research.

Full-scale modelling provides a very useful tool as the situation is true to life rather than being a simulation. The cost of equipment, time and expertise along with the unreliability of wind direction and speed are however, some of the disadvantages. Also, tests may only be applicable to the building tested if it is individual in nature.

A general lack of information seems to be provided from the literature obtained on full-scale investigations of natural ventilation. Because of this the overview has tended to be rather qualitative which may reflect the general pattern of such studies. Reasons for this may be the costs involved and time required to measure numerous parameters with many investigations concentrating on very few.

2.5.6 Wind Tunnel Modelling of Ventilation

Scale modelling has a number of advantages over full-scale investigations. The cost of materials and construction are reduced as are the man power requirements. If tests are undertaken within a controlled environment such as the laboratory or wind tunnel, the control of conditions such as windspeed and direction as well as influences of topography can be changed to suit individual tests.

When wind tunnel modelling is undertaken at a scale smaller than the full-scale situation it is necessary to ensure certain modelling requirements are checked in order to ensure that the similarity between the two cases is consistent. Jensen (1958) stated that “the correct model test for phenomena in the wind must be carried out in a turbulent boundary layer and the model law requires that this boundary layer be to scale as regards the velocity profile”. Cermak (1982) provides full details of the main requirements for similarity parameters that must be accounted for in scale modelling

of natural ventilation. These include undistorted scaling of the geometry, equality in the model and prototype of dimensionless numbers that characterise the flow (e.g. Reynolds number).

With respect to Reynolds number similarity it is practically impossible to match the full-scale values with small-scale models. It has been shown however, that turbulent flows are approximately Reynolds number independent when the significant Reynolds number of the flow is greater than 2×10^4 (Cermak et al (1984)). Other researchers have been critical of this and have stated that flows at small scales are still effected by so-called Reynolds number effects. Richardson et al (1995) stated that vortices in model scale experiments have much greater viscous stresses (relative to inertial stresses) than they would at full-scale. Such theories have shed doubt over the ease of Reynolds number similarity for small-scale experiments.

The type of scale tests undertaken depends on individual projects. Kayo et al (1992) undertook wind tunnel testing in order to investigate the mechanisms involved in cross ventilation and the velocity and pressure fields of airflows in and around buildings. They aimed to validate computational large eddy simulations with the wind tunnel data. Openings introduced for ventilation purposes were confined to approximately 6% of the building wall on which they were located. This was supposed to ensure that openings had little influence on the external building flows. Some discrepancy between the wind tunnel and computational experiments were found which were most obvious in regions of more negative pressure. The authors draw the attention to the fact that the approaching wind in the two cases was not exactly the same, such factors make it difficult to compare results to any great degree. The building height utilised in the wind tunnel was 18 cm. Air exchange rates were monitored using a tracer gas method. Wind velocity was measured with a thermistor anemometer and a tandem type hot-wire anemometer which is capable of providing the 3-D components of velocity. No mention was made of any Reynolds number effects that may occur due to the domination of viscous forces through small orifices that may have effected the ventilation rates.

Choiniere et al (1992) made use of a 1:20 scale model in wind tunnel tests for the prediction of wind-induced ventilation of livestock housing. By measuring external and internal pressure coefficients numerous tests were carried out including:

- Visualisation of the effect of various structural configurations on the variation of external pressure coefficients around the building and on the variations of internal pressure coefficients;
- Identification of the airflow inlet and outlet zones and the relative magnitude of ΔCps and Q_j over each opening area;
- Calculating the ventilation rate coefficients;
- Comparison of the external pressure coefficients and ventilation rate coefficients for open versus sealed scale models.

The reference wind speed used in the wind tunnel was 16 ms^{-1} (free stream wind speed of 20 ms^{-1}) which gave a Re of 6.5×10^4, based on a length scale equal to the width of the building. A scale of 1:20 and free stream windspeed of 20 ms^{-1} were used in order to exceed the recommended minimum Re of $2x10^4$ which should be maintained for natural ventilation studies (Cermak et al (1984)). The building

modelled represented a typical dairy or swine, gable roof barn, 12.2m wide by 24.4m long having side walls 2.7m high, a roof with a slope 4/12 and a 300 mm eave overhang. Opening sizes (for ventilation purposes) were 110 mm x 40 mm and 110 mm x 55 mm.

Natural ventilation was calculated, using the pressure difference method, for the low-rise structure. Choiniere et al provided theoretical estimates of airflow rates using the external pressure distributions around an open or sealed model assuming:

- Internal flow does not disturb the external pressure fields;
- Configuration of external wall openings and internal partitioning is known;
- Discharge through openings calculated using pressure difference method;
- Internal pressure coefficient assumed to be uniform inside ventilated space and inflow equal to outflow (hence continuity is satisfied).

Measured and calculated values of pressure distributions and ventilation rate coefficients are compared from numerous cases. With respect to the effects of wind direction on the wind induced ventilation Choiniere et al found ventilation rates to approximately halve when the wind was directed in a plane parallel to that of the openings compared to the wind direction normal to openings. This was significant since the predicted ventilation rates for the wind normal to the openings planes was far lower than actually measured. Discrepancy between predicted and measured ventilation rates was found to increase for increased opening area. This was attributed to larger openings leading to changes in the external pressure distribution not accounted for when predicting ventilation rates using pressures measured on sealed structures. Measurements on sealed models showed the external pressure coefficients along the ridge of a pitched roof to be considerably higher and lower (in positions of peak and minimum pressures respectively) over the leeward wall when compared to a model with ventilation openings.

2.5.7 Computational Modelling of Ventilation

With the significant improvements in both computing power and software over recent years, the role of computational modelling in the field of ventilation studies has rapidly increased. Here, computational modelling refers to investigations that involve developing and utilising computational fluid dynamics (CFD).

Earlier in this chapter, the driving mechanisms responsible for natural ventilation of structures were discussed. It was shown that the external conditions and pressure distributions around a building were responsible for the internal-external air exchange. This suggests that it is important, when modelling a natural ventilation system, to take into account the external (outdoor) wind environment. This involves modelling the region around a building and internal airflow simultaneously. Such an approach was utilised by Kindagen et al (1997) when studying the effects of roof shape on wind induced ventilation. However, not all investigations follow this path. Yuguo and Holmberg (1994) acknowledge three approaches available when considering interaction between indoor and outdoor environments;

- Use a computational domain which includes the outdoor and indoor regions of a building;
- Divide the indoor and outdoor environments into sub-domains, solve them individually and match local solutions by interpolation at joined or overlapped regions;
- Limit the computational domain to the indoor environment.

The advantage of modelling both the indoor and outdoor environments simultaneously is that the interaction between both regions can be seen directly. It is also possible to see the effects that changes in external conditions (building shape, surrounding topography and wind structure) have on internal flows as well as assess the efficiency of the computational method. The main disadvantage of such an approach is the computational power required.

In order to model internal and external regions, a large computational domain would be required. When undertaking this approach both Borth and Suter (1994) and Kindagen et al (1997) state 'rough mesh cells are suitable for CFD simulations' and 'a coarse grid is sufficient to provide a good qualitative prediction of the fluid flow'. However, it is normal procedure (in any CFD study) to ensure that the grid utilised is optimised in order to ensure it does not effect the flow structure produced i.e. grid independence is ensured.

Murakami and Kato (1989) investigated the validity of three-dimensional numerical simulations for turbulent internal airflow. When a coarse grid was tested, the model was found not to reproduce a rising stream of air between two ventilation inlets which was present in physical tests and when a finer mesh was used. This highlights the errors that could be incurred by following the statement made by Kindagen et al (above) that coarse grids are sufficient for a general view of the flow.

Kato and Murakami (1992) utilised a large eddy simulation (LES) to investigate the mechanism of cross ventilation with open windows. The building studied was a simple block with openings at ground level on the windward and leeward faces. The openings were small having areas 6 % that of each face on which they were located. This study modelled the external and internal regions of the structure to find a relationship between the two. At the inlet (opening on the windward face) the approaching flow near to ground level was not induced into the building. The reason for this was due to the external airflow pattern. It was discussed in section 2.5.1 how a small vortex forms in front of the windward face of a building when wind acts normally to the face (see Figure 2.6(a)). As shown in Figure 2.14, the air trapped in the vortex does not enter the inlet however, air above and in front of the vortex forms a downdraft that flows into the opening. As the air exited the building, via the outlet on the leeward face, the discharged jet was induced upward by the presence of the recirculating flow located in the wake of the building (flow in a buildings wake is discussed in section 2.5.1).

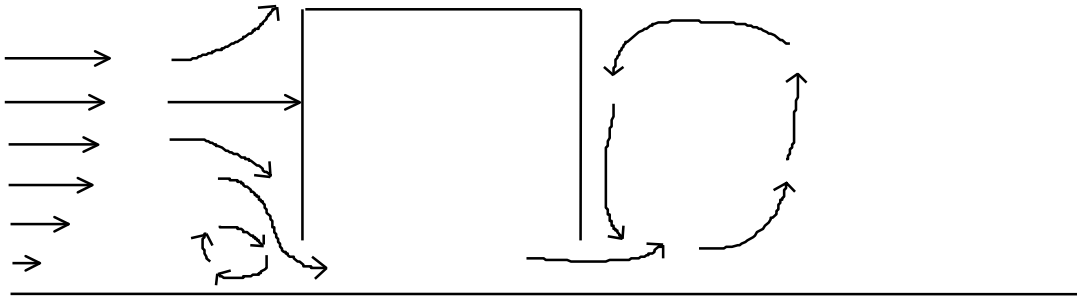

Figure 2.14 CFD model of air entering and leaving a structure

Source: Kato & Murakami (1992) , Velocity-pressure field of cross ventilation with windows analysed by wind tunnel and numerical simulation, *Journal of Wind Engineering and Industrial Aerodynamics*, pp. 2575-2586.

The number of CFD investigations, which have involved simulations of both the external and internal environments in a naturally ventilated structure, are at present low. A reason for this could be the limitations of CFD simulations of external flow fields as discussed in section 2.5.5. Great care must be taken in a study of this nature to ensure that the external conditions are simulated as accurately as possible before internal flows are studied.

There are a number of methods available when modelling wind induced ventilation computationally, as mentioned previously. The simultaneous modelling of both the external and internal environments has already been discussed. However, the reduction of the computational domain to include only the internal environment has not been considered. The main advantage of minimising the region of study to include only the ventilated region is the saving in computer resources. By utilising known conditions at ventilation openings, greater detail can be paid to the pattern of internal flows. Many studies of this nature have been involved in the modelling of mechanically ventilated spaces when assessing the efficiency of air conditioning systems e.g. Awbi (1989). However, unlike a wind induced ventilation system the air entering the ventilated region in such cases is controlled. In order to analyse a wind induced ventilation system when the computational domain is reduced, information of the flow conditions at the ventilation openings is required. Few investigations seem to have paid attention to the effects of the external environment at the inlets and outlets.

2.6Summary

One of the major factors that becomes evident from this chapter is the vast number of variables associated with wind induced ventilation. The effects of the wind structure within the atmospheric boundary layer, external building aerodynamics as well as opening geometry and configuration are all inextricably linked.

The complexity of the mechanisms involved in wind driven ventilation has lead to significant deficiencies in prediction techniques. The review of previous investigations highlighted the limitations of current assessment methods. The use of pressures measured on sealed building surfaces and the use of mean pressures alone have been identified as causes of deficiencies in the commonly applied steady-state pressure difference technique for ventilation prediction. The failure to account for the effects of turbulence driven ventilation flows is addressed within this thesis.

Computational fluid dynamics simulations of wind driven ventilation, and atmospheric flows in general, have highlighted difficulties in reproducing accurate and realistic results. With respect to computational modelling, the field of wind engineering has been shown to be highly complex due to the nature of turbulent flow fields experienced. This highlights the necessity for further investigation and validation at fundamental levels to improve CFD techniques in the application of wind induced engineering. Not only has this chapter provided the necessary theoretical basis for the remainder of this research but also acted as justification of the proposed CFD investigations and unique full-scale experimental research into wind induced ventilation.

3. FULL-SCALE VENTILATION EXPERIMENTS

3.1Introduction

This chapter provides details of the rationale, equipment, methodology and results gained from the full-scale wind-induced ventilation experiments undertaken at Silsoe Research Institute, Bedfordshire, England between May 1997 and April 1999.

An extensive discussion of the apparatus and methodology follows in section 3.3. The full-scale test structure and its location are detailed, followed by the different experimental techniques applied. The way in which the results were processed and utilised for the assessment of wind induced ventilation are then outlined.

The experiments were undertaken using a simple geometrically shaped structure with simple ventilation configurations. By investigating basic ventilation configurations it was hoped that insight into the ventilation mechanisms could be gleaned. From this any inadequacies in current predictive techniques could be identified more easily than if more complex building geometries or ventilation configurations were studied.

The chapter ends with a discussion of the results and conclusions found from the experiments. These experiments provide a rare fundamental and comprehensive full-scale study of ventilation. The results also provide data with which to validate the computational and analytical modelling discussed in Chapters 4 and 5.

3.2Full-Scale Test Structure

The purpose-built unique test structure was constructed in the form of a cube with external dimensions of 6x6x6 m^3. The cube was constructed on a large rotating turntable. This enabled the cube orientation to be altered to account for any desired wind direction. The profiled cladding on the cube was overlaid with flat PVC-coated steel sheets to provide smooth, uniform external surfaces to the walls and roof.

The structure was secured in position by four adjustable legs located internally in each corner. These could be raised hydraulically when the structure was rotated. As well as the ability to rotate laterally to any orientation required, the structure was capable of being tilted in a vertical orientation to a maximum roof angle of 10° to the horizontal. This function was not utilised in this study.

The presence of removable panels meant that the structure could be tested as a sealed structure or, by removal of the panels, as a ventilated structure. Figure 3.1 shows a photograph of the cube when sealed. The metal plates visible on the surface of the structure are the locations of surface pressure taps described in section 3.5.2.2.

Figure 3.1 Experimental test structure (sealed)

Figure 3.2 shows a photograph of the test cube with the ventilation openings present. The ventilation openings were designed to be sealed with ease for the purposes of external pressure measurement. The openings were positioned on opposing faces of the structure. Each opening measured 1x1 m^2. The openings were located such that the centre point was positioned on the vertical centre-line at a height of 3.5m above the ground. Figure 3.3 gives all of the necessary dimensional information of the cube and opening locations.

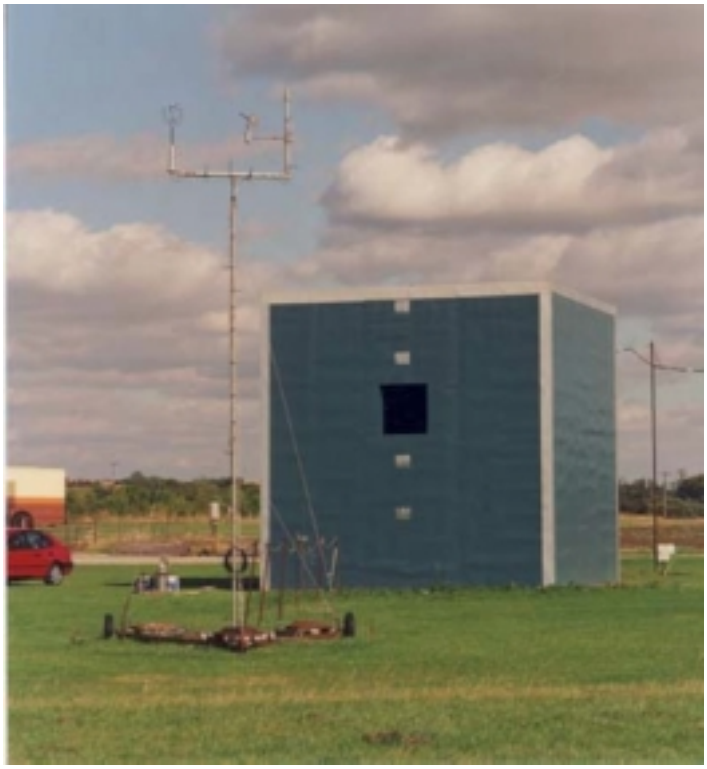

Figure 3.2 Experimental test structure (open)

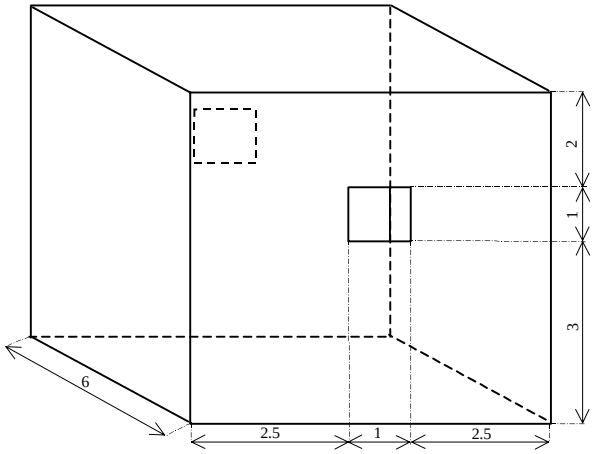

Figure 3.3 Dimensions of test cube

3.3The Site

The cube was located at Silsoe Research Institute (SRI), Wrest Park, Bedfordshire. Figure 3.4 shows a site plan of the cube and its immediate surroundings. The structure is located in rural surroundings with good exposure to winds over a wide range of directions from south west to east.

Figure 3.5 shows a view of the long fetch to the west of the test cube (photograph looking from east to west). It is obvious from this view that the cube is located in an area of low roughness and very little obstruction. "The fetch (of over 500m) is open country… and the profile is well represented by a log-law profile with a roughness length, z_0, in the range of 0.01 to 0.04m (Richardson et al (1995)). Hoxey (1999-Personal communication) undertook a series of boundary layer investigations during the period of this investigation and measured the surface roughness for the site to be 0.01m. An advantage of the rural test site was the lack of interference from obstructions and topographic features that can have a significant effect on experimental results.

3.4Experimental Definitions

Throughout this chapter (and the thesis) a number of different cases are referred to with respect to ventilation configurations and wind directions, it is therefore necessary to define and clarify the terms that will be used commonly throughout this work.

Experiments were all undertaken on the cubic structure described above. However, some experiments were carried out when the structure had no ventilation openings present, termed the *sealed* case. Tests undertaken when the ventilation openings were present are referred to as the *open* case.

Experiments were carried out with a number of incident wind directions. Tests that were undertaken with the sealed cube involved incident wind directions of 0° and 45°. The 0° case refers to the wind oriented normally to one of the faces of the cube. Here, the upstream face is termed the windward face, and the back face the leeward face. The 45° incident wind is at an angle of 45° to this same face i.e. wind approaching a corner of the structure.

With respect to the ventilation experiments undertaken on the open structure, the 0° wind direction corresponds to the incident wind being normal to the windward face containing a ventilation opening. The 90° case refers to the incident wind passing in a plane parallel to the planes of the ventilation openings. Figure 3.6 shows the incident wind directions diagramatically.

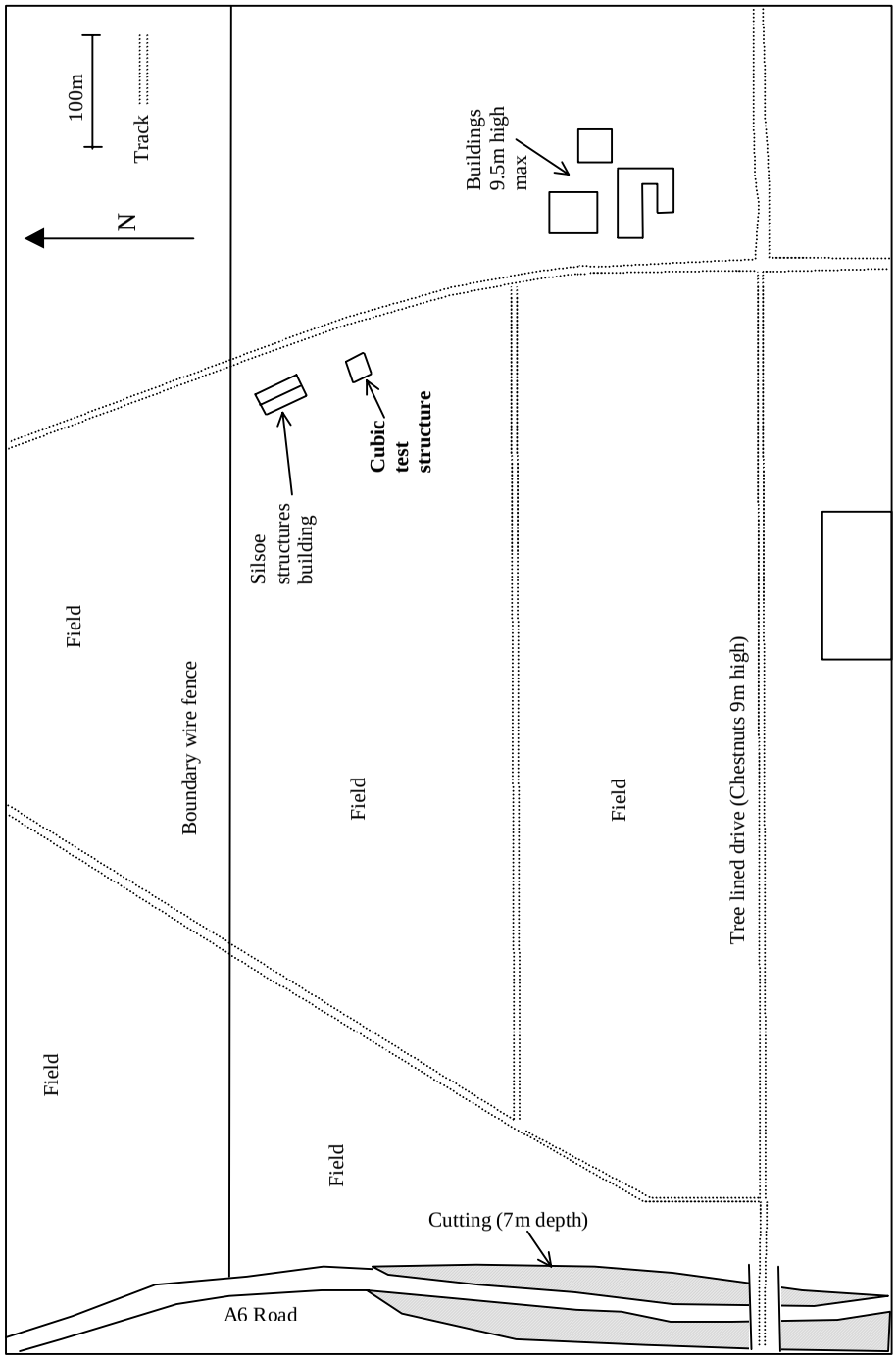

Figure 3.4 Site plan of the cubic test structure

Figure 3.5 Photograph showing fetch leading up to test cube

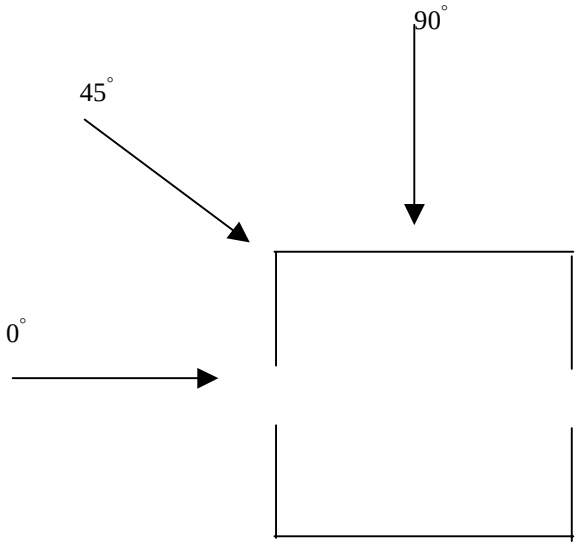

Figure 3.6 Definition of wind angles relative to cubic structure

3.5Experimental Techniques and Equipment

The following details the equipment required and the techniques utilised for the full-scale experiments undertaken. Where necessary, the operating details of equipment are provided along with methods of calibration.

3.5.1 Ultra-Sonic Anemometry

Anemometers were employed for the measurement of reference wind conditions and internal airflow distributions within the test structure.

3.5.1.1 Ultrasonic Anemometer Details

Two ultra-sonic anemometers were used, one for the reference wind measurements and the other for internal airflow measurements. The anemometers were Solent research ultra-sonic anemometers manufactured by Gill Instruments. The instrument comprises a sensing head with six ultrasonic transducers arranged in three pairs, mounted on a cylindrical base housing the electronics. The anemometer can be seen in Figure 3.7.

Figure 3.7 Ultra-sonic anemometer

The anemometer provides instantaneous readings of three components of velocity. A pair of transducers act alternately as transmitters and receivers, sending pulses of high frequency ultrasound between themselves. The transducer acting as a transmitter sends an ultrasonic pulse that propagates through the air to the receiving transmitter. The times of flight in each direction, say t_1 and t_2, are proportional to the separation distance of the transducers, L_t, and inversely proportional to the speed of sound propagation between the sensors. This final element is made up of the speed of sound in air, c, plus the air speed in the axis of the sensors, v. The times of flight of the pulse between sensors is given from

$$t_1 = \frac{L_t}{(c+v)} \tag{3.1}$$

$$t_2 = \frac{L_t}{(c-v)} \tag{3.2}$$

By solving the above equations and eliminating *c*, *v* can be solved explicitly as shown in equation (3.3).

$$v = \frac{L_t}{2}\left(\frac{1}{t_1} - \frac{1}{t_2}\right) \tag{3.3}$$

By repeating this process for each pair of transducers, a simultaneous measure of air speed in three components is produced which can be combined to give the cartesian components of air velocity. The Cartesian co-ordinate system from the anemometer output is fixed with respect to the sensor head. It is therefore necessary to know the orientation of the anemometer sensor head relative to a fixed point during measurement in order for directional features of data to be known. Distortion of air flow due to the presence of the sensor head within the flow is automatically accounted for by the instrument.

The two ultra-sonic anemometers had different frequency responses. The anemometer recording the reference wind data was capable of sampling at a maximum frequency of 20.8 Hz (one measurement every 48 ms). The anemometer used internally within the test space was capable of sampling at a frequency of 100Hz (one measurement every 10 ms). The sampling rate of the anemometers could be varied with a frequency of 5 Hz being used for both anemometers throughout these experiments (one measurement every 0.2 s). This sampling rate corresponded to that of the external pressure measuring sampling rate.

3.5.1.2 Reference Anemometry

The reference wind conditions were monitored at a location 18m upstream of the windward face of the cube and 3m to one side of the structure. The sonic anemometer was mounted on a mast in order to measure the three components of velocity at a reference height of 6m. The reference mast and anemometer can be seen in Figure 3.2 in front of the test cube.

3.5.1.3 Internal Anemometer and Mounting Rig

The internal anemometer was fixed to a mounting rig. This comprised a swing arm that was attached to a hydraulic mast fitted to a trolley that was designed to run along two steel beams secured within the test structure. The trolley could be traversed along the beams to the desired location and the mast adjusted vertically to provide velocity profiles within the internal test space. Figure 3.8 shows a photograph of the trolley and mast assembly with the anemometer fitted.

Figure 3.8 Internal trolley and rig for traversing ultra-sonic anemometer

3.5.1.4 Internal Anemometry Experimental Configuration

Measurements of internal air flow distributions were limited to a height corresponding to the centre height of the ventilation openings (3.5m). This was due, in part, to problems encountered with the leakage of fluid from the hydraulic mast and time constraints. The loss of hydraulic fluid from the mast meant it was not possible to hold the anemometer at different vertical positions.

Measurements were made for the 0° incident wind angle with ventilation openings located on the windward and leeward faces of the test structure. For the internal velocity measurements, a sampling period of 15 minutes at each location was utilised. Velocity measurements were also made for the 90° wind direction. In the 90° case measurements were only made at ventilation openings with no internal velocity profiles measured.

For the 0° case, velocity distributions were made in two orientations. Firstly, measurements were made in a streamwise orientation on a plane directly between the centres of the ventilation openings. The second orientation of velocity measurements was on a plane transversally across the width of the internal space. The transverse plane was at a streamwise distance of 3m from the front face of the cube and measurements were again at the height of the opening centres (3.5m), thus providing details of the internal flow between the cube side walls.

The physical size of the ultra-sonic anemometer and mast assembly coupled with the design of the ventilation openings presented problems in measuring velocities in the plane of the openings. The openings were constructed with beams surrounding the internal perimeter giving the openings a streamwise depth of 0.2m. Velocity measurements were not therefore possible at closer than 0.2m to the plane of the opening.

3.5.2 Surface Pressure Experiments

Surface pressures were required for the steady-state pressure difference method of predicting wind induced ventilation. They are also very useful for understanding the flow mechanisms in the vicinity of a building surface.

3.5.2.1 Pressure Measurement

Surface pressures were measured by the use of pressure taps. The tappings were simple 7mm diameter holes located centrally on $0.6m^2$ steel panels which were mounted flush to the cladding of the structure in order to maintain a smooth surface and minimise their impact on the pressures measured.

Pressure signals were transmitted pneumatically, using 6mm internal diameter plastic tube, to transducers located within the cube. The pressure taps at the surface of the cube were open to the environment. To ensure any moisture forced into the exposed openings of the taps did not adversely affect the data, drains were fitted at the point where the tapping and the tube were connected. The drain utilised was in the form of a Y-shaped connector. One branch of the connector was attached to the back of the pressure tap, another branch was connected to the pressure transducer whilst the third branch, which pointed vertically downwards was sealed using a porous bung through which any moisture drained.

The pressure transducers connected to the taps converted the pneumatic pressure into a voltage signal. The transducers contain a silicon diaphragm that deflects when a pressure is applied to it and provide an output voltage that is proportional to the applied pressure. Individual transducers were used for each pressure tap in order to monitor pressures simultaneously at each of the sixteen measurement locations.

A reference pressure was measured in addition to the sixteen surface measurements. The reference pressure was taken at a location 18m upstream of the cube at a height of 6m. This reference pressure was measured using a static pressure probe. A reference dynamic pressure was taken at the same position using a directional pitot tube and differencing the total and static pressures. This dynamic pressure was used to calibrate the pressure transducers (see section 3.5.2.3).

3.5.2.2 Pressure Tap Distributions

The 16 pressure taps were positioned on the same centre-line of the structure with five taps on two opposing vertical faces and six along the roof. The lowest tap on each wall was at a height of 1.5 m above the ground. A subsequent spacing of 1 m between the remaining four taps was used, leaving 0.5 m between the highest tap on each vertical face and the corresponding edge of the roof. The roof pressure taps were positioned such that there was a gap of 0.5m between either edge of the roof and adjacent pressure tap and again with a spacing of 1m between the remaining taps.

The pressure taps are identified by individual numbers (1 to 16) with pressure tap 1 corresponding to the lowest tap on the first vertical face. When the wind is normal to the vertical faces containing the taps, tap 1 will be the lowest tap on the windward face and 16 the lowest on the leeward face. When the wind is parallel to the faces containing the pressure taps, tap 1 will correspond to the lowest tap on the northerly side face and 16 the lowest on the southerly face. Figure 3.9 shows the pressure tap configuration around the test structure.

Figure 3.9 Pressure tap locations

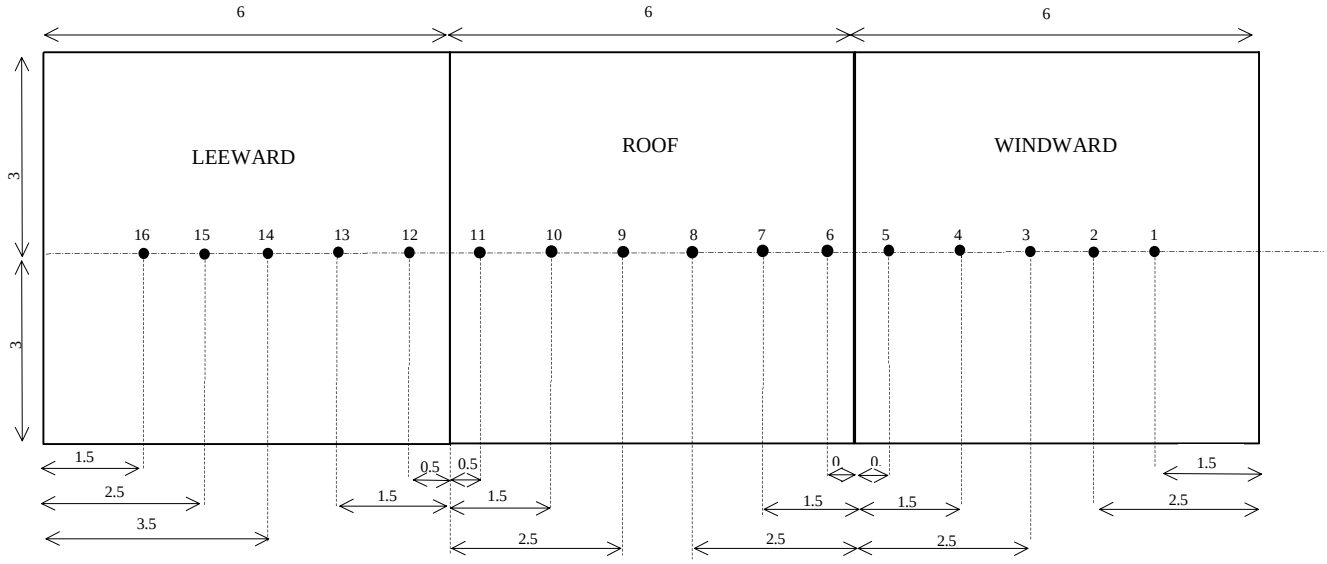

3.5.2.3 Running and Calibration of Pressure Taps

The data from the pressure taps was logged using an IBM compatible PC. Pressures were logged at a frequency of 5Hz and a single run was made for a period of one hour. Each run followed a procedure undertaken to ensure reliable results. The procedure followed for each individual one hour pressure run comprised:

- 10 seconds of zero measurements
- 4 minutes of calibration of pressure transducers
- 1 hour of pressure measurements (18000 measurements)
- 4 minutes of calibration of pressure transducers
- 10 seconds of zero measurements

The repetition of the zero measurements and calibration at the beginning and end of each run ensured that any zero drift and calibration variations could be corrected.
The method of calibration of each pressure tap was (Prevezer (1998)):

- A mean start zero value is calculated
- A mean end zero value is calculated
- The zero drift is found from the difference between values in steps 1 and 2
- A mean start calibration value is calculated from the difference between the total head from the pitot tube and the static probe
- A mean value of dynamic pressure (q), from the reference ultrasonic anemometer, over the start calibration period is calculated
- The calibration start value is calculated as the difference between the mean starting calibration and zero values, all divided by the mean q (this calibrates the reference ultrasonic anemometer with the transducers)
- The calibration end value is calculated in a similar manner
- The final calibration value is calculated as an average of the start and end values
- For each pressure measurement, an appropriate value of zero is calculated from linear interpolation between the static zero and end zero
- Interpolated value of zero is subtracted from the pressure measurement giving a zeroed pressure
- Final pressure measurement in Pascals is calculated as the zeroed pressure divided by the calibration value.

3.5.2.4 Pressure Experiment Configurations

Surface pressure measurement was undertaken for a number of experimental configurations. Although the main purpose of the pressure experiments was to provide details of the wind-induced external pressure distribution caused by wind interaction, pressures were also measured when ventilation openings were present. Pressure tappings were located at the centre of each of the plates used to cover the ventilation openings on the structure. When the cover plates were removed, these two tapping lines were used to measure the internal pressure within the test space.

Pressure measurements were made around the sealed surface of the cube for the following cases:

- 0° wind

- 90° wind
- 45° wind

For the pressure measurement data, 0° and 90° cases are discussed together as the same wind direction. The symmetry of the cubic test structure meant that the 0° and 90° wind directions both provided pressure data for the incident wind normal to a vertical face i.e. the same flow field is produced. The location of pressure taps on two vertical faces and the roof meant that a 0° wind produced windward, roof (streamwise orientation) and leeward pressures. A 90° wind angle provided the side faces and roof (in transverse orientation) pressures (Figure 3.6 defining the incident wind direction and Figure 3.9 showing the location of the surface pressure taps demonstrate this).

In addition to surface pressure measurement on the sealed cube, pressures were also measured for the 0° case with the openings present on the windward and leeward faces. This was undertaken in order to assess the effect of the ventilation openings on external pressure distributions around the openings

3.5.3 Tracer Gas Experiments

Tracer gas techniques provide the direct measurement of total airflow rate (including infiltration and turbulent air exchanges) of outdoor air to buildings. Tracer gas testing involves the release of a readily detectable tracer into the space under consideration with the subsequent concentration history being recorded. The inflow of free air can be calculated from the concentration history. Tracer gas tests provide a direct measure of the total number of air exchanges that take place within a ventilated space.

3.5.3.1 Tracer Gas Techniques

There are a number of techniques available in tracer gas testing which depend on the type and control of the injection method. The three main forms of testing are (Etheridge & Sandberg (1996)):

- Decay method. A short burst of tracer gas is injected into the space in order to establish a uniform concentration within the building and the concentration decay of the tracer is recorded.
- Constant injection. Gas is injected at a constant rate and the concentration response is recorded.
- Constant concentration method. Gas is injected into the space under control in order to keep a constant concentration.

The constant injection method was utilised for the purposes of this research. It was preferred to the decay method as it provides a direct measure of the total ventilation rate whilst the decay method provides an indirect method. The constant concentration method can be expensive because of the volume of tracer gas required, and hence it too was not applied.

The total ventilation rate, Q_T, can be measured directly from the relationship between the mass flow rate of tracer gas, $\dot{m}$, and the mean tracer gas concentration over the measurement period, $\overline{C}$

$$Q_T = \frac{\dot{m}}{\overline{C}} \tag{3.4}$$

At constant ventilation flow rate the equilibrium concentration attained is governed by equation (3.4). If the region of interest is made up of more than one zone, there may be errors in the measurement of ventilation flow rate. However 'if gas is injected only into the room where the outdoor air enters, the constant injection method will predict the correct flow rate regardless of where the concentration is measured' (Etheridge and Sandberg (1996)).

3.5.3.2 Tracer Gas Equipment

The equipment required for the undertaking of constant injection, tracer gas tests was:

- Carbon monoxide calibration gas (17 ppm concentration)
- Nitrogen calibration gas (0 ppm CO)
- Carbon monoxide tracer gas
- Carbon monoxide analyser
- Orion data logger
- Gas sampler
- Mass flow controller
- Tracer gas distribution system

Tracer Gas and Calibration Gases
The choice of tracer gas was important. An ideal tracer gas should have the following properties (Etheridge and Sandberg (1996)):

- Not be present in environment to be investigated;
- Density close to air;
- Easily measurable (preferably at low concentrations);
- Non-toxic (in occupied areas);
- Non-reactive and non-flammable;
- Environmentally friendly;

In order to undertake tracer gas experiments a number of gases were required:

- Calibration tracer gas;
- Zero gas (for calibration);
- Tracer gas.

It was decided that carbon monoxide (CO) would be utilised as the tracer gas for the experiments undertaken since it was readily available, has a density similar to that of air and an analyser was available for its measurement. The gas used was 99.9% technical grade CO stored in 50 litre tanks.

The calibration and zero gases were both utilised in the calibration of the CO analyser. The nitrogen (N_2) zero gas contained zero concentration of CO. The carbon monoxide (CO) calibration gas was a 17ppm standard CO in air mixture. The zero and calibration gas tanks were fitted with a swage lock secure valve system in order to be connected directly to the CO analyser.

It was stated earlier that an ideal tracer gas would be non-toxic if the experiments are to be undertaken in occupied areas. CO is, however, extremely hazardous since even at low concentrations it replaces oxygen in the blood stream starving the body of the oxygen it needs. The fact that it is colourless and odourless makes it impossible to detect without some form of monitor. Since the experiments were to be undertaken in an unoccupied structure, the toxic nature of the tracer gas did not cause undue risk. It was necessary to control all experiments externally and take care to ensure the test space was not accessed whilst CO was being released, or was present after tests were conducted.

Carbon Monoxide Gas Analyser – Operation and Calibration

The carbon monoxide analyser was a model 48 Gas Filter Correlation (GFC) CO Ambient Analyser manufactured by Thermo Environmental Instruments Inc. The analyser uses the technique of infrared (IR) absorption spectrophotometry. This is based upon the fact that when light is passed through a sample gas, some of the frequencies are absorbed and the remainder pass through the light. The intensity of the light source has a given distribution with respect to the wavelength. The fraction of the incident light at a certain frequency that is absorbed per path length in the medium is directly proportional to the concentration of the absorbing compound (Etheridge and Sandberg (1996)). The concentration is then found from the following equation

$$C = \frac{1}{\varepsilon_c} \log A_c \tag{3.5}$$

where C is the concentration of the absorbing compound, ε_c is the extinction coefficient, and A_c is the absorbancy ($A_c = \log\left(I_0 / I\right)$) , where I_0 is the intensity of the light entering the cell and I is the intensity when leaving the cell.

Prior to tracer gas monitoring, the carbon monoxide analyser was calibrated over a span of concentrations to ensure the concentrations measured were reliable.

The calibration exercise required the following stages:

- The CO analyser was supplied with the dilution gas (zero CO gas). Nitrogen was used as the zero CO concentration gas. By releasing this gas into the analyser manifold, zero CO was measured. The analyser reading was allowed to stabilise and then adjusted to ensure that a reading of zero was produced.
- The dilution gas line was removed from the analyser and the CO concentration standard line fitted directly. The CO concentration standard was 17 ppm. Again

the analyser was left until a stable reading was obtained when it was altered so that it read 17 ppm.

- The 17 ppm calibration gas was approximately 80 % of the upper range limit (URL) for the analyser. For this reason the equipment was adjusted to read concentrations between 0 and 20 ppm CO. Any readings above 20 ppm could not be assumed to be accurate as this would be beyond the calibrated range of the analyser.

The calibration exercise was undertaken once per week throughout the test periods or prior to any testing if a period of more than one week had elapsed since a previous test.

Mass Flow Control and Tracer Gas Distribution

Controlling the delivery of the tracer gas and its distribution into the structure for ventilation measurement is important. It was necessary to ensure that the concentration of CO emitted into the ventilated space did not exceed the detection limits of the analyser but was sufficiently high that it could be reliably analysed.

Due to the toxic nature of CO and the danger involved with pressurised gas cylinders, the tracer gas cylinder was stored in a secure tank container away from the test structure. This required an underground supply system using a 9mm internal diameter tubing, entering the structure via a service tunnel.

In order to obtain a well-mixed and evenly distributed sample in the test space, the sample was introduced at nine equally spaced points at a height of 1.5m. It was important to ensure that the gas entered the test space equally from each of the nine positions. This required the use of a sealed manifold into which the main supply pipe introduced tracer gas. Nine equal lengths of 6mm internal diameter pipes were fitted to the outputs from the manifold which were used to distribute the gas. The nine pipes were suspended from wires, fastened across the test space at 1.5 m intervals.

The mass flow controller used for introduction of tracer gas was a Bronkhurst Hitec F100 that utilised a direct relationship with voltage to control the flow. The mass flow control unit was located in a secure housing outside of the test space due to the hazardous nature of carbon monoxide.

Calibration of the mass flow controller involved the release of a gas sample through a bubble flow meter. The bubble flow meter consists of a graduated vertical glass tube. The gas sample is passed up through the tube and a bubble (or horizontal film) is produced which is carried up the vertical tube of the meter. By timing the passage of the bubble between graduations, a direct measure of the volume flow rate of the gas sample is obtained. By varying the discharge of the gas sample, a relationship between the voltage set at the flow controller and the corresponding flow rate of the gas is obtained and is used to control the discharge of tracer gas.

3.5.3.3 Tracer Gas Data Acquisition

The mass flow rate of the tracer gas released into the test space and the subsequent concentrations of tracer gas were recorded on an Orion data logger which undertook the analogue to digital conversion required for data acquisition. The data logger was connected to an IBM-compatible 386 computer that logged CO concentration and mass flow rate of CO released. The CO analyser limited the frequency of data acquisition to 0.1Hz.

The CO analyser was set so that it offered two scales over which concentrations were measured. One channel of the analyser recorded concentrations between 0 and 10 ppm and a second between 10 and 20 ppm.

3.5.3.4 Tracer Gas Experimental Methodology

All tracer gas experiments were controlled externally due to the risks involved in the release of carbon monoxide. A control box was located safely outside of the test space from where it was possible to control the volumetric flow rate of tracer gas into the test space, and to monitor concentrations measured by the CO gas analyser. Figure 3.10 shows a schematic of the experimental arrangement in relation to the test structure.

The steps followed for each experiment were as follows:

- Check tracer gas cylinder for leakage;
- Begin release of CO tracer gas;
- Allow CO concentrations to increase until within measurable range;
- Start reference anemometer logging;
- Start logging tracer gas concentrations and mass flow rate;
- Continue to ensure concentrations are within calibrated concentrations (0-20 ppm);
- Measure experimental variables for period of experiment (at least 30 minutes);
- Turn off tracer gas release;
- Allow internal CO concentrations to reduce before entering test space.

Tracer gas tests were undertaken for periods of not less than 30 minutes in order to provide a representative data set.

3.5.3.5 Tracer Gas Experimental Configurations

Tracer gas tests were carried out for the following experimental configurations of incident wind direction and opening position and number:

- 0°, 0 openings (to establish leakage);
- 0° wind, 2 openings;
- 90° wind, 2 openings.

Section 3.4 defines the orientation of the cubic structure relative to the incident wind direction for further clarification.

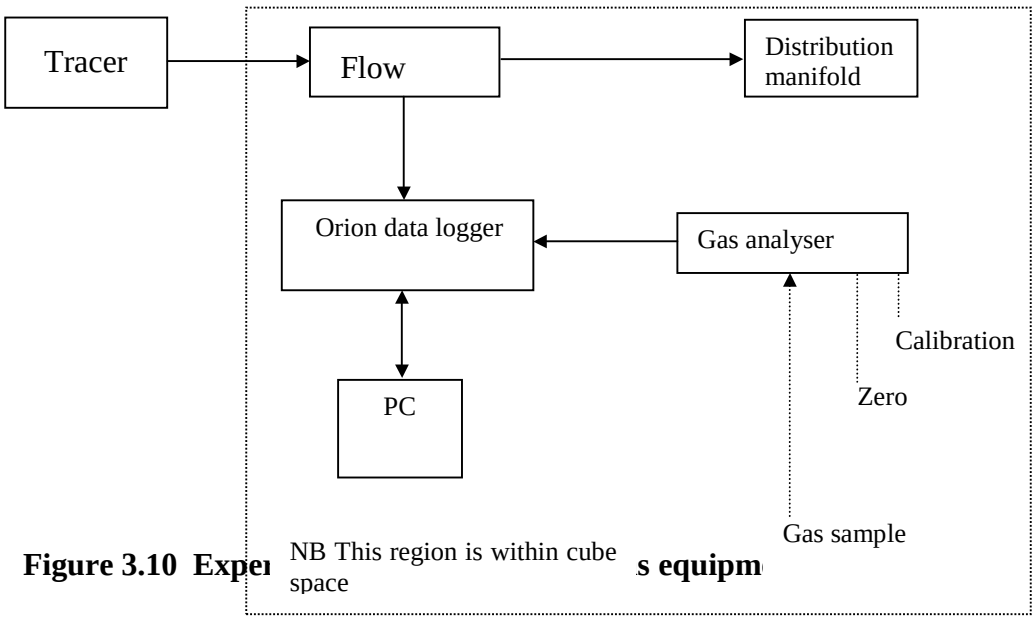

Figure 3.10 Experi s equipm

3.6Presentation of Results

The proceeding sections of this chapter deal with the results obtained from the experimental techniques described above. Certain terminology and conventions are used which should first be clarified:

- A right-handed coordinate system is adopted such that,
- x increases with streamwise distance
- y is the lateral distance
- z is the vertical distance.

- Velocity components u, v and w correspond to planes x, y and z respectively;
- Lengths are given as non-dimensional distances using the relevant cube dimension, $x_{cube,}y_{cube}$ and z_{cube} as the normalising function;
- Velocities are non-dimensionalised using the reference wind speed for each run, U_{ref};
- Pressures are given in coefficient form i.e. normalised by the reference dynamic head, $0.5\rho U_{ref}^2$;
- Discharges are non-dimensionalised using the opening area of a single ventilation opening and the reference wind speed, A and U_{ref} respectively;

3.7Full-Scale Experiment Results

3.7.1 Reference Velocity Data

The reference anemometer recorded wind speed data throughout all of the experiments undertaken. Since reference wind speeds were measured only at a single point the data available about the nature of the incident wind was limited in terms of velocity and turbulence profiles. Table 3.1 shows a representative sample of the mean wind speed and related turbulence quantities measured by the reference anemometer.

Table 3.1 Typical reference wind characteristics

Quantity	Units	Value
U_{ref}	ms^{-1}	11.91
σ_u	ms^{-1}	2.58
σ_v	ms^{-1}	2.05
σ_w	ms^{-1}	1.14
Turbulence intensity	-	0.22
u_*	ms^{-1}	0.744
${}^{x}L_u$	m	77
$\overline{u'w'}$	$(ms^{-1})^2$	0.33

Velocity spectra corresponding to the reference velocity data were calculated using 4096 samples collected at a frequency of 5Hz for periods of one hour. Mathcad version 8 was used for performing the fast Fourier analysis required to transform the velocity data from the time domain to the frequency domain. Figure 3.11 shows a log-log plot of the calculated spectral density, *S(n)*, versus the frequency, *n*, for each of the three velocity components.

Also shown on Figure 3.11 is a theoretical high frequency decay line with a slope of –5/3. The theoretical, –5/3, gradient line is highly significant in power spectra analysis. Firstly, since the –5/3 line is derived from the von Karman spectrum (equation 2.13) it defines whether a spectrum is behaving correctly and whether the experimental data are valid. It should be noted that the theoretical decay line has been displaced for ease of comparison with the experimental spectra decay.

The region over which the experimental data has a gradient of –5/3 corresponds to the inertial sub-range that can be seen to be present for frequencies of between approximately 0.1 and 1 Hz. This implies that the inertial sub-range has been correctly shown and is a method for proving the reliability of the spectra. For

frequencies greater than approximately 1 Hz, the effects of aliasing or the proximity of the ground distort the spectrum of Figure 3.11 although the exact cause cannot be identified.

The low frequency region of Figure 3.11, where the experimental spectra exhibit gradients of less than –5/3 shows the presence of the production range of turbulence. In this region turbulence is generated in the form of large eddies produced by instabilities of the mean flow.

Figure 3.12 shows the normalised streamwise velocity spectrum, $nS_{uu}(n)/\sigma_u^2$, versus frequency, n. From this plot it is possible to identify the frequency containing the highest spectral density for the streamwise velocity component of approximately 0.02 Hz.

In Figure 3.13, the non-dimensional spectral density, $nS_{uu}(u)/\sigma_u^2$, versus the log of the non-dimensional frequency, ${}^{x}L_u n/U_{ref}$ is shown for the streamwise component of velocity along with the theoretical von Karman curve, where U_{ref} is the mean reference velocity, σ_u^2 is the variance, n is the frequency, S_{uu} is the spectral density for the u component of velocity and ${}^{x}L_u$ is the characteristic length scale of the dominant turbulence in the streamwise direction. Fitting the von Karman curve to the experimental results provided a convenient method for the determination of the longitudinal length scale of turbulence for the measured wind velocity data. The longitudinal length scale is an important characteristic of an atmospheric boundary layer as it describes the size of the predominant turbulent gusts for the height of velocity measurement.

Finding the best fit of the von Karman spectrum to the experimental data involved identifying the peak of the non-dimensional spectral density. Differentiation of the von Karman spectrum shows the peak to occur when the non-dimensional frequency, ${}^{x}L_u n/U_{ref}$, equals 0.146 (found by differentiating von Karman equation (2.14)). Substituting this maximum frequency into the non-dimensional frequency expression provides a first approximation of the integral length scale. From this first approximation it is possible to find a value of ${}^{x}L_u$ which provides a best fit of the von Karman curve on the experimental spectrum. The longitudinal length scale that provides the best fit curve in Figure 3.13 is 77m.

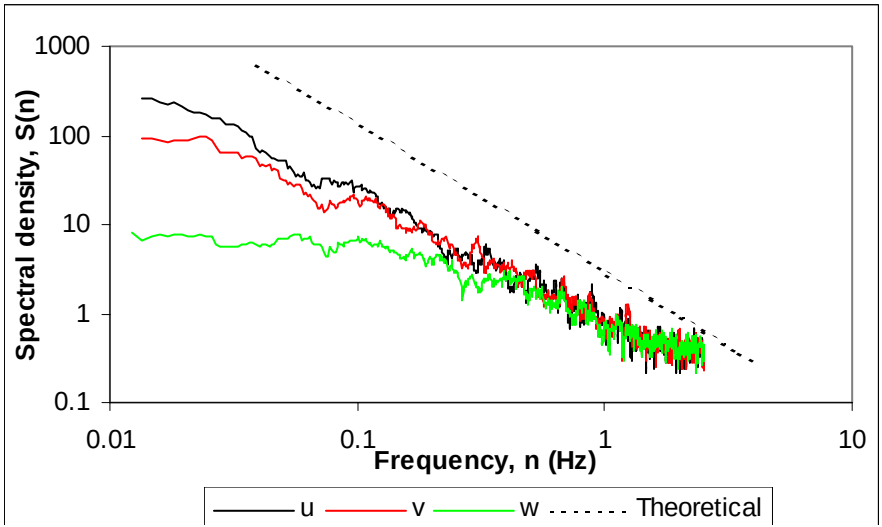

Figure 3.11 Velocity spectra of reference wind

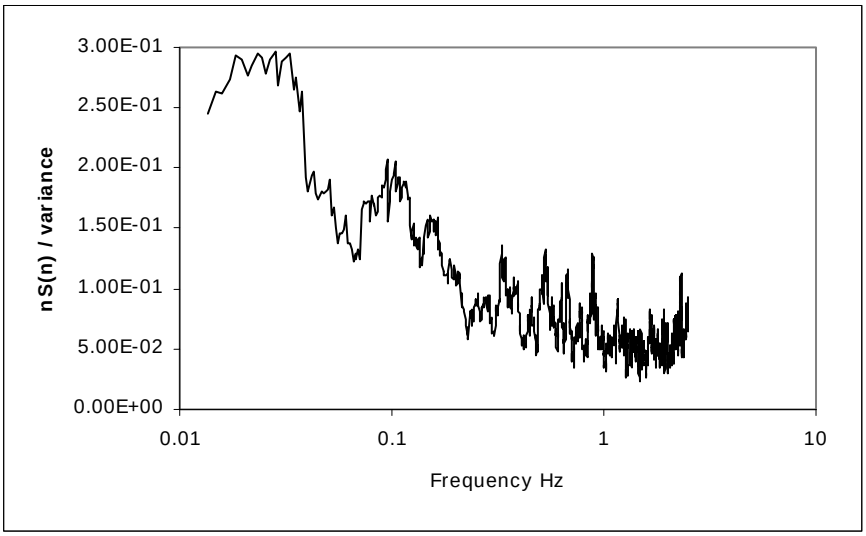

Figure 3.12 Streamwise velocity spectra

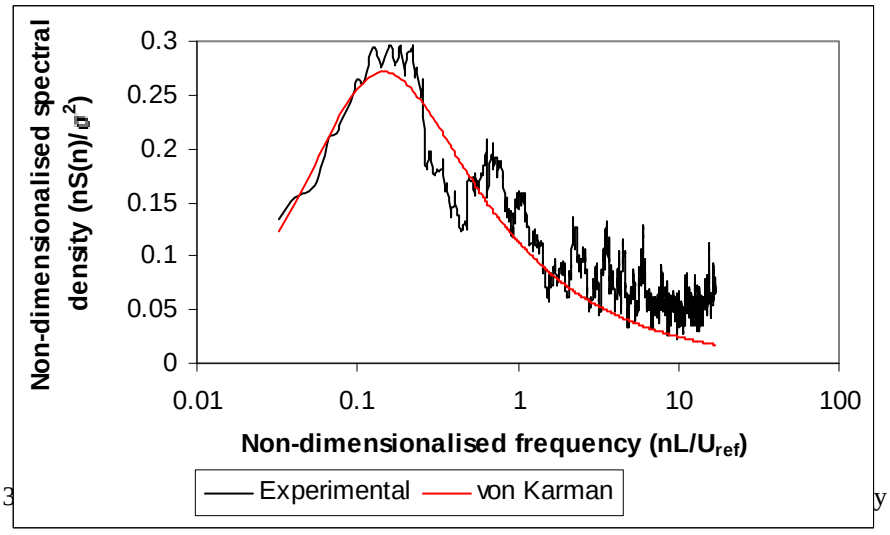

Figure 3 y

3.7.2 Internal Velocity Measurements

The internal anemometer was manoeuvrable, making it possible to determine velocity profiles within the ventilated space and so gain an insight into the wind induced flow field produced.

Figure 3.14 shows the velocity profiles of the three velocity components on a plane directly between the centres of the ventilation openings for the 0° incident wind angle (wind normal to openings). The streamwise component of velocity can be seen to be significantly higher than either the lateral or vertical components.

The velocity is greatest close to the inlet owing to contraction when passing through the ventilation opening. Peak inlet velocities are approximately 90% of the free stream reference velocity (measured at a height of 6m). Streamwise velocity decreases with distance through the cube away from the inlet. The minimum streamwise velocity was found to occur approximately three-quarters of the way through the cube. This minimum is less than 50% of those measured near the inlet. From this minimum, the velocity increases as air approaches the outlet and exits the cube. From continuity, the flow entering the cube must equal the flow leaving. With ventilation openings of equal area the velocity at each opening must also be equal (with negligible density variations). It is obvious from Figure 3.14 that the velocities are not equal at the inlet and outlet. The explanation for this difference is due to the positions of velocity measurement. It was not possible to measure velocities in the planes of the openings due to the physical size of the anemometer used. At the inlet, velocity measurements would be measured at a point where the flow is at (or close to) its maximum contraction whilst at the outlet the flow will not have contracted to the same extent. For this reason, velocities measured close to the inlet were greater than those at the outlet.

In comparison to the streamwise velocity, the lateral component is almost insignificant and can be seen to be very close to zero with little variation. The vertical component is also very small. However, it does show more variation than the lateral component profile. As air enters the opening (at the centre point of the opening) it exhibits a slightly negative vertical component (air is directed towards the ground). This negative vertical component increases towards zero with distance through the cube and is very close to zero before the mid-point. From this point the vertical component becomes insignificant.

Figure 3.15 shows profiles of the three components of velocity in a lateral orientation, centrally across the cube for a 0° incident wind direction. Although it was not possible to make velocity measurements across the full width of the cube (sidewall to sidewall), the general velocity distributions are clear from the measurements made.

Even halfway through the cube (where all of the velocities were shown to reduce significantly in Figure 3.14), there is a much higher streamwise velocity at the centre line with a significant reduction in velocity with distance to either side of the centre. This would suggest the presence of a strong central jet of fast moving air with much slower moving regions in the areas away from this dominant jet, with velocities reducing towards zero approximately 25% and 75% of the way across the cube.

Further measurements closer to the side walls would have shown if these velocities continued to decrease, but further measurements were not possible in the available time.

The lateral component of velocity for this lateral distribution displays more variation than was found for the same component in the streamwise orientation. The lateral component across the cube exhibits very low values centrally in the cube where the streamwise velocity is high (the prominent jet). To either side of the central position, the lateral component can be seen to increase in magnitude (although the directions are different). One side of the centre shows the lateral component increasing to a maximum positive value before decreasing back towards zero, a mirror image of this occurs to the other side of the central measurement, although, the signs are reversed. The lateral velocity profile shows the widening of the central jet as it spreads across the internal space as the lateral components increase before again decreasing towards zero and changing sign again. The vertical component of velocity in this lateral orientation is not shown as variation was found to be insignificant.

3.7.3 Assessment of Mean Ventilation from Anemometry Measurements

Measured velocities at the centre of the opening provided data of the air flowing into or out of the test space. Integration of the velocity over the opening area provided a mean discharge for each opening. Two major shortcomings in this method were identified in this instance. Firstly, using only a single measurement in the opening would induce errors since the velocity in the centre of the opening will be greater than around the edges. The assumption that the velocity at the centre of the opening is representative of the whole opening would lead to an over estimation of the flow through the opening. Secondly, it was not possible to measure velocities in the plane of the opening (as previously discussed), instead they were made at a distance of 0.2m from the plane of the opening.

For the conservation of mass to be observed for the ventilating flow through the cube, flow entering the ventilated space will equal that leaving (assuming an incompressible flow). It was found in the experiments that measured velocities at the inlet and outlet differed, this would therefore produce different discharges for the openings. This highlighted the problems of making a single measurement for each opening as the distributions of flow through the inlet and outlet were obviously different.

The effects of the flow profile in the opening had to be accounted for when assessing the discharge through the openings. The best way of accounting for this would have been to make measurements at different positions within the opening however, this was not undertaken. The two identified problems were overcome by making use of computational simulations of wind induced ventilation of the cube (these are discussed in detail in Chapter 4).

CFD simulations of the ventilating flow field provided significantly more detail (these are discussed in Chapter 4). CFD simulations calculated velocities at nine points within each opening. Using the average of the measured and computed velocities at the position where experimental measurements were taken (0.2m from opening

plane), a correction factor was defined. This factor accounted for the flow over the whole of the opening and for the problem of not being able to measure velocities

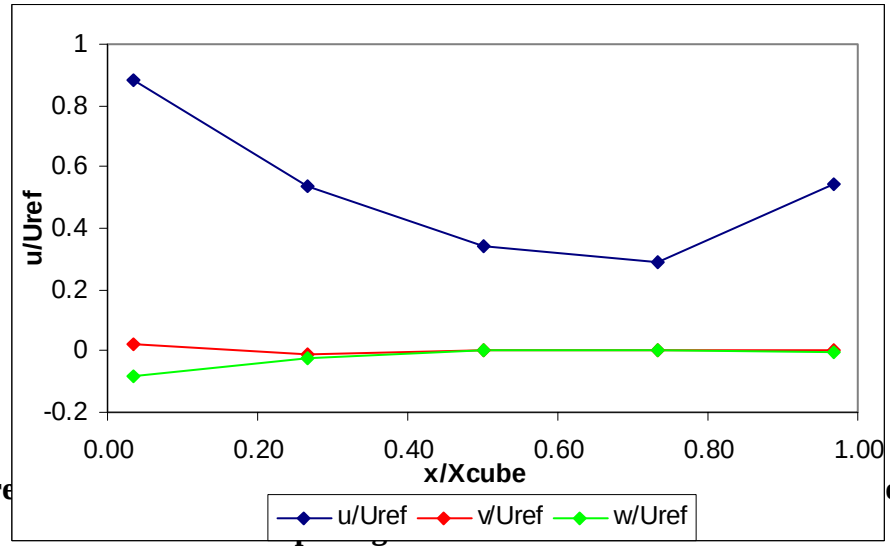

Figure **etween**

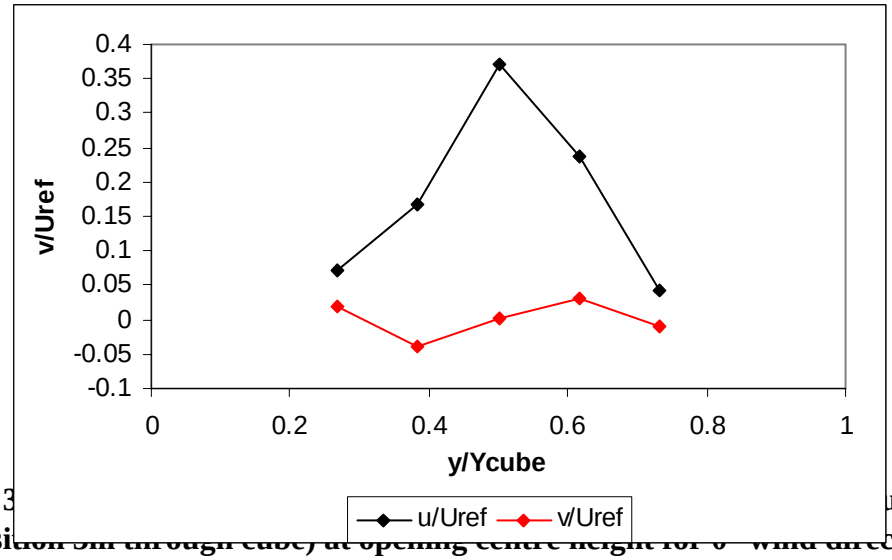

Figure 3 **ube (at a position 5m through cube) at opening centre height for 0° wind direction**

directly in the plane of the openings. The measured, mean ventilation rate, $\overline{Q}_{measured}$, was found from

$$\overline{Q}_{measured} = \overline{u}_m A \tag{3.6}$$

where $\overline{u_m}$ is the mean, measured velocity (0.2m from plane of opening) and A is the opening area.

The measured ventilation rates were then corrected by applying the correction factor, F,

$$F = \frac{\overline{u_{0_{CFD}}}}{\overline{u_{m_{CFD}}}} \tag{3.7}$$

where $\overline{u_{0_{CFD}}}$ is the mean, computed velocity over the opening area and $\overline{u_{m_{CFD}}}$ is the mean, computed velocity at the point where experimental measurements were made (0.2m from opening plane).

The corrected ventilation rate was then found from

$$\overline{Q}_{corrected} = F\overline{Q}_{measured} \tag{3.8}$$

Table 3.2 and 3.3 provide the measured ventilation rates for the 0° and 90° wind directions respectively. For the 0° case, the measured values for both windward and leeward openings are provided along with the corrected values. Measured values for the two side openings are provided for the 90° case. It is clear that for the 0°, the correction of the ventilation rates brings the values for openings much closer together than was indicated by the initially measured values. The mean ventilation rate was found from the mean of the two corrected values.

3.7.4 Mean Surface Pressure Distributions

External surface pressure distributions are discussed in the following sections with respect to the angle of the incident wind relative to the cube. The wind normal to the cube is discussed, followed by the 45° wind direction case.

Table 3.2 Ventilation rate assessments from anemometer for 0° wind direction

	Windward opening	**Leeward opening**	**% difference**	**Mean ventilation rate**

Measured ventilation rate, $\overline{Q}/U_{ref}A$	0.88	0.68	22	0.78
Corrected ventilation rate, $\overline{Q}/U_{ref}A$	0.67	0.71	6	0.69

Table 3.3 Ventilation rate assessments from anemometer for 90° wind direction

	Side opening 1	**Side opening 2**	**% difference**	**Mean ventilation rate**
Measured ventilation rate, $\overline{Q}/U_{ref}A$	0.107	0.109	2	0.108
Corrected ventilation rate, $\overline{Q}/U_{ref}A$	0.113	0.115	2	0.114

3.7.4.1 Normal Wind Direction

Figure 3.16 shows the windward face pressure distribution for the wind normal to the windward face of the cube. The maximum pressure is located between two-thirds and three-quarters of the way up the windward face. The maximum measured pressure coefficient on the windward face was measured to be approximately 0.87. The number of measuring points make it difficult to establish exactly where the maximum value is located.

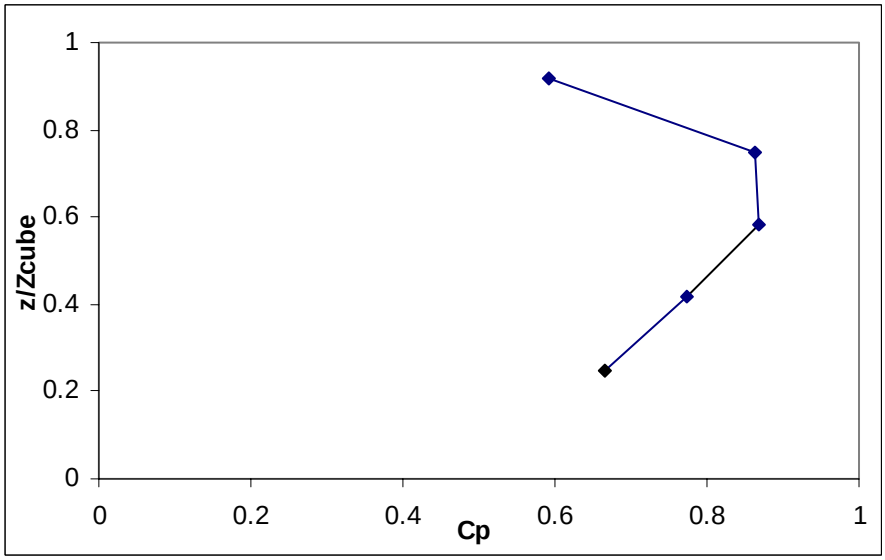

Figure 3.16 Windward face pressure distributions for 0° wind direction

Above the point of maximum pressure, values decrease with distance towards the leading edge of the roof of the cube. Below the peak pressure, values also decrease with distance towards the ground.

Figure 3.17 depicts the pressure coefficient distribution measured over the roof of the cube for the wind normal to the windward face. The streamwise distribution is measured in a streamwise orientation along the roof centre-line (measured using the 0° orientation of the cube). The lateral distribution is measured across the width of the roof, half way along the streamwise length (measured using the 90° orientation of the cube).

The streamwise distribution shows a large negative peak pressure not far from the leading edge of the roof with a recovery of pressure with distance along the roof towards the leeward edge. The peak negative pressure coefficient of approximately –1.2 was located approximately 25% of the way along the roof. This distribution is consistent with the separation, recirculation and reattachment of flow over the leading edge and roof of a cube as discussed previously in Chapter 2. The lateral distribution of pressure across the roof shows far less variation with pressure coefficients of around –0.8 measured across the full width of the roof.

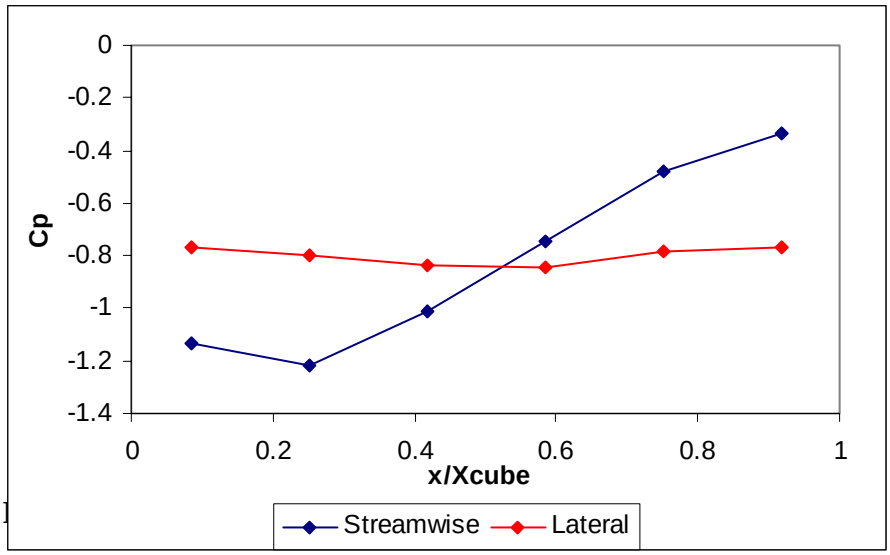

Figure 3.18 shows the mean pressure coefficient distribution along the vertical centre-lines of the sides of the cube, measured simultaneously. It is obvious from the plot that the pressures on both sides of the cube are almost symmetrical in terms of mean pressures. These mean pressures will always show small discrepancies due to

turbulent fluctuations. The pressure up the cube sides exhibit negative pressure coefficients varying from between –0.6 and –0.7.

The leeward pressure distribution for the 0° case is shown in Figure 3.19. The leeward face exhibits a negative pressure (suction) over its entire height. This is due to the leeward face being located within the large separated flow in the building. The pressure varies between –0.3 at the upper and lower areas of the leeward face and –0.4 at the tap 60% of the way up the face.

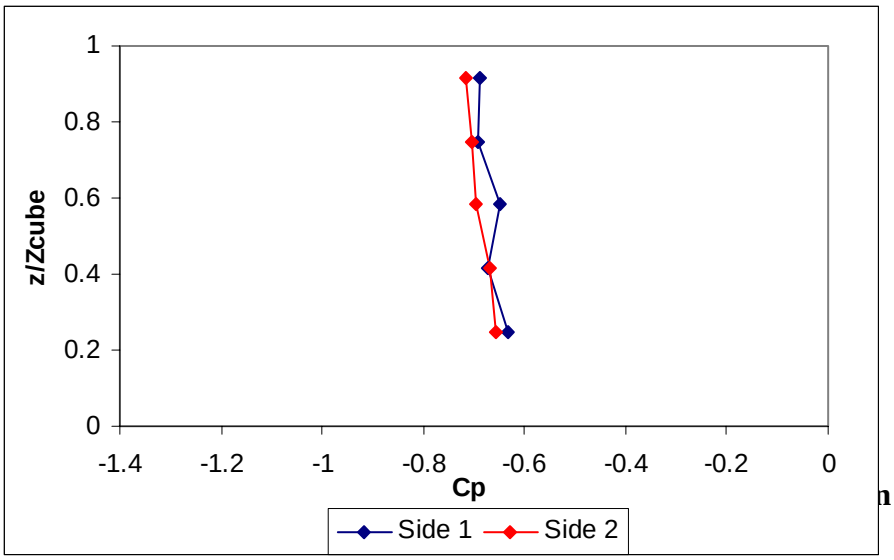

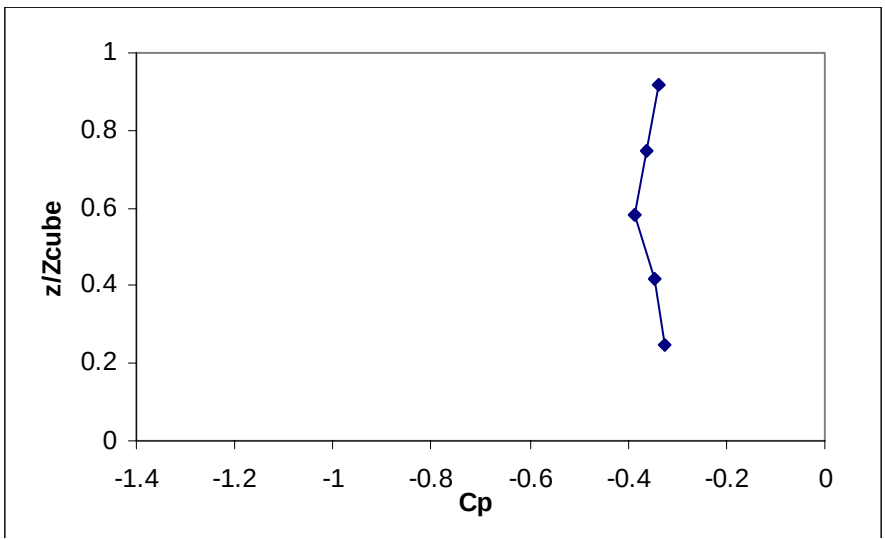

Figure 3.19 Leeward face pressure distribution for 0° wind direction

3.7.4.2 Skewed Wind Direction (45° case)

The pressure distribution for the windward face of the cube for an incident wind angle of 45° is shown in Figure 3.20. The distribution exhibited is of a similar profile to the 0° case shown in Figure 3.16. The pressure coefficients however, are significantly reduced from those measured for the 0° case. Although it is difficult with the number of data points to define the exact position of the peak pressure, the tap located 60% of the way up the face provided a maximum pressure coefficient of approximately 0.45.

Figure 3.21 shows the roof pressure. The peak negative pressure here can be seen to be slightly more negative than for the 0° streamwise profile. The pressure recovery with distance along the roof shows a much more rapid increase than for the 0° case.

The pressure coefficient profile for the leeward face is shown in Figure 3.22. As in the normal wind case (Figure 3.19) the leeward face experiences suction (negative pressures) for the full height of the face on the central plane. Almost constant negative pressure coefficients of around –0.5 were measured. Again, the tap located 60% of the way up the leeward face (tap 14) exhibits a more negative pressure than the other four taps. It is not known whether this was an unreliable tapping point or if the value measured at this tap was valid. For symmetry, the side pressures for a wind angle of 45° would be identical to those on the windward and leeward faces shown above.

3.7.5 Effect of Ventilation Openings on Surface Pressures

The effect of the ventilation openings on the local pressure field around the openings was not a primary aim of the investigation. However, during analysis of the pressure data it was found that the introduction of ventilation openings (see Figures 3.1 and 3.2) had an effect on the external pressures.

In removing the cover panels to create the ventilation openings, a pressure tap on the windward and leeward faces was removed (taps 3 and 14 were located in the centre of the plates used to cover the openings). The pressure taps located 0.5m from the openings remained and were recorded in the usual manner. Since this was not

thought to be an issue at the time of experimentation, data were collected for the normal wind direction only.

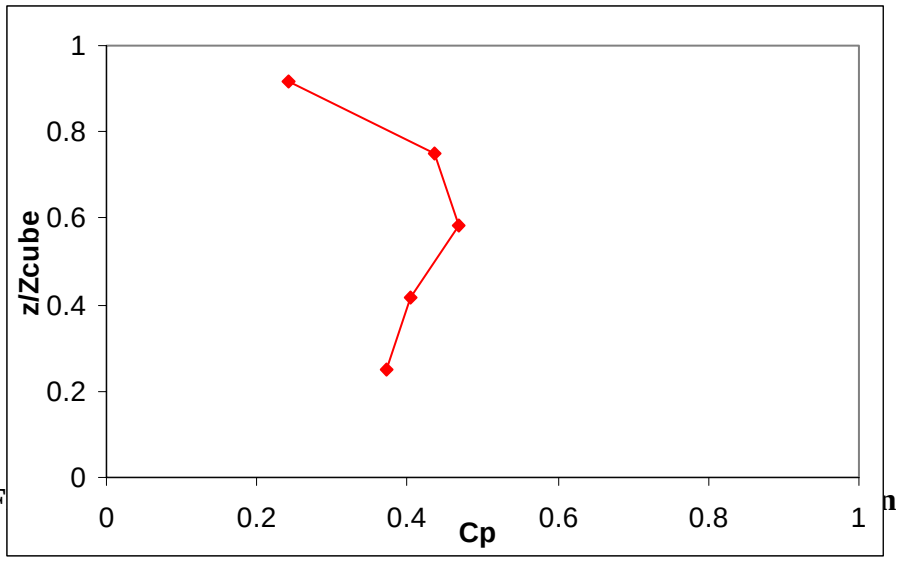

F n

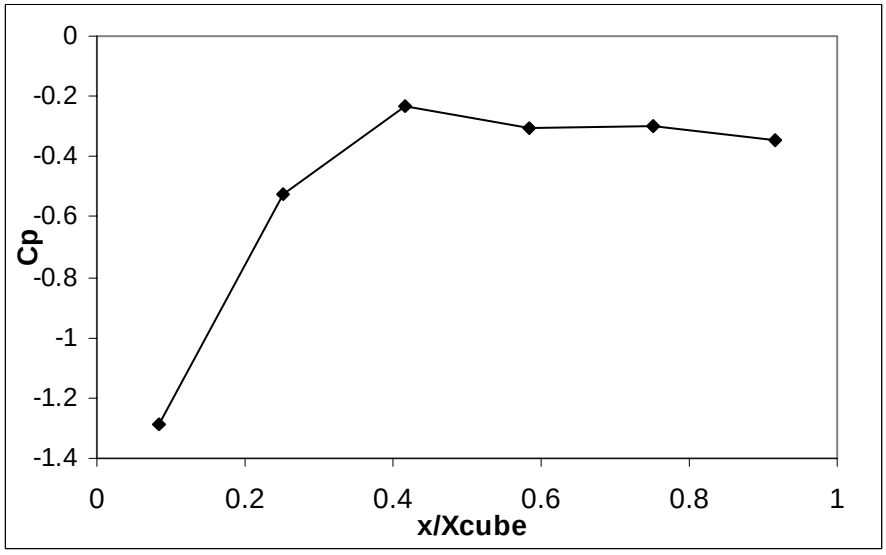

The pressure coefficient measured 0.5m above the windward opening when the cube was sealed was 0.864, however, when the opening was introduced, this pressure was found to increase to by 7% up to 0.933. A similar effect was found to occur at the pressure tap located just below the windward opening. The pressure for the sealed

case was measured as 0.773 compared to the open case of 0.827, again an increase in pressure coefficient of 7%.

The pressure taps located above and below the leeward ventilation opening also exhibited changes in pressure upon the introduction of the opening. The tap 0.5m above the leeward opening gave a pressure coefficient of –0.36 for the sealed case that was found to decrease by 8% to –0.39 for the open case. The tap 0.5m below the opening exhibited a different change with the pressure coefficient increasing from –0.34 when the cube was sealed to –0.29 for the open case, a more significant increase of 17%.

It is difficult to hypothesise whether the difference in pressures close to the ventilation openings for the sealed and open cases is due to the presence of the opening or reflects experimental accuracy. It is interesting however, to note that the pressure distributions over the roof shown in Figure 3.23 for the open and sealed cases show much less difference than the pressures just above and below the position of the opening.

3.7.6 Internal Pressure

When the openings were introduced, the pressure taps that were previously located in the panels that covered them became redundant. This meant that they could be used to obtain a measure of the internal pressure in the proximity of the leeward and windward openings.

Since only two measurements could be taken, detailed description of any pressure gradients was not available. The two pressure coefficients measured for the case of wind normal to the openings were 0.144 and 0.015 at the windward (inlet) and leeward (outlet) openings respectively. This suggests the presence of a pressure variation in the internal region of the test structure. Detailed pressure measurement would be required in order to find where the internal pressure changes occurred most rapidly.

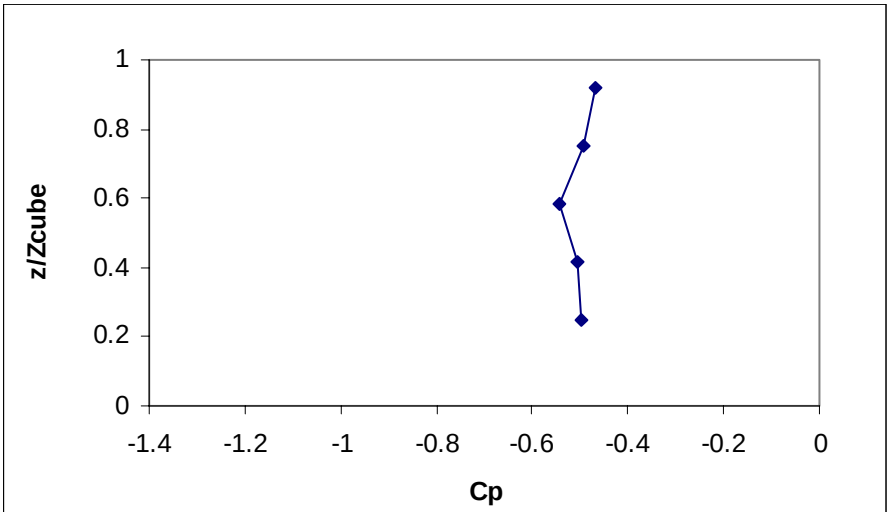

Figure 3.22 Leeward face pressure distribution for 45° wind direction

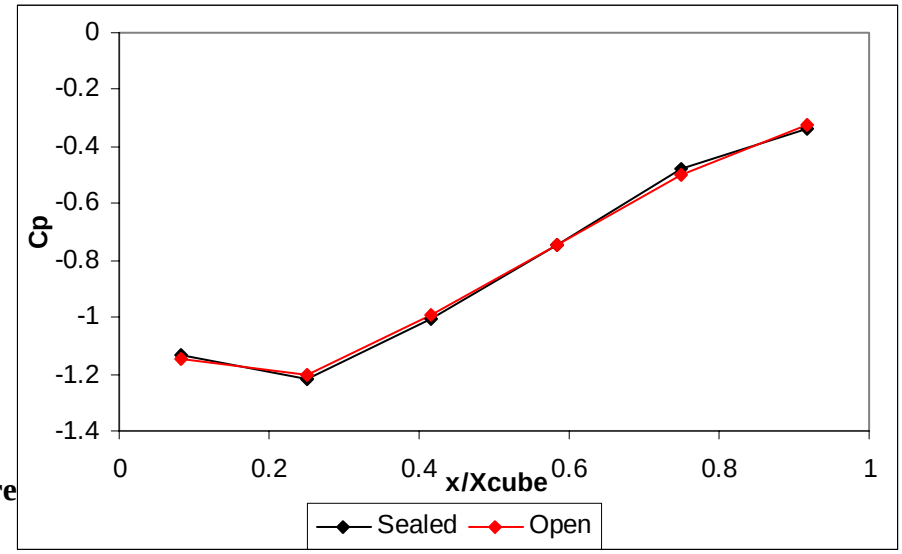

Figure wind

3.7.7 Mean Ventilation Predictions - Pressure Difference Method

The steady-state pressure difference method was described previously in the background Chapter 2. The prediction of wind-induced ventilation using this method required the use of surface pressures measured on the sealed cube in the locations where openings would be positioned.

Ventilation rates were predicted for three configurations. Firstly, for the normal (0°) wind direction with two ventilation openings, one on the windward and one on the leeward face. Secondly, with the two ventilation openings located on opposing sides of the cube and a parallel to the sides, the 90° wind. The final configuration was with the wind at an angle of 45° to the windward face containing the opening.

The standard equation and discharge coefficients from equation (2.15) were utilised and the predicted ventilation rates are provided in Table 3.4 along with all required parameters.

The predicted ventilation rates for the two wind directions of 0° and 45° show that the pressure difference method predicts ventilation rates that are very close together even

though the difference in wind angle is great. For the 0° case, the air entering the windward opening (opening 1) would be travelling almost normal to the plane of the opening maximising the ventilation opening area. For the 45° case, air entering opening 1 would be at a significant angle to the opening plane. This would, in effect, lead to a reduced opening area consequently a lower ventilation rate would be expected.

The 90° case shows very low predicted ventilation rates using the pressure difference method. This may be expected when the pressure distribution is examined. The incident wind is parallel to the plane of the openings that are symmetrically positioned on the cube sides. The mean pressure difference between the two openings in this situation is very low as would be expected, hence the pressure difference method predicts very low ventilation rates.

Table 3.4. Predicted mean ventilation rates from external pressures for variation in wind angle

Wind direction	C_p (opening 1)	C_p (opening 2)	C_d	Ventilation rate, $\overline{Q}/U_{ref}A$
0	0.869	-0.385	0.61	0.483
45	0.583	-0.545	0.61	0.458
90	-0.649	-0.698	0.61	0.095

3.7.8 Total Ventilation Rate Measurements - Tracer Gas Tests

The tracer gas method provided a direct measure of the total ventilation rate in the test space under consideration. The measured ventilation rate from these experiments is effectively the number of air exchanges that occur over the measured period. Using the constant injection method, it was possible to see how the ventilation rate alters through time as well as provide an average value for the period of measurement. Figure 3.24 shows a trace of ventilation rate change with time for the normal wind direction case.

A number of tests were undertaken with the mean incident wind direction normal (or as close as possible) to the windward face containing an opening. The sampling position was varied in order to assess how well the air was mixing within the ventilated space, the positions were close to the outlet and in the cube centre, both at a

height corresponding to the opening centre height. The differences between measurements made at the two positions were found to be within 10% of each other. For this reason, tests were run at both points and average values used.

Table 3.5 provides a summary of the measured ventilation rates for the two experimental cases investigated. For the 0° case where openings were located on the windward and leeward faces, the non-dimensionalised ventilation rate was measured as 0.79. The total ventilation rate was found to reduce by over 50% to a non-dimensionalised value of 0.38 for the 90° case where ventilation openings were located on opposing side faces.

Table 3.5 Measured total ventilation rates from tracer gas experiments for test configurations

Number of openings	**Wind direction (°)**	**Total Ventilation rate,** $Q_T / U_{ref} A$
2	0	0.79
2	90	0.38

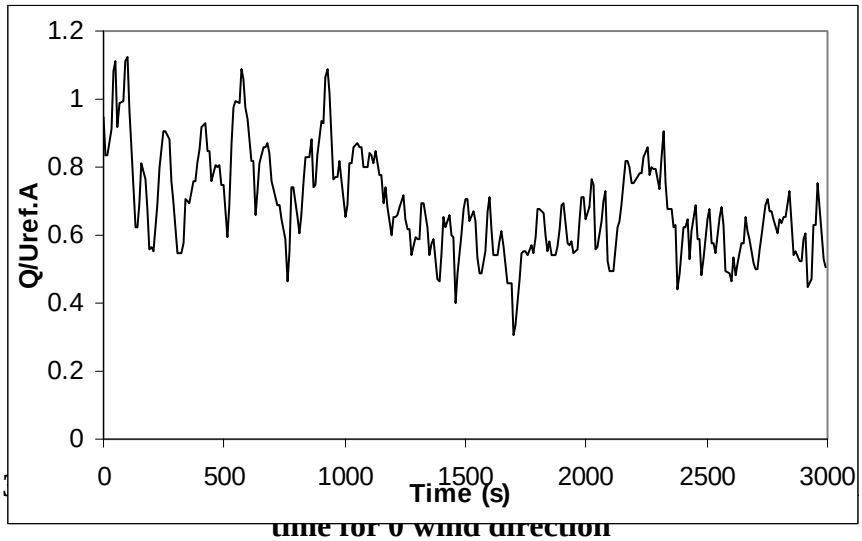

Figure 3 through time for 0 wind direction

3.8Summary

The results provided within this chapter have been discussed as three separate investigations. All of them were undertaken with a common theme that was to assess the wind induced ventilation of a cubic structure.

The external surface pressures were utilised in the application of the pressure difference method for predicting the mean ventilation rate. Anemometry measurements were applied in order to measure the velocity (hence the discharge) through the ventilation openings. Tracer gas tests provided a direct measure of the total airflow through the ventilated cube.

One of the main conclusions that can be drawn form these experiments was the spread in data for the three methods applied in the assessment of ventilation. For the two opening, 0° case (where the incident wind was normal to the windward face opening) a 61% difference between the predicted ventilation rate and the tracer gas measured ventilation rate suggests a large under-prediction by the pressure difference method. The anemometry measurements provided a reduced difference for the 0° wind direction with a ventilation rate only 13% lower than that measured from tracer gas tests.

Under-prediction of ventilation rates using the pressure difference method become even more apparent when the two opening, 90° case was assessed. The symmetrical nature of this configuration meant that ventilation openings were located in regions of similar mean pressure (due to symmetry of the cube). Any differences in pressures would have been caused by turbulent fluctuations. Here, the steady-state pressure difference method predicted only 25% of the ventilation rate measured using the tracer gas technique and the anemometry measurements gave only 30% of the tracer gas measurements. The tracer gas tests provided a measured total ventilation rate of 0.38 nearly half of that found for the 0° case.

The difference between the anemometry measured ventilation rate and tracer gas measurement for the 90° case is most likely to be due to the nature of the flow through the openings. In the 0° case, flow through the two ventilation openings did not change direction however, in the 90° case, (where the pressure difference between the ventilation openings was very low) it was found that the direction of flow changed in each of the two openings. If the period of time over which flow enters and exits an opening is similar, the mean velocity through the opening would be close to zero. If this same situation is considered when measuring ventilation rates from tracer gas tests, the direction of flow through an opening will always add to the ventilation. The entrainment of clean air from the external environment (into the internal region) and the exit of internal air and tracer gas (to the external environment) lead to a net decrease in the tracer gas present within the internally ventilated region.

The differences between the tracer gas measurements and the pressure difference method could be due to two factors. The first is the value of the discharge coefficient used in the pressure difference method. The second is the inability of the pressure difference method to account for the effects of turbulence (since mean pressures are utilised).

Two issues arise with respect to the orifice discharge coefficient applied in the steady-state pressure difference technique. The standard value of discharge coefficient quoted in BS 5925 (1991) for the application of the pressure difference method is 0.61. This value corresponds to that of a sharp-edged orifice for flows are oriented normally to the opening plane. The ventilation openings on the test structure described in this research were not sharp edged and had a significant depth in the direction of flow. Flows entering ventilation openings located on the surface of a building are likely to impinge at angles to the plane of the openings. Both of these factors make the application of a standard value of the discharge coefficient disputable.

The other issue arising from the discharge coefficient is the fact that the standard value is applicable to the flow through a single opening. In the application of the pressure difference method the flow through two openings is predicted using the pressure difference between the two openings. Measurements of internal pressures proved that there was pressure loss throughout the internal ventilated region that is not accounted for in a discharge coefficient applicable to a single opening. This internal pressure drop is another factor that makes the standard discharge coefficient inaccurate for such applications.

The second factor that causes problems with the steady-state pressure difference method occurs when openings are located such that the pressure difference between them is low. This was the situation for the 90° case discussed above. A low mean pressure difference leads to a low predicted ventilation rate however, even for such cases tracer gas measurements showed a significant amount of ventilation occurred. Turbulent induced flows can account for a significant proportion of the total ventilation that the tracer gas measurements will detect. In the 90° case, where the mean pressure between ventilation openings is very small, it is turbulent fluctuations that account for the vast majority of air exchange.

The steady-state pressure difference method relies on the prediction of ventilation rates using pressures measured when no ventilation openings are present. The external pressures measured showed that the validity of such a technique is questionable. Pressures measured in regions close to the ventilation openings for both the sealed and ventilated cases highlighted differences that were not apparent on faces of the structure where openings were not present. It is therefore debatable as to whether the pressure difference between the ventilation openings measured when ventilation openings remains unaltered when the ventilation openings are present.

The main conclusion to be drawn from these full-scale experiments is that the application of methods for predicting, or measuring, mean ventilation rates underpredict the total ventilation rates (found from tracer gas tests). These differences would seem to be due, in part, to the effects of turbulent air exchanges that

cannot be accounted for using mean pressures and velocities alone. Current predictive methods have been shown to lead to major discrepancies with measured ventilation rates. This implies that improvements are required in the form of more rigorous prediction methods for mean ventilation rates and techniques capable of accounting for turbulent processes.

4. COMPUTATIONAL FLUID DYNAMICS

4.1 Introduction

Computational fluid dynamics (CFD) is the analysis of systems involving fluid flow, heat transfer and associated phenomena such as chemical reactions by means of computer based simulation. The fundamental governing equations of fluid dynamics (continuity, momentum and energy conservation) are the foundation of fluid flow computations, and it is these highly complex equations that are solved in CFD. These governing equations are introduced at the start of this chapter as are the problems associated with the modelling of three-dimensional turbulence and methods available for its simulation. The techniques available for solving the governing equations of fluid flow are discussed along with the known inadequacies and strong points of each method wherever applicable.

Once the theoretical basis of CFD has been discussed, the computational modelling undertaken within this research is introduced. The numerical methods and techniques employed are described, as are the relevant details to any modelling undertaken.

The CFD investigations described here can be divided into a number of individual categories (although each is linked in some way), these are:

- Modelling of the atmospheric boundary layer
- Modelling the external flow and pressure field around a cubic structure
- Modelling the externally induced internal flow field within a cubic structure.

All of the computational testing was undertaken in order to assess the application of CFD to wind engineering flows, with particular emphasis on its use in simulating wind induced ventilation.

4.2 Governing Equations of Fluid Flow

In this section, the equations that govern any fluid flow problem are introduced. These equations arise from the conservation laws of physics, from which it is possible to derive the most fundamental equations of motion for a fluid, the Navier-Stokes equations. In order to explain the conservation laws, it is useful to consider a finite-sized volume (control volume) through which flow passes.

4.2.1 Conservation of Mass

The increase in mass within a control volume must be equal to the mass inflow minus the mass outflow through the control volume's surface since mass can neither be created or destroyed. This can be expressed mathematically for an incompressible fluid as

$$\frac{\partial u}{\partial x}+\frac{\partial v}{\partial y}+\frac{\partial w}{\partial z}=0 \tag{4.1}$$

where *u*, *v* and w are the three components of velocity corresponding to the *x*, *y* and *z* directions respectively.

4.2.2 Navier-Stokes Equations

The other fundamental set of equations that govern the flow of a fluid are derived from Newton's second law (the conservation of momentum). The equations are called the Navier-Stokes equations, and for an incompressible fluid the full instantaneous equations take the form

$$\frac{\partial(\rho u)}{\partial t}+\frac{\partial(\rho uu)}{\partial x}+\frac{\partial(\rho vu)}{\partial y}+\frac{\partial(\rho wu)}{\partial z}=-\frac{\partial p}{\partial x}+\mu\left(\frac{\partial^2 u}{\partial x^2}+\frac{\partial^2 u}{\partial y^2}+\frac{\partial^2 u}{\partial z^2}\right) \tag{4.2}$$

$$\frac{\partial(\rho v)}{\partial t}+\frac{\partial(\rho uv)}{\partial x}+\frac{\partial(\rho vv)}{\partial y}+\frac{\partial(\rho wv)}{\partial z}=-\frac{\partial p}{\partial y}+\mu\left(\frac{\partial^2 v}{\partial x^2}+\frac{\partial^2 v}{\partial y^2}+\frac{\partial^2 v}{\partial z^2}\right) \tag{4.3}$$

$$\frac{\partial(\rho w)}{\partial t}+\frac{\partial(\rho uw)}{\partial x}+v\frac{\partial(\rho vw)}{\partial y}+w\frac{\partial(\rho ww)}{\partial z}=-\frac{\partial p}{\partial z}+\mu\left(\frac{\partial^2 w}{\partial x^2}+\frac{\partial^2 w}{\partial y^2}+\frac{\partial^2 w}{\partial z^2}\right) \tag{4.4}$$

where *u*, *v* and *w* are the streamwise, lateral and vertical velocity components respectively, *x*, *y* and *z* are the corresponding directions to the velocity components, μ is the fluid viscosity, ρ is the fluid density and p is the pressure.

It is more compact to write equations (4.2) to (4.4) in Cartesian tensor notation as (Gatski et al (1996))

$$\frac{\partial(\rho u_i)}{\partial t}+\frac{\partial\left(\rho u_j u_i\right)}{\partial x_j}=-\frac{\partial p}{\partial x_i}+\frac{\partial}{\partial x_i}\left\{\mu\left(\frac{\partial u_i}{\partial x_i}+\frac{\partial u_i}{\partial x_i}\right)\right\} \tag{4.5}$$

where the suffixes *i* and *j* represent the three co-ordinate directions upon expansion back to equations (4.2) to (4.4).

For a Newtonian fluid (where a linear shear-stress law applies to the fluid) with constant viscosity, the continuity equation and the Navier-Stokes equations provide

the four equations required for solving the four flow variables for an isothermal flow (velocity components *u*, *v* and *w* and the pressure, p).

The instantaneous Navier-Stokes equations can, at present, only be solved for the most simple flows, i.e. laminar flows and some transitional flows (transitional in terms of a laminar fluid becoming turbulent). For more complex turbulent flow that display high Reynolds number, such as those found in the vast majority of wind engineering situations, the Navier-Stokes equations need to be averaged in order to be applied.

The instantaneous velocity, *U*, can be assumed to comprise the sum of a mean component, $\overline{U}$, and a turbulent component, u' as shown in equation (4.6)

$$U = \overline{U} + u' \tag{4.6}$$

In order to produce a set of time-averaged Navier-Stokes equations, equation (4.6) is substituted into equation (4.5) which is then integrated over time to obtain mean flow equations. All terms except the second term on the left of equation (4.5) (the convective transport of x_i momentum) contain only a single fluctuating quantity. For this reason, the averaging process results in the instantaneous value being replaced by the mean of each variable in question. However, for the convective transport term that differs from the others, the following results from the averaging process (Launder (1994))

$$\begin{aligned}\overline{u_j u_i} &= \overline{\left(U_j + u_j'\right)\left(U_i + u_i'\right)} \\ &= \overline{U_j U_i} + \overline{U_j u_i'} + \overline{u_j' U_i} + \overline{u_j' u_i'} \\ &= U_j U_i + \overline{u_j' u_i'}\end{aligned} \tag{4.7}$$

where the overbar indicates time-averages.

The averaged equations of motion therefore become

$$\frac{\partial \rho}{\partial t} + \frac{\partial \rho U_i}{\partial x_i} = 0 \tag{4.8}$$

$$\frac{\partial(\rho U_i)}{\partial t} + \frac{\partial(\rho U_j U_i)}{\partial x_i} = -\frac{\partial p}{\partial x_i} + \frac{\partial}{\partial x_j}\left\{\mu\left[\frac{\partial U_i}{\partial x_j} + \frac{\partial U_j}{\partial x_i}\right] - \rho\overline{u_i' u_j'}\right\}_i \tag{4.9}$$

The averaged equations of motion are commonly known as the Reynolds equations. The only difference between these and those that describe a laminar flow is the

presence of the term containing averaged products of fluctuating velocities. The physical process represented by this term is the additional transfer rate of x_i momentum due to turbulent fluctuations.

The term in square brackets in equation (4.9) is the viscous stress, hence the proceeding term containing the fluctuating velocities is also interpreted as a turbulent stress and is usually referred to as the *Reynolds stress* tensor. The Reynolds stress tensor is symmetric, hence there are six independent Reynolds stress components (three normal stresses and three shear stresses). Due to the time-averaging procedure of the Navier-Stokes equations all details concerning the state of the fluid flow in the instantaneous fluctuations are lost and as a result, the Reynolds stress components are obtained in the time-averaged Navier-Stokes equations. The presence of the Reynolds stress terms leads to an additional six unknowns forming a total of ten unknowns with only four equations of flow, hence the set of governing equations are not *closed*. This is termed the *closure* problem and requires the development of *turbulence models* to represent these Reynolds stresses over a wide range of flow fields.

4.3Turbulence Modelling

Turbulence models are numerical methods to achieve closure of the time-averaged governing fluid flow equations, described previously, by providing a scheme for the evaluation of the Reynolds stress terms. The aim of any turbulence model is that it can be applied to a wide range of fluid flow situations and provide realistic solutions to mean flow patterns and scalar transport. In the case of engineering applications, it is the effect of turbulence on the main flow that is most often sought, rather than resolving the details of the turbulent fluctuations.

4.3.1 Eddy Viscosity Concept

Before the introduction of some of the classical turbulence models (those based on the time-averaged Reynolds equations), it is necessary to introduce the concept of *eddy viscosity* on which a number of the most common models are based. Eddy viscosity is based on an assumption that there exists an analogy between the action of viscous stresses and Reynolds stresses on the mean flow. According to Newton's law of viscosity, the viscous stresses are proportional to the rate of deformation of fluid elements, i.e. for an incompressible fluid

$$\tau_{ij} = \mu e_{ij} = \mu\left(\frac{\partial u_i}{\partial x_j} + \frac{\partial u_j}{\partial x_i}\right) \tag{4.10}$$

where μ is the fluid viscosity and other terms are as previously defined. Boussinesq proposed that the Reynolds stresses could be linked to mean rates of deformation, i.e.

$$\tau_{ij} = -\rho\overline{u_i' u_j'} = \mu_t\left(\frac{\partial u_i}{\partial x_j} + \frac{\partial u_j}{\partial x_i}\right) \tag{4.11}$$

where μ_t is the turbulent or eddy viscosity. It is obvious that equations 4.10 and 4.11 are analogous to one another apart from the appearance of this new eddy viscosity term. It is the method of finding a model to provide values of the eddy viscosity on which a number of classical turbulence models are based.

4.3.2 Mixing Length Model

Mixing length turbulence models attempt to describe the Reynolds stresses by means of simple algebraic formulae for the eddy viscosity, μ_t , as a function of position. In order to outline the mixing length model, it is first necessary to define a kinematic eddy viscosity, ν_t, which is defined as

$$\nu_t = \frac{\mu_t}{\rho} \tag{4.12}$$

Kinematic eddy viscosity has dimensions of m^2s^{-1}, and it is then assumed that it can be expressed as the product of a turbulent velocity scale, ϑ (ms^{-1}), and a length scale, ℓ (m). If one velocity scale and one length scale suffice to describe the effects of turbulence, dimensional analysis yields (Versteeg and Malalasekera (1995))

$$\nu_t = C\vartheta\ell \tag{4.13}$$

where C is a dimensionless constant of proportionality. The eddy viscosity is therefore defined as

$$\mu_t = C\rho\vartheta\ell \tag{4.14}$$

the turbulent length scale, ℓ , is characteristic of the largest eddies in the flow under consideration since it is these which contain most of the kinetic energy in the flow. Since there is a strong connection between these largest eddies and the mean flow, the velocity scales of these eddies can be linked with those of the mean flow. Simple, two-dimensional turbulent flows with only one significant Reynolds stress (e.g. $u'w'$) and with U/z the only significant velocity gradient have been found to agree well with this description. In such 2-D flows the eddy length scale can be defined as

$$\vartheta = c\ell\left|\frac{\partial U}{\partial z}\right| \tag{4.15}$$

where c is a dimensionless constant. The magnitude is taken to ensure a positive velocity scale quantity irrespective of velocity gradient. By combining equations (4.13) and (4.15) *Prandtl's mixing length model* is obtained

$$\nu_t = \ell_m^2 \left| \frac{\partial U}{\partial z} \right| \tag{4.16}$$

where ℓ_m^2 is a new length scale containing the dimensionless constants *C* and *c*. The expression for the only significant Reynolds stress can be found from equation (4.11) giving

$$\tau_{xy} = \tau_{yx} = -\rho\overline{uw} = \rho\ell_m^2 \left| \frac{\partial U}{\partial z} \right| \frac{\partial U}{\partial z} \tag{4.17}$$

In order for the mixing length model to account for turbulence changes within a flow, the value of ℓ_m must be changed. For simple turbulent flows, this change is accounted for by the use of algebraic formulae and is useful in situations where turbulence properties develop in proportion to a mean flow length scale. However, in situations where flows undergo separation and recirculation, the simple mixing length model is incapable of predicting the flow field. Because of such short-comings, the mixing length model is of greater interest in flows found in the aerospace industry and of little use in the complex flow fields found in many wind engineering situations.

4.3.3 The k-ε Model

The k-ε turbulence model is, like the mixing length model, based on the eddy viscosity concept. However, it is a more sophisticated description of turbulence, allowing for transport of turbulence properties by the mean flow, diffusion and also the production and destruction of turbulence.

The k-ε model solves transport equations for the turbulent kinetic energy, *k*, and the rate of dissipation of turbulent kinetic energy, ε. As with the mixing length model, it is necessary to define a number of terms before providing a full description of the model equations.

The instantaneous kinetic energy, *k(t)*, is defined as the sum of the mean kinetic energy, *K*, and the turbulent kinetic energy, *k*.

$$k(t) = K + k \tag{4.18}$$

$$K = \frac{1}{2}\left(U^2 + V^2 + W^2\right) \tag{4.19}$$

$$k = \frac{1}{2}\left(\overline{u'^2} + \overline{v'^2} + \overline{w'^2}\right) \tag{4.20}$$

The standard k-ε model developed by Launder and Spalding (1974) has two model equations, one for *k* and one for ε.

Here, k and ε are utilised in order to define the velocity scale and length scale representative of the large scale turbulence

$$\vartheta = k^{1/2} \tag{4.21}$$

$$\ell = \frac{k^{3/2}}{\varepsilon} \tag{4.22}$$

The eddy viscosity is defined using the same approach as for the mixing length model

$$\mu_t = C\rho\vartheta\ell = \rho C_\mu \frac{k^2}{\varepsilon} \tag{4.23}$$

where C_μ is a dimensionless constant.

The exact equation for the turbulent kinetic energy, k, is derived by multiplying the instantaneous Navier-Stokes equations by the corresponding fluctuating velocity components (x-component equation is multiplied by u' etc.). Summing of the results produces the instantaneous turbulent kinetic energy equation. Repeating this process on the Reynolds equations (4.8) and (4.9) and subtracting the two resulting equations leads to an equation for the turbulent kinetic energy (Ferziger and Peric (1997)).

$$\frac{\partial(\rho k)}{\partial t} + \frac{\partial(\rho U_j k)}{\partial x_j} = \tau_{ij}\frac{\partial U_i}{\partial x_j} - \rho\varepsilon + \frac{\partial}{\partial x_j}\left[(\mu + \mu_t/\sigma_k)\frac{\partial k}{\partial x_j}\right] \tag{4.24}$$

where the σ_k is a model constant and τ_{ij} is the Reynolds stress tensor defined below

$$\tau_{ij} = 2\mu_t S_{ij} - \frac{2}{3}\rho k\delta_{ij} \tag{4.25}$$

where δ_{ij} is the Kronecker delta and equals 1 if i=j and 0 if $i \neq j$. This inclusion means that the three normal Reynolds stresses are apportioned a third of the total each. This leads to the k-ε model to calculate the normal Reynolds stresses as being isotropic.

The exact equation for the dissipation of turbulent kinetic energy can also be derived from the Navier-Stokes equations. However, the equation requires so much modelling it is convenient and more applicable to regard the entire equation as a model. The most common form of the dissipation equation is

$$\frac{\partial(\rho\varepsilon)}{\partial t} + \frac{\partial(\rho U_j \varepsilon)}{\partial x_j} = C_{\varepsilon 1} P_k \frac{\varepsilon}{k} - \rho C_{\varepsilon 2}\frac{\varepsilon^2}{k} + \frac{\partial}{\partial x_j}\left[(\mu + \mu_t/\sigma_\varepsilon)\frac{\partial \varepsilon}{\partial x_j}\right] \tag{4.26}$$

where $C_{\varepsilon 1}$, $C_{\varepsilon 2}$ and σ_ε are model constants, the values of which are defined in Table 4.1. Versteeg and Malalasekera (1995) provide a description of equations 4.24 and 4.26 as shown below

Rate of change of k or ε	+	*Transport of k or ε by convection*	=	*Transport of k or ε by diffusion*	+	*Rate of production of k or ε*	-	*Rate of destruction of k or ε*

A number of model constants have been utilised in equations (4.24) to (4.26) which are required because of a number of simplifications made to the models. They have been derived through rigorous investigation of experimental data and have been found to provide the most suitable solutions to the equations over a wide range of turbulent flows. The values used in the standard k-ε model are provided in Table 4.1 below.

Table 4.1 Constants used in standard k-ε turbulence model

Model constant	**Value**
C_μ	0.09
$C_{\varepsilon 1}$	1.44
$C_{\varepsilon 2}$	1.92
σ_k	1.0
σ_ε	1.3

4.3.4 The RNG k-ε Model

The RNG k-ε model provides an alternative technique for deriving turbulence closure models. It was first introduced by Yakhot et al (1986) who applied a complex mathematical technique termed the Renormalisation Group Theory (RNG) to the Navier-Stokes equations and derived an alternative two-equation k-ε turbulence model. The RNG mathematical derivation is highly complex and is not discussed here. However, full details can be found in Gatski et al (1996).

Essentially, the difference between the standard k-ε and RNG k-ε turbulence models arises in the kinetic energy dissipation rate transport equations. The original derivation of coefficients and constants used in the RNG model were theoretical, unlike the standard model. An expansion technique has since been applied in order to improve the model's application to wall-bounded flows (original models were unable

to satisfy the logarithmic profile in the near-wall region). The coefficients in the latest RNG models are not a result of the RNG theory, but of model calibration to experimental data (as with the standard model).

In the RNG k-ε turbulence model the constant $C_{\varepsilon 1}$ takes on a revised value of 1.42 (1.44 for the standard k-ε model) and $C_{\varepsilon 2}$ is no longer a constant but becomes dependent on strain rate

$$C_{\varepsilon 2} \rightarrow C_{\varepsilon 2} + \frac{\eta\left(1-\frac{\eta}{4.38}\right)}{1+0.015\eta^3} \tag{4.27}$$

where

$$\eta = S\frac{k}{\varepsilon} \tag{4.28}$$

and S, the linear strain rate is defined as

$$S = \sqrt{\left(\frac{\partial U_i}{\partial x_j} + \frac{\partial U_j}{\partial x_i}\right)\frac{\partial U_i}{\partial x_j}} \tag{4.29}$$

The changes made to the standard model in the RNG model make it better suited to the modelling of flows that experience separation and curvature.

4.3.5 Other Turbulence Models

Many turbulence models exist for application to closure of the time-averaged Navier-Stokes equations. Those discussed here have particular significance to applications within this research. It is however, worthwhile briefly discussing other available turbulence models.

Numerous modified forms of the standard k-ε model have been developed. With regard to wind engineering applications, the MMK k-ε model is one that has been applied and tested thoroughly. The MMK modification to the standard model occurs in the value of C_μ which, for the standard model has a constant value of 0.09. The MMK modifications lead to C_μ no longer being a constant value but instead being dependent upon the value of the shear velocity in order to alter the eddy viscosity calculated. The aim of this model was to improve the predictions for wind engineering flows compared with the standard k-ε model.

Another modified k-ε model was devised by Kato and Launder (1993). The Kato-Launder model differs from the standard k-ε model by the modification of the term responsible for calculating the production of turbulent kinetic energy, P_k. Equations

(4.30) and **(**4.31) show the differences between the two models with (4.30) used in the standard model and (4.31) the modified term introduced in the Kato-Launder model.

$$P_k = C_\mu \varepsilon S_1^2 \tag{4.30}$$

$$P_k = C_\mu \varepsilon S_1 S_2 \tag{4.31}$$

where

$$S_1 = \sqrt{\left[0.5\left(U_{ij} + U_{ji}\right)\right]^2}\,\frac{k}{\varepsilon} \tag{4.32}$$

$$S_1 = \sqrt{\left[0.5\left(U_{ij} - U_{ji}\right)\right]^2}\,\frac{k}{\varepsilon} \tag{4.33}$$

where C_μ is a constant (=0.09), ε is the dissipation of turbulent kinetic energy, k and U_{ij} and U_{ji} are the mean velocity (where the subscripts refer to tensor notation)

All of the turbulence models described prior to this point have been based on the eddy viscosity concept described in section 4.3.1, where an eddy viscosity is computed and utilised in order to predict values of the Reynolds stresses present in the time-averaged Navier-Stokes equations. Second moment closure models (SMC) take a different approach from the eddy viscosity models described. The Reynolds stress model (RSM) is a second moment closure model where transport equations for the six individual Reynolds stresses are computed along with an equation for the dissipation of turbulent kinetic energy, ε. The increased number of equations that must be solved in such turbulence models make them more computationally intensive than eddy viscosity models. However, they are capable of modelling anisotropic turbulence and are physically more rigorous in their treatment of turbulence than are the isotropic turbulence models discussed previously.

4.3.6 Near-Wall Flow Treatment

The presence of a solid boundary (wall) leads to considerable differences in the flow behaviour and turbulence structure when compared to free turbulent flows (those not affected by a solid boundary). The effects of a wall boundary are best explained by defining a Reynolds number, *Re*, with a length scale based upon the normal distance, *y*, from the wall

$$Re = \frac{Uy}{\nu} \tag{4.34}$$

where U is the velocity and ν is the kinematic viscosity of the fluid.

The Reynolds number of the flow provides a measure of the relative contribution of inertia forces to viscous forces. Inertia forces dominate in the flow far from the wall, however, as the distance decreases towards zero, the Reynolds number also decreases.

Just before y becomes zero there is a range of values of y for which the Reynolds number is of the order of 1. At this distance from the wall, and closer, the viscous forces are equal in order of magnitude, or larger, than the inertia forces.

There are a number of individual layers with differing flow characteristics in the near wall region that can be defined. In order to explain these layers it is necessary to introduce two dimensionless parameters.

A velocity parameter

$$u^+ = \frac{\left(\rho u_\tau y_p\right)}{\mu} \tag{4.35}$$

and a distance parameter

$$y^+ = \frac{\Delta y_p}{\nu}\sqrt{\frac{\tau}{\rho}} \tag{4.36}$$

where Δy_p is the distance from the wall to the nearest point, y_p, where velocity is to be calculated, u_τ is the shear velocity, μ is the dynamic viscosity of the fluid and τ is the shear stress which, according to the wall law, is related to the turbulent kinetic energy by

$$\tau = \rho C_\mu^{1/2} k \tag{4.37}$$

4.3.6.1 Linear (or Viscous) Sub-Layer

A fluid must be stationary at the surface of a solid with turbulent eddying motions reducing and stopping very close to the wall. As the turbulent Reynolds stresses become negligible, viscous stresses become dominant. This layer is called the linear sub-layer and is in practice extremely thin ($y^+ < 5$). The shear stress is approximately constant and equal to the wall shear stress throughout this layer. The linear relationship between the two non-dimensional parameters u^+ and y^+ in this region of fluid adjacent to the wall provides the name for the linear sub-layer.

4.3.6.2 Log-Law Layer

Outside the viscous sub-layer ($30<y^+<500$) is the log-law layer. In this layer, viscous and turbulent effects are both important. The shear stress varies slowly with distance from the wall and is assumed to be constant and equal to the wall shear stress. The relationship between u^+ and y^+ in this layer is

$$u^+ = \frac{1}{\kappa}\ln y^+ + B = \frac{1}{\kappa}\ln\left(Ey^+\right) \tag{4.38}$$

where κ, B and E are constants, the values of which are found from measurements. Wall roughness leads to a decrease in the value of B. The log-layer has this name due to the logarithmic relationship between u^+ and y^+.

4.3.6.3 Outer Layer

The outer layer is the inertia dominated region far from the wall. The log-law layer is valid in the region $0.02 < y/\delta < 0.2$, where y is the normal distance from the wall and δ is the thickness of the sub-layer. For larger values of y, the velocity defect law provides the correct form. There exists an overlap region in which the log-law and the velocity-defect law become equal. Tennekes and Lumley (1972) showed that the matched overlap is obtained by assuming the following logarithmic form

$$\frac{U_{\max} - U}{u_\tau} = \frac{1}{\kappa}\ln\left(\frac{y}{\delta}\right) + D \tag{4.39}$$

where D is a constant.

4.3.6.4 Wall Functions

At high Reynolds number, the viscous sub-layer of a boundary layer is so thin it would require large computational resources to resolve flows at such small scale. In order to avoid this problem in CFD, *wall functions* are applied in the near wall region that rely on the existence of the logarithmic region in the velocity profile.

Implementation of wall boundary conditions for turbulence models is assessed by evaluating the scaled wall distance, y^+, between the wall surface and the computational node nearest the wall. For distances where $y^+ \geq 11.63$, the flow is turbulent and the wall function approach is used, for y^+ values less than 11.63 the near wall flow is taken as laminar. If y_p is the normal distance from the wall, the mean velocity at a position within the range of $30 < y_p < 500$ satisfies the log-law and measurements of turbulent kinetic energy budgets indicate that the rate of turbulence production equals the rate of dissipation (Versteeg and Malalasekera (1992)). From this assumption and the eddy viscosity formula, the following wall functions are developed

$$u^+ = \frac{U}{u_\tau} = \frac{1}{\kappa}\ln\left(Ey_p^+\right) \tag{4.40}$$

$$k = \frac{u_\tau^2}{\sqrt{C_\mu}} \tag{4.41}$$

$$\varepsilon = \frac{u_\tau^3}{\kappa y} \tag{4.42}$$

where κ=0.41 is the Von Karman constant and E is a wall roughness parameter.

4.4Discretisation Methods for CFD

In terms of computational fluid dynamics, numerical methods refer to techniques that can be developed in order to solve the governing equations of fluid flow. It is not possible to solve directly the governing set of partial differential equations (except for some very simple flows), hence a suitable method for approximating the differential equations by forming a set of algebraic equations for the variables involved must be formed. This process is called *discretisation*. There are a number of numerical methods that can be used in order to produce the equations which must be solved, the main ones are:

- Finite difference methods;
- Finite element methods;
- Finite volume methods.

The finite volume method is utilised in this research. However, for completeness it is necessary to mention the other techniques available. The process through which all numerical methods work is the same in terms of a number of basic steps:

- Approximation of the unknown flow variables by means of simple functions;
- Discretisation by substitution of the approximations into the governing flow equations and subsequent mathematical manipulations;
- Solution of the algebraic equations.

The following aims to give brief details of some of the main numerical techniques available for application in CFD. In depth details of numerical methods have not been included. Full descriptions can be found in most CFD literature, e.g. Versteeg and Malasekera (1995).

4.4.1 Finite Difference Methods

Finite difference methods aim to describe certain unknowns (ϕ, say) in the flow problem by means of point samples at the node points of a grid of co-ordinate lines. Truncated Taylor series expansions are often used to generate finite difference approximations of derivatives of ϕ in terms of point samples of ϕ at each grid point and its immediate neighbours. Those derivatives appearing in the governing

equations are replaced by finite differences yielding an algebraic equation for the values of ϕ at each grid point.

4.4.2 Finite Element Methods

Finite element methods use simple piecewise functions (e.g. linear or quadratic) valid on elements to describe the local variations of unknown variables ϕ. The governing equation is precisely satisfied by the exact solution of ϕ. If the piecewise approximating functions for ϕ are substituted into the equation they will not hold exactly and a residual is defined to measure the errors. Next the residuals (and hence the errors) are minimised in some sense by multiplying them by a set of weighting functions and integrating (Versteeg and Malalasekera (1995)). As a result, a set of algebraic equations for the unknown coefficients of the approximating functions are obtained.

4.4.3 Finite Volume Methods

Originally developed as a special finite difference formulation, the finite volume method has become one of the more popular numerical techniques in CFD codes. The code utilised within this research is based on the finite volume method and is therefore highly relevant. The numerical algorithm consists of a number of steps (Versteeg and Malalasekera (1995)):

- formal integration of the governing equations of fluid flow over all the (finite) control volumes of the solution domain;
- discretisation involving the substitution of a variety of finite-difference-type approximations for the terms in the integrated equation representing flow processes such as convection, diffusion and sources - this converts the integral equations into a system of algebraic equations;
- solution of the algebraic equations by an iterative method.

It is the first step in the above list that distinguishes the finite volume technique from other CFD methods. The finite volume method uses the integral form of the conservation equations as the starting point. The solution domain is subdivided into a finite number of continuous control volumes (CVs) and the conservation equations are applied to each CV. At the centre of each CV is a computational node at which the variable values are to be calculated. Interpolation (differencing) is used to express variable values at the CV surface in terms of the nodal values. A number of methods are available for calculating the value of transported properties at control volume faces as well as the convective (and diffusive) fluxes across CV boundaries.

4.5Differencing Schemes for CFD

Consider a one-dimensional control volume as shown in Figure 4.1. The point P is the node of interest. However, neighbouring nodes *W* and *E* must also be considered. The dashed lines (denoted by lower case symbols, *w* and *e*) denote cell face boundaries and the symbol ϕ denotes the value of the property of the variable being calculated (the subscript corresponds to the position at which the variable is calculated).

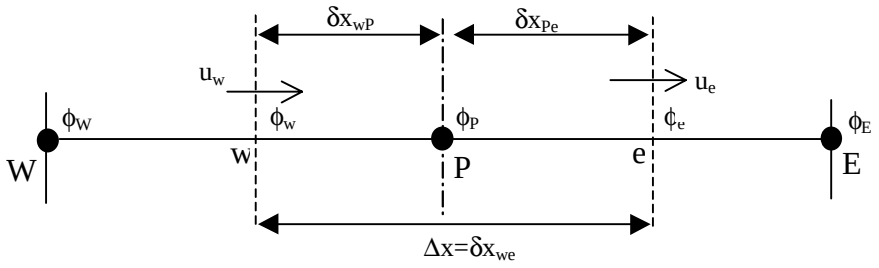

Figure 4.1 A control volume around node P

Source: Versteeg and Malalasekera (1995)

In what follows, the velocity field is assumed to be known (the actual method for solving the flow field is discussed in section 4.6 below). In theory, numerical results obtained would be indistinguishable from the exact solution of the transport equations when the number of computational cells is infinitely large, irrespective of which numerical method is utilised, i.e. as grid spacing tends to zero, the solution obtained should become exact. This situation is impractical to achieve in reality hence a number of properties of the numerical scheme are utilised to assess its performance and applicability, the main fundamental properties of interest here are discussed in the following before the main differencing schemes used in CFD practice are described.

4.5.1 Consistency

As stated previously, the discretisation should become exact as the grid spacing tends to zero. The difference between the discrectised equation and the exact one is termed the truncation error. This error is estimated by replacing all nodal values in the discrete approximation by a Taylor series expansion about a single point resulting in the original differential equation plus a remainder. This remainder represents the truncation error.

In order for a method to be consistent, the truncation error must become zero as the mesh spacing (in terms of time or space) tends to zero. Truncation error is usually proportional to a power of the grid spacing and/or the time step. Ideally, all terms should be discretised with approximations of the same order of accuracy, however, some terms may be dominant in a particular flow and it is then acceptable to treat them with more accuracy than the others, i.e. convective terms in high Reynolds number flows.

4.5.2 Conservation

The equations that govern fluid flow are based on the conservation laws of physics. Any numerical scheme utilised in order to solve the equations must therefore also respect these laws. For a steady-state solution, in the absence of sources, the amount of a conserved quantity leaving a closed volume must be equal to the amount entering that volume. In the case of the finite volume technique, conservation is guaranteed for each individual control volume as well as for the solution domain as a whole.

Conservativeness of a solution method is an important property as it imposes a constraint on the solution error. If the conservation of mass, momentum and energy are ensured, error can only improperly distribute these quantities over the solution domain. Conservative schemes are preferred.

4.5.3 Boundedness

Physically, non-negative quantities (e.g. density, turbulent kinetic energy) must always be positive. Other quantities such as concentration must lie between 0% and 100%. In the absence of sources, some equations (e.g. heat) require that the internal nodal values of a property should be bounded by its boundary values. These bounded conditions should be inherited by the numerical approximation used.

Boundedness is not easy to guarantee, with only some first order schemes guaranteeing this. All higher order schemes can produce unbounded solutions (usually only when the grid used is too coarse). This leads to undershoots and overshoots (termed wiggles) which can often be eliminated by grid refinement.

4.5.4 Transportiveness

The transportiveness property of a fluid is best described if one considers two sets of extreme conditions. In a highly diffusive situation with no convection, the spread of a constant source of a scalar, say ϕ, would be equal in all directions i.e. the influence of the source at all neighbouring nodes would be equal. However, in the case where there is no diffusion and the flow is purely convective the conditions at the neighbouring node to the source of ϕ upstream would be unaffected where as the conditions at the neighbouring downstream node would be strongly influenced by the source upstream.

As the relative strength of convection to diffusion increases, the numerical method must allow for the increased influence at downstream nodes and the consequent

decrease in influence for nodes upstream. It is important that the directionality of influencing (transportiveness) is accounted for in the discretisation scheme used.

4.5.5 Central Differencing

Central differencing approximations of values at the faces of control volumes utilises linear interpolation between the two nearest nodes. At location *e* on a uniform cartesian grid (as in Figure 4.1)

$$\phi_e = \frac{\phi_P + \phi_E}{2} \tag{4.43}$$

Central differencing is the simplest second order scheme and one of the most widely used for diffusion dominated situations. However, central differencing does not possess the transportiveness property as flows become convective (higher Reynolds number) and has a major short-coming in that it is unable to recognise direction of flow, making it impractical for convective situations. Accuracy of the central differencing scheme is second order in terms of Taylor series truncation (terms of second order and higher are truncated).

4.5.6 Upwind Differencing

Approximating ϕ_e by its value at the node upstream of *e* is equivalent to using a backward or forward differencing approximation for the first derivative (depending on flow direction), hence the name *upwind differencing scheme*. For upwind, ϕ_e is approximated as

$$\phi_e = \begin{cases} \phi_P & if \quad u_e > 0; \\ \phi_E & if \quad u_e < 0. \end{cases} \tag{4.44}$$

The above approximation is the only one that satisfies the boundedness criterion unconditionally (it never yields oscillatory solutions). However, upwind interpolation is numerically diffusive as described below.

The Taylor series expansion about the node *P* (for a Cartesian grid and $u_e>0$) gives

$$\phi_e = \phi_P + (x_e - x_P)\left(\frac{\partial \phi}{\partial x}\right)_P + \frac{(x_e - x_P)^2}{2}\left(\frac{\partial^2 \phi}{\partial x^2}\right)_P + H \tag{4.45}$$

where *H* denotes higher order terms. The upwind scheme approximation only retains the first term on the right side of equation (4.45) making it a first order scheme. The effect of using only the first term is the numerical diffusion due to this truncation error which is especially pronounced when flow is oblique (not aligned) to the grid.

Here, the truncation error produces diffusion in the direction normal to the flow as well as in streamwise direction. The result is a smearing out of peaks or rapid variations in variables since the rate of error reduction is only first order. Very fine grids are required to obtain accurate results.

4.5.7 Hybrid Differencing

The hybrid differencing scheme is based on a combination of central and upwind differencing schemes. The relative contribution of convection and diffusion is the factor used in the decision of which scheme to utilise. The Peclet number (*Pe*) gives a measure of the relative contributions of convection and diffusion. For small Peclet numbers ($Pe<2$) the central differencing scheme is employed whilst the upwind scheme is used for higher Peclet numbers ($P_e \geq 2$).

The hybrid differencing scheme is fully conservative and is unconditionally bounded. For convective flows it also satisfies the transportiveness criteria by the use of upwind for high Peclet number flows. The major disadvantage of the scheme is in terms of its accuracy since the Taylor series truncation error is only first order for the upwind scheme. It has, however, been widely applied and proven in a wide range of practical flows.

4.5.8 Quadratic Upwind Differencing Scheme (QUICK)

The **q**uadratic **u**pstream **i**nterpolation for **c**onvective **k**inetics (QUICK) scheme uses three points with a quadratic interpolation for calculating cell face values. The face value of ϕ is found by the application of a quadratic function passing through two bracketing nodes (one each side of the face) and a node on the upstream side as shown in Figure 4.2.

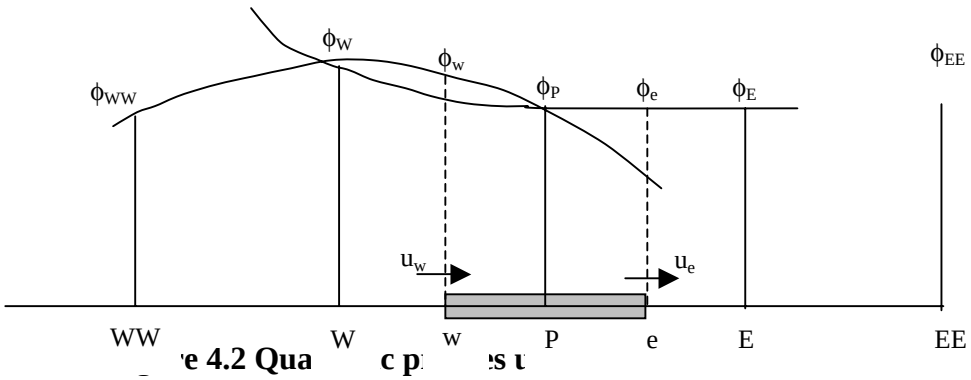

e 4.2 Qua c p s u

Source: Versteeg and Malalasekera (1995)

In order to understand how the QUICK scheme works, when both u_w and u_e are positive, a quadratic fit through WW, W and P is used to evaluate ϕ_w, and a further quadratic fit through W, P and E used to calculate ϕ_e.

For the situation shown in Figure 4.2 and for a positive value of u_w, the bracketing nodes for the west face, w, are W and P, and the upstream node WW and

$$\phi_w = \frac{6}{8}\phi_W + \frac{3}{8}\phi_P - \frac{1}{8}\phi_{WW} \tag{4.46}$$

Similarly, for u_e positive, the bracketing nodes for the east face ,e, are P and E, and the upstream node is W and

$$\phi_e = \frac{6}{8}\phi_P + \frac{3}{8}\phi_E - \frac{1}{8}\phi_W \tag{4.47}$$

The QUICK scheme is conservative since the cell face values of fluxes are always calculated by quadratic interpolation between two bracketing nodes and an upstream node. As the scheme is based on a quadratic function, in terms of Taylor series truncation error, it is third order on a uniform mesh (terms of third order and higher are truncated). Transportiveness is inherently built into the scheme as the quadratic function is based on two upstream and one downstream nodal values.

Stability problems may arise with the QUICK scheme and unbounded solutions may be produced under certain flow conditions as demonstrated in Figure 4.3. The production of unbounded solutions (undershoots and overshoots) due to the application of quadratic functions has led to further developments of schemes based on QUICK with further refinement.

4.5.9 CCCT Differencing Scheme

The curvature-compensated convective transport (CCCT) scheme was devised in order to conserve the boundedness property where the QUICK scheme (described above) may produce unbounded results.

In regions where there are sharp gradients of variables, other higher order schemes such as QUICK can produce unbounded solutions in the form of over or undershoots due to the curvature of the quadratic profiles utilised (as shown in Figure 4.3). The CCCT scheme overcomes steep gradient problems by employing physically realistic constraints to ensure monotonic (bounded) solutions are found whilst retaining a higher degree of accuracy (Gaskell et al (1988)). Figure 4.4 demonstrates the comparison between CCCT and QUICK.

CCCT is actually a modified version of the QUICK scheme where the value of ϕ at the west face, w, is given by (referring to Figure 4.4)

$$\phi_w = \left(\frac{3}{8} - \alpha\right)\phi_P + \left(\frac{3}{4} + 2\alpha\right)\phi_W - \left(\frac{1}{8} + \alpha\right)\phi_{WW} \tag{4.48}$$

where α depends on the curvature of the variable ϕ. The scheme then acts as the QUICK scheme described above.

4.6 Solution Procedures for Pressure and Velocity Fields

When the differencing schemes were discussed previously with respect to the convection of a scalar, it was stated that the velocity and pressure fields were assumed to be known. The velocity field is, however, not usually known and emerges as part of the overall solution process along with all other flow variables.

Problems encountered in solving the pressure and velocity fields include non-linear convective terms in the momentum equation, and intricate coupling of the three momentum equations as every velocity component appears in each momentum equation as well as in the continuity equation. The most complex problem involves the role played by the pressure. Pressure appears in all of the momentum equations, however, there is no equation for pressure.

In the vast majority of cases, the pressure field is required as part of the overall solution. If the flow is compressible, the continuity equation can be used as a transport equation for density. In addition to this, the energy equation is a transport equation for temperature. Using these two equations and the equation of state ($p = p(\rho, T)$), pressure can be calculated. This is not the case for incompressible flows where the density is constant and so cannot be linked to pressure. For incompressible flows, coupling between pressure and velocity introduces a constraint on the solution of the flow field. If the correct pressure field is applied in the momentum equations, the resulting velocity field should satisfy continuity (Versteeg and Malalasekera (1995)).

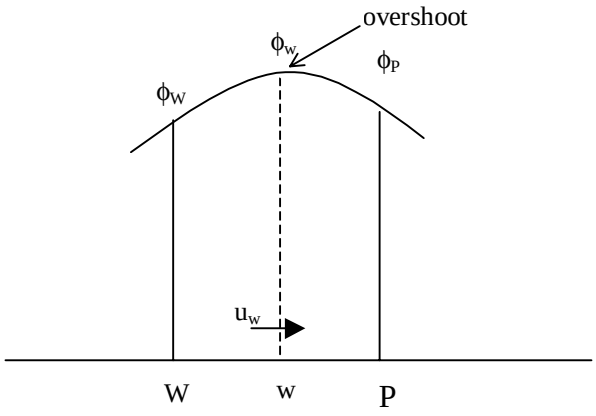

Figure 4.3 Overshoot across west face, w, by quadratic relationship applied in QUICK differencing scheme

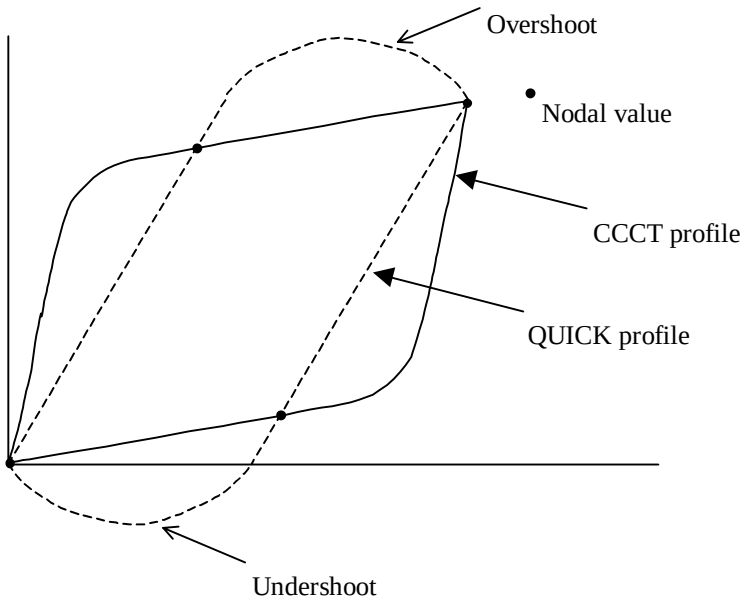

Figure 4.4 Illustration of CCCT monotonic interpolative profile eliminating overshoots produced by quadratic profile of QUICK

The problems of the non-linearities in the set of equations and the coupling of the velocity and pressure are resolved by the adoption of iterative solution procedures including the SIMPLE algorithm. The acronym SIMPLE stands for **S**emi-implicit **M**ethod for **P**ressure-**L**inked **E**quations.

The SIMPLE calculation begins with a guessed pressure field. This guessed pressure field is utilised in the discretised momentum equations in order to produce initial values for the velocity components. The pressures and velocity components are then corrected using functions relating to the values produced at the latest iteration and the values from the previous iteration (details of this procedure can be found in Versteeg

and Malalasekera (1995)). All of the other discretised transport equations are then solved (e.g. scalar variables). The solution is then checked for convergence, if the solution has converged then a solution is reached. However, if convergence criteria are not met, the procedure is repeated until a converged solution is obtained.

4.7 Computational Fluid Dynamics Model Formulation

The computational investigations undertaken within this research make use of the theoretical techniques discussed in the previous sections of this Chapter. All of the computational simulations were related to the assessment of wind induced ventilation of a structure.

The two major parts of the computational tests were:

1. Modelling the external flow conditions around a cubic structure;
2. Modelling internal flow within a cubic structure.

In order to produce a reliable computational simulation, it is necessary to ensure that the results produced are consistent and that all variables that may affect the simulation have been checked and compared with other methods. The wind induced ventilation of any structure is governed by the pressure and velocity field around the surface of the structure and in particular in the vicinity of ventilation openings. For this reason, it was very important that the CFD simulations within this work modelled both the external region around the structure and the internally ventilated space.

4.7.1 CFD Code

The computational fluid dynamics package utilised throughout this work was CFX version 4.2 produced by CFX International, a company owned by AEA Technology Plc. The software is based on the finite volume method (discussed in section 4.3.3).

The software is devised into a number of components:

- Pre-processor;
- Solver;
- Post-processor.

The pre-processor in CFX is named CFX-Meshbuild. In the pre-processor, the computational model is configured in terms of the geometry of the solution domain and the division of the domain into the finite control volumes for the solution procedure. In the pre-processor, the boundary conditions such as wind velocities and wall boundaries are initialised.

The solver is utilised to integrate the governing equations of fluid flow and to solve the algebraic expressions produced by the numerical approximations of these equations in order to provide a solution to the fluid flow problem. The post-processor is then utilised in order to visualise the resulting fluid flow in terms of velocities, pressures and other flow variables.

4.7.2 Computational Geometry and Domain

The computational domain is the geometry that is constructed for the simulation and solution of a fluid flow problem. All of the modelling within this thesis has been conducted on a cubic structure with dimension of 6m. In order to model the external and internal flow fields, it was necessary to model the structure in a simulated atmospheric boundary layer.

The model was constructed in order that it could be utilised to model both the external and internal ventilation flows. This required the ventilation openings to be incorporated in external flow studies such that no alteration to the computational grid was required when ventilation simulations were undertaken. When modelling external conditions, the openings were set as rough walls (as was the rest of the building's surface), these were then removed when ventilation mechanisms were modelled. Two, square ventilation openings were positioned on opposite faces of the cube and each had an area of $1m^2$. The centre of each opening lay on the vertical centre-line of the cube face at a height of 3.5m above the ground, as shown in Figure 3.3.

The computational domain was constructed so that the inlet, outlet and domain edges did not interfere with the flow in the region of interest (around and within the test structure). A distance of five building heights (30 m) was used between the domain inlet and the windward face of the building, five building heights between the sides of the building and the sides of the domain, and between the building roof and the top of the domain, and a distance of ten building heights between the leeward face of the building and the domain exit. The position of the domain outlet was important and had to be positioned at a distance downstream from the test building where there were no streamwise flow gradients. The computational domain is shown in Figure 4.5.

The top and sides of the domain were given symmetry boundary conditions in order to further reduce the effects of the domain sides. The conditions at a symmetry boundary are:

- No flow across the boundary;
- No scalar flux across the boundary.

The normal velocities were set to zero at the symmetry boundaries and the values of all other properties just outside the solution domain equated to the values at the corresponding nearest nodes just inside the domain. The advantage of a symmetry boundary is that the edges of the domain do not affect the flow as wall boundary conditions would.

The building sides were set as no-slip walls with wall functions providing the correct wall roughness (0.005m), velocity and shear stress in the near wall region. The same procedure was used for the ground, although different surface roughness were set for the two surfaces (see boundary layer modelling below).

4.7.3 Model Parameters

Two turbulence models were utilised in this work:

1. Standard k-ε model;
2. RNG k-ε model.

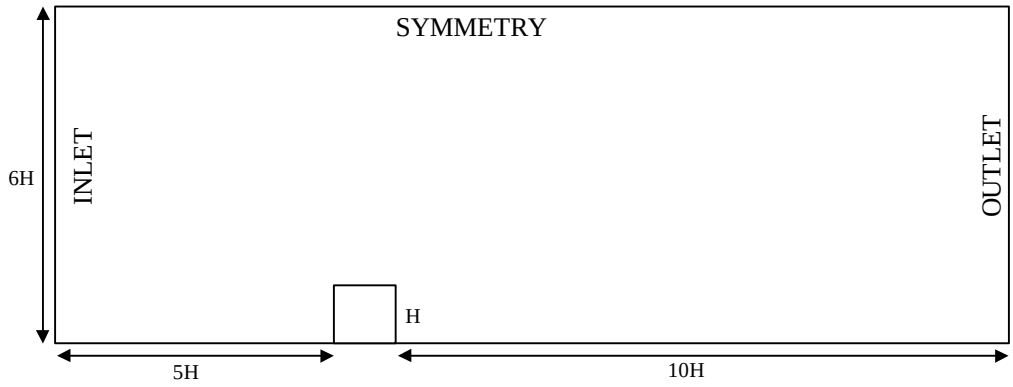

(a) Side elevation

(b) Plan elevation

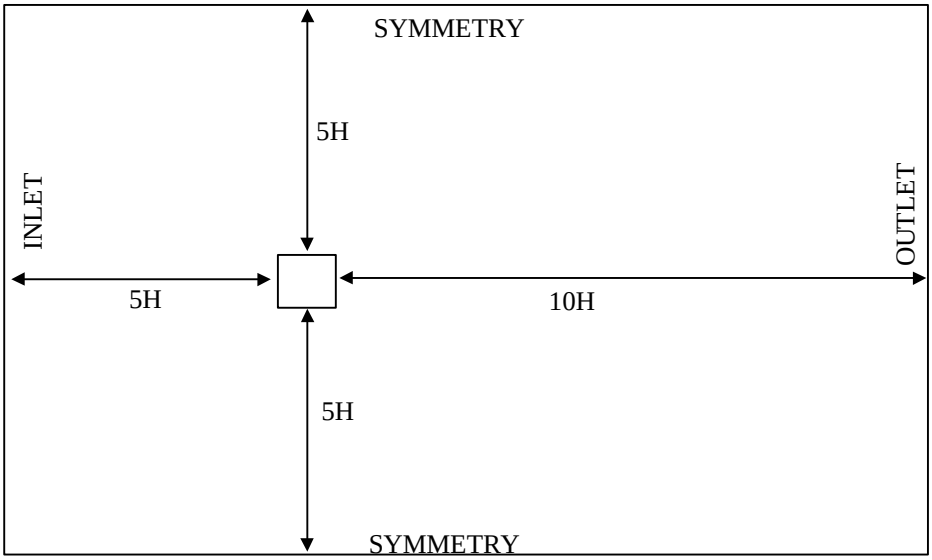

Figure 4.5 Computational domain geometry and boundary conditions

Both models were tested with respect to the simulation of external surface pressures. However, only the RNG k-ε model was utilised for the wind induced ventilation investigations.

Initial investigations into the application of different differencing schemes led to the use of CCCT differencing for all of the modelling described within this research, because this offered high order accuracy and numerical stability.

4.7.4 Grid Development and Refinement

Any rigorous CFD investigation requires a grid dependency check. In certain circumstances, coarse grids can lead to the conservativeness property not being fulfilled. Also, to ensure that a solution is fully converged it is necessary to solve a problem utilising successively refined grids until the solution remains unchanged. Convergence criteria throughout all of the CFD tests described here required the ratio between the first and last residual error values (produced through the iterative solution of the equations) to be at least $1x10^5$.

For the purposes of this investigation, grid independency tests were undertaken on the external flow simulations. A number of grid refinements were made to ensure that both the large scale external flows (e.g. wake recirculation) and small scale external flows (e.g. recirculation over roof) were modelled on grids which were of sufficient density to reliably model the processes involved.

The grid refinement involved:

- Increasing the density of the grid surrounding the test structure;
- Increasing the density of the grid on the test structure.

For the grid tests, three grids were developed for the same solution domain. The first contained 116000 cells, the other two grids had a 200% and 400% increase in cell numbers compared with the first grid. The distribution of the 116000 cell grid was made up of 20^3 equally spaced cells around the cube sides, 18 cells between the domain inlet and the cube, 20 cells between the cube roof and domain top and 20 cells between the back face of the cube and the domain outlet. The grid was designed so that geometric progressions led to the grid being finer close to the cube and gradually coarser with distance to provide as much detail as possible in the region of

importance. Figure 4.6 shows a cross-section of the 116000 cell computational grid from the front of the domain.

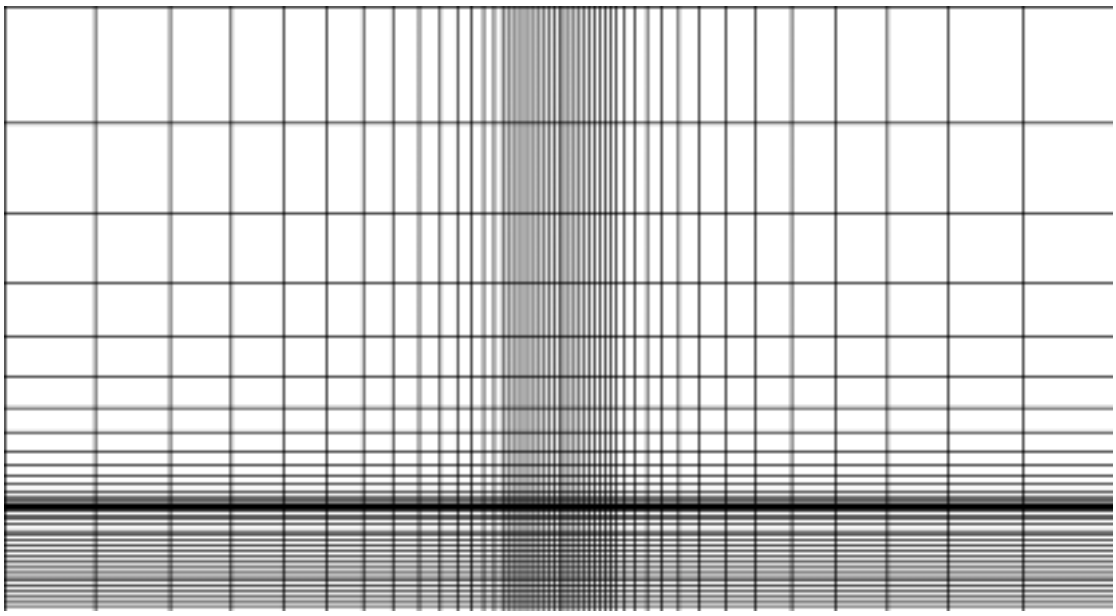

Figure 4.6 Computational grid used around test cube

By comparing the results of each of the three simulations it was found that even the coarsest grid produced the same (or very similar) results as the finest. This is demonstrated in Figure 4.7 which shows windward face pressure distributions for the coarsest and finest grids for a perpendicular wind angle, as predicted by the standard k-ε turbulence model. Due to computational constraints, it was not possible to refine the grid further to test still more strenuously, grid independency.

The grid around the cube sides was tested with grid distributions of 20^3 and 40^3 in order to ensure that small scale flow phenomena would not be missed by utilising a grid that had spacing which was larger than the scale of the flows of interest. The roof pressure distributions using the standard k-ε model are shown in Figure 4.8 for the two grids that show minimal difference between the two profiles. The grid distribution of 20 cells along each edge of the cube was therefore utilised with the coarsest domain grid tested.

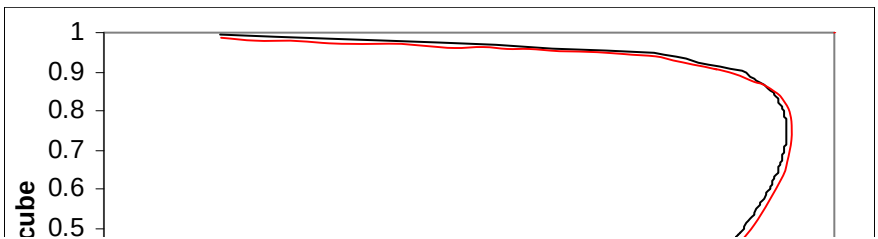

Figure 4.7 Effect of grid density on windward face pressures for 0° incident wind

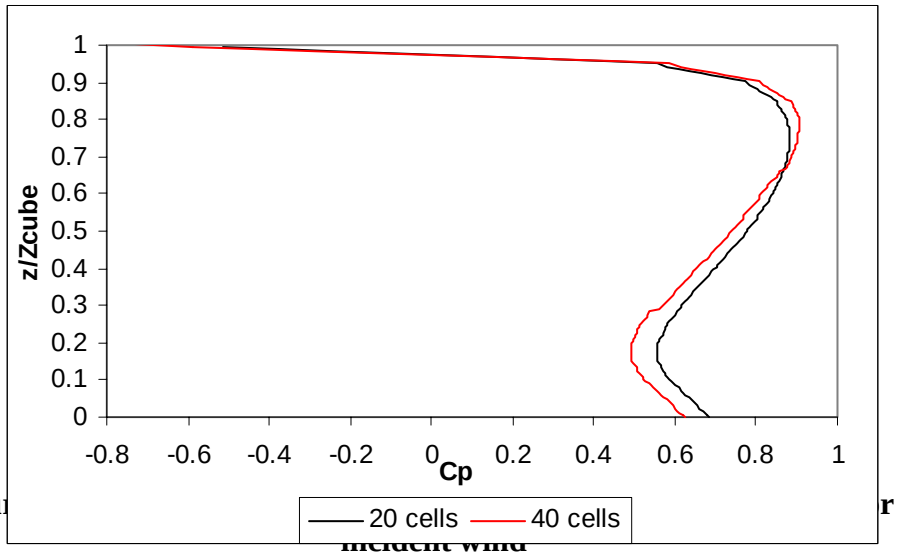

Figu **r 0°**
incident wind

4.7.5 Atmospheric Boundary Layer Simulation

For any CFD simulation to be accurate, it is important to define boundary conditions that match as closely as possible those applicable to the case being modelled (in this investigation, the atmospheric boundary layer). For any k-ε turbulence model it is necessary when developing inlet boundary conditions to provide the inlet velocity profiles for the velocity, kinetic energy and kinetic energy dissipation.

The development of atmospheric boundary layer conditions required the simulation of an equilibrium boundary layer (one that does not alter if no obstruction is present in the flow) in terms of velocity profile with height as well as turbulence profiles.

Implementation of complex boundary conditions in CFX 4.2 involves the development of user-FORTRAN routines that enable the user to manipulate the code in order to set the required conditions for a simulation.

The boundary layer profiles utilised within this work were developed from investigations by Richards (1989) and Richards et al (1993) when attempting to develop boundary conditions for 2-D CFD simulations of flow over a structure. The test structure simulated by Richards was located at the same site as the test cube investigated here. The profiles developed for the atmospheric boundary layer used are as follows.

The streamwise velocity profile,

$$U(z) = \frac{u_*}{\kappa} \ln\left(\frac{z + z_0}{z_0}\right) \tag{4.49}$$

the kinetic energy profile

$$k = \frac{u_*^2}{\sqrt{C_\mu}} \tag{4.50}$$

and the dissipation of kinetic energy

$$\varepsilon = \frac{u_*^3}{\kappa(z + z_0)} \tag{4.51}$$

where

$$u_* = \frac{\kappa U_{ref}}{\log\left(\frac{z_{ref}}{z_0}\right)} \tag{4.52}$$

Comparisons of the above boundary layer conditions with those measured at the SRI site by Richards (1993) showed acceptable agreement.

4.7.5.1 Effect of Ground Roughness

Full-scale measurements of the boundary layer have been undertaken over many years at the site of the full-scale test structure described in Chapter 3. As stated above, the surface roughness has been measured on many occasions and found at different times to vary between 0.01m and 0.04m according to the type and height of the crop in the upwind field. Preliminary CFD tests were therefore undertaken for external flow

parameters to see what effect a change in surface roughness had on the external pressures and velocity flow field.

Figure 4.9 shows the windward face centre-line pressures for a normal wind direction obtained using the RNG k-ε turbulence model for surface roughness of both 0.01m and 0.05m. A slight increase in peak pressure (the stagnation point) for the higher surface roughness is apparent, due to the increased turbulence present in the flow. The increased retardation of the flow close to ground level is responsible for the slight decrease in pressures lower down the windward face for the higher roughness flow. The effect of the surface roughness change on roof pressures can be seen in Figure 4.10 where the negative pressure close to the front corner of the roof becomes more negative for the higher roughness flow. Increased turbulence in the approach flow has been found in many previous investigations (e.g. Castro and Robins (1977)) to lead to higher suctions in the separations region and earlier reattachment of flow along the roof.

The effects of surface roughness have been investigated to check that there are no significant changes in the external pressure distributions and flow conditions within the limits of 0.01m and 0.04m. Researchers at SRI (Hoxey (1999)) have confirmed that the full-scale tests described in Chapter 3 were conducted under upwind fetch conditions consistent with a surface roughness of 0.01m. For this reason, the remainder of the CFD testing utilised the lower value of roughness.

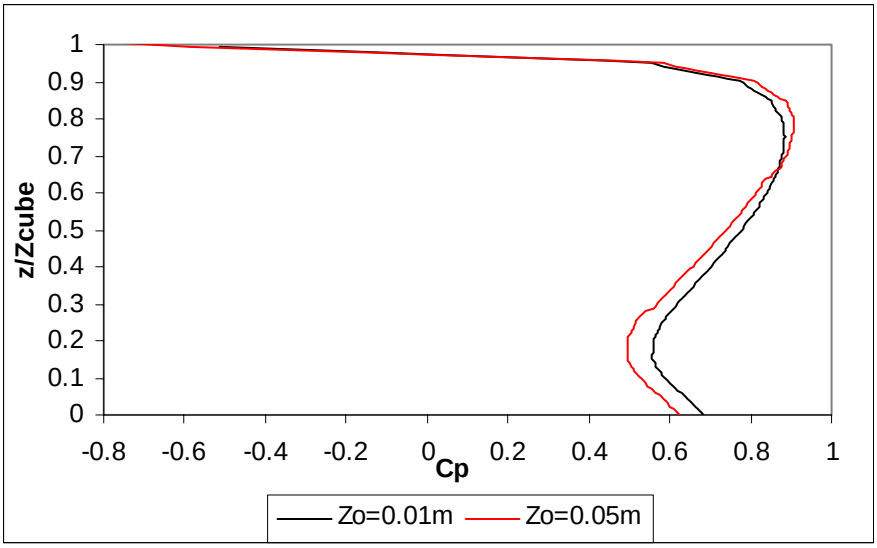

Figure 4.9 Effect of ground roughness on windward face pressures

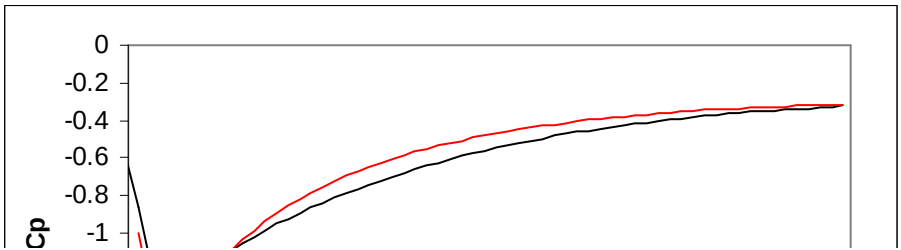

Figure 4.10 Effect of ground roughness on roof pressures

4.7.6 CFD Test Configurations

The CFD investigations are divided into two parts. Firstly the external pressure and flow field simulations were undertaken. From this, the external and internal flow fields were simulated simultaneously. The external flow simulations were validated with experimental data in order to identify the numerical technique (in terms of turbulence model) that agreed best with the measured results. The external simulations were undertaken for the incident wind normal to the cube (0° case) which provided the validating test case. For the ventilation simulations a number of incident wind directions were assessed. Figure 4.11 (a) shows the definitions of the wind direction used throughout the results section.

Throughout the results, the surface pressure distributions given are those measured along face centre-lines in the orientations shown in Figure 4.11 (b).

All results given in this Chapter are provided in non-dimensional form following the same conventions as used in the full-scale experiments described in Chapter 3 (the parameters used for non-dimensionalising are provided in section 3.6).

4.8CFD Results

The design, preparation and implementation of the computational simulations of external flows and wind induced ventilation flows were discussed in section 4.7 previously. This section deals with the results gained from these investigations. Starting with the modelled profiles of the atmospheric boundary layer, the predictions of external pressure around the test structure are discussed and compared wherever possible with measured distributions found from the full-scale experiments (see Chapter 3). It should be noted that the conventions used in Chapter 3 (section 3.6) also apply in the CFD results in terms of data normalisation and orientation.

The effect of the turbulence model used is discussed with respect to the flow field as well as turbulence structure around the external region of the cube. As no external flow field data were measured during the full-scale experiments, it is not possible to fully validate these parameters. However, attempts are made to draw from the results

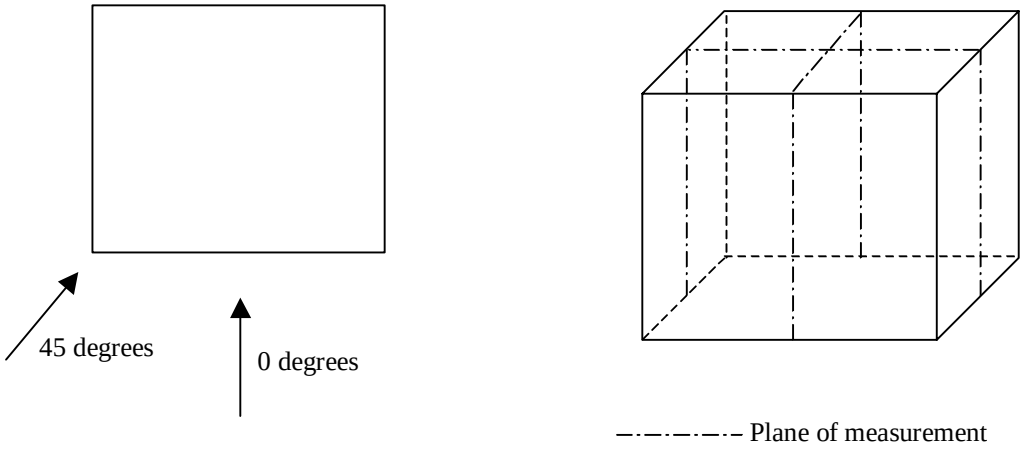

(a) Definitions of wind directions **(b) Planes of surface measurement**

Figure 4.11 Definitions of wind directions and measurement positions in CFD modelling

of other investigations in order to identify any inadequacies in the computational simulations.

The reason for including comparisons between experimental measurements and the external flow simulations is to identify which turbulence model provides the best predictions of the surface pressures and external flow and turbulence fields, before attempting to simulate the wind induced ventilation of the structure.

Following the external flow investigations, and identifying which turbulence model to utilise, the computational simulations turn to the application of CFD to model wind induced internal airflow within the test cube. Ventilation is modelled simultaneously with the external environment by the introduction of openings on two of the faces of the cube (the positions of these were detailed in section 3.2). The structure of the internal flow field is discussed before the results are used to quantify the induced ventilation rate.

4.8.1 Atmospheric Boundary Layer

In Chapter 2, the presence of an atmospheric boundary layer was shown to affect both the external surface pressure distribution and the velocity flow field around a bluff

body. For a full-scale building to be simulated properly, the boundary layer must be modelled in terms of both velocity and turbulence profiles.

Figure 4.12 shows the vertical wind speed profile in the computational domain at a position where the effects of any obstruction are not present. It can be seen that there is a logarithmic increase in velocity with height since the boundary layer velocity was modelled on a log-law profile. The lateral and vertical components of velocity were set to zero.
Figure 4.13 depicts the reduction in turbulent kinetic energy (divided by the reference wind speed) with height through the domain (shown as height divided by the domain height). Figure 4.14 depicts the profile of the dissipation of turbulent kinetic energy vertically through the domain. As with the velocity profile of Figure 4.12, both the turbulent kinetic energy profile and that of its dissipation were measured in regions of unobstructed flow.

4.8.2 External Surface Pressures

The external surface pressure distributions discussed here are compared to the full-scale measurements discussed in Chapter 3. The incident wind direction for the following external pressures is normal to the windward face (0° case). The data available from the experimental results provide pressure measurement at only five or six (depending on the face) locations whilst CFD provided data at as many locations as required down to a spacing of 0.0036m between points. For this reason, the CFD data are provided over wider ranges than were the experimental data.

4.8.2.1 Windward Face Pressures

The expected distribution of pressure over the windward face of a cubic structure in a sheared flow was introduced in Chapter 2. Figure 4.15 shows the distributions of pressure for a 0° wind direction as predicted by both the standard k-ε and the RNG k-ε models; the measured distribution is also shown. The general profiles of pressure follow that expected from the theoretical description however, it is obvious that the RNG model provides a pressure profile that is closer to the measured distribution.

The maximum peak pressure on the front face of the structure corresponds to the stagnation point where flow is brought to rest. At this maximum all of the dynamic (velocity) head of the approaching flow is converted to pressure on the building surface. The standard k-ε model predicts the peak pressure to be positioned at a height 85 % of the way up the windward face with a peak pressure coefficient of 0.98 whilst the RNG model predicts a value of 0.88 occurring 75% of the way up the face. The measured pressures show a peak pressure of 0.87 at a height of approximately 70% of the face height.

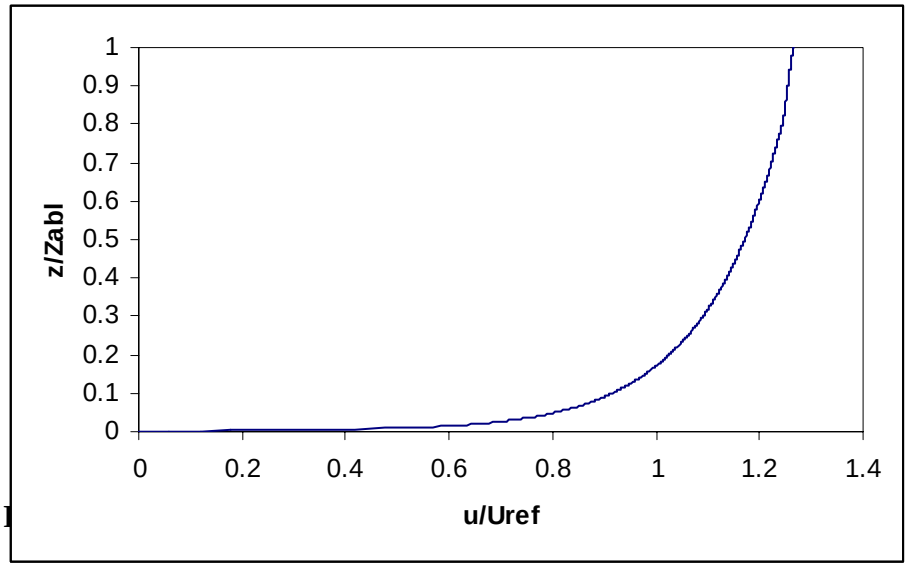
z/Zabl
u/Uref
0
0.1
0.2
0.3
0.4
0.5
0.6
0.7
0.8
0.9
1
0.2
0.4
0.6
0.8
1.2
1.4

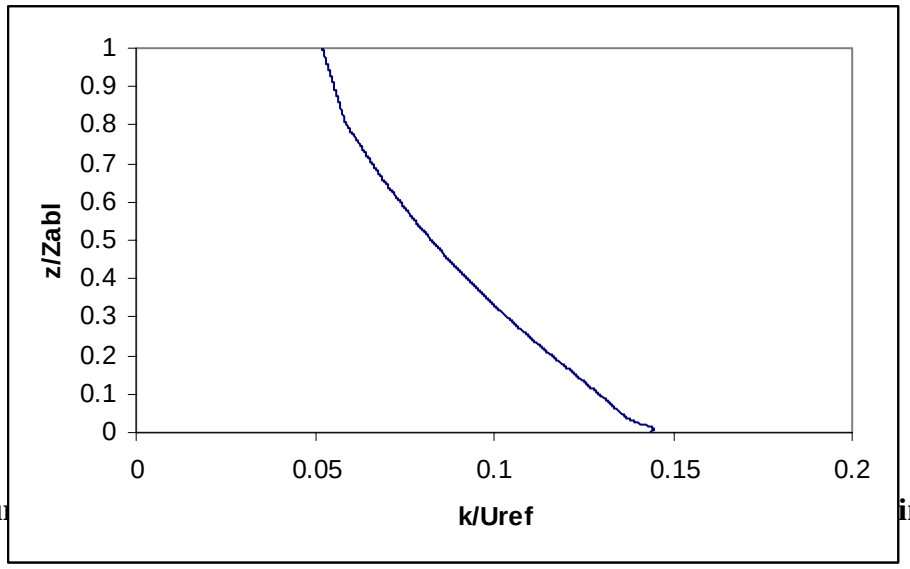
z/Zabl
k/Uref
0
0.1
0.2
0.3
0.4
0.5
0.6
0.7
0.8
0.9
1
0.05
0.15


z/Zabl
0
0.1
0.2
0.3
0.4
0.5
0.6
0.7
0.8
0.9
1

Figure 4.14 Free stream dissipation of turbulent kinetic energy profile in CFD domain

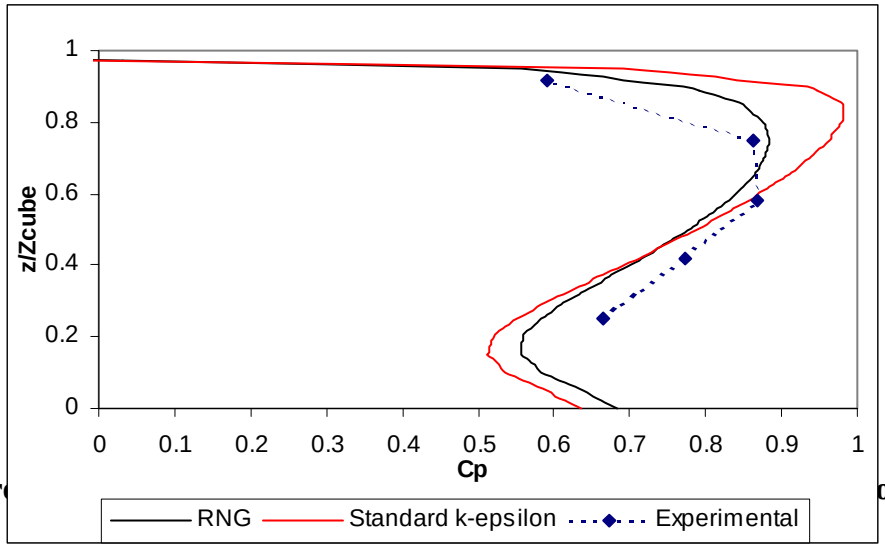

Figur on

4.8.2.2 Roof Pressures

Pressure distributions streamwise along the lateral centre-line of the roof are shown in Figure 4.16. Both the computational simulations can be seen to significantly over-predict the negative peak pressure around the leading edge of the roof. The standard k-ε model can be seen to produce the poorest prediction of roof pressure. It gives a peak negative pressure of –1.77, which is almost 50% more negative than the measured value (-1.22). The predicted recovery of pressure with streamwise distance along the roof also occurs much more rapidly than was measured.

As with the windward face, the RNG model predicts an improved roof pressure distribution when compared to the measured values. The peak negative pressure is closer in terms of magnitude at –1.37 (approximately 13% more negative than the measured value). However, the location of this peak suction does not compare so favourably. Experimental measurements show the peak negative pressure to occur approximately one-quarter of the way along the roof however, both computational predictions show it to be located much closer to the windward edge of the roof.

As with the standard k-ε model, the RNG prediction of pressure recovery differs from the measured distribution that shows a much steadier increase in pressure towards the leeward edge of the roof. Convergence of pressures of both computational simulations towards the leeward edge of the roof do however, lead to agreement with measured values in this region.

Figure 4.17 shows roof pressures across the transverse centre-line for the 0° wind direction. The difference between both computational predictions and the measured distribution is significant. The standard k-ε model predicts pressures which are approximately half of those measured whilst the RNG predicts a slightly improved distribution but still with significant discrepancy compared with the measured values.

4.8.2.3 Leeward Face Pressures

Measured and predicted vertical profiles of leeward face surface pressures are shown for the centre-line of the face in Figure 4.18. The distributions predicted by both turbulence models show similar results with negative pressures ranging from approximately –0.25 at the ground to –0.35 towards the top of the face, although the standard k-ε model exhibits slightly lower pressures than the RNG model. The pressures in both cases become slightly more negative with height up the leeward face.

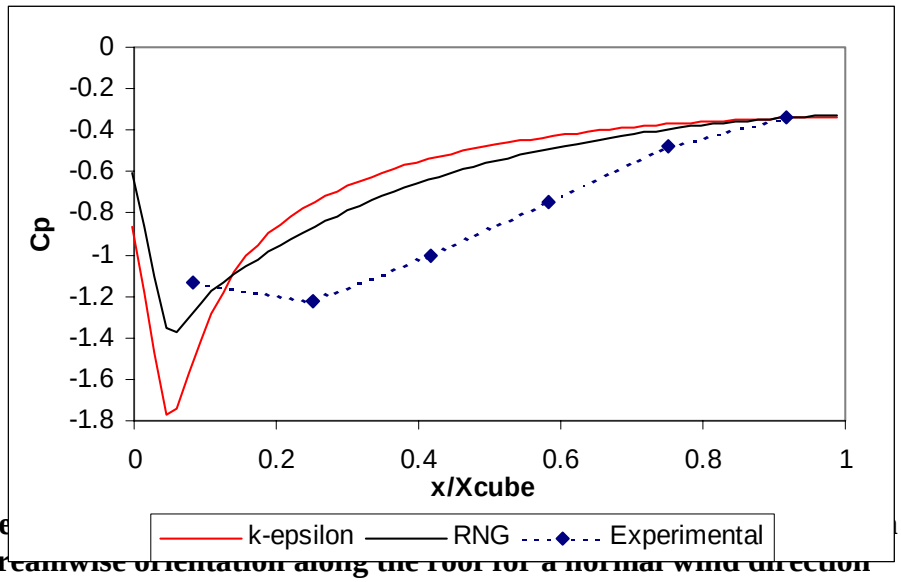

Figure [illegible] a streamwise orientation along the roof for a normal wind direction

Both turbulence models fail to predict the strength of the negative pressure close to the ground where there is approximately 33% difference between the predictions and measured values. This difference does however, reduce over the upper half of the face where the distributions are within 10% of each other.

4.8.2.4 Side-Wall Pressures

The pressure predictions vertically up the centre of the side walls are shown in Figure 4.19. As with the pressures on the leeward face, the predicted pressures are relatively close to each other with values ranging from –0.45 at ground level to maximum negative values of around –0.65 midway up the side wall. Both predictions under-estimate the measured suctions by least 25%.

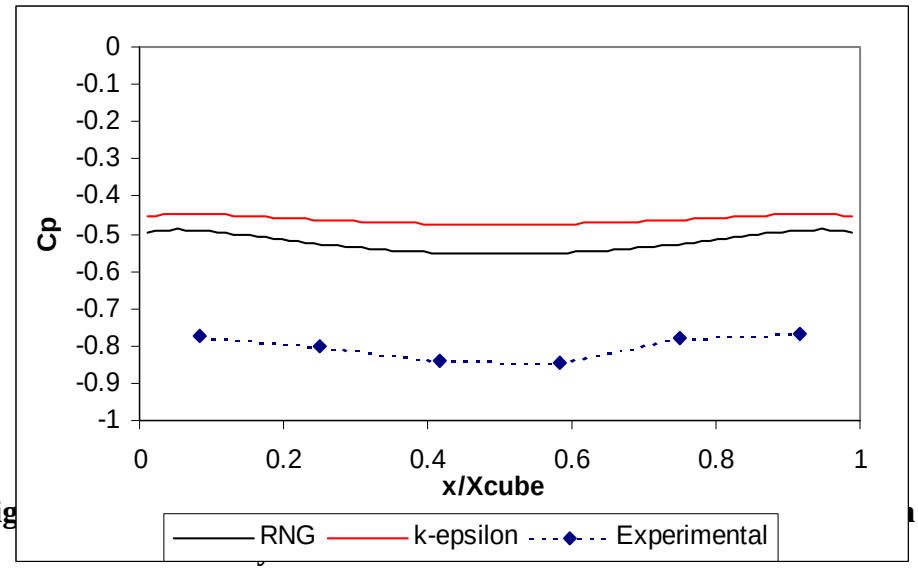

Fig

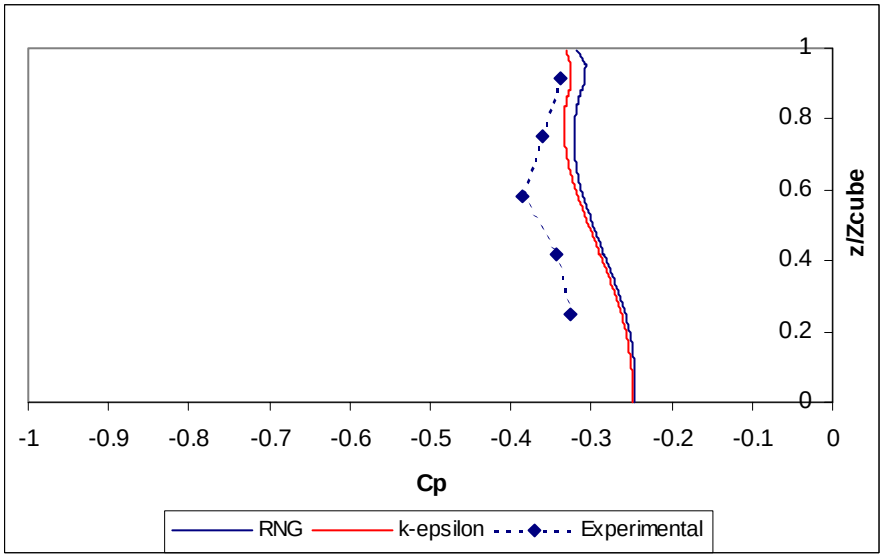

Figure 4.18 Measured and predicted pressure coefficient distribution on the leeward face centre-line for normal wind direction

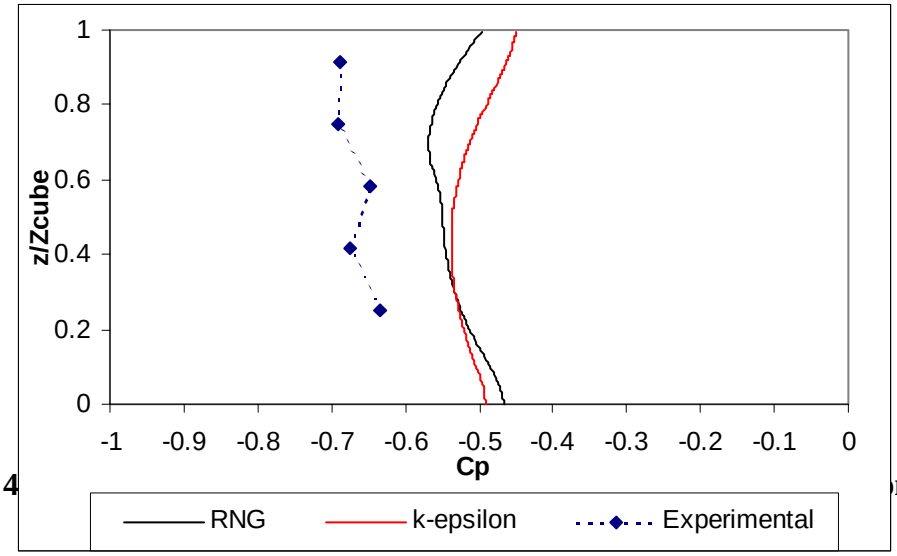

Figure 4 ng the

4.8.3 External Velocity Fields

The following results illustrate the overall flow field prediction obtained from the two models and highlight any differences between the two simulations. In order to compare the results, a number of regions of the flow field are targeted, these are:

- Windward face flow;
- Flow over roof;
- Flow in wake region;
- Flow around side faces.

Unfortunately, there are no experimental data from the full-scale investigations for the validation of the flow field data. The lack of similar full-scale research in this field makes it also difficult to draw from the results of other investigations. The flow field results are therefore discussed mainly in terms of the expected theoretical patterns as described in Chapter 2.

Figures 4.20 and 4.21 show the velocity flow fields as predicted by the standard and RNG k-ε models respectively along the cube centre-line for a 0° incident wind direction. These Figures give a view of the full flow field and all of the associated patterns that are to be discussed in greater detail in the following. The shaded contour plots of CFD results (e.g. Figures 4.20 and 4.21) present velocity in ms^{-1}.

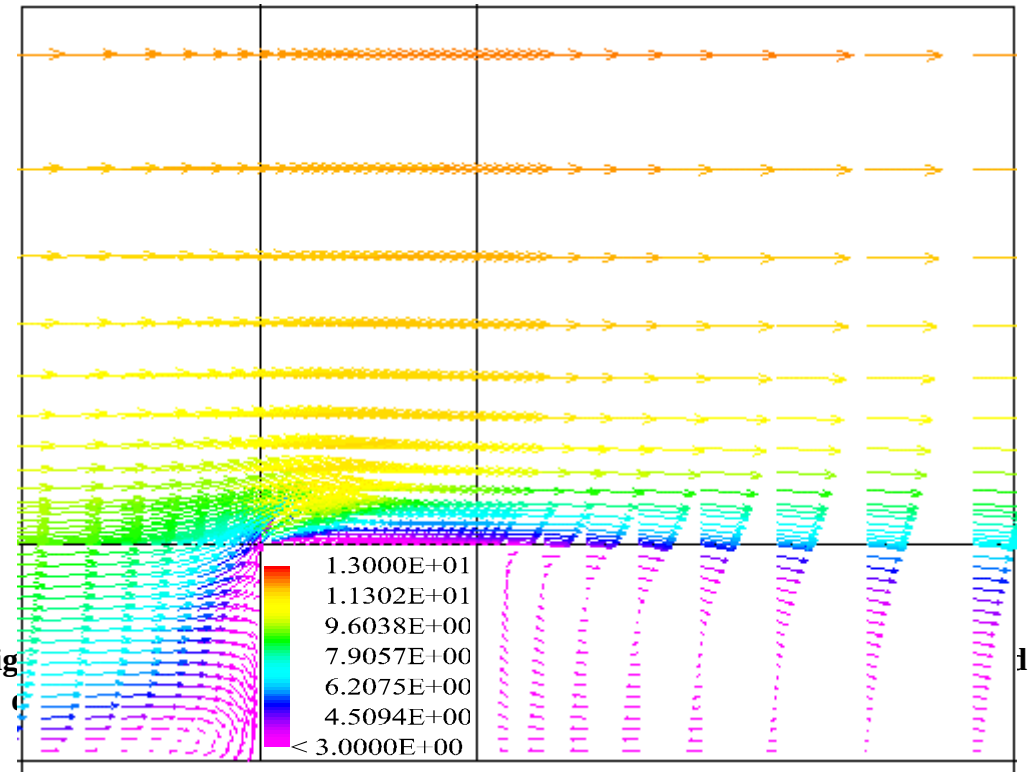

Fig

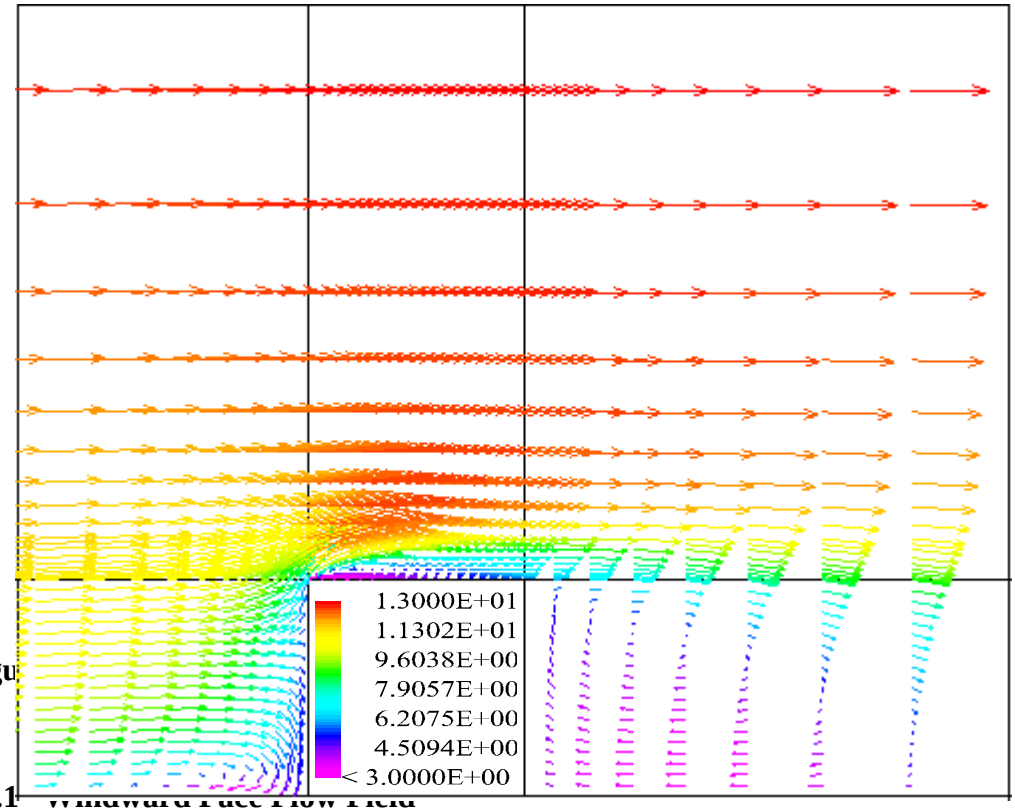

Figu

4.8.3.1 Windward Face Flow Field

The two flow field predictions shown in Figures 4.20 and 4.21 are very similar with respect to the windward face of the cube. Two main phenomena apparent in these flow fields are the position of the stagnation point and the recirculating flow at ground level in front of the face.

The stagnation point (where flow is brought to rest on the windward face) is predicted to be at 85% of the face height by the k-ε model and at 75% by the RNG k-ε model. Any flow above the stagnation point is directed vertically upwards over the leading edge of the roof. Below the stagnation point on the windward face, flow is directed downwards towards the ground. Upon reaching ground level, the flow moves backwards against the incident wind direction until it is eventually rolled into a vortex at ground level. The vortex is predicted to be of the same size by both turbulence models although the strength is predicted to be slightly stronger (faster velocities) by the RNG model.

4.8.3.2 Roof Flow Field

The roof flow fields predicted by the two turbulence models are shown most clearly in the velocity vector plots in Figures 4.22 and 4.23 (the k-ε and RNG models respectively). The flow over the cube roof is predicted differently by the two models.

The RNG turbulence model exhibits flow separation over the leading edge of the roof with a recirculating flow developed within this separated zone. The separated flow reattaches with the roof at a position 68% of the way along the streamwise length of the roof. In the case of the standard k-ε model, flow does not separate at the leading edge of the roof as shown in Figure 4.22 where no recirculation is predicted. Murakami et al (1990) amongst others have also found flow fields from CFD analysis that agree with the k-ε prediction described above where the expected recirculating flow over the roof is not present. This would seem to suggest the k-ε model is not suited to such flow fields.

4.8.3.3 Wake Flow Field

Flow separates around the sides and over the rear of the roof of the cube. A large recirculating wake is formed behind the structure. Figures 4.20 and 4.21 were described previously and show velocity vector plots of the flow field at the streamwise centre-line of the cube as predicted by the k-ε and RNG models respectively.

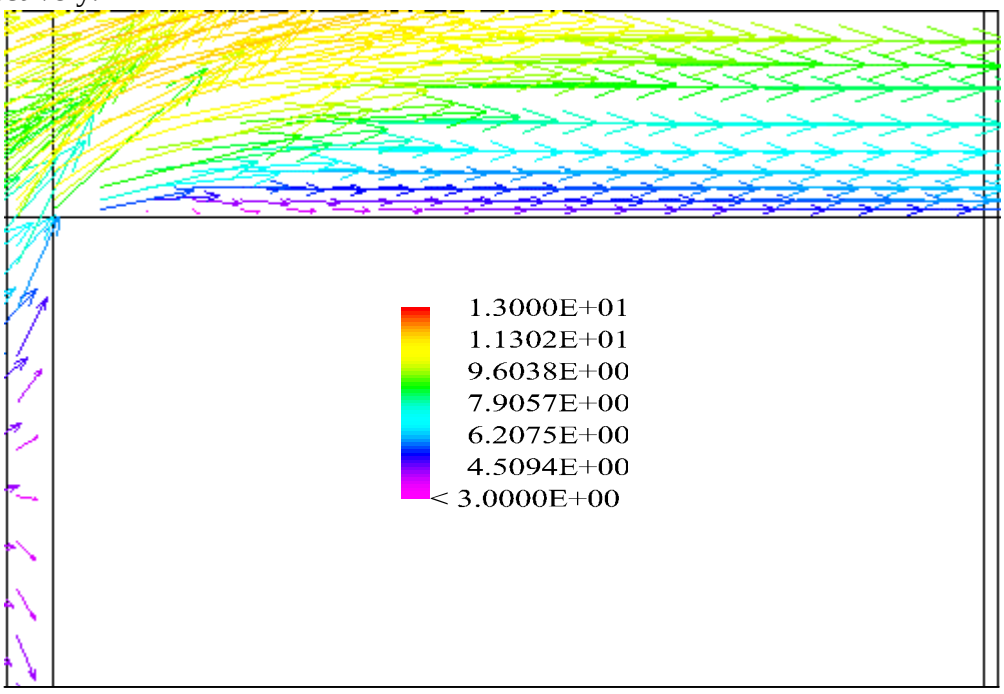

Figure 4.22 Cross section of velocity flow field over the roof of the cube as predicted by the standard k-ε turbulence model (units ms^{-1})

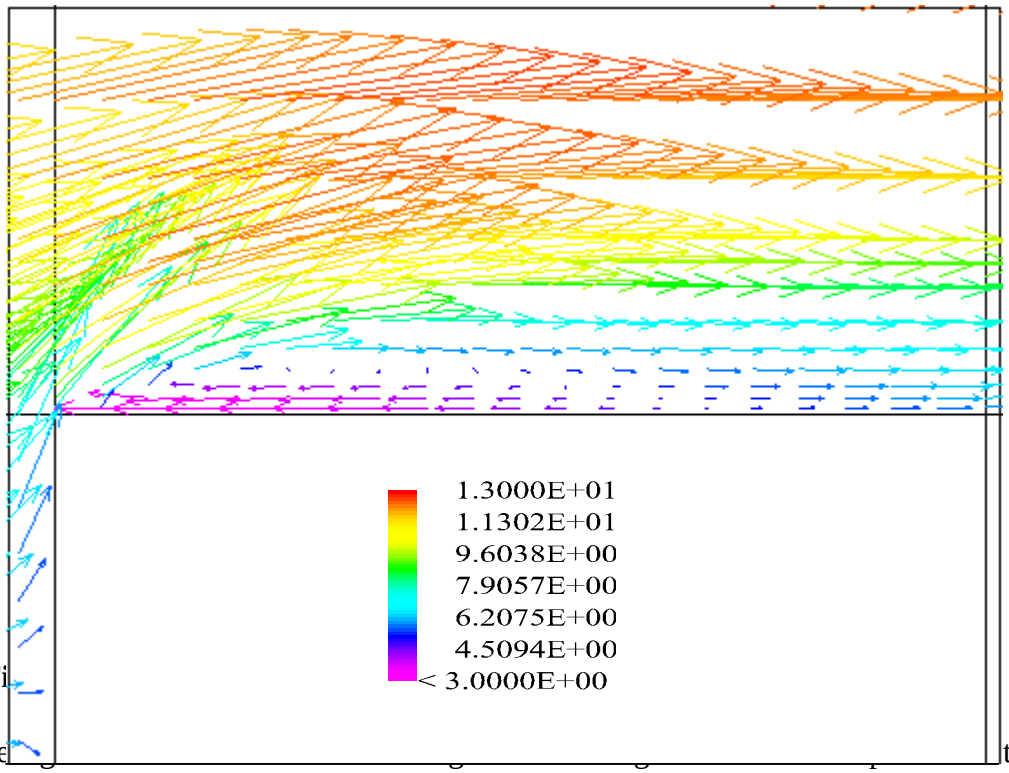

Fi

These the leeward face. The extent of the wake recirculation is predicted to be 2.1H by the k-ε model and 2.3H by the RNG model. Without full-scale experimental measurements of the wake flow it is not possible to conclude which of the models predicts the extent of the wake most accurately.

4.8.4 External Turbulent Kinetic Energy Distributions

It is important for any turbulence model to be able to predict the distribution of turbulent kinetic energy (k) in a sensible and accurate manner since it is turbulence that it is attempting to model. As with the flow field predictions, there are no experimental data with which to compare the results.

The shaded contour plot of Figures 4.24 and 4.25 show the prediction of turbulent kinetic energy around the cube as predicted by the k-ε and RNG k-ε models respectively (the units for turbulent kinetic energy in the figures is m^2/s^2). The standard k-ε model predicts far higher values than the RNG model around the windward face and the leading edge of the roof. The over production of k was discussed briefly with respect to the standard k-ε model in Chapter 2.

This very large production of turbulent kinetic energy by the k-ε model leads to high levels of eddy viscosity and consequently a high level of mixing in the flow that leads to the flow remaining attached over the roof. The RNG model predicts appreciably lower values of k around the leading edge of the roof which in turn enables the separated flow over the roof and the prediction of a roof recirculation.

4.8.5 Turbulence Model Assessment

Throughout the majority of the external flow results, the RNG k-ε turbulence model produced better predictions than the standard k-ε model. The external surface pressure which could be validated by corresponding full-scale experimental data showed the RNG model to predict improved distributions up the windward face where the standard k-ε model significantly over-predicted the peak stagnation pressure.

The roof pressure distributions were not predicted very well by either turbulence model. The k-ε model over-predicted the peak negative pressure by approximately 45% and failed to predict the position of this pressure correctly. The absence of the roof recirculation in the standard k-ε simulation would also suggest that there is an

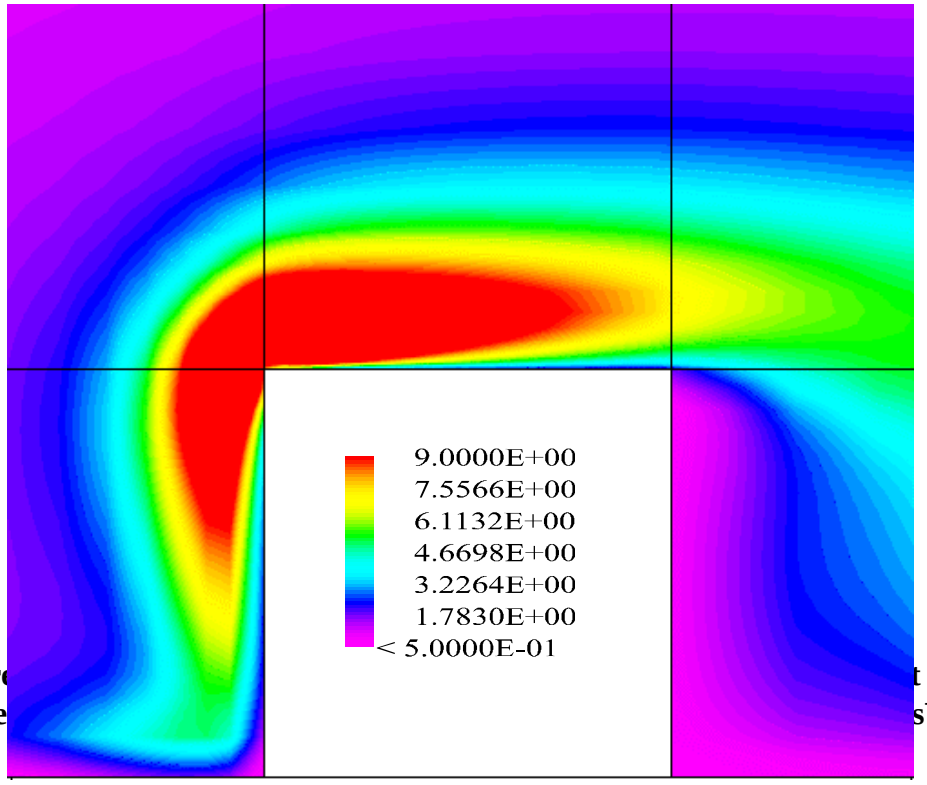

Figur t kinetic e s^{-2})

Figure 4.25 Shaded contour plot of the external distribution of turbulent kinetic energy as predicted by the RNG k-ε turbulence model (units m^2s^{-2})

inherent problem in applying this model to the flow around a cubic structure. The major problem with the standard k-ε model arises from the excessive prediction of turbulent kinetic energy levels around the windward face stagnation point and leading edge of the roof.

The predictions by the RNG k-ε turbulence model suggest that it is better suited to modelling bluff body flows. The ability of the RNG model to predict the separation of flow over the roof of the cube is a fundamental improvement that leads to better predictions of pressure distribution. The improvements of the RNG model compared to the standard k-ε model are due to two factors:

1. Modified model constants;
2. Strain dependent term in ε equation.

The modified set of model constants used in the RNG k-ε model arise from the renormalisation group analysis of the Navier-Stokes equations which is the basis of the model.

The equation for the dissipation of turbulent kinetic energy also differs in the RNG model and has a strain dependent term (see equation 4.27) which helps in the modelling of flows that exhibit large rates of deformation (such as impingement and separation). The modifications in the RNG model lead to a decrease in the production of turbulent kinetic energy which in turn leads to a reduced eddy viscosity and therefore less mixing and retardation of the flow which is one of the major short-comings of the standard k-ε model.

The overall improved performance of the RNG k-ε turbulence model over the standard k-ε model suggests that it would be best suited in the modelling of wind induced ventilation which will be driven by the external flow conditions around the test cube.

4.8.6 Wind Induced Flow Through the Cube

The aim of the external pressure and flow testing discussed in sections 4.8.2 and 4.8.3 was to identify which turbulence model would be best suited to simulating such wind engineering flow fields. The RNG k-ε turbulence model was found to perform significantly better than the standard k-ε model. For this reason only the RNG k-ε model is utilised throughout the computational, wind driven ventilation simulations.

The computational domain and grid used for both the sealed structure and ventilation investigation were identical apart from the openings introduced when modelling the ventilation. The aim was to first reproduce the best external flow conditions and then apply them to solve the internal flow simultaneously.

4.8.6.1 Internal Velocity Profiles

Figure 4.26 shows a velocity vector plot (in ms^{-1}) of the streamwise component of velocity through a vertical cross-section at the centre-line of the cube for the 0° wind angle. In this plane, it is obvious that the flow through the cube is dominated by a jet passing directly between the ventilation openings (positioned on the windward and leeward faces). Both above and below the dominant jet region are slower moving zones. In both of these slow moving regions there is a region close to the windward face where flow is being drawn towards the jet. Close to the leeward face there are recirculating zones formed both above and below the jet. These develop as the jet reaches the leeward opening with a width greater than that of the opening. Some of the jet contracts to exit through the opening. However some of the faster moving flow is directed up the inside of the leeward face above the jet and down the face below the jet. This flow reaches the top or bottom of the leeward face and is directed along either the roof or floor where it moves against the direction of the jet until it is retarded by the action of the main flow. The effect of this is the production of the two circulating regions of flow close to the leeward face.

Figure 4.27 also shows the internal velocity flow field however, this time in a horizontal cross section at a height of 3.5m (halfway up the ventilation openings). Again the dominating jet flow is obvious. Either side of the jet region are slower moving zones that exhibit circulatory flows driven by the jet. The positions of the openings would suggest that although a significant volume of air is entering the ventilated space, the distribution of the flow would not provide efficient ventilation in the regions away from the main flow. Since it is modelling the flow phenomena that is of importance to this research, no attempts to improve the overall action of the ventilation was made (i.e. improvement of the overall distribution of flow within the cube was not attempted)

Figure 4.28 shows the velocity profiles on a line between the centres of the ventilation openings as predicted by the RNG k-ε model. As the air enters the windward opening (inlet) the flow accelerates before decelerating through the central region, with recovery of speed occurring closer to the leeward opening (outlet).

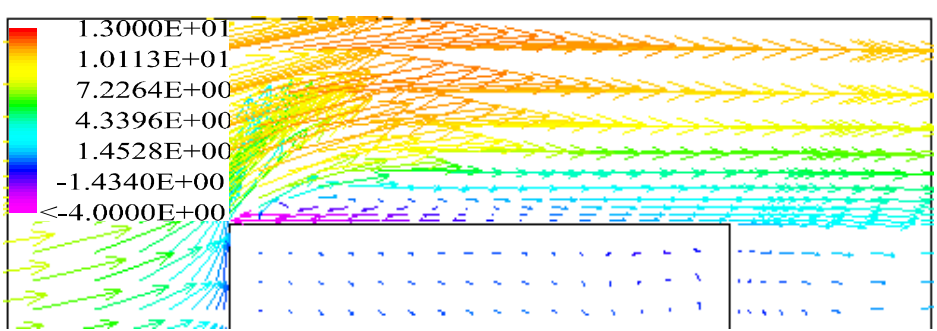

Figure 4.26 Cross sectional view of velocity flow field on vertical mid-plane for normal wind direction predicted by RNG k-ε turbulence model (units ms^{-1})

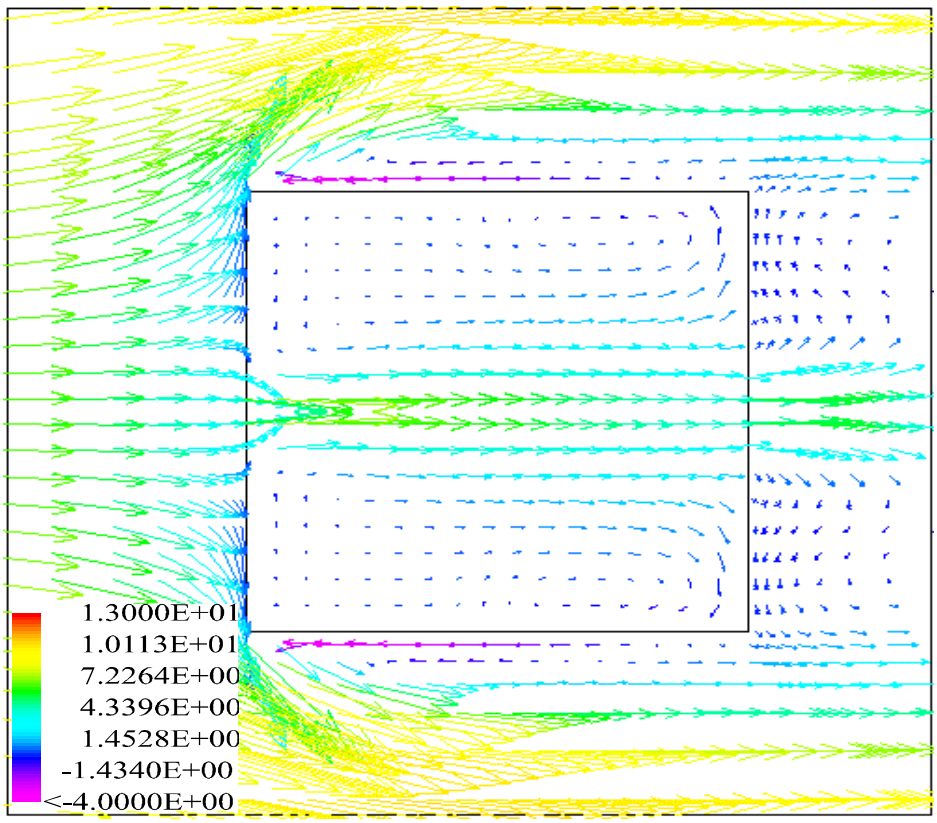

Figure 4.27 Plan view of velocity flow field for normal wind direction at opening centre height predicted by RNG k-ε turbulence model (units ms^{-1})

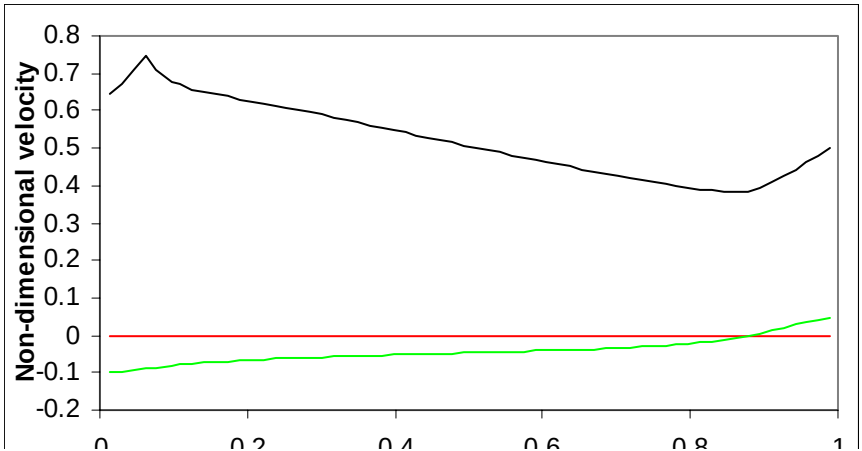

Figure 4.28 Profiles of velocity components for a normal wind direction directly between opening centres as predicted by the RNG k-ε turbulence model

Figures 4.29 and 4.30 shows plan views of the internal flow structure for incident wind direction of 5° and 10° respectively. The wind approaching at an angle of 5° can be seen to have little effect on the general structure of the flow with the dominant jet between the openings still driving two recirculating flows either side. When the wind enters the cube at an angle of 10°, the flow structure is more severely disrupted. The flow entering the windward opening is skewed and the fast moving jet is directed to one side of the outlet opening with only some of the fast moving jet exiting through the leeward opening. The jet is slower moving than for the lower incident wind angles but is distributed more evenly across the width of the internal region. The two large recirculating regions that were present for lower wind angles are disturbed with the majority of the flow now moving in the direction of the jet.

The differences in internal flow structure for different incident wind angles can also be seen in Figure 4.31. The three profiles are streamwise velocity components taken directly between the ventilation openings. As with the velocity vector plots of Figures 4.26 to 4.30, there is minimal difference between the jet flow between the openings for 0° and 5° whilst the 10° incident wind leads to a more rapid decay of velocity along this plane as the incoming air is skewed away from the centre-line.

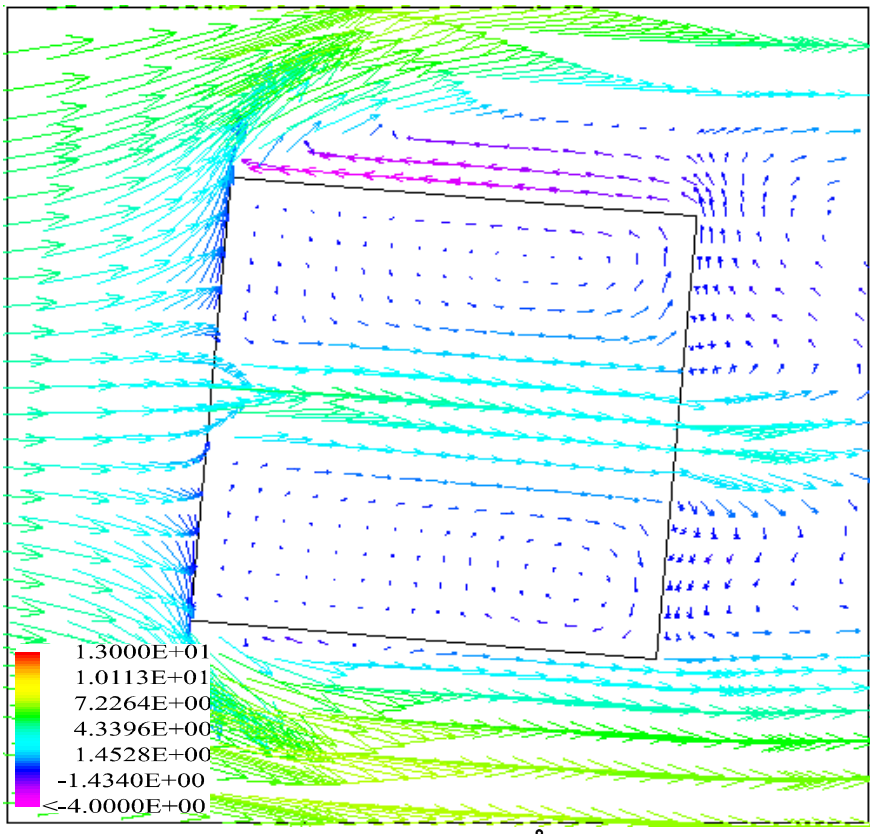

Figure 4.29 Plan view of velocity flow field for 5° wind direction at opening centre height predicted by RNG k-ε turbulence model (units ms^{-1})

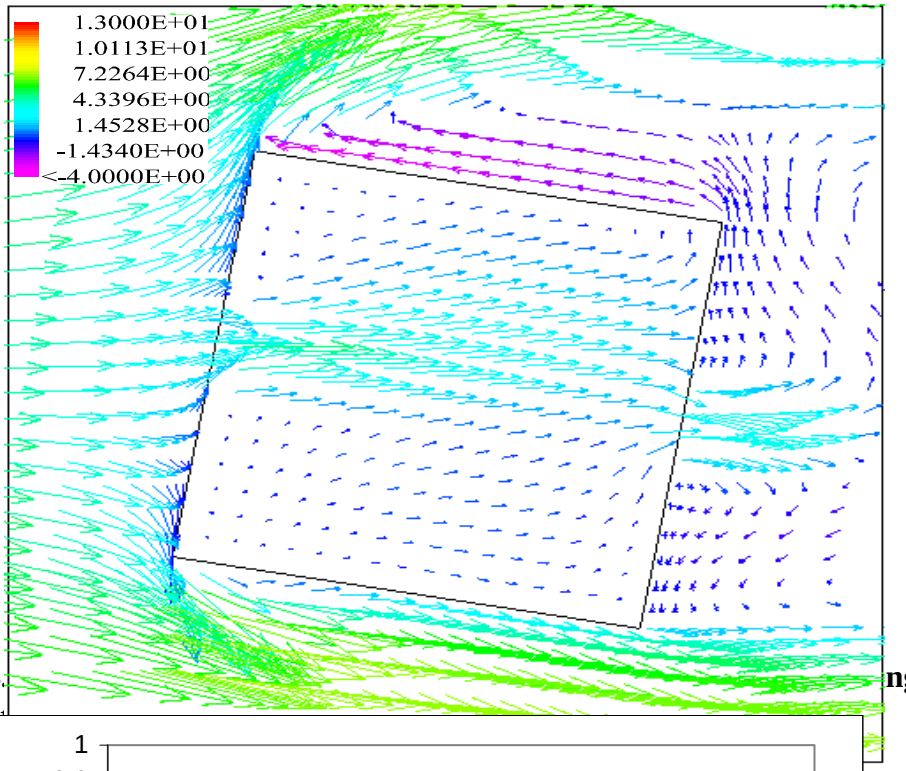

Figure 4. ng cen

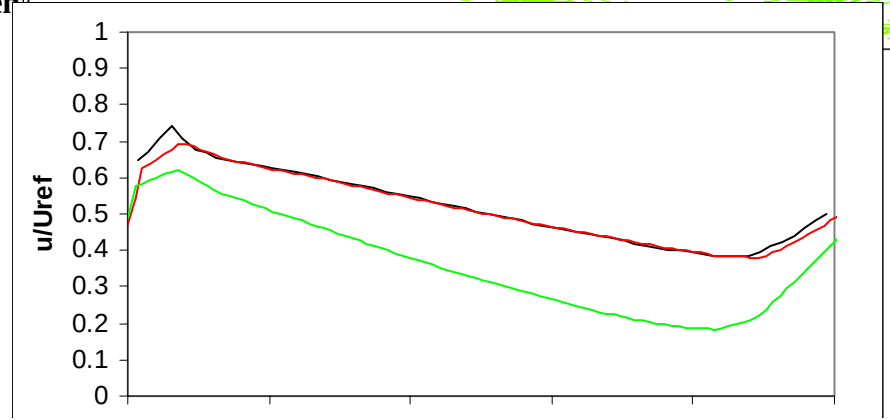

Figure 4.31 Streamwise component of velocity directly between ventilation opening centres for different wind directions

4.8.6.2 Velocity Profiles in Ventilation Openings

Figure 4.32 show distributions of the three components of velocity along the horizontal centre-line of the windward opening. The streamwise component is significantly greater than either the lateral or vertical components. The lateral component shows positive values on one side of the opening and negative values on the other side of the centre-line. This is due to air contracting as it enters the plane of the opening. The vertical component of velocity exhibits negative values across the width of the opening centre-line hence along this plane the air entering the structure is directed slightly downwards.

Velocity profiles were taken at three lines transversely across both of the ventilation openings. Profiles were taken along the opening centre line (in a horizontal plane) and at positions 0.1m from both the top and bottom of the openings. Figure 4.33 shows profiles of the streamwise component of velocity at the three positions across the opening. It can be seen that velocities through the centre of the opening are significantly greater than those at the edges.

Figure 4.34 shows the effect of the angle of the incident wind on the streamwise velocity profile at the central plane of the opening. The difference between the profiles for wind angles of 0° and 5° is very small and it is not until wind angles reach 10° before differences become significant in any way. The change in angle of the incident wind entering the openings leads to a slight skewing of the streamwise velocity profile with the fastest region just off centre when compared to the 0° wind angle.

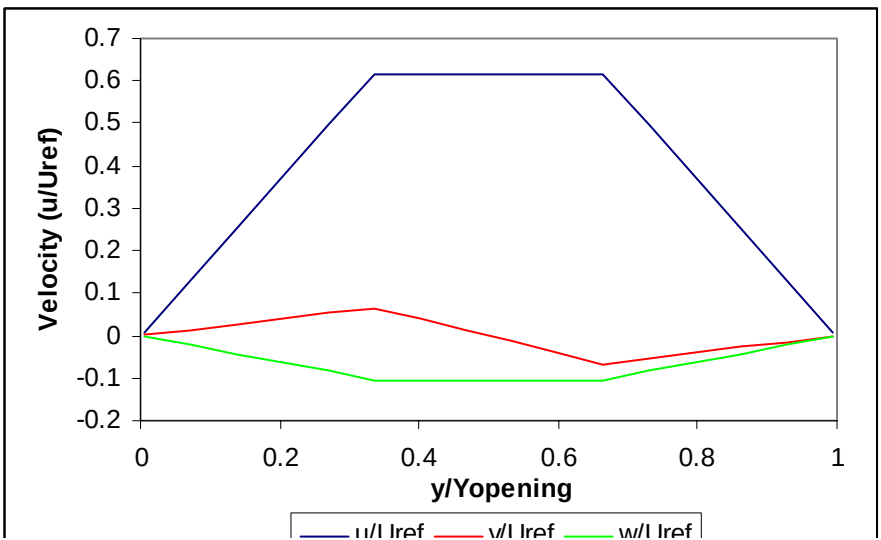

Figure 4.32 Velocity component profiles transversally across centre of windward opening

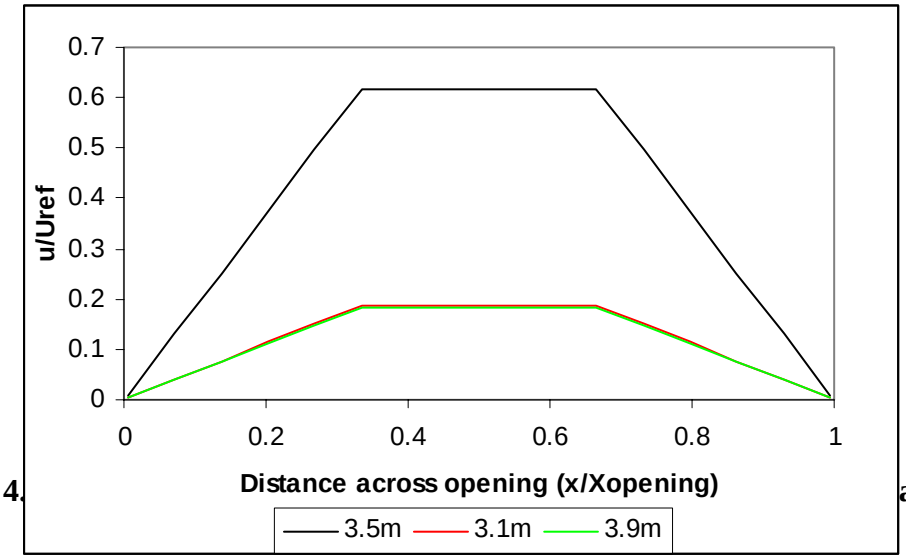

Figure 4. at

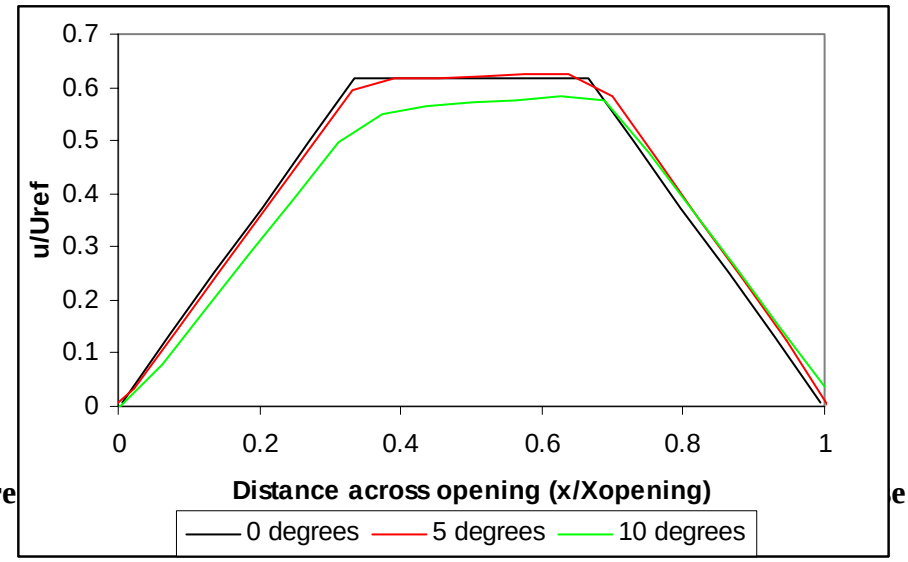

Figure e velocity

Figure 4.35 shows the three components of velocity across the central plane of the leeward opening (outlet) for the 0° incident wind angle. As with the windward opening the streamwise component is far greater than either the lateral or vertical components. Both the lateral and vertical components of velocity are very low and almost insignificant. Figure 4.36 presents the streamwise velocity profiles at three

lateral planes in the leeward opening for the 0° wind angle. The highest velocities can be seen to be located across the centre-line profile as the air contracts.

The effect of wind angle on the streamwise velocities across the horizontal centre-line of the leeward opening are shown in Figure 4.37. With the wind at an angle of 5° to the windward face, the velocity profile follows the 0° profile with a slight skewing to one side. However, the effect of a wind angle of 10° is far more pronounced. The profile for the 10° incident wind exhibits far lower velocities (approximately 80% lower) than arise with the other two wind angles.

4.8.6.3 Internal Pressure

The internal pressure directly between ventilation openings is shown in Figure 4.38. It can be seen that the pressure decreases with distance away from the opening to a constant internal pressure coefficient of approximately 0.07, the pressure then reduces further as flow reaches the leeward opening.

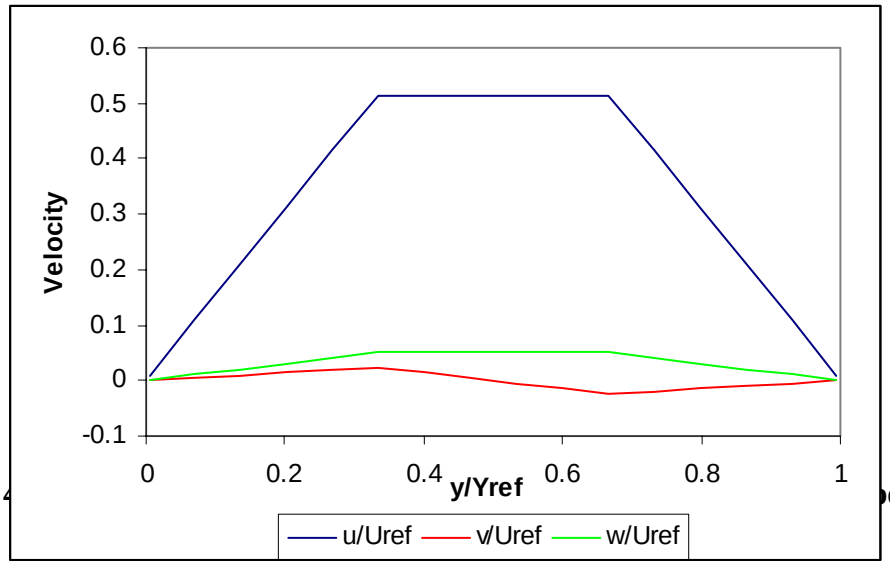

Figure 4 ... pening at

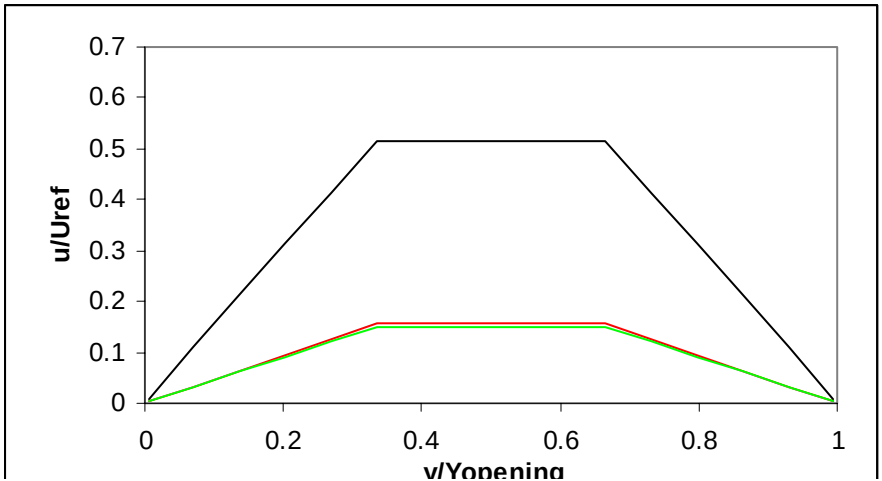

Figure 4.36 Leeward face ventilation opening streamwise velocity profiles at different heights

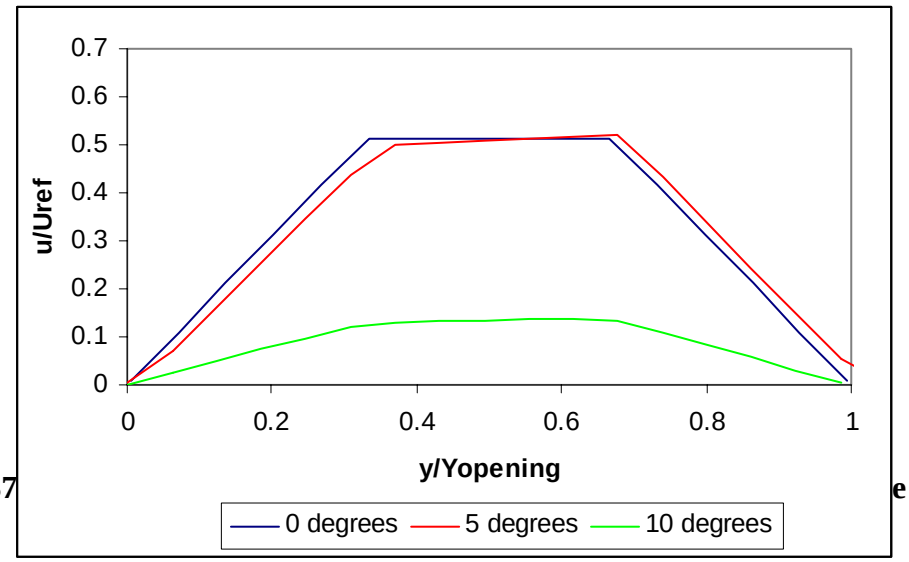

Figure 4.37 **e in**

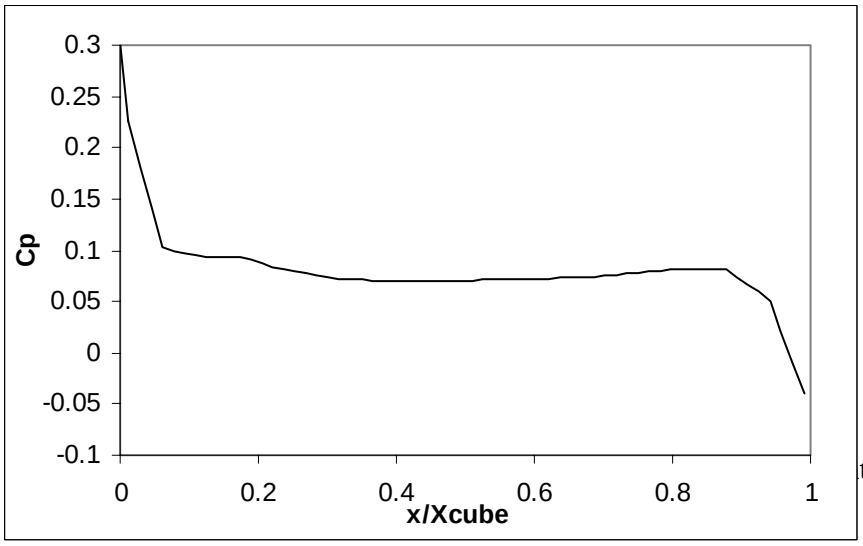

Figure **tres**

4.8.7 Assessment of Ventilation Rates

The modelling discussed in the previous sections of this chapter have been concerned with pressure distributions, velocity flow fields and turbulence parameters both around and within the test structure. The aim of this was to produce the best simulation possible of the actual flow mechanisms that drive wind induced ventilation.

The CFD assessments of mean ventilation rates utilised the open cube simulations described previously (when predicting the internal flow fields). Determination of the ventilation flow rate for the structure required the integration of velocities over all cells in the plane of the inlet and outlet openings. This involved the use of user FORTRAN routines within the CFD package.

A discrepancy was found when using the standard method for outputting integrated velocities over a plane (in this case the ventilation opening). For continuity to apply to the ventilation, the flow entering the inlet opening had to equal that leaving the structure through the outlet. This was found not to be the case. It was discovered that the problem arose because the results produced by the CFD software were for the computational node nearest to the opening plane, rather than for the plane of the opening itself (which corresponded to a cell face). The velocities (hence the discharge) in the plane of the opening were estimated from the velocities at the nearest nodes either side of the opening by taking a weighted difference of the two (the weighting accounted for nodes on either side of the opening being different distances from the opening).

Ventilation rates were calculated for wind directions of 0°, 5° and 10°. The values calculated are provided in Table 4.2. It can be seen that the non-dimensional ventilation rate decreases with increased wind angle away from the normal direction. This would be expected since the change in angle effectively reduces the ventilation opening area.

Table 4.2 Predicted mean ventilation rates from direct CFD simulations

Wind angle	Ventilation Rate, $\overline{Q}/U_{ref}A$
0	0.65
5	0.61
10	0.59

4.9 Summary

The computational modelling of the external flow environment was undertaken using both the standard k-ε and RNG k-ε turbulence models. The RNG model was found to

perform significantly better than the standard k-ε model, as discussed in detail in section 4.7.5, and was therefore utilised for the ventilation modelling.

The majority of wind induced ventilation modelling with CFD has, in the past, concentrated on the internal environment alone. Using the flow conditions at ventilation openings to produce inlet boundary conditions, only the internally ventilated region is considered within the computational domain, e.g. Choi et al (1988), Li et al (1993) and Kurabachi and Kusuda (1987). The advantage of this approach is the high number of computational cells (providing greater detail) that can be utilised in the regions of interest. The limitation is that the external environment that drives the internal flow and the interaction between them which determines the ventilation flow is taken in to account.

The modelling in this investigation has simultaneously solved the external and internal wind induced flows around and within the ventilated cube and so has simulated, as fully as possible, the true physics of the problem. CFD studies in which a similar approach was attempted have in certain cases shown serious inadequacies. Kindagen et al (1992) and Tsutsumi et al (1996) both attempted to model the internal and external environments simultaneously. In both cases, the size of the computational domain in which the structure was located was too small. By using a domain of insufficient width and height leads to local speeding up of flows around the building sides and over the roof. Consequently, the flow patterns and pressure distributions are adversely effected. The domain constructed through this research was designed such that it had no effect on the local flow and pressure fields around the structure.

CFD provides a powerful engineering tool in the simulation of mean ventilation flows. The advantage over many other analytical methods is the level of detail of flow variables that can be gained from a single simulation in terms of external pressures and flow, as well as internal flow patterns throughout the ventilated space.

5. TURBULENT VENTILATION INVESTIGATIONS

5.1Introduction

The effect of turbulence has been widely investigated with respect to the atmospheric boundary layer (e.g. Berkooz et al (1993), (1994)) and wind induced surface pressure on structures (e.g. Lee (1975), Best and Holmes (1983), Bienkiewicz et al (1993), Ho et al (1995) and Holmes (1990)). The effect of turbulence on wind induced ventilation, although recognised as important, has not to date been studied or assessed in great depth. The significance of turbulent ventilation has been identified in a small number of physical investigations where discrepancies between measured ventilation rates and steady-state predictions have been evident (e.g. Potter (1979), Etheridge and Nolan (1979)).

Malinowski (1971) identified a number of turbulent flow mechanisms induced through buildings and individual orifices. These mechanisms were discussed in detail in Chapter 2. Few previous studies have however, attempted to make analytical assessments of the contribution of turbulent ventilation to the overall ventilation. However, the attempts of Haghighat (1991, 1992) have provided invaluable background information.

Within this chapter, two analytical techniques are developed with the purpose of quantifying the effects of turbulence on the wind induced ventilation of a cubic structure. The methods described are:

1. Time domain approach
2. Frequency domain approach

The time domain method is based on an expansion of the steady-state pressure difference method introduced in Chapter 2. Time series of the external surface pressures in positions of the ventilation openings are utilised in this technique rather than the mean pressures used previously in Chapters 3 and 4. The aim of the time domain approach is to predict the process defined as continuous unsteady ventilation described in Chapter 2.

The frequency domain approach is more complex although external, surface-pressure time-series data are again utilised. The frequency domain method is based upon the technique of *proper orthogonal decomposition* (POD) or Karhunen-Loeve decomposition (Loeve (1955)).

5.2Time Domain Method

The time domain method is based on the steady-state pressure difference method described in Chapter 2 and applied in Chapter 3 (in the full-scale experiments). The previous application of the pressure difference method utilised mean pressure differences between ventilation openings, measured on a sealed structure. Here, mean pressure differences are replaced by instantaneous pressure differences providing instantaneous predictions of ventilation over a period of measurement.

In the time domain method, instantaneous ventilation rates are calculated from

$$Q = \pm A\rho U_{ref}\sqrt{\Delta C_P'} \tag{5.1}$$

where Q is the instantaneous discharge, A is the ventilation opening area, ρ is the density of air, U_{ref} is the reference wind speed, $\Delta C_P'$ is the instantaneous pressure difference across the openings and the sign ensures flow direction is accounted for.

The root mean square (rms) value of any time varying series of data is often used as a measure of fluctuation. In wind induced ventilation, fluctuations are the effects of turbulence in the wind. For this reason, the root mean square value of the ventilation rate is taken as the turbulent ventilation predicted using this method. By applying this simple technique in a time varying way accounts for a broad banded fluctuating ventilation rate

$$\sigma_Q = \left[\frac{1}{N_m}\sum_1^{N_m}\left(Q-\overline{Q}\right)^2\right]^{\frac{1}{2}} \tag{5.2}$$

where σ_Q is defined as the fluctuating ventilation rate, N_m is the number of measurements of the instantaneous ventilation rate in the time series, Q is the predicted instantaneous ventilation rate and $\overline{Q}$ is the predicted mean ventilation rate.

The broad banded ventilation is analogous to the turbulent, continuous ventilating flow described in Chapter 2 and is a result of fluctuations in the incoming wind across a wide range of frequencies. With broad banded fluctuations being driven by a wide spectrum of frequencies in the incoming wind, the majority of the energy in such fluctuations will be at relatively low frequencies (<0.1 Hz) as shown in the peak in the spectrum shown in Figure 3.13. These frequencies correspond to large scale variations in wind direction that lead to changes in the flow pattern and pressure fluctuations around a structure.

The broad banded ventilation mechanism can effectively be regarded as a modification of the mean ventilation mechanism and it is necessary to account for the two simultaneously. The relative contribution of the broad banded ventilation to the total ventilation is dependant on the direction of the incoming wind relative to the plane of the ventilation openings. For a two opening enclosure, the total ventilation due to the mean and broad banded fluctuating mechanisms together is given by the area beneath the ventilation time history divided by the length of the record. If the

ventilation time history does not change sign i.e. the magnitude of the fluctuations are less than the mean, this corresponds only to the mean ventilation rate. If however, the fluctuations are greater than the mean, there will be some rectification of the ventilation time series around zero and the total ventilation due to both the mean and broad banded mechanisms will be in excess of the mean value.

It is assumed that the broad banded ventilation fluctuations vary sinusoidally. The total non-dimensional ventilation rate due to the mean and broad banded ventilation mechanisms, Q_B, is given by

$$Q_B = \overline{Q}\left(1+\frac{2\sqrt{2}}{\pi}\left(\frac{\sigma_Q}{\overline{Q}}\right)\sqrt{1-\frac{1}{2}\left(\frac{\overline{Q}}{\sigma_Q}\right)^2}\right) \tag{5.3}$$

where $\overline{Q}$ is the non-dimensional mean ventilation rate and σ_Q is the non-dimensional rms value of the ventilation rate. Appendix A provides the derivation of equation (5.3).

5.3Frequency Domain Method

The mathematical study of random variables has revealed that the turbulent pressure on a building surface can be considered to be composed of an infinite series of sine waves at different frequencies. The contribution of the sine wave of a particular frequency to the total turbulent pressure is invariant with time for a particular wind type. This contribution by each frequency to the total pressure can be more precisely represented by the concept of power spectra (discussed in Chapter 2). As with the turbulent wind, a turbulent pressure can be described and represented by its power spectrum. Hence it is hypothesised that the ventilation, driven by such turbulent pressures, can be described in the same way.

The following sections introduce the concept of proper orthogonal decomposition (POD) and its application for the assessment of turbulent pressures. The development of a POD technique and its subsequent application to the prediction of turbulent wind driven ventilation are discussed. The approach was introduced by Baker (1998 and 1999) where the use of the technique was hypothesised but not fully tested or validated.

The frequency domain method is based on the assessment of turbulent pressures measured on the surface of a structure. In Chapter 2, it was discussed how turbulent pressures drive pulses of flow into and out of ventilation openings. Consequently, it is this pulsating form of ventilation that this technique aims to predict. The frequency domain method is incapable of accounting for other forms of turbulent ventilating flow mechanisms such as eddy penetration.

5.3.1 Proper Orthogonal Decomposition

The method of proper orthogonal decomposition (POD) provides a basis for the modal decomposition of an ensemble of functions, for example wind induced surface pressures on a structure. In the case of wind induced pressures, POD provides a method for assessing the contributions of individual modes of pressure to the total pressure distribution. It has been hypothesised in previous research that individual modes of pressure are caused by specific physical phenomena as discussed in section 5.3.1.2 (Holmes (1990) and Armitt (1968)).

POD was first introduced with respect to turbulence in the work of Lumley (1967). The method has been developed in other fields of application under different names including Karhunen-Loeve decomposition, principal components analysis, singular systems analysis and singular value decomposition. Other fields of use (other than fluid mechanics) have included random variables (Papoulis (1965)), image processing (Rosenfield and Kak (1982)), signal analysis (Algazi and Sakrison (1969)), data compression (Andrews et al (1967)), process identification and control in chemical engineering (Gay and Ray (1986)), and oceanography (Preisendorfer (1988)).
POD is utilised for the analysis of experimental data to extract dominant features and trends or coherent structures. With respect to turbulence, such patterns are in both space and time. The application of POD to wind engineering was introduced by Armitt (1968) in the consideration of pressure fluctuations on a full-scale cooling tower. The following provides details of the theoretical basis of POD with respect to pressures on structures and is further expanded to its relevance in the prediction of turbulence induced, wind driven ventilation.

5.3.1.1 POD Theory- Assessment of Turbulent Pressures

The approach taken in this section is derived from Baker (1997) when reviewing the application of proper orthogonal decomposition (POD) to the field of wind engineering.

As with all turbulent analysis the variable under consideration, in this case wind induced surface pressure *p(x,t)*, is split into its mean and fluctuating components $\overline{p(x)}$ and $p'(x,t)$ respectively, where *x* is a spatial coordinate on the building surface and *t* is time.

$$p(x,t) = \overline{p(x)} + p'(x,t) \tag{5.4}$$

The mean value of pressure is a function of spatial position only whilst the fluctuating component is a function of both position and time. Pressures are more commonly presented in their coefficient form by normalising with the reference mean dynamic head, $0.5\rho\overline{U_{ref}}^2$, where $\overline{U_{ref}}^2$ is the mean reference velocity (usually taken at building roof height). In coefficient form the equivalent form of equation (5.4) is

$$C_p(x,t) = \overline{C_p}(x) + C_p'(x,t) \tag{5.5}$$

where C_p denotes a pressure coefficient.

In POD, as in modal analysis, the fluctuating component of the pressure coefficient can be written as a sum of a series of dimensionless modal functions

$$C_p(x,t)' = T_1(t)P_1(x) + T_2(t)P_2(x)..... = \sum_{k=1,n} T_k(t)P_k(x) \tag{5.6}$$

where $P_1(x)$, $P_2(x)$ and $P_k(x)$ are modal pressure fields (individual modal distributions around the surface of the building), $T_1(t)$, $T_2(t)$ and $T_k(t)$ are modal time functions where the subscript k refers to individual mode numbers. Armitt (1968) made the assumption that

a) modal time functions are uncorrelated i.e.

$$\overline{T_j(t)T_k(t)} = 0, \ if \quad j \neq k \tag{5.7}$$

or

$$\overline{T_j(t)T_k(t)} = \overline{T_k(t)^2}, \ \ if \quad j = k \tag{5.8}$$

where the overbar denotes a time average and the subscripts j and k refer to individual mode numbers.

b) modal spatial functions are orthogonal i.e.

$$\int P_j(x)P_k(x)dx = 0, \ if \quad j \neq k \tag{5.9}$$

or

$$\int P_j(x)P_k(x)dx = 1, \ \ if \quad j = k \tag{5.10}$$

Due to the orthogonality assumption, the spatial integral of the product of two modes is zero if the modes are different and unity if the modes are the same.

By defining a covariance, R, of fluctuating pressure coefficients between two spatial locations x_r and x_s

$$R(x_r, x_s) = \overline{C_p(x_r,t)' C_p(x_s,t)'} \tag{5.11}$$

and after manipulation, equations (5.6) to (5.11) result in the following matrix equation (as shown in Appendix B)

$$[R(x_r, x_s)][P_k(x_r)] = \overline{T_k(t)^2}[P_k(x_r)] \tag{5.12}$$

where the components and subscripts in the equation have been previously defined.

Equation (5.12) presents an eigenvalue problem. The mode spatial functions of equation (5.12) are the eigenvectors of the surface pressure covariance matrix and the eigenvalues represent the mean square of the modal time functions.

From equation (5.6) it is possible to write

$$\int \overline{C_p(x,t)'^2}\, dx = \int \overline{\left(\sum_{k=1,n} T_k(t) P_k(x)\right)^2} dx \tag{5.13}$$

Expanding the terms on the right hand side of equation (5.13) only leaves terms when k (the mode number) is the same in both series hence (from equations (5.7) to (5.10))

$$\int \overline{C_p(x,t)'^2}\, dx = \int \sum_{k=1,n} \overline{T_k(t)^2} (P_k(x))^2\, dx = \sum_{k=1,n} \overline{T_k(t)^2} \tag{5.14}$$

Thus from equation (5.14) the sum of the eigenvalues of the surface pressure covariance matrix equals the integral of the root mean square (rms) pressure fluctuations over the surface of the building.

Finally, it is necessary to derive an explicit expression for the modal time function $T_k(t)$. From the product of the fluctuating pressure field and an arbitrary mode shape, the following spatial integral is formed

$$\int C_p(x,t)' P_k(x) dx = \int \left(\sum_{j=1,n} T_j(t)\, P_j(x) \right) P_k(x) dx \tag{5.15}$$

where $C_p(x,t)'$ is the fluctuating pressure field and $P_k(x)$ is an arbitrary mode shape.

From the orthogonality condition the integral in equation (5.15) only exists for $j=k$ giving

$$\int C_p(x,t)' P_k(x) dx = T_k(t) \tag{5.16}$$

or in series form assuming $dx_r=1$

$$T_k(t) = \sum_{r=1,n} C_p(x_r, t)' P_k(x_r) \tag{5.17}$$

Thus the time variation of mode k can be found by weighting the fluctuating pressure coefficient with the spatial mode function at each point and summing.

The individual power spectra for each mode can be found from analysis of the modal time series that are found from applying equation (5.17).

One can write, from equation (5.6)

$$C_p(x_s,t)' = T_1(t)P_1(x_s) + T_2(t)P_2(x_s) + ...T_n(t)P_n(x_s) \qquad (5.18)$$

5.3.1.2 Relevance of POD in the Assessment of Fluctuating Pressures

The aim of POD, when applied to wind surface pressure, is to decompose the total fluctuating pressure into individual pressure modes. It is the next stage to attempt to explain the physical meaning of these modes.

Armitt (1968) was the first to attempt to attribute different physical phenomena to each of the modes of pressure fluctuations. However, numerous others have since investigated this further e.g. Holmes (1990) and Baker (1999).

In Armitt's work on cooling towers, he found that the first mode of pressure contained the vast majority of the total energy of the fluctuations and resembled the mean pressure distribution. Armitt hypothesised that this first mode was primarily the result of large-scale longitudinal gusts. This has been widely accepted in many other investigations including Baker (1997). The second mode was apportioned to lateral shear flows across the cooling towers under investigation with the third mode thought to be the first derivative of the first mode. Armitt could find no physical explanation for the fourth, and higher, modes of pressure although he speculated that they could be due to the interaction of small-scale turbulence, from a variety of causes.

The orthogonality and non-correlation assumptions (equations (5.7) and (5.10)) imply that individual modes are both spatially and temporally independent. If, as suggested, calculated pressure modes represent distinct physical mechanisms, these phenomena should be spatially and temporally independent. Using the flow around a building as an example, Baker (1999) discusses how surface pressure fluctuations are effected by different components of turbulence in the upstream flow, by large-scale wake unsteadiness and by smaller scale unsteadiness in separated flow regions. To first approximations, Baker suggests that these physical phenomena would be completely independent and uncorrelated and lower modes of pressure expected to reflect specific physical mechanisms. Baker goes on to discuss that it is likely however for each mode to be effected, to some degree, by mechanisms.

Attempting to discuss all pressure modes with respect to physical mechanisms can be misleading. The number of calculated pressure modes is a function of the number of data points used experimentally. This, in some cases, may lead to hundreds of different modes. It would be impractical to assume that so many modes could be caused by individual mechanisms. It is more practical to deal with the first few modes that contain the vast majority of the fluctuating energy and that can be explained with greater certainty.

5.3.1.3 Hypothesis of the Application of POD to Ventilation

Since it is the wind induced pressure field within and around openings in the building envelope that are responsible for the action of wind induced ventilation, it is reasonable to suggest that the technique can be further expanded to the assessment of turbulence driven, wind induced ventilation. The action of turbulent pressures drive the mechanism of pulsating flow predicted by this technique.

The measurement of wind induced pressures on the surface of a structure and subsequent POD analysis can provide the spectra of individual *modes* of pressure. It is hypothesised that the application of proper orthogonal decomposition can be utilised to assess the contribution of pulsating flow to the total turbulent wind induced ventilation. T*ransfer functions* can be applied to find pulsating ventilation spectra, the integration of which provides the root mean square of ventilation.

5.3.1.4 Development of POD for Wind Induced Ventilation

Assessing turbulent induced ventilation (through POD) makes use of the theory described in section 5.3.1 however, the modal time functions derived from the surface pressures, must be transformed in order to account for ventilation parameters.

The method is developed for a multi-opening enclosure with N openings. For opening j, the linearised momentum equation is (Haghighat (1991))

$$\frac{\rho L}{A}\frac{dQ}{dt}+\frac{K}{A}q_j = p_j' - p_i' \tag{5.19}$$

where q_j is the fluctuating discharge through opening j, p_j' is the fluctuating pressure at opening j, p_i' is the fluctuating internal pressure, ρ is the density of air, A is the area of the opening, L is the effective length of the opening (this is related to the streamwise depth of the opening and is given by the actual opening length plus $0.89\sqrt{A}$ (Chaplin (1997)) and K is a coefficient of linearisation that is assumed to be the same for all orifices. By continuity

$$\frac{dp_i}{dt} = \frac{k_b}{V}\sum_{j=1,N} q_j \tag{5.20}$$

where V is the volume of the enclosure and k_b is the effective bulk modulus. Summing equation (5.19) for all openings we have

$$\frac{\rho L}{A}\frac{d\Sigma q_j}{dt}+\frac{K}{A}\Sigma q_j = \Sigma p_j' - N p_i' \tag{5.21}$$

from equations (5.20) and (5.21)

$$\frac{\rho LV}{Ak_bN}\frac{d^2p_i'}{dt^2}+\frac{KV}{AkN}\frac{dp_i'}{dt}+p_i'=\frac{\Sigma p_j'}{N} \tag{5.22}$$

If pressures are expressed in their coefficient form that are then expressed in modal form (of equation (5.6)), after manipulation (see Baker (1997) for details), these equations can be solved to give expressions for the spectra of the internal pressure coefficient and pulsating ventilation rate within the structure under consideration.

The expressions for the internal pressure and ventilation rate are provided in equations (5.23) and (5.24)

$$S_{Cp_i}=\frac{\left[\Pi_1^2S_{T1}+\Pi_2^2S_{T2}...+\Pi_N^2S_{TN}\right]}{\left(\left(1-\frac{\omega^2}{\omega_n^2}\right)^2+\left(\frac{2c\omega}{\omega_n}\right)^2\right)} \tag{5.23}$$

$$S_{QQ}=\frac{\left(\omega\rho V\frac{U_{ref}^2}{2}k_b\right)\left[\Pi_1^2S_{T1}+\Pi_2^2S_{T2}....+\Pi_N^2S_{TN}\right]}{\left(\left(1-\frac{\omega^2}{\omega_n^2}\right)^2+\left(\frac{2c\omega}{\omega_n}\right)^2\right)} \tag{5.24}$$

where ω is an angular frequency, ω_n is the natural frequency of the system defined as

$$\omega_n=\sqrt{\frac{Ak_bN}{\rho LV}} \tag{5.25}$$

c is the damping of the system and is defined as

$$c=\frac{k_b}{2}\sqrt{\frac{V}{AkN\rho L}} \tag{5.26}$$

$$\Pi_i=\frac{\left(P_i(x_1)+P_i(x_2)+.....\right)}{N} \tag{5.27}$$

where the subscript, i, indicates the mode number and x_j are the positions of the openings. S_{Ti} is the modal spectrum for mode i. Direct integration of the above spectra (equations (5.23) and (5.24)) provides the variances (square of the rms values) of the internal pressure and turbulent ventilation rate.

In many cases the first few modes (say, 1 to 3) will be expected contain the vast majority of the total energy. Hence equations (5.23) and (5.24) provide a

straightforward technique for estimating wind driven turbulent ventilation from the time series of surface pressure data.

5.3.1.5 Methodology of POD Application

The procedure followed for the prediction of pulsating ventilation can be summarised in the following stages:

1. Production of surface pressure covariance matrix;
2. Eigenvalue/eigenvector analysis of covariance matrix;
3. Production of modal time series from fluctuating pressure coefficient and corresponding eigenvectors for each mode of interest (it is assumed that the first three modes suffice);
4. Calculate spectra of modal time series;
5. Transform spectra of modal time series to produce turbulent ventilation spectra for modes of interest;
6. Sum the individual modal ventilation spectra to provide total pulsating ventilation spectra;
7. Integrate total ventilation spectra to assess the total pulsating turbulent ventilation.

5.4 Test Cases - Ventilation Configurations

Two test cases were investigated with respect to assessing the turbulence induced, wind driven ventilation of the cubic structure with two ventilation openings located on opposing faces (described in Chapter 3):

- 0° case
- 90° case

In the 0° case, the incident wind was normal to the faces containing the openings. In the 90° case, the wind was parallel to the faces containing the openings. Although sealed pressures were used, it was assumed that the ventilation openings were located along the cube centre-line at a height of 3m and an opening area of $1m^2$. Full details of the test structure and ventilation configurations were provided previously in Chapter 3.

5.5 Presentation of Results

All ventilation rates given in the results are normalised by the area of a single ventilation opening and the mean reference velocity at roof height (18 metres upstream of the windward face of the cubic structure). Table 5.1 below gives the relevant normalising values for each of the two cases.

Table 5.1. Data used for normalising ventilation rates for experimental configurations

Wind direction (°)	**Opening area (m^2), A**	**Reference Velocity (ms^{-1}), U_{ref}**
0	1	6.7
90	1	11.4

5.6Results

The processing and transformation of the time series involved a number of mathematical and statistical techniques in order to obtain a prediction. The following results provide details of each stage of the data analysis and manipulation that are necessary for predicting turbulent ventilation through the two methods discussed.

5.6.1 Time Domain Method

The time domain method for the prediction of the broad banded continuous unsteady ventilation was introduced in section 5.2 and the relationship between the mean flow and broad banded fluctuations was described. The contribution of broad banded fluctuations is dependant upon the relative magnitude of the fluctuations in the total ventilation to the magnitude of the mean ventilation rate. This implies that although the time domain method aims to predict an unsteady broad banded flow mechanism, it cannot be applied without first considering the mean flow as the two are very much related. In reality the broad banded component can be regarded as a modification of the mean ventilation mechanism to account for turbulent fluctuations.

Figure 5.1 shows a plot of the predicted instantaneous ventilation rates over an arbitrary interval period for the 0° wind direction. It is immediately apparent from Figure 5.1 that for the ventilation rate is always positive indicating that there are no periods of flow reversal through the ventilation openings. This would be expected for the 0° case where the mean pressure difference between ventilation openings is relatively high. The mean non-dimensional ventilation rate for the period of data shown in Figure 5.1 is approximately 0.45 with an rms value of 0.2. Here, the total ventilation due to the mean and broad banded mechanisms (found by integration of the region beneath the data) corresponds to the mean ventilation rate alone (it should be noted that the plot in Figure 5.1 does not represent a full data set as the large number of data points obscures the clarity of the data).

The predicted instantaneous ventilation rates for the 90° wind direction are shown in Figure 5.2. This configuration exhibits a very different pattern from that shown in Figure 5.1 for the 0° case. In the 90° case, the instantaneous ventilation rate can be seen to fluctuate about zero exhibiting both positive and negative values. The two ventilation openings, for the 90° case, were located on opposing sides of the cubic test structure with the wind oriented parallel to the opening planes. The symmetry of this configuration lead to the mean pressures at the two openings being similar. Fluctuations in the pressure at the openings lead to periodic changes in flow direction which correspond to the changes in sign on Figure 5.2. In the 90° case, the mean ventilation rate is close to zero (approximately 0.03 over the time interval shown in Figure 5.2). The use of the mean ventilation alone would, in this case, be misleading. A change in flow direction will always lead to an addition to the ventilation, this would not be apparent from the mean ventilation rate. For this reason, the ventilation rate due to the mean and broad banded mechanisms requires the sum of the two components (through the application of equation (5.3)).

Table 5.2 shows the mean ventilation rates for the two wind directions considered. The sum of the mean and broad banded ventilation is also shown for the 90° case. As can be seen, the sum of the two components is significantly greater than the mean ventilation rate alone.

Table 5.2 Predicted mean and turbulent ventilation rates using pressure difference method

Wind direction (°)	**Mean ventilation** $\overline{Q} / AU_{ref}$	**Mean + Broad Banded ventilation** Q_B / AU_{ref}
0	0.48	-
90	0.095	0.214

5.6.2 Frequency Domain Method

The frequency domain technique was applied to predict the contribution of the pulsating flow mechanism to the total unsteady ventilation. The process required a number of stages of numerical analysis as outlined in section 5.3. In the following section each stage of the frequency domain analysis is explained individually in order to detail the prediction process.

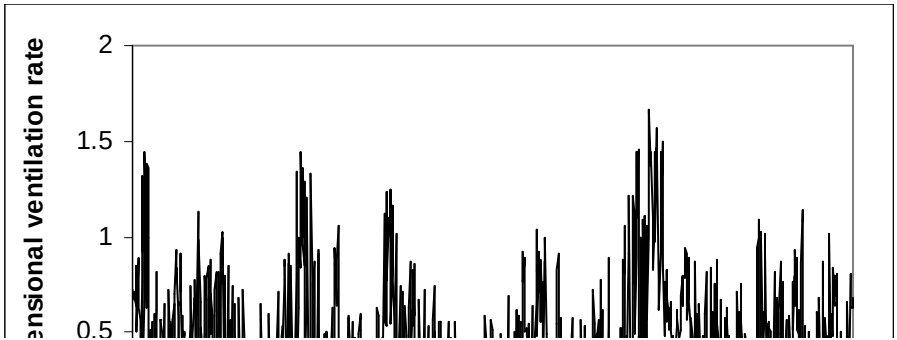

Figure 5.1 Time series of predicted non-dimensional ventilation rate using time domain technique for 0° case

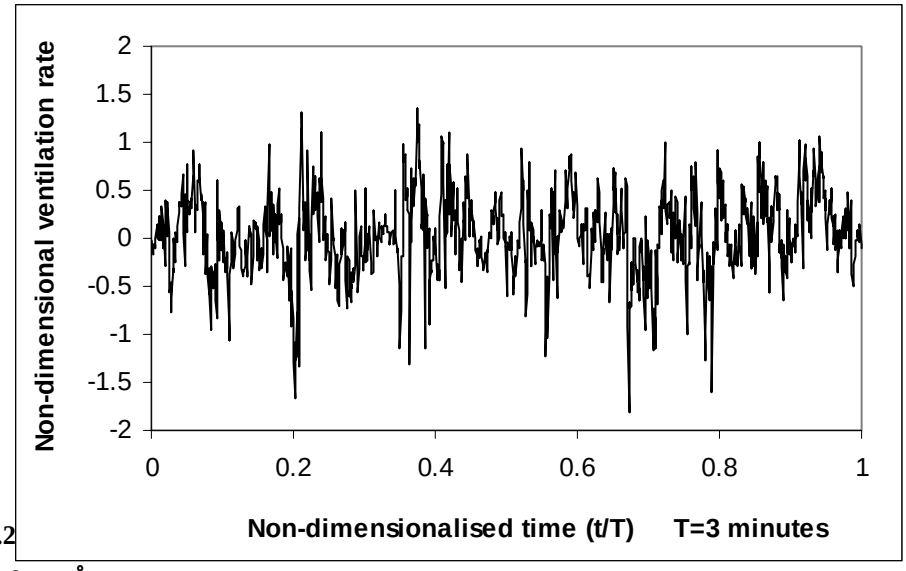

Figure 5.2 domain technique for 90° case

5.6.2.1 Pressure Coefficient Covariances

Covariances were calculated from one hour runs of pressure collection providing 18000 measurements in each data set. Covariances give a measure of correlation between the pressure coefficients at two points on the surface of the structure in order to assess how pressures at one point fluctuate relative to those at another position. For this reason it would be expected that in a matrix of covariances for pressures measured at differing positions on a structure, covariance of points close together should be higher since it would be expected that these would be well correlated.

The covariances of the 16 pressure tappings around the test structure form a 16x16 matrix. Sample covariance matrices are presented in Appendix C for the 0° and 90° cases.

5.6.2.2 Eigenvector and Eigenvalues of Pressure Covariance Matrices

The eigenvalues calculated from the pressure coefficient covariance matrices can be used to assess the percentage of total fluctuating energy present in each mode of pressure. Samples of an eigenvector matrix and list of eigenvalues are presented in Appendix C for both the 0° and 90° wind directions.

Figures 5.3 and 5.4 show the relative percentages of the total fluctuating energy in each mode for the two wind directions (0° and 90° respectively). It is apparent from both of the graphs that a large proportion of the total energy of the fluctuating pressure is represented within the first three modes with the first mode, in each case, containing the vast majority of the energy.

Figure 5.5 shows the distribution of the eigenvectors (of the first three pressure modes) for the 16 pressure tappings around the surface of the structure for the 0° case. It is apparent from Figure 5.5 that the distribution of eigenvectors of mode 1 resemble the form of the mean pressure distribution shown in Figure 3.17. However, the signs are reversed and magnitudes are below half of those of the pressure coefficients. It is the distribution rather than the values that are comparable. This is in agreement with results from previous investigations (e.g. Armit (1968)) and adds weight to the argument that the first pressure mode is related to longitudinal fluctuations in the wind.

The distribution of eigenvectors for mode 2 (for the 0° case) are presented in Figure 5.5 and show an almost linear increase up to tap 7 after which the eigenvectors decrease rapidly before becoming almost constant for taps 11 to 16 (leeward face).

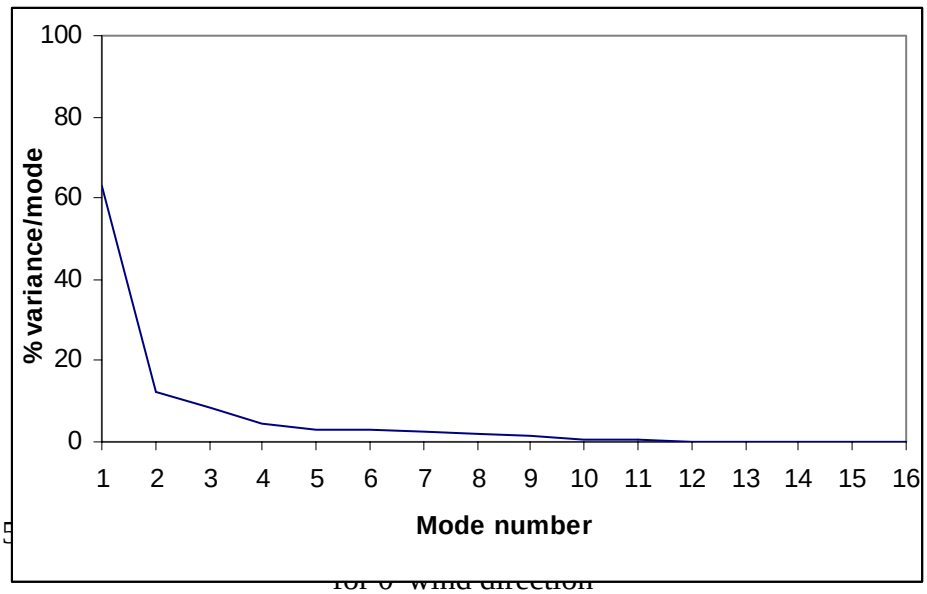

Figure 5 modes for 0° wind direction

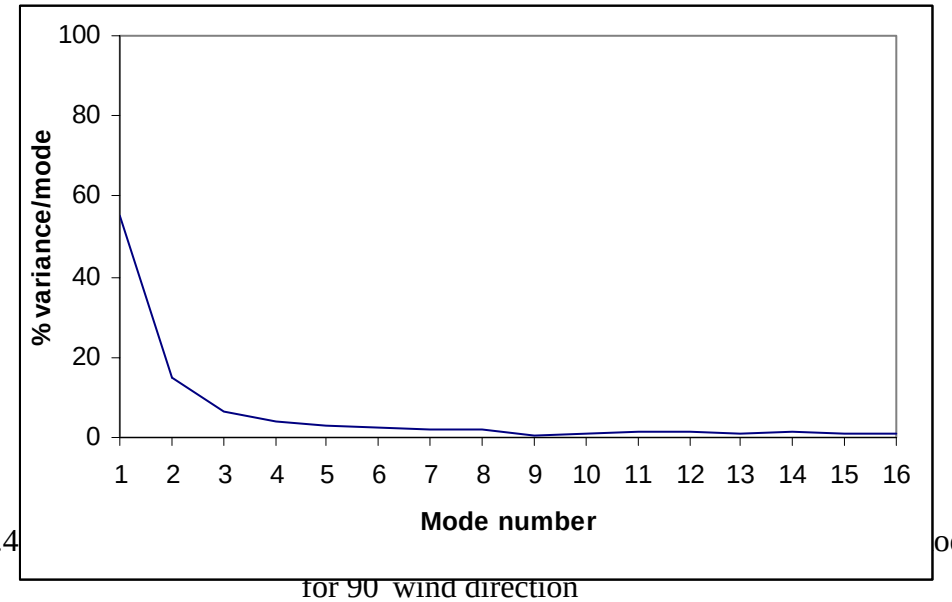

Figure 5.4 odes for 90° wind direction

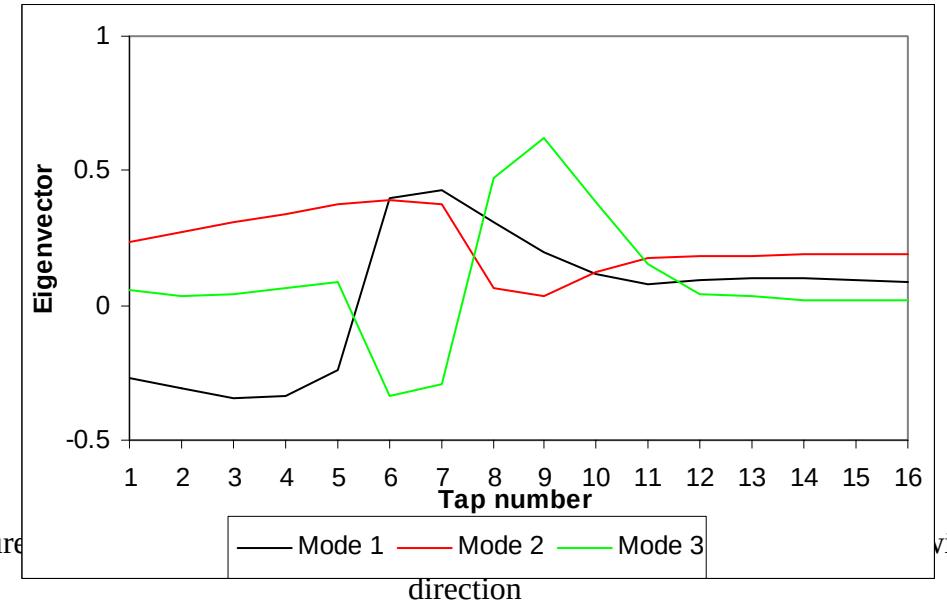

Figure vind direction

The distribution of the eigenvectors of mode 3 are almost constant for taps 1 to 5 as they are for taps 12 to 16 (leeward face), however, for taps 6 to 11 (roof) there is far more variation.

Figure 5.6 shows the eigenvector distributions for the 16 surface pressure taps for the 90° case. In this configuration, the pressure taps are located on the side faces (faces where ventilation openings are present) and transversally across the roof. The

distribution of mode 1 eigenvectors show almost constant values that correspond (in profile) to the mean pressure distributions for this wind direction (see Figure 3.17 lateral and Figure 3.19).

The distribution of mode 2 in Figure 5.6 display almost constant eigenvectors for pressure taps 1 to 5 and 12 to 16 (building side faces) with the only significant variation occurring in taps 6 to 11 transversally across the roof. Mode 3 exhibits decreasing eigenvectors with height on each of the side faces whilst the roof displays an increase towards one side of the roof.

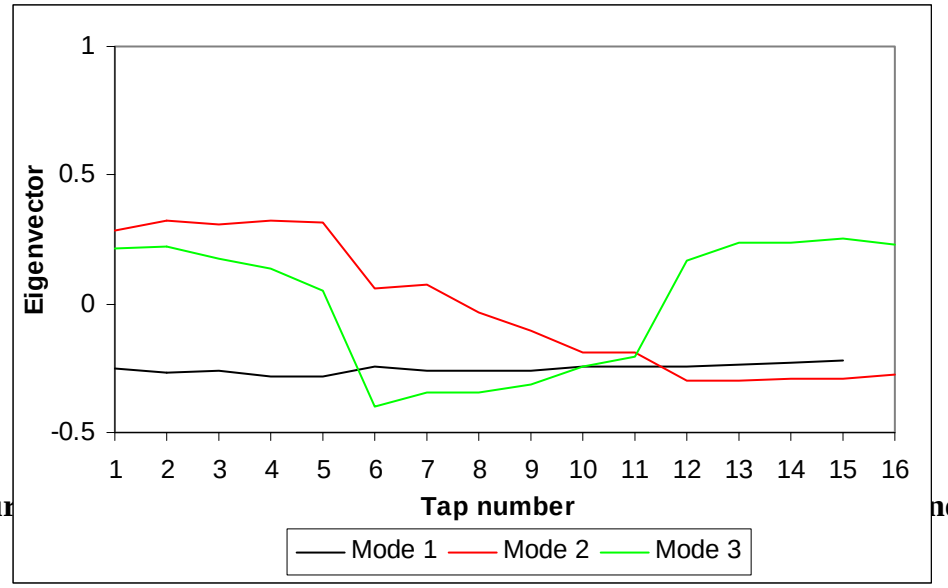

Figur **nd**

5.6.2.3 Modal Pressure Spectra

Throughout the frequency domain ventilation predictions, only the first three pressure and ventilation modes were assessed. Although the number of modes calculated always equals the number of data collection points on the building, the first three modes have been found to contribute the significant proportion of the total fluctuating energy.

Before it is possible to find the unsteady pulsating ventilation it is necessary to find the modal pressure coefficient spectra. In order to carry out the spectral analysis, modal time series were produced. The modal time series were formed from equation (5.16) through the multiplication of the individual pressure coefficient time history for each pressure tap by the relevant eigenvector for each pressure tap and pressure mode.

Fast Fourier transforms (FFT's) were found of the modal time series (produced for each mode) from which the power spectra, of each mode of pressure, were produced. Figure 5.7 shows the calculated pressure spectra for the first three modes for the 0° case. The spectra have all been normalised by the total variance of the fluctuating pressure in order to represent the relative contributions of each to the total fluctuating pressure.

Figure 5.8 shows the modal pressure spectra for the first three modes respectively for the wind at an angle of 90° to the faces containing the openings. The modal pressure spectra have been normalised in the same way as above.

5.6.2.4 Pulsating Ventilation Rates

Calculation of the unsteady pulsating ventilation spectra required the transformation of the corresponding modal pressure spectra. The transform function utilised in this technique was defined in equation (5.27). Table 5.3 gives the values of the components used in the transform equation for both 0° and 90° cases. The sum of the individual modal ventilation spectra provides the total pulsating ventilation spectra. It should be noted that only the first three modes (out of 16) were utilised.

Table 5.3 Transform parameters for derivation of modal ventilation spectra

Parameter	***Notation***	**Value**	**Units**
Natural angular frequency	ω_n	12.57	**Hz**
System damping	c	0.119	-
Density of air	ρ	1.25	$kg\ m^{-3}$
Reference velocity	U_{ref}	6.7/11.4	ms^{-1}
Volume of enclosure	**V**	216	m^3
Coefficient of linearisation	**K**	10	-
Effective orifice length	**L**	1.09	m
Ratio of specific heat	**γ**	1.4	-
Reference pressure	$\mathbf{P_R}$	101000	**Pa**
Number of orifices	**N**	2	-
Area of orifice	**A**	1	m^2

Figure 5.9 shows the spectra of the first three modes of pulsating ventilation for the 0° case. It is obvious from Figure 5.9 that the first and second ventilation modes contain similar amounts of energy and would make significant contribution to the total pulsating ventilation spectra shown in Figure 5.10. The natural frequency of the system was calculated to be 4.9 Hz, however, the internal pressure spectrum showed peaks at 2 Hz. This measured value of 2 Hz was therefore taken as the natural

frequency of the pulsating ventilation system. The differences between the calculated and measured natural frequency of the system is most likely a result of leakage from the cube and the flexibility of the sides of the structure, leading to a change in the bulk modulus of the flow (equal to the product $P_R\gamma$).

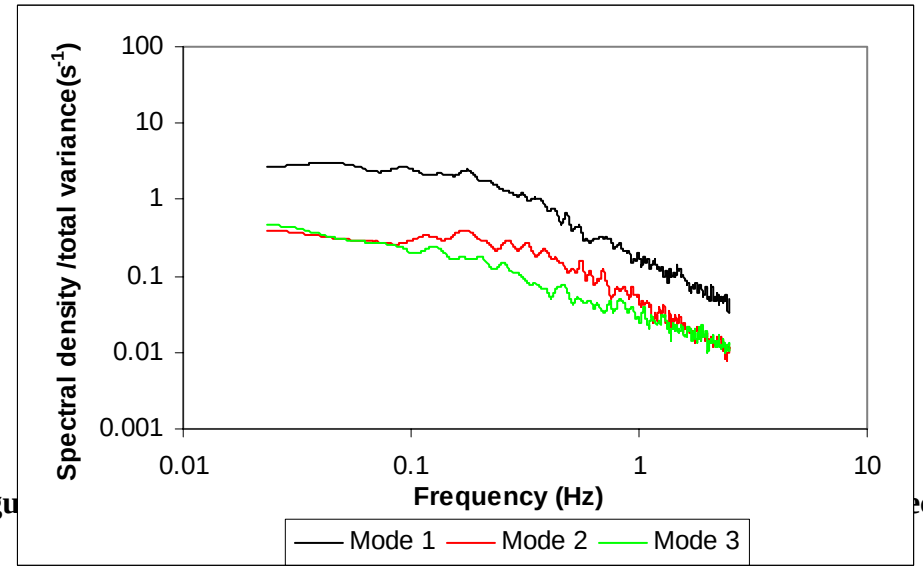

Figu **ection**

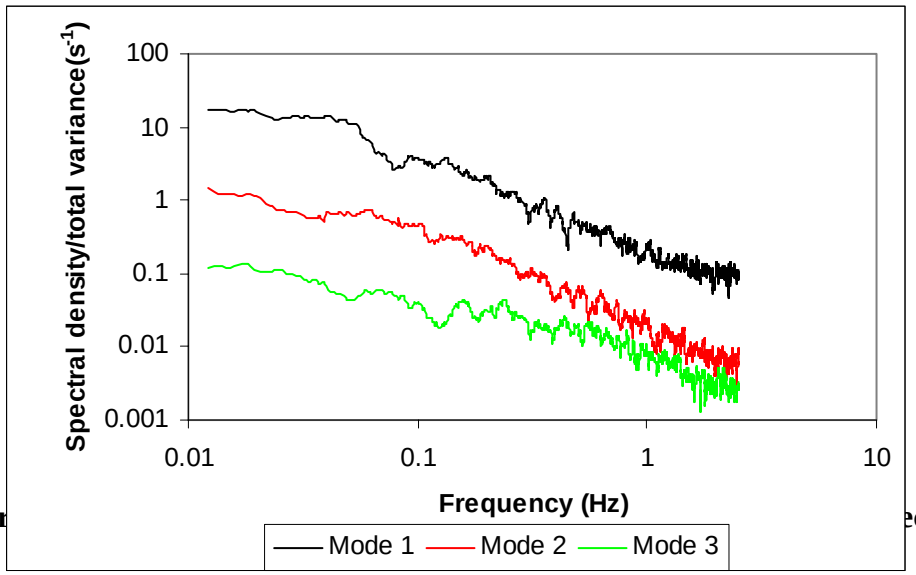

Figur **ection**

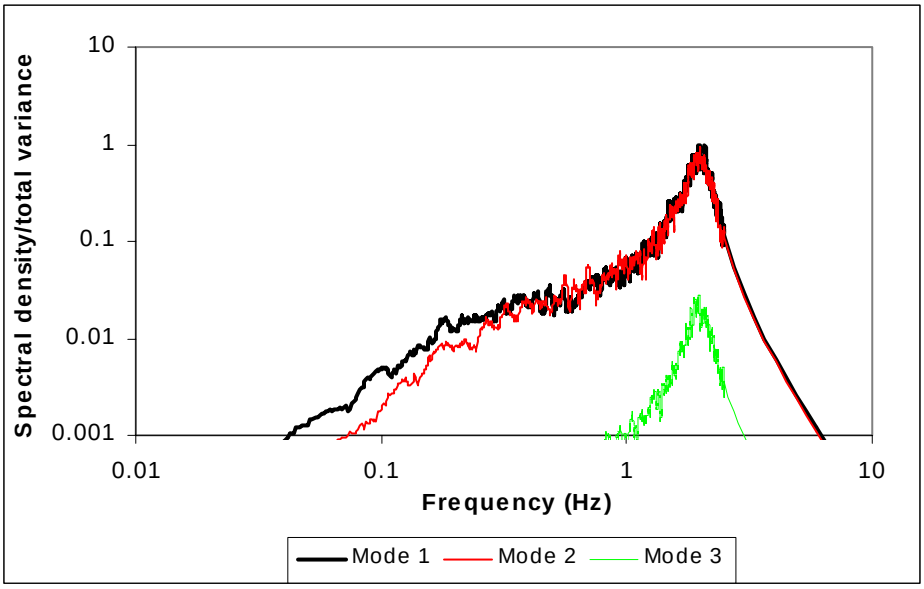

Figure 5.9 Predicted modal pulsating ventilation rate spectra for 0° wind direction for first three modes

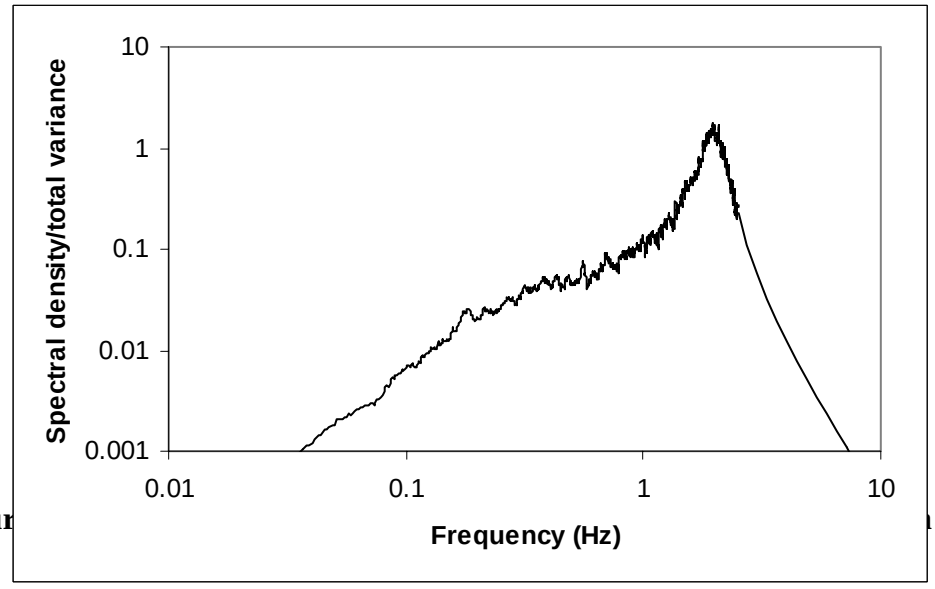

Figur for 0°

Vickery and Bloxham (1992) discussed how the effect of building flexibility can reduce the effective value of the bulk modulus of the flow to as low as 20% of the normal value. This is consistent with the observed shift in the natural frequency from its predicted value. In order to allow for this effect, the measured natural frequency was used to calculate all of the ventilation rate spectra.

In terms of pressure modes around a structure, mode 1 tends to contain far more of the fluctuating energy than the rest of the pressure modes (as shown in Figures 5.3 and 5.4). This is obviously not the case when the pressure modes are transformed to

predict the pulsating ventilation. One of the key transformations of the modal pressure spectra to the modal ventilation predictions involves the calculation of the transform parameter Π_i (from equation (5.27). When the energy contained in each pressure mode is assessed, Π_i accounts for the effect of each mode around the whole structure. When the ventilation rate transformation is undertaken, it is the difference in eigenvectors of each mode at the ventilation openings that effectively defines the relative contribution of individual modes. It is this step in the predictions that defines which mode makes significant contribution to the ventilation and therefore the mode containing the highest energy in terms of pressure may not necessarily be responsible for the same relative contribution to the pulsating ventilation.

Figure 5.11 displays the pulsating ventilation spectra for the first three modes of ventilation and Figure 5.12 the spectrum of the total pulsating ventilation for the 90° case. For this configuration, mode one again dominates the pulsating flow. Here however, mode 2 made insignificant contribution and is not visible in the spectra shown in Figure 5.11. Mode 3 exhibits a greater contribution than in the 0° case. It is not possible to speculate with any certainty why modes 2 and 3 make the corresponding contributions since there is, to date, no general consensus on the physical mechanisms responsible for these modes. It is however, generally accepted that mode1 is driven by longitudinal fluctuations which explains why the eigenvectors of this mode exhibit profiles similar to the mean pressure distributions.

5.6.3 Quantifying Pulsation Flow Mechanism

Integration of the pulsating ventilation spectra (Figures 5.9 to 5.12) provide a measure of the variance of the ventilation rate from which the rms value can be obtained. This rms corresponds to the peak pulsating flow rate and would in reality be fluctuating. If the fluctuation of the pulsating flow mechanism is assumed to be sinusoidal in nature it can be shown that the pulsating ventilation rate is given by (see Appendix D for derivation)

$$Q_{pulse} = \sigma_{Q_{pulse}} \frac{\sqrt{2}}{\pi} \tag{5.28}$$

where Q_{pulse} is the pulsating ventilation rate and $\sigma_{Q_{pulsae}}$ is the rms of the ventilation rate derived from the ventilation rate spectra.

In order to quantify the non-dimensional, predicted pulsating ventilation it is necessary to integrate the area beneath each modal spectra for the contribution of each mode to the total. The integrals were calculated using simple trapezoidal integration techniques. Table 5.4 shows the contribution of each individual ventilation mode to the total pulsating ventilation flow.

Table 5.4 Predicted relative contributions of modal ventilation to total pulsating ventilation

Wind direction (°)	**$Q_{mode\ 1}$ / %**	**$Q_{mode\ 2}$/ %**	**$Q_{mode\ 3}$/ %**	**Total pulsating Q_{pulse} / AU_{ref}**
0	50.7	47.7	1.6	0.008
90	86.4	0	13.6	0.014

For the 0° case the first and second modes make up the vast majority of the pulsating flow with the contribution of the third mode being almost negligible. The first mode of ventilation would be driven by longitudinal fluctuations in the mean flow that would be expected to be significant when the longitudinal flow is normal to the plane of the openings. It would be expected that the first few modes would be most significant in the 0° case since the mean flow mechanisms would be responsible for the majority of the flow with turbulent mechanisms having a lesser effect. The contribution of the pulsating flow mechanism to the overall ventilation flow is unlikely to be significant for the 0° case since the large mean pressure difference between the openings would be high. Such large mean pressure differences would tend to lead to the effects of pulsating flow being small.

In the 90° case, mode 1 contributed 86% of the total pulsating ventilation, this is a more significant proportion than for the 0° case. The second mode of ventilation made no contribution whilst mode 3 was responsible for approximately 14% of the pulsating flow.

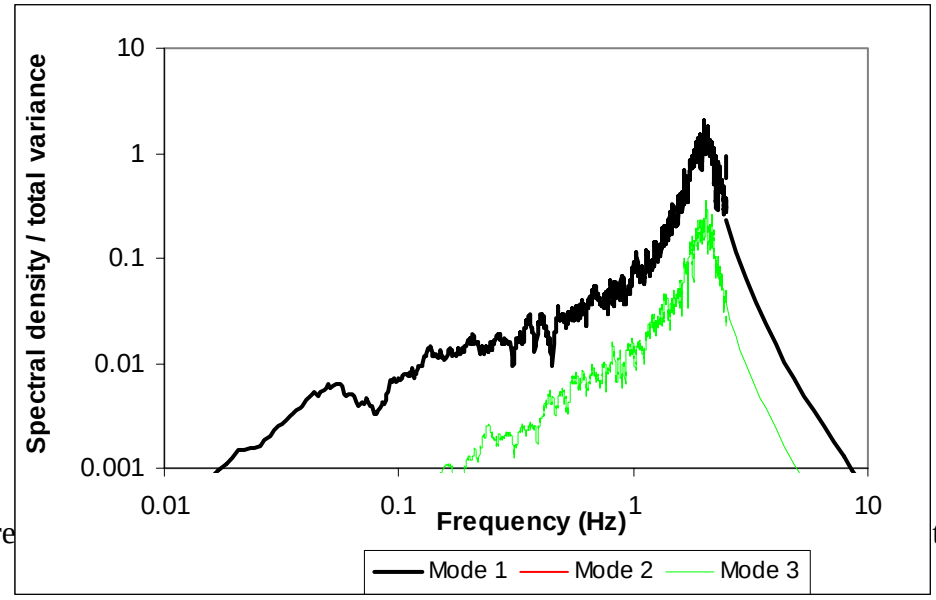

Figure the first

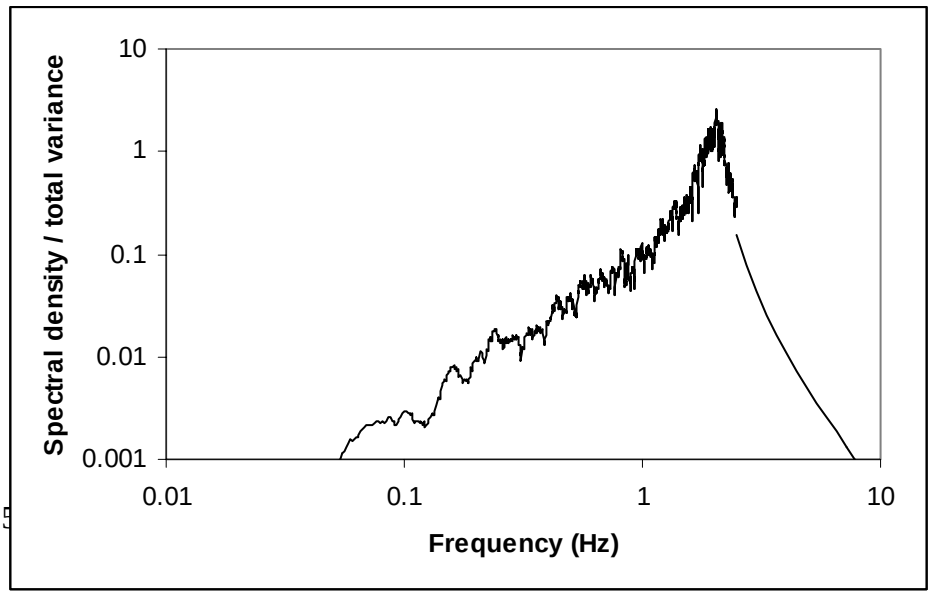

Figure 5 wind

The most significant difference in contributions made by individual ventilation modes for the 0° and 90° cases is apparent in mode 2. In the 0° case, almost half of the pulsating flow was attributable to mode 2 whilst the same mode made no contribution in the 90° case. Previous investigations into wind driven surface pressures (e.g. Armitt (1968)) have related mode 2 to transverse fluctuations. If this is true, mode 2 would be expected to contribute to the pulsating flow in the 90° case where the transverse component of the fluctuations in the wind would drive flow normal to the opening planes. It is possible however, that the mechanism responsible for mode 3 might dominate in the 90° case over mode 2. This could indicate that mode 3 is related in some way to mechanisms that are dominant around the cube sides e.g. the unsteady separation and reattachment of flow.

5.7Summary

The main objectives of this chapter were to investigate whether it was possible to predict the contribution of turbulent mechanisms to the overall wind induced ventilation. It has been known for some time that a number of physical mechanisms lead to turbulent air exchange across ventilation openings. However, very little work has previously been undertaken in attempting to quantify these mechanisms. Two approaches have been described here for the prediction of turbulent ventilation.

The time domain method was an expansion of the steady-state pressure difference method and utilised time dependant data from which the turbulent mechanisms could be predicted. The application of this method to time varying data (in terms of pressure differences across openings) leads to a prediction of a broad banded, turbulent ventilation driven by longitudinal fluctuations in the wind. The flow mechanisms detected through this technique are likely to encompass the lower

frequency fluctuations since instantaneous pressure differences between the ventilation opening positions would be governed by larger scale turbulence.

The broad banded turbulent ventilation is analogous to the continuous ventilation mechanism introduced by Malinowski (1971) and discussed in Chapter 2. This form of ventilation is, in reality, a modification of the mean ventilation flow to account for the broad banded fluctuations in the oncoming wind. These fluctuations contain most of their energy at relatively low frequencies (< 0.1 Hz). The action of the broad banded mechanism is dependant upon the magnitude of the fluctuations around the mean ventilation rate. Consequently the mean and broad banded mechanisms must be considered simultaneously.

For the 0° case, fluctuations in the ventilation rate were found to be small in comparison with the mean ventilation rate. In this case the contribution of the mean and broad banded ventilation is simply equivalent to the mean ventilation rate and the broad banded mechanism is not considered. However, for the 90° case the mean ventilation rate is low. The fluctuations in the ventilation rate time series were found to be in excess of the mean value. In this case, the mean ventilation rate cannot be used alone and the broad banded mechanism must also be considered. Accounting for both ventilation components made significant changes to the total ventilation driven by these two mechanisms.

The frequency domain method required far more rigorous numerical processing and only predicted the contribution of the pulsating ventilation mechanism (described in Chapter 2). Compared to the broad banded unsteady contribution of fluctuating ventilation predicted using the time domain method, the predicted contribution of the pulsating flow mechanisms was low for both the 0° and 90° wind directions. For the 0° wind direction the predicted pulsating flow would be expected to be very low since the configuration is far from a classic pulsed flow configuration. Pulsating flow becomes more significant when pressure fluctuations result in flow periodically changing direction across an opening.

Although the 90° case was also not the best configuration for a significant pulsation flow to occur, it was found to be more significant than for the 0° wind direction. The relative contribution of pulsating flow to the mean flow rate (predicted using the steady-state pressure difference method) was far greater for the 90° case than for the 0° case. This was because the mean flow rate was predicted to be significantly lower (for the 90° case) but pulsating flow was found to be similar for both configurations investigated.

The different contributions of individual modes of pulsating ventilation for the two configurations investigated showed interesting results. For both wind directions the first calculated pressure modes contained significantly more energy than the other modes of pressure. The transformation of pressure spectra to ventilation rate spectra lead to a reduction in the dominance of mode 1 for the 0° wind direction. Modes 1 and 2 were found to be almost equal and together were responsible for 98% of the pulsating flow. For the 90° wind direction, the first mode made a more significant contribution to the pulsating ventilation than in the 0° case. Mode 2 however, made no contribution whilst mode 3 contributed a greater proportion of the pulsating flow than

in the 0° case. Since the orientation of the wind to the openings differed by 90° for the two configurations investigated it would be expected that different physical mechanisms would be responsible for pulsating flows in each case. This is borne out in the different contributions of the first three modes for each configuration. Further clarification into the mechanisms that control the pressure modes would be required before it would be possible to conclude as to what exactly is responsible for each mode of pressure and therefore pulsating ventilation.

6. RECONCILING THE INVESTIGATIONS

6.1 Introduction

In this chapter, an attempt will be made to draw together the full-scale experimental, computational and analytical work previously described. In essence, the proceeding work will be a validation of the computational fluid dynamics modelling and analytical predictions of wind induced ventilation by comparison, wherever possible, with results obtained experimentally. It is through rigorous comparison with experimental data that the application of numerical predictions to wind driven ventilation studies can be assessed.

6.2 Validation of CFD Predictions

The computational fluid dynamics simulations described in Chapter 4 involved a number of distinct parts. Within this section, comparisons are drawn between experimental measurements and computational predictions of internal flow structure. The external pressure distributions predicted using CFD models are not included within this Chapter and were compared with the experimental data previously in Chapter 4. There is good reason for taking this approach. The computational simulations of primary relevance to this work are the wind driven ventilation models. In order for the best computational configuration to be utilised, the simulations of the external environment around the test cube were validated with experimental data prior to the simulation of internal flows.

6.2.1 Internal Pressure

Measurements of internal pressures were limited. It was described in Chapter 3 that internal pressures were only measured when ventilation openings were present. The pneumatic pipes (in the locations of the opening centres) were disconnected when the panels covering the openings were removed. This left the open-ended pipes to monitor internal pressures in positions just above the ventilation openings (within the internal region). Figure 6.1 shows the internal pressure coefficients as predicted by the RNG k-ε turbulence model directly between ventilation openings for the 0° wind direction. The two experimental measurements made close to the ventilation openings are also shown on Figure 6.1 and can be seen to agree well with those predicted computationally. The CFD predictions show an almost uniform pressure distribution internally along the profile measured. The experimental results alone could be interpreted to suggest the presence of an internal pressure gradient between

the two measured positions. Without further data it is not possible to speculate on the experimental results further.

6.2.2 Internal Velocity Profiles

Figure 6.2 shows profiles of the measured and predicted internal streamwise component of velocity (using the RNG k-ε turbulence model) in a streamwise orientation for the 0° wind direction. The measured plane lies between the centres of the ventilation openings. The CFD simulation under-predicted the velocity in the region close to the ventilation inlet. The CFD results exhibit the flow accelerating from the inlet plane to a peak located approximately 5% of the streamwise distance through the test cube. This peak corresponds to the narrowest point of the vena contracta region of the jet passing through the inlet (this can be seen visibly in the velocity vector plots of Figures 4.26 and 4.27). The lower number of data points from the experimental results show no indication of the continued acceleration of the flow from the plane of the inlet. This could be a result of not being able to measure velocities in the plane of the ventilation openings due to the physical size of the anemometer.

After the peak velocity close to the ventilation inlets, both predicted and measured profiles in Figure 6.2 display a deceleration as the jet of air passing through the inlet widens. The measured profile exhibits a more rapid reduction in streamwise velocity than the computational prediction that follows an almost linear deceleration of flow with distance. The measured velocity accelerated after passing approximately 75% of the way through the internal region whilst the computational predictions do not show this same acceleration until the air approaches the ventilation exit. Both profiles exhibit closer agreement near to the exit as the flow again accelerates due to the contraction towards the outlet.

Figure 6.3 again shows the streamwise component of velocity for the 0° wind direction however the profile is taken transversally within the cube at the streamwise centre-line. The CFD predictions agree well with the measured profile although velocities are slightly over-predicted through the central region that corresponds to the faster flowing air between ventilation openings.

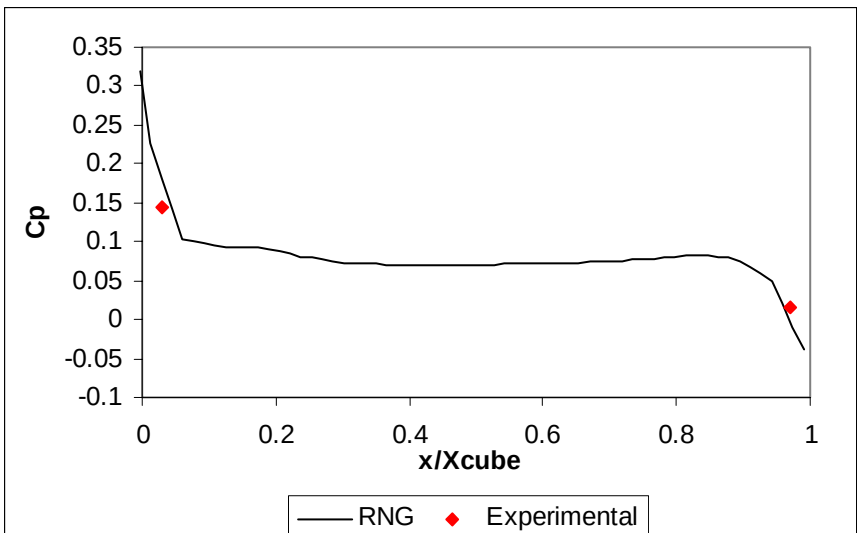

Figure 6.1 Measured and predicted internal pressure between ventilation openings for the 0° wind direction

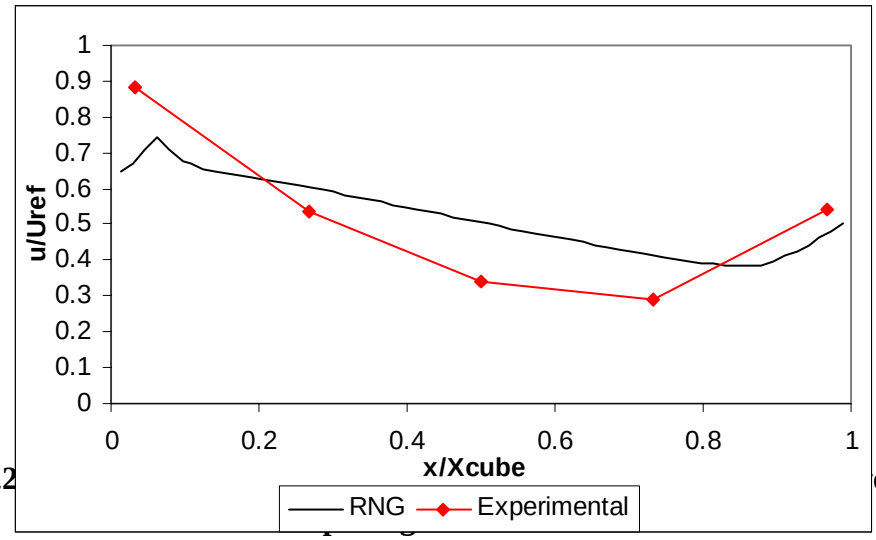

Figure 6.2 elocity

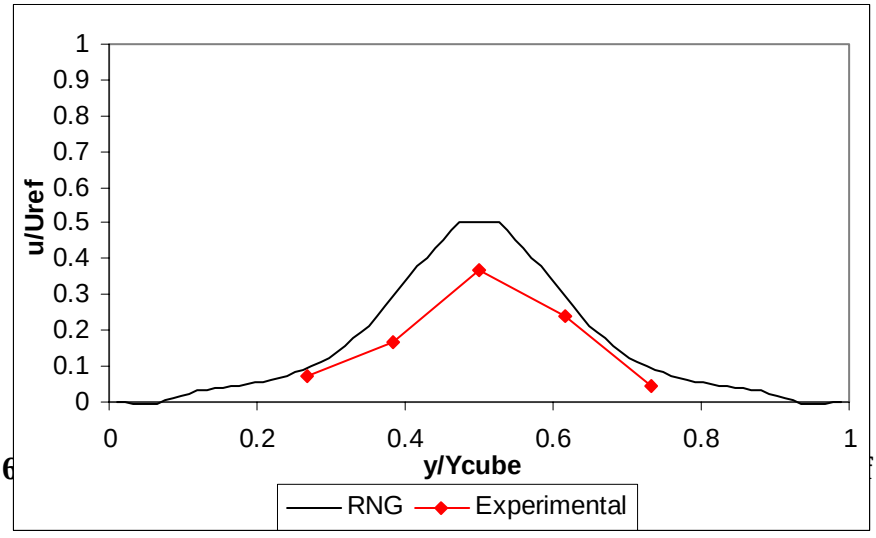

Figure 6 velocity

The distribution of the transverse component of velocity both between the ventilation opening centres and transversally across the cube centreline are shown in Figures 6.4 and 6.5 respectively. For the profile between the ventilation openings, the lateral velocity is insignificant (in comparison with the streamwise component) with the computational prediction being zero and the measured value very close to this. The predicted and measured profiles of transverse velocity across the transverse centre-

line of the cube show good agreement (Figure 6.5). At the centre-point of the profiles the transverse component of velocity is zero. This coincides with the region of flow passing between ventilation openings with little deviation from the streamwise orientation. Away from this central point the lateral velocity component suggests the flow is diverging transversally with positive velocities one side and negative velocities on the other side. The CFD vector plot shown in Figure 4.26 suggests the presence of recirculating flows either side of the central region which explains the profiles shown in Figure 6.5 further.

The vertical components of velocity are only shown between ventilation openings in Figure 6.6. The measured and predicted profiles transversally across the cube showed negligible velocities. Both the measured and predicted vertical components show slightly negative vertical velocities as air enters the cube (travelling at an angle downwards towards the ground) with the flow levelling out with distance through the cube. The computational predictions show that the flow leaving the cube has a positive vertical component whilst it was measured to be very close to zero. This increase in the vertical component of velocity could be the result of flow exiting the cube and being drawn upwards by the recirculating flow in the wake of the building. Experimental measurement closer to the exit plane of the cube would have helped confirm this.

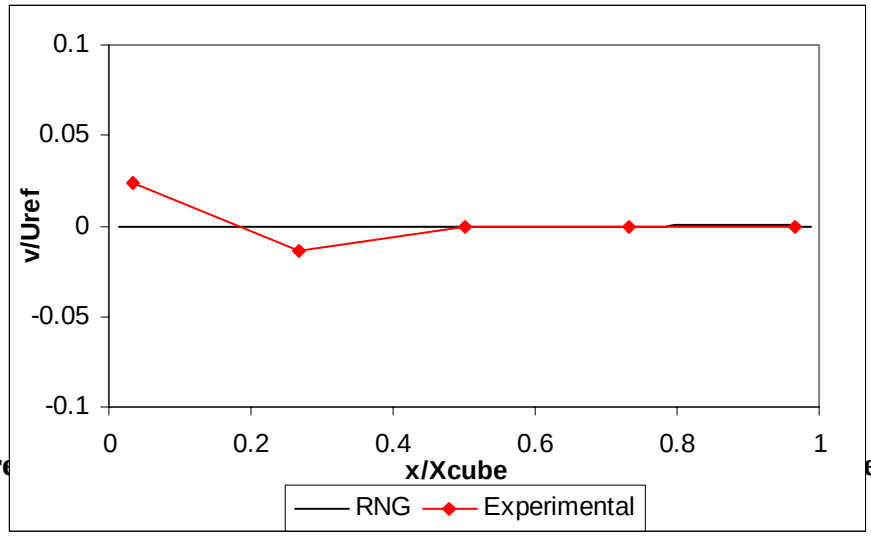

Figure **elocity**

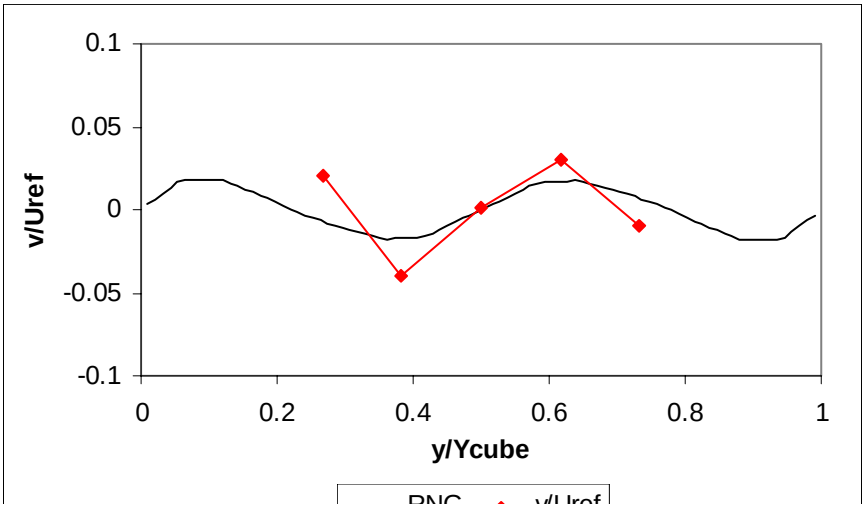

Figure 6.5 Measured and predicted profile of lateral component of velocity transversally across cube centre-line for 0° wind direction

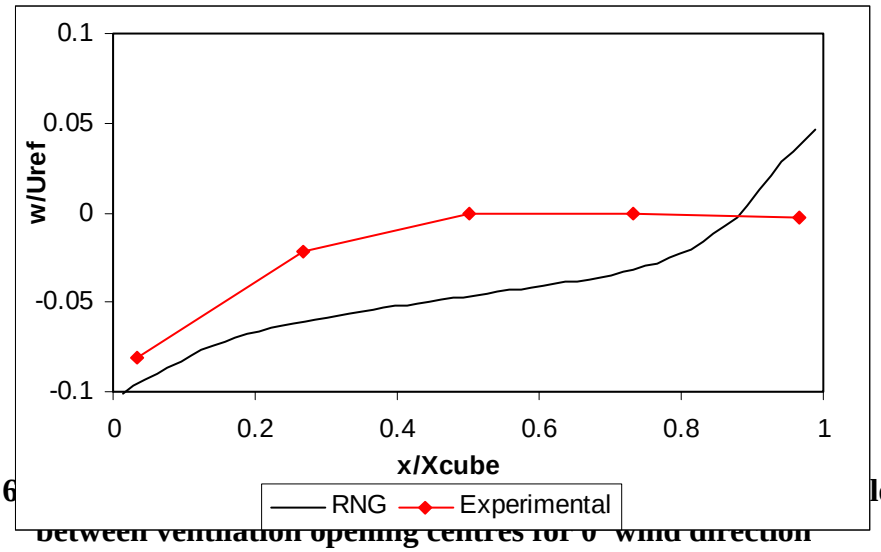

Figure 6 … locity between ventilation opening centres for 0° wind direction

Internal air flow patterns for the 90° wind direction are not included. Computational predictions for this case produced no flow within the internal region (or velocities of negligible magnitude). Experimental measurements proved that there was a significant flow of air through the internal region for the direction at 90° to the plane of the opening. The differences in this case are due to the effects of turbulence. In the steady-state computational simulations, the two openings were located in regions of equal pressure hence no flow is driven between them. In reality, turbulent fluctuations in the wind produce fluctuating pressures and instantaneous pressure differences across the ventilation openings of significant magnitude resulting in internal flows.

6.3Ventilation Rate Validation

Wind driven ventilation consists of two components – a mean component driven by the mean pressure field at ventilation openings, and a fluctuating component driven by the fluctuating pressures and unsteady flows around the openings. In Chapters 3 and 4, a number of methods were described through which the mean ventilation rates were measured and predicted using both experimental and computational techniques. Methods for determining turbulent components of ventilation were described in

Chapter 5. In the proceeding sections the different methods for predicting individual components of ventilation are discussed and compared with experimental measurements culminating in an attempt to draw the results together to predict the total ventilation rate. Ventilation rates will be given in their non-dimensional form by dividing through by the product of the reference mean wind speed and the area of a single ventilation opening

Two wind directions were investigated for the two opening ventilation configuration. The 0° case corresponds to the incident wind normal to the ventilation openings (openings are located on the windward and leeward faces). The 90° case corresponds to the incident wind being parallel to the planes of the openings (effectively the same wind direction but with the openings located on the cube sides).

6.3.1 Mean Ventilation Rate Assessment

Mean ventilation rates were assessed through experimental and computational techniques. Three methods were applied;

1. Measured experimentally through the integration of measured velocities over the ventilation openings.
2. Prediction using CFD through the integration of predicted velocities over ventilation openings
3. Predictions using the steady-state pressure difference method (experimental)

The steady-state pressure difference method was explained in Chapter 2 and applied in Chapter 3. In the following, ventilation rates found through the integration of velocities over the plane of ventilation openings (from anemometer measurements and computational predictions) will be referred to as velocity integrated ventilation rates. The measured velocity integrated ventilation rates are the results used to compare the two predictive techniques.

Table 6.1 shows the non-dimensional ventilation rates for the 0° wind direction for the three mean ventilation rate assessment methods. The application of the pressure difference method relies on the difference between external pressures measured in the positions of ventilation openings on the sealed cube and can be seen to under-predict the measured velocity integrated ventilation rate by 30%. The velocity integrated ventilation rates from anemometer measurements and CFD predictions agree well with less than 10% difference between the two.

Table 6.1 Predicted and measured mean ventilation rates from experimental and computational investigations for 0° wind

Technique	Method	Wind direction (°)	Mean ventilation

			$\overline{Q}/U_{ref}A$
Experimental	Velocity integrated	0	0.69
CFD	Velocity integrated	0	0.65
Experimental	Pressure difference	0	0.48

Table 6.2 shows the mean ventilation rates for the 90° case. The pressure difference method predicted 85% of the measured mean ventilation rate however, the computational technique predicted zero ventilation. In the computational simulations (when the openings were located on the cube sides) the pressure difference between the openings was zero since the solution was symmetrical. The mean pressures measured experimentally however, showed that there was a pressure differential between the openings. This pressure difference was caused by turbulent fluctuations in the wind and resulting surface pressures. Experimental measurements using the velocity integrated ventilation rates verified the presence of a ventilating flow for the 90° case. This ventilation configuration highlights the limitations of using time-averaged, steady-state computational simulations for predicting flow mechanisms driven by turbulent processes.

In both the 0° and 90° cases, the pressure difference method under-predicted the mean ventilation. There are a number of reasons for this under-prediction:

- Inaccurate measurement of experimental ventilation rate (velocity integrated)
- Ventilation configuration used is not applicable to pressure difference method
- The value of discharge coefficient used is wrong
- The pressure difference between ventilation openings is different for the open and sealed cases.

With respect to inaccuracies in the methods of measuring the experimental discharges, this is unlikely since repetition of the experiments gave consistent data. The CFD predictions also agreed well with the experimental measurements (for the applicable 0° case). It is more probable that the differences in the pressure difference method predictions lie in the technique itself.

Table 6.2 Predicted and measured mean ventilation rates from experimental and computational investigations for 90° wind

Technique	**Method**	**Wind direction (°)**	**Mean ventilation** $\overline{Q}/U_{ref}A$
Experimental	Velocity integrated	90	0.114
CFD	Velocity integrated	90	0
Experimental	Pressure difference	90	0.095

The pressure difference method may not be applicable to the ventilation configurations tested. The technique would be expected to be best suited to the 0°

case where the pressure difference between ventilation openings is large, however, the size of the openings may have been too large. The standard value of discharge coefficient applied was developed for steady flows, normal to the opening plane of a sharp edged orifice. In the case of flows around a building envelope, flows through openings will often have a significant crossflow component that could effectively change the discharge coefficient, this would be especially so in the 90° case. Some unpublished experimental data obtained recently by Silsoe Research Institute suggested that the discharge coefficient might reach values as high as 0.75 in the presence of a high cross flow velocity. The effect of the opening depth (in the direction of flow) will also have had an effect. The change in pressure difference between openings for the open and sealed cases is another possible reason for the poor performance of the pressure difference method. The presence of openings in a building envelope were assumed to have little effect on the external pressure distribution. However, in Chapter 3 a change in pressure in the region around the ventilation opening was measured when openings were introduced. Detailed pressure measurement around ventilation openings would be required for further validation of this phenomenon.

6.3.2 Total Ventilation Rate Assessment

The total ventilation rate refers to the total ventilating airflow (effectively equal to the mass of air entering or leaving the ventilated space) and encompasses both mean and turbulent flows. In section 6.3.1, mean predicted ventilation rates were compared to measured values. In this section the mean ventilation rates are drawn together with the turbulent ventilation predictions described in Chapter 5 and an attempt at predicting the total ventilation is made. The total ventilation rate was measured experimentally using a tracer gas technique.

The tracer gas experiments described in detail in Chapter 3 are the only method through which it is possible to measure the total ventilation rate. It would be expected that when mean flows dominate a flow situation (as is the case for the 0° casse) that the mean ventilation predictions should be close to the total ventilation rate and turbulent ventilation contributions would be small. For the situation where the mean flows are lower (as in the 90° case) one would expect the mean flow predictions to become lower and turbulent predictions should dominate. It was shown in Chapter 3 that even when the pressure difference between ventilation openings was very low and mean predictions showed little ventilation taking place, experimental measurements proved that a significant ventilating air flow was occurring. Such cases prove the need for accounting for turbulent processes in wind driven ventilation predictions.

Although the tracer gas tests provide the only direct measure of the total ventilation taking place, a number of different methods are to be compared which culminate from measurements and predictions of mean and turbulent ventilation components. The methods from which the total ventilation rate will be assessed are:

1. Tracer gas measurements
2. Anemometry measurements plus pulsation flow

3. Pressure difference methods plus pulsation flow
4. CFD predictions plus pulsation flow (for 0° case only)

The two ventilation configurations required different approaches and combinations of the above techniques and hence they are to be considered individually in what follows.

6.3.2.1 0° wind direction

For the 0° wind direction, the total ventilation consists of the mean and pulsating components of flow. In Chapter 5 a time domain technique was introduced to account for the bulk unsteadiness of the ventilating flow due to large scale fluctuations in the wind, termed the broad banded ventilation. The broad banded mechanism is a large scale effect that is very much related to the mean flow. If the fluctuations of the total ventilation (as a result of the mean and broad banded mechanisms) are relatively small in comparison to the mean flow then it was shown in Chapter 5 that the broad banded flow is accounted for within the mean flow component.

Table 6.3 provides the calculated and measured total ventilation rates. Table 6.3 also includes the components necessary for the calculations. The calculation of the pulsating ventilation mechanism employed the frequency domain technique described in detail in Chapter 5.

Table 6.3 Total ventilation rates for 0° case

	Mean ventilation, $\overline{Q}/U_{ref}A$	**Pulsating ventilation,** $Q_{pulse}/U_{ref}A$	**Total ventilation** $\left(\overline{Q}+Q_{pulse}\right)/U_{ref}A$
Tracer gas	-	-	0.79
Anemometry	0.69	0.008	0.698
Pressure difference	0.483	0.008	0.491
CFD	0.648	0.008	0.656

The measured ventilation rate and the pulsating flow produce a total ventilation rate which sums to 88% of the total measured ventilation from tracer gas experiments. The pressure difference approach plus the pulsation flow only predicted 62% of the total whilst the CFD predictions plus the pulsation flow was found to account for 83% of the total ventilation.

6.3.2.2 90° Wind Direction

For the 90° wind direction where wind flows parallel to the planes of the ventilation openings, the calculation of the total ventilation rate is different from the 0° case. Here, the total ventilation rate is calculated from the mean component, broad banded component and the pulsating flow. In the 0° case, it was explained that the broad banded fluctuations were accounted for by the mean flow. This however, is not the case for the 90° configuration.

When ventilation openings are located in regions of similar pressure, the mean pressure difference between the openings is low and any attempt to predict the mean flow will be accordingly low. If in cases where the mean flows are low and the magnitude of the fluctuations of the flow are greater than mean (as was shown to be the case here in Chapter 5) then the broad banded fluctuations are not accounted for in the mean component and must be considered separately. It was demonstrated in Appendix A that the non-dimensional ventilation rate due to the mean and broad banded mechanisms is given by equation (5.3) which is repeated below for convenience.

$$Q_B = \overline{Q}\left(1+\frac{2\sqrt{2}}{\pi}\left(\frac{\sigma_Q}{\overline{Q}}\right)\sqrt{1-\frac{1}{2}\left(\frac{\overline{Q}}{\sigma_Q}\right)^2}\right) \tag{6.1}$$

Table 6.4 provides the measured and calculated total ventilation rates from the three techniques applied along with the relevant individual components required for any calculations.

Table 6.4 Total ventilation rates for 90° case

	Mean ventilation $\overline{Q}/U_{ref}A$	**rms ventilation** $\sigma_Q/U_{ref}A$	**Broad banded ventilation** $Q_B/U_{ref}A$	**Pulsating ventilation** $Q_{pulse}/U_{ref}A$	**Total ventilation** $\frac{(Q_B+Q_{pulse})}{U_{ref}A}$
Tracer gas	-	-	-	-	0.38
Anemometer	0.114	0.103	0.172	0.014	0.186
Pressure difference	0.095	0.165	0.231	0.014	0.245

The anemometer measured data and pulsating flow provide a total ventilation rate that only accounts for 49% of the total measured by tracer gas techniques. The pressure difference method produced an improved total ventilation that is 65% of the measured value. CFD predictions were not included as no mean flow was induced in this configuration. The very low prediction of the anemometer measurements is most likely to be caused by the flow reversal that was periodically shown to occur in Figure 5.2. As the flow changes direction, the mean value is adversely affected producing a

lower ventilation rate than would be measured from tracer gas experiments where flow in to or out of an opening always adds to the total ventilation.

6.4Summary

Numerous techniques for measuring and predicting the mean, turbulent and total wind driven ventilation have been detailed throughout this thesis with the results being brought together throughout this chapter.

The internal airflow patterns predicted computationally agreed favourably with the full-scale experiments. There were no obvious differences between the predictions and measurements for the 0° case which adds confidence when applying CFD to the simulation of wind driven ventilation flows. The most obvious short-coming in the application of CFD to this field was shown in the 90° case. When openings are located in regions of equal mean pressure, steady-state calculations predict no flow. In practice, turbulent fluctuations have been shown to drive significant airflows. The application of time dependent CFD simulations would help address this issue.

For the 0° case, where the wind was normal to the ventilation openings, the mean component of ventilation was found to be significantly greater than the fluctuating component. The mean ventilation rates predicted by CFD simulation compared well to the measured mean velocity integrated ventilation rate from anemometry data. The pressure difference method provided very poor mean flow predictions in this case. The total ventilation rate was under-predicted by all three techniques (anemometry, pressure difference method and CFD) when compared to the tracer gas results. The pressure difference method proved to be the poorest prediction of the methods tested. The problems related to this technique were due to a number of factors. These included, the application of inappropriate values of the discharge coefficient that did not account for flow direction (cross flows) or opening geometry (opening depth) and the effect of using pressures measured on a sealed structure and assuming that these pressures remain unaltered when ventilation openings were introduced. In order to allow for the effects of crossflow in the openings, an increase in discharge coefficient would provide a simple and convenient means of improving predictions in the 0° case.

The total ventilation rate calculations for the 0° case were made up from the sum of the mean and pulsating components. The broad banded ventilation component is accounted for within the mean flow since the mean flow is greater than the fluctuations. The under predictions of the total ventilation rates by all predictive techniques was not unexpected. In Chapter 2, three turbulent ventilation mechanisms were discussed however, within this work only the pulsating and broad banded (continuous) turbulent mechanisms have been accounted for. The third mechanism of eddy penetration (driven by unstable shear layers around ventilation openings) has been ignored. To date no technique for quantifying eddy penetration has been devised

hence its effect cannot be considered but must be acknowledged. This will help explain some of the discrepancies observed.

The pulsating flow was calculated to be responsible for only 1% of the total measured ventilation for the case. This pulsating flow would be expected to be low for this 0° case. With the mean flow being responsible for the majority of the ventilation, pulsating flow would be minimal.

In the 90° case the total ventilation was computed by accounting for the mean flow, broad banded component and the pulsating flow. Since the mean flow was low and the fluctuations large in comparison, the broad banded mechanism would not have been accounted for if the mean ventilation rate was used alone.

The total ventilation rate calculated from anemometer measurements (and the frequency domain calculation for pulsating flow) accounted for only 49% of the total measured from tracer gas tests. The main reason for this (as well as the difference by not accounting for eddy penetration) was the effect of flow reversal reducing the mean measured, velocity integrated ventilation rate. It would be expected however, for the broad banded component to be high but this did not make up the difference. The pressure difference produced an improved prediction accounting for 76% of the total ventilation. As with the 0° case, it is thought that an increased value of discharge coefficient would be appropriate to account for the cross component of flow. This, along with the omission of the eddy penetration will mean that an under prediction would be expected. The pulsating flow mechanism was predicted to be responsible for only 4% of the total ventilation. The 90° configuration would have been expected to produce a higher pulsating ventilation rate as turbulent mechanisms drive a higher proportion of flow than the 0° case. It is however, expected that pulsating flows would have greater significance in single opening enclosures or where openings are located closer together.

7. CONCLUSIONS AND FUTURE WORK

7.1 Introduction

In this chapter the conclusions from the research described throughout this thesis are set out. They are presented in the form of a list that is followed by recommendations for future work within this field.

7.2 Conclusions

7.2.1 Full-Scale Ventilation Experiments

The experiments were unique in the development of a full-scale, purpose built test structure for the measurement of wind induced ventilation. The test structure gave a unique control of the orientation relative to the incident wind angle through the construction of a turntable on which the structure was built. The location of the purpose built test structure provided a unique opportunity to make full-scale measurements without interference from nearby structures. The cubic structure has been investigated in numerous instances within wind tunnel investigations however, this is the first investigation that has provided full-scale data of a fundamental bluff body with respect to surface pressures and wind driven ventilation.

The use of a purpose built research structure allowed a number of methods to be applied for the prediction and measurement of wind induced ventilation to be compared. The techniques applied aimed to measure the mean, turbulent and total ventilation.

Mean ventilation rates were measured using anemometry data in the planes of ventilation openings integrated over the opening areas to produce a discharge (ventilation rate). Mean ventilation rates were predicted by the application of the steady-state pressure difference method. This method made use of external pressures measured at the ventilation openings when the openings were sealed. The technique is derived from the standard discharge equation for a single orifice and adapted to account for multiple openings.

The only method for the direct measurement of the total wind driven ventilation through a test space is tracer gas methods. In this research a constant injection method was utilised.

The major conclusions drawn from the full-scale wind induced ventilation results are as follows:

1. Measurement of external surface pressure distributions for the wind normal to the windward face of the cube showed the stagnation point was located approximately 66% to 75% of the way up the face and exhibited a peak non-dimensional pressure coefficient of 0.87. The pressure distribution over the roof for the normal wind direction showed a peak suction located close to the leading edge with peak negative pressure coefficient of –1.2. The leeward face exhibited negative pressure coefficients that remained almost constant up the face (pressure coefficient of approximately –0.3).

2. For a 45° incident wind direction (relative to the windward face), the peak pressure measured on the windward face decreased when compared to the normal wind direction. The peak negative pressure measured over the roof became slightly more negative (higher suction) although the recovery of pressure with downstream distance was more rapid. The pressures on the leeward face were again constant however, they were more negative than in the normal wind direction.

3. For an incident wind direction parallel to the plane of the ventilation openings, the total non-dimensional ventilation rate was measured to be approximately 50% of that measured with the wind normal to the plane of the openings. For the incident wind direction parallel to the plane of the ventilation openings, the measured mean ventilation rate (from anemometry data) was found to be approximately 16% of that measured with the wind normal to the plane of the openings. For an incident wind parallel to the plane of the ventilation openings, the mean ventilation rate from the pressure difference method was predicted to be only 20% of that predicted with the wind normal to the plane of the openings. The difference between mean measurements and predictions of ventilation and measurement of the total ventilation for the normal and parallel wind directions shows the significance of turbulent flow mechanisms when the mean flow was low.

4. For the incident wind direction normal to the plane of the ventilation openings, the steady-state pressure difference method significantly under-predicted the mean ventilation rate when compared to the measured mean ventilation rates (from anemometer techniques).

5. For the incident wind direction parallel to the plane of ventilation openings, the steady-state pressure difference method under-predicted the mean measured ventilation rate (from anemometry data) to a lesser degree than for the normal wind direction.

6. The under-prediction of the wind driven ventilation using the steady-state pressure difference method was attributed, in part, to the application of a standard discharge coefficient. The standard discharge coefficient was developed for steady flows through sharp-edged orifices for flows normal to the opening plane. In the test cases within this research the flow was far from steady and was not always normal to the opening planes. The openings also had a significant length

in the direction of flow. An increased value for the discharge coefficient would provide a convenient method to account for the effects of crossflow components and orifice depth.

7. The application of a standard discharge coefficient was questioned after the measurement of internal pressures showed significant difference between internal pressures at the inlet (windward opening) and outlet (leeward opening) for the wind normal to the ventilation openings. This suggested the presence of an internal pressure gradient that is not accounted for by the standard discharge coefficient. The standard discharge coefficient was developed for flow through a single orifice i.e. all pressure drop assumed to occur over a single opening.

8. The surface pressures close to ventilation openings were found to differ depending upon the presence of ventilation openings. When openings were present, pressures just above and below the windward face opening were higher than if the openings were sealed. This finding was another factor that effected the steady-state pressure difference predictions of ventilation. The pressure difference approach made use of pressures obtained on the test structure when ventilation openings were not present. Changes in the external pressure distribution around the openings was therefore another factor controlling the accuracy of the pressure difference method.

9. The techniques used to measure and predict mean ventilation rates all under-predicted the total ventilation rate measured through tracer gas investigations. This was found for wind directions both normal and parallel to the ventilation openings. This under-prediction was a result of the mean assessment techniques being incapable of accounting for the effects of turbulent flow mechanisms. The differences between measurements of mean and total ventilation rates have demonstrated the significance of turbulent flow mechanisms.

7.2.2 Computational Fluid Dynamics Simulations

The construction of the test structure provided a unique opportunity to validate CFD predictions of external and internal flow and pressure fields at full-scale for a fundamental wind engineering test case. A detailed investigation into the external predictions of the predicted pressure and velocity fields around a 6m test cube were used for comparison with experimental measurements for the evaluation of the most commonly used turbulence models.

The following conclusions can be drawn from the computational modelling techniques investigated throughout this research.

1. The standard k-ε turbulence model failed to predict the expected recirculation over the roof of the test structure that was modelled using the RNG k-ε model. This was due to the over-prediction of turbulent kinetic energy around the corner of the windward face and roof by the k-ε model leading to high levels of mixing

and the inability to predict the recirculating region. Turbulent kinetic energy levels were reduced around the frontal corner when the RNG k-ε model was used

2. Both the standard k-ε and RNG k-ε turbulence models predicted greater suction close to the leading edge of the roof of the cube than measured experimentally. However, the RNG model displayed significant improvement over the standard model.

3. The standard k-ε model was found to be inapplicable for modelling the flow around a bluff body such as the test cube. The improvements of the RNG model, through the incorporation of a strain related term in the dissipation of turbulent energy make it a significant improvement over the standard model.

4. Specification of boundary conditions is very important in any computational simulation. In the case of wind engineering, the velocity and turbulence profiles must be correctly defined if results are to be compared to full-scale situations.

5. External surface pressures were effected by surface roughness of the ground. The correct stipulation of ground surface roughness is important for experimental validation. An increase in surface roughness was found to lead to a corresponding increase in the peak surface pressure on the windward face of the structure. The increased retardation of flow at ground level of the greater surface roughness lead to pressures being reduced at lower levels for greater roughness. Pressures over the roof exhibited greater suction close to the leading edge for increased surface roughness. Correct definition of the surface roughness will have a direct impact on the comparison of computational and experimental data.

6. The quality of the computational grid is important in all CFD models. Ensuring that a model is grid independent is a necessary part of all studies. 116000 cells produced a grid independent solution to the test cube simulations in this research (when compared to the finest grid tested).

7. From the external flow simulations it was found that the RNG k-ε turbulence model provided the most accurate simulation of the external flow conditions around the test cube. This lead to the application of this turbulence model to wind driven ventilation modelling.

8. Predicted internal velocity profiles showed good agreement with those measured experimentally proving CFD a reliable tool for modelling such flows. The general flow structure within the internally ventilated space was well represented using CFD predictions.

9. For the 0° incident wind direction, the predicted mean ventilation rate agreed well with experimental measurements of mean ventilation. The prediction did however, exhibit under-prediction compared to total measured ventilation rates from tracer gas tests.

10. For the 90° incident wind direction, no wind driven ventilation was modelled. CFD within this research was undertaken using the time-averaged flow equations. This, coupled with the symmetry of the cubic test structure (for this

configuration), meant that the ventilation openings were located in regions of equal pressure. With no pressure differential between the openings, no ventilation flow was predicted. This highlights the problem of applying time-averaged CFD simulations for turbulence dominated flows with very low or zero mean pressure differentials.

7.2.3 Turbulent Ventilation Assessment

1. A time domain technique was developed by expansion of the steady-state pressure difference method to account for a fluctuating time series of pressure differences across ventilation openings. This enabled the technique to account for a broad banded frequency range of turbulent fluctuations analogous to the continuous unsteady ventilation mechanism.

2. The broad banded fluctuating ventilation predictions provided a measure of ventilation fluctuations over a wide range of frequencies, the majority of the energy of these would be at relatively low frequencies (corresponding to the maximum energy in the wind). These fluctuations correspond to large scale variations in direction and consequent changes in the flow pattern around the structure considered.

3. The broad banded ventilation mechanism can effectively be regarded as a modification of the mean ventilation. For the two opening enclosure investigated here, the total ventilation due to the mean and broad banded, fluctuating mechanisms together is given by the area beneath the ventilation time history divided by the length of the record.

4. For a two opening enclosure, the total ventilation due to the mean and broad banded mechanisms together is given by the area beneath the time history divided by the length of record. If the ventilation time history does not change sign i.e. the magnitude of the fluctuations is less than the mean, this corresponds simply to the mean ventilation rate. In this case, the ventilation rate produced through the mean and broad banded fluctuations is equal to the mean flow alone.

5. If the fluctuations in the ventilating flow are greater than the mean ventilation, there will be some rectification of the ventilation time series around zero and the total ventilation rate due to the mean and broad banded flow mechanisms will be in excess of the mean value. In this case the broad banded ventilation rate must be accounted for alongside the mean ventilation.

6. The consequence of the previous two conclusions is that for the incident wind normal to the ventilation openings, the broad banded ventilation mechanism is accounted for through the mean component alone. However, for the wind parallel

to the ventilation openings the broad banded ventilation component must be accounted for alongside the mean flow.

7. A frequency domain method introduced a novel technique for predicting the contribution of the unsteady pulsating ventilation mechanism. The method utilised the technique of proper orthogonal decomposition. The transformation of a proper orthogonal decomposition of surface pressure around a structure produced the contributions of different modes of pressure to pulsating ventilation.

8. The proper orthogonal decomposition of the external surface pressure field around the test cube produced a number of pressure modes, the sum of which form the total fluctuating pressure field. Pressure mode 1 was found to resemble the mean external surface pressure distribution. The mechanism responsible for mode 1 was thought to be longitudinal fluctuations in the incoming wind.

9. The first three modes of fluctuating pressure were found to contain the vast majority of the total fluctuating energy. This meant that the lower pressure modes could be ignored when transforming the fluctuating pressures to account for pulsating ventilation.

10. For the wind normal to the ventilation openings, ventilation modes 1 and 2 were found to contribute equally (approximately 50% each) to the pulsating ventilation whilst mode 3 made a negligible contribution.

11. For the wind parallel to the ventilation openings, ventilation mode 1 made a far more significant contribution to the pulsating ventilation (86%) whilst mode 2 made no contribution and mode 3 was responsible for the remaining 14%.

12. For both 0° and 90° wind directions, the contribution of the pulsating ventilation flow mechanism was predicted to be small. However, the relative contribution of pulsating flow to the total ventilation for the 90° wind direction was more significant than for the 0° case . This would be expected since pulsating flows are related to flows being driven by high frequency pressure fluctuations across openings with low pressure differentials.

7.2.4 Total Ventilation Assessment

1. The total ventilation was calculated from a number of combinations of measured and predicted mean and turbulent ventilation rates. The choice of combination was different and depended upon the incident wind direction relative to the ventilation openings.

2. By incorporating the mean and turbulent predicted ventilation rates together, a significant improvement in ventilation predictions was gained when compared to mean predictions alone.

3. The total predicted ventilation rates were all found to be below the total measured through tracer gas experiments. This was because the contribution of the turbulent mechanism of eddy penetration was not accounted for throughout this work.

7.3Further Work

Research is often a slow process and many unsuccessful attempts and investigations often precede the unearthing of ground breaking discoveries. That is why questions arising from research are as important as the conclusions that are drawn. These questions lead to the development of further work, which could be undertaken for further validation, or investigation of a hypothesis or technique. The conclusions of this research were discussed in the previous section, here the ideas for developments from the research are outlined.

1. With respect to experimental development, the test cube provides a unique opportunity for further investigation. Extensive investigation into appropriate discharge coefficients for ventilation openings located on building surfaces would be of significant benefit in the application of steady-state pressure difference predictions.

2. Further parametric experimental investigations into the effects of ventilation position, configuration and opening area would be another area for the use of the test cube.

3. It would be a worthwhile undertaking to further measure external parameters around the test structure. Flow details such as separation and reattachment of flow over the roof would help the understanding of the flow mechanisms and provide further data for the validation of computational investigations.

4. Detailed pressure measurements when ventilation openings are open and sealed would help clarify the effect of ventilation openings on external pressure distributions around the openings. This would be useful in the improvement of the pressure difference technique.

5. With respect to computational simulations, the development of transient, time-dependant simulations would help to extend the capabilities of CFD techniques in predicting total ventilation rates and accounting for turbulent ventilation mechanisms.

6. For a more rigorous test of the frequency domain method for predicting pulsating flow, the investigation of a ventilation opening configuration where pulsating flows dominate the ventilation process would provide a good validation exercise.

7. The difference found between the total predicted ventilation rates and total measured ventilation rates was attributed to the eddy penetration mechanism. A method for accounting for this ventilation process would a worthwhile exercise.

8. BIBLIOGRAPHY

Abbott, M. Basco, D. (1989), *Computational Fluid Dynamics- an introduction for engineers*, Longman Scientific & Technical, New York.

Abe, K., Nagano, Y., Kondoh, T. (1993), Numerical prediction of separating flow with a modified low-Reynolds number k-ε model, *Journal of Wind Engineering and Industrial Aerodynamics*, Vol. 46 & 47, pp. 83-94.

Afonson, C., Maldonado, E., Skaret, E. (1986), Single tracer gags method to characterise multi-room air exchanges, *Energy and Buildings*, vol. 9, no. 4, pp.273-280.

Algazi, V.R., Sakrison, D.J. (1969) On the optimality of the Karhunen-Loeve expansion, *IEEE Trans. Inform. Theory*, vol.15, pp.319-21.

Andrews, C.A., Davies, J.M., Schwartz, G.R. (1967) Adaptive data comp*ression*, *Proc. IEEE*, vol.55, pp.267-277.

Armitt, J. (1968), *Eigenvector analysis of pressure fluctuations on the West Burton Instrumented Cooling Tower*, Central Electricity Research Laborotories, Report RD/LN114/68.

Awbi, H. B. (1989), Application of computational fluid dynamics in room ventilation, *Building and Environment*, vol.24, no.1, pp.73-84.

Awbi, H. B. (1991), *Ventilation of Buildings*, E & F Spon, London.

Aynsley, R. (1988), A resistance approach to estimating airflow through buildings with large openings due to wind, *ASHRAE Transactions*, vol. 94, pp. 1661-1669.

Aynsley, R., Melbourne, W., Vickery, B. (1977), *Architectural aerodynamics*, Applied Sciences, London.

Baker, A. J., Subrata, R., Kelso, R. M. (1994), CFD experiment characterisation of airborne contaminant transport for two practical 3-D room airflow fields, *Building and Environment*, vol.29, No. 3, pp. 253-259.

Baker, A. J., Williams, P.T., Kelso, R. M. (1994), Development of a robust finite element CFD procedure for predicting indoor room air motion, *Building and Environment*, Vol.29, No.3, pp261-273.

Baker, C. J. (1997), *Analysis of the surface pressure field on buildings using the technique of orthogonal modal decomposition*, Internal Report, Department of Civil Engineering, University of Nottingham.

Baker, C., J. (1998), The use of the technique of orthogonal modal decomposition in understanding the unsteady wind driven ventilation through buildings, *Proceedings of the United Kingdom Wind Engineering Conference*, Bristol.

Baker, C., J. (1999), Aspects of the use of the technique of orthogonal decomposition of surface pressure fields, *Proceedings of the 10th International Conference on Wind Engineering*, Copenhagen, pp. 393-400.

Basara, B., Younis, B. (1992), Progress in the prediction of turbulent wind loading on buildings, *Journal of Wind Engineering and Industrial Aerodynamics*, vol. 41-44, pp. 2863-2874.

Berkooz, G., Holmes, P., Lumley, J. (1993), The proper orthogonal decomposition in the analysisof turbulent flows, *Annual Review of Fluid Mechanics*, vol. 25, pp. 539-575.

Berkooz, G., Elezgaray, J., Holmes, P., Lumley, J. (1994), The proper orthogonal decomposition, wavelets and modal approaches to the dynamics of coherent structures, *Applied Scientific Research*, vol. 53, pp. 321-338.

Best, R., Holmes, J. (1983), Use of eigenvalues in the covariance integration method for determination of wind load effects, *Journal of Wind Engineering and Industrial Aerodynamics*, Vol. 13, pp. 359-370.

Bienkiewicz, B., Ham, H., Sun, Y. (1993), Proper orthogonal decomposition of roof pressure, *Journal of Wind Engineering and Industrial Aerodynamics*, Vol. 50, pp. 193-202.

Bienkiewicz, B., Tamura, Y., Ham, H., Ueda, H., Hibi, K. (1995), Proper orthogonal decomposition and reconstruction of multi-channel roof pressure, *Journal of Wind Engineering and Industrial Aerodynamics*, vol. 54/55, pp. 369-381.

Bonnet-Heude, N., Marchal, P., Favre-Marinet, M., Arroyo, G. (1996), Estimation of flow through porous and perforated plates with CFX and scale model validations, *Third CFX International Users Conference*, London, pp.589-600.

Boulard, T., Baille, A. (1995), Modelling of air exchange rate in a greenhouse equipped with continuous roof vents, *Journal of Agricultural Engineering Research*, vol. 61, pp.37-48.

Boulard, T., Draoui, B. (1995), Natural ventilation of a greenhouse with continuous roof vents: Measurement and data analysis, *J. Agricultural Engineering Resources*, vol.61, pp.27-36.

Bradshaw, P. (1971), *An introduction to turbulence and its measurement*, Pergamon Press, Oxford.

BRE (1994), *Natural ventilation in non-domestic buildings*, BRE Digest:399, BRE, England.

Bruce, J. M. (1978), Natural convection through openings and its application to cattle building ventilation, *J. Agricultural Engineering and Resources*, vol.23, pp.151-167.

British Standards Institution (1991), *BS 5925: 1991 Code of practice for Ventilation principles and designing for natural ventilation*.

Castro, I. P., Robins, A. G. (1977), The flow around a surface-mounted cube in uniform and turbulent streams, *Journal of Fluid Mechanics*, vol.79, part 2, pp.307-335.

Cermak, J.E., Poreh, M., Peterka, J. A., Ayad, S. S. (1984), Wind Tunnel Investigations of Natural Ventilation, *Journal of Transportation Engineering*, vol. 110, pp.67-81.

Chadwick, A., Morfett, J. (1994), *Hydraulics in civil and environmental engineering*, Second Edition, E & F Spon, London.

Chaplin, G. (1994), *Predicting ventilation in gust-driven flows*, Report number: FR94019, Department of Civil Engineering, University of Nottingham.

Chen, Q., Chao, N. (1997), Comparing turbulence models for buoyant plume displacement simulation, *Indoor and built environment*, vol. 6, no. 3, pp. 140-149.
Cherry, N., Hillier, R., Latour, M. (1984), Unsteady measurements in a separating and reattaching flow, *Journal of Fluid Mechanics*, vol. 144, pp.13-46.

Choi, H, Albright, L, Timmons, M, Warhaft, Z. (1988), An application of the k-ε turbulence model to predict air distribution in a slot-ventilated enclosure, *Transactions of the ASAE*, pp. 1804-1813.

Choiniere, Y., Tanaka, H., Munroe, J.A., Suchorski-Tremblay, A. (1992), Prediction of wind induced ventilation for livestock housing, *Journal of Wind Engineering and Industrial Aerodynamics*, vol.41-44, pp.2563-2574.

Cook, N.J. (1990), *The designers guide to wind loading of building structures Part 1: Static structures*, Butterworths, London.

Cook, N.J. (1990), *The designers guide to wind loading of building structures Part 2: Static structures*, Butterworths, London.

Cooper, P., Linden, P. (1996), Natural ventilation of an enclosure containing two buoyancy sources, *Journal of Fluid Mechanics*, vol. 311, pp. 153-176.

Crommelin, R. D., Vrins, E. M. (1988), Ventilation through a single opening in a scale model, *Air Infiltration Review*, vol.9, no.3, pp11-15.

Dalley, S., Baker, C.J., Yang, X., Kettlewell, P., Hoxey, R. (1996), An investigation of the aerodynamic and ventilation characteristics of poultry transport vehicles: Part 3, internal flow field calculations, *J. Agricultural Engineering Resources*, vol.65, pp.115-127.

Dalley., S. (1996), Surface spectra on a model of the Silsoe structures building and comparison with full-scale, *Journal of Wind Engineering and Industrial Aerodynamics*, Vol.60, pp. 177-187.

Demuren, A. (1993), Influence of the turbulence model in calculations of flow over obstacles with second moment closure, *Journal of Wind Engineering and Industrial Aerodynamics*, Vol. 46 &47, pp. 95-104.

Dutt, A.J., de Dear, R.J., Krishnan, P. (1992), Full scale and model investigation of natural ventilation and thermal comfort in a building, *Journal of Wind Engineering and Industrial Aerodynamics*, vol.41-44, pp.2599-2609.

Ernest, D. R., Bauman, F. S., Arens, E. A. (1992), The effects of external wind pressure distributions on wind induced air motion in side buildings, *Journal of wind engineering and industrial aerodynamics*, vol41-44, pp.2539-2550.

Etheridge, D. W. (1998), *Unsteady flow effects in natural ventilation design-mean flow rates*, Internal report, School of building technology, University of Nottingham.

Etheridge, D. W., Nolan, J. A. (1979), Ventilation measurements at model scale in a turbulent flow, *Building and Environment*, vol.14, pp33-64.

Etheridge, D., Sandberg, M. (1996), *Building Ventilation: Theory and Measurement*, British Gas Research and Technology, Wiley and Sons.

Fernandez, J. E., Bailey, B. J. (1992), Measurement and prediction of greenhouse ventilation rates, *Agricultural and Forest Meteorology*, vol.58, pp.229-245.

Ferziger, J. (1993), Simulation of complex turbulent flows: recent advances and prospects in wind engineering, *Journal of Wind Engineering and Industrial Aerodynamics*, vol. 46 & 47, pp. 195-212.

Ferziger, J.H., Peric, M. (1997), *Computational Methods for Fluid Dynamics*, Springer, Berlin.

Feustel., H, Dieris., J. (1992), Survey of airflow models for multi-zone structures, *Energy and Buildings*, vol.18, no.2, pp.79-100.

Garratt, J. R. (1992), *The atmospheric boundary layer*, Cambridge University Press, Cambridge.

Gaskell, P.H., Lau, A.K.C. (1988), *Curvature-compensated convective transport: Smart, A new boundedness preserving transport algorithm*, International journal for numerical methods in fluids, pp.617-641.

Gay, D.H., Ray, W.H. (1986), Identification and control of linear distributed parameter systems through the use of experimentally determined singular functions, *Proc. IFAC Symp. Control of Distributed Parameter Systems*, LA, CA, pp.173-179.

Ghazi, M., Mohsen, M., Olwi, I. (1990), Comparitive study of airflow in and around buildings, *Experiments in Fluids*, vol. 9, no. 4, pp. 235-237.

Gill Instruments, *3 Axis research ultrasonic anemometer: Product specification*, Issue 4.

Haghighat, F., Fazio, P., Rao, J. (1990), A procedure for measurement of ventilation effectiveness in residential buildings, *Building and Environment*, vol.25, no.2, pp.163-172.

Haghighat, F., Rao, J., Fazio, P. (1991), The influence of turbulent wind on air change rates- a modelling approach, *Building and Environment*, vol.26, no.2, pp.95-109.

Haghighat, F., Rao, J., Riberon, J. (1992), Modelling fluctuating airflow through large openings, *Ventilation for Energy Efficiency and optimum Indoor Air Quality*, 13th AIVC Conference, Paper 6, pp.77-85, France.

Harris, R.I. (1990), The propagation of internal pressures in buildings, *Journal of Wind Engineering and Industrial Aerodynamics*, vol.34, pp.169-184.

Ho, T., Davenport, A., Surry, D. (1995), Characteristic pressure distribution shapes and load repetitions for the wind loading of low building roof panels, *Journal of Wind Engineering and Industrial Aerodynamics*, Vol. 57, pp. 261-279.

Holmes, J. D. (1990), Analysis and synthesis of pressure fluctuations on bluff bodies using eigenvectors, *Journal of wind engineering and industrial aerodynamics*, vol. 33, pp. 219-230.

Holmes, J. D. (1997), Eigenvector modes of fluctuating pressure on low rise building models, *Journal of wind engineering and industrial aerodynamics*, vol. 69-71, pp.607-707.

Holmes, J., Sankaran, R., Kwok, K., Syme, M. (1997), Eigenvector modes of fluctuating pressures on low-rise building models, *Journal of Wind Engineering and Industrial Aerodynamics*, Vol. 69-71, pp. 697-707.

Jeong, S., Bienkiewicz, B. (1997), Application of autoregressive modelling in proper orthogonal decomposition of building wind pressure, *Journal of Wind Engineering and Industrial Aerodynamics*, Vol. 69-71, pp. 685-695.

Jozwiak, R., Kacpryk, A., Zuranski, J.A. (1995), Wind tunnel investigations of inteference effects on pressure distribution on a building, *Journal of Wind Engineering and Industrial Aerodynamics*, vol.57, pp.159-166.

Jozwiak, R., Kacpryk, A., Zuranski, J.A. (1996), Influence of wind direction on natural ventilation of apartment buildings, *Journal of Wind Engineering and Industrial Aerodynamics*, vol.60, pp.167-176.

Kareem, A., Cermak, J. (1984), Pressure fluctuations on a square building model in boundary layer flows, *Journal of Wind Engineering and Industrial Aerodynamics*, Vol. 16, pp. 17-41.

Kato, S., Murakami, S., Mochida, A., Akabayashi, S., Tominaga, Y. (1992), Velocity-pressure field of cross ventilation with open windows analysed by wind tunnel and numerical simulation, *Journal of wind engineering and Industrial Aerodynamics*, vol.41-44, pp.2575-2586.

Kato, S., Murakami, S., Mochida, A., Akabayashi, S., Tominaga, Y. (1992), Velocity-pressure field of cross ventilation with open windows analysed by wind tunnel and numerical simulation, *Journal of wind engineering and Industrial Aerodynamics*, vol.41-44, pp.2575-2586.

Kindangen, J., Krauss, G., Depecker, P. (1997), Effects of roof shapes on wind-induced air notion inside buildings, *Building and Environment*, vol.32, no.1, pp.1-11.

Kikucji, H., Tamura, Y, Ueda, H., Hibi, K. (1997), Dynamic wind pressures acting on a tall building model – proper orthogonal decomposition, *Journal of Wind Engineering and Industrial Aerodynamics*, Vol. 69-71, pp.631-646.

Klobut, K., Siren, K. (1994), Airflows measured in large openings in a horizontal partition, *Building and Environment*, vol.29, no.3, pp.325-335.

Kurabuchi., T, Kusuda. (1987), T, Numerical prediction for indoor air movement, *ASHRAE Journal*, pp.26-30.

Laurence, D. (1993), Modelling flows around bluff bodies by Reynolds averaged equations, *Journal of Wind Engineering and Industrial Aerodynamics*, Vol. 46 & 47, pp.53-68.

Lee, B. (1975), The effect of turbulence on the surface pressure field of a square prism, *Journal of Fluid Mechanics*, vol. 69, pp. 263-282.

Leschziner, M. (1993), Computational modelling of complex turbulent flow-expectations, reality and prospects, *Journal of wind engineering and industrial aerodynamics*, vol. 46 & 47, pp.37-51.

Liu, H., Saathof, P.J. (1981), Building internal pressure: Sudden change, *Journal of the Engineering Mechanics Division*, pp.309-321.

Liu, F., Wen, J.X., Karayiannis, T.G., Matthews, R.D. (1996), Simulations of room fire behaviours using CFX, *Third CFX International Users Conference*, London, pp.385-391.

Lumley, J. (1996), *Simulation and Modelling of Turbulent Flows*, Oxford University Press.

Malinowski, H. K. (1971), Wind effect on the air movemetn inside buildings, *3rd International conference on Wind on Buildings and Structures*, Tokyo, pp.125-134.

Manson, J., Wallis, S. (1997), Accuracy characteristics of traditional finite volume discretisations for unsteady computational fluid dynamics, *Journal of computational physics*, vol. 132, no. 1, pp.149-153.

Maruyama, T. (1992), Numerical simulation of boundary layer wind tunnel, *Journal of Wind Engineering and Industrial Aerodynamics*, vol.41-44, pp.2827-2838.

Massey, B. S. (1989), *Mechanics of fluids*, Sixth edition, Chapman & Hall, London.

Matthews, E.H., Rousseau, P.G. (1994), A new integrated design tool for naturally ventilated buildings part 1: Ventilation model, *Building and Environment*, vol.29, no.4, pp.461-471.

Miguel, A. F., van de Braak, N. J., Silva, A. M., Bot, G. P. (1998), Physical modelling of natural ventilation through screens and windows in greenhouses, *J. agricultural engineering resources*, vol. 70, pp.165-176.

Mokhtarzadeh-Dehghan, M.R., El Telbany, M.M.M., Reynolds, A. (1990), Transfer rates in single sided ventilation, *Building and Environment*, vol.25, no.2, pp.155-161.

Murakami, S. (1993), Comparison of various turbulence models applied to a bluff body, *Journal of wind engineering and Industrial Aerodynamics*, vol.46 & 47, pp 21-36.

Murakami, S., Kato, S. (1989), Numerical and experimental study on room airflow-3D predictions using the k-ε turbulence model, *Building and Environment*, vol.24, no.1, pp85-97.

Murakami, S., Mochida, A., Hayashi, Y., Sakamoto, S. (1992), Numerical study on velocity-pressure fields and wind forces for bluff bodies by k-ε, ASM, LES, *Journal of wind engineering and industrial aerodynamics*, vol.41-44, pp.2841-2852.

Murakami, S. (1997), Overview of turbulence models applied in CWE-1997, *2nd EACWE*, Italy, pp.3-23.

Murakami, S., Mochida, A., Ooka, R., Kato, S., Izuka, S (1996), Numerical prediction of flow around a building with various turbulence models: Comparison of k-ε, EVM, ASM, DSM and LES, *ASHRAE Transactions*, vol.102, no.1, pp.741-753.

Narasaki, M., Yamanaka, T., Higuchi, M. (1989), Influence of turbulent wind on the ventilation of an enclosure with a single opening, *Environment International*, vol.15, pp.627-634.

Ohba, M. (1993), Study on three-dimensional characteristics of natural ventilation in half enclosed buildings using video imaging equipment, *Journal of wind engineering and industrial aerodynamics*, vol.46-47, pp.831-836.

Owczarek, E. (1996), Fires in tunnels: Study of the impact of various parameters on the critical ventilation speed, *Third CFX International Users Conference*, London, pp.225-244.

Papadakis, G., Mermier, M., Meneses, J., Boulard, T. (1996), Measurement and analysis of air exchange rates in a greenhouse with continuous roof and side openings, *J. agricultural engineering and resources*, vol.63, pp219-228.

Papoulis, A. (1965), *Probability, Random variables and stochastic processes*, McGraw-Hill, New York.

Parameswaran, S., Kiris, I., Sun, R., Gleason, M. (1993), Flow structure around a 3D bluff body in ground proximity: A computational study, *Journal of wind engineering and industrial aerodynamics*, vol.46-47, pp.791-800.

Paterson, D.A. (1993), Predicting r.m.s. pressures from computed velocities and mean pressures, *Journal of Wind Engineering and Industrial Aerodynamics*, vol.46-47, pp.431-437.

Pearce, J., Qasim, A., Maxwell, T., Paramesawaran, S. (1992), A computational study of coherent wake structures behind 2-D bluff bodies, *Journal of Wind Engineering and Industrial Aerodynamics*, vol. 41-44, pp. 2853-2861.

Pearson, C. C., Owen, J. E. (1994), The resistance to airflow of farm building ventilation components, *J. Agricultural Engineering Resources*, vol.57, pp.53-65.

Perera, M, Gilham, A., Clements-Croone, T. (1996), Natural ventilation in the United Kingdom: Design issues for commercial and public buildings, *Proc. CIBSE A: Building Services Engineering Research Technology*, vol 17 (1), pp.1-5.

Peterka, J, Cochran, L, Pielke, R. (1996), Progress in modelling external atmospheric flows around buildings, *ASME, Fluids Engineering Division*, vol.238, no.3, pp 535-539.

Potter, N.J. (1979), Effect of fluctuating wind pressures on natural ventilation, *ASHRAE Transactions*, vol.85, pp.445-457.

Preisendorfer, R. W. (1988), *Principal component analysis in meteorology and oceanography*, Elsevier, Amsterdam.

Randall, J. M., Battams, V. A. (1979), Stability criteria for airflow patterns in livestock buildings, *J. agricultural Engineering Resources*, Vol.24, pp. 361-374.

Randall, J. M., Patel, R. (1994), Thermally induced ventilation of livestock transporters, *Journal of Agricultural Engineering*, vol. 57, pp. 109-107.

Reynolds, A. (1997) A Langrangian stochastic model for particle trajectories in non-Gaussian turbulent flows, *Fluid Dynamics Research*.

Riberon, J., Bienfait, D., Barnaud, G., Villain, J. (1990), Effects of wind pressure fluctuations on air movement inside buildings, *11th AIVC Conference*, Belgirate, Italy.

Richards, P., Hoxey, R. (1992), Computational and wind tunnel modelling of mean wind loads on the Silsoe Structures Building, *Journal of Wind Engineering and Industrial Aerodynamics*, vol.41-44, pp.1641-1652.

Richards, P., Hoxey, R. (1993), Appropriate boundary conditions for computational wind engineering models using the k-ε turbulence model, , *Journal of Wind Engineering and Industrial Aerodynamics*, vol.46 & 47, pp.145-153.

Richardson, G. M., Hoxey, R. P., Robertson, A. P., Short, J. L. (1995), The Silsoe Structures Building: The completed experiment part 1. *Wind Engineering Retrospect and Prospect: Papers from the 9th International Conference*, vol. 3.

Roache, P. (1997), Quantification of uncertainty in computational fluid dynamics, *Annual Review of Fluid Mechanics*, vol. 29, pp. 123-160.

Rosenfield, A., Kak, A. C. (1982), *Digital Picture Processing*, New York.

Rousseau, P.G., Matthews, E.H. (1994), A new integrated design tool for naturally ventilated buildings part 2: Integration and application, *Building and Environment*, vol.29, no.4, pp.473-484.

Selvam., R. (1996), Computation of flow around Texas Tech building using k-ε and Kato-Launder k-ε turbulence model, *Engineering Structures*, Vol.18, no.11, pp.856-860.

Snykers, WA. (1970), Wind tunnel studies of the flow through rectangular openings with application to natural ventilation of buildings, *MSc thesis*, University of Pretoria, South Africa.

Speziale, C., Gatski, T. (1997), Analysis and modelling of anisotropies in the dissipation rate of turbulence, *Journal of Fluid Mechanics*, vol. 344, pp. 155-180.

Speziale, C., Ngo, T. (1988), Numerical solution of flow past a backward facing step using a nonlinear k-ε turbulence model, *International Journal of Engineering Science*, vol. 26, no. 10, pp. 1099-1112.

Sreenivasan, K., Antonia, R. (1997), The phenomenology of small-scale turbulence, *Annual Review of Fluid Mechanics*, vol. 29, pp. 435-472.

Stathopoulos, T, Baskaran, B, Computer simulation of wind environmental conditions around buildings, *Engineering Structures*, Vol.102, pp.741-753.

Shrestha, G., Cramer, C., Holmes, B., Kammel, D. (1993), Wind-induced ventilation of an enclosed livestock building, *American Society of Agricultural Engineers*, vol. 36, no. 3, pp. 921-932.

Surry, D. (1982), Consequences of distortions in the flow including mismatching scales and intensities of turbulence, *Wind tunnel modelling for civil engineering applications*, (Ed: Reinhold T A), Cambridge University Press, Cambridge, pp. 137-185.

Tamura, Y., Ueda, H., Kikuchi, H, Hibi, K., Suganuma, S., Bienkiewicz, B. (1997), Proper orthogonal decomposition study of approach wind-building pressure correlation, *Journal of Wind Engineering and Industrial Aerodynamics*, Vol. 72, pp. 421-431.

Vickery, B.J. (1991), Comments on "the propagation of internal pressures in buildings" by R.I. Harris, *Journal of Wind Engineering and Industrial Aerodynamics*, vol.37, pp.209-212.

Woods, A.R., Blackmore, P.A. (1995), The effect of dominant openings and porosity on internal pressures, *Journal of wind engineering and industrial aerodynamics*, vol.57, pp.167-177.

Yamamoto, T., Ensor, D.S., Sparks, L.E. (1994), Evaluation of ventilation performance for indoor space, *Building and environment*, vol.29, no.3, pp.291-296.

Yuguo, L., Holmberg, S. (1994), General flow and thermal boundary conditions in indoor air flow simulation, *Building and Environment*, vol.29, no.3, pp.275-281.

Zhan, Y.G., Huber, A.H., Arya, S.P.S., Snyder, W.H. (1993), Numerical simulation to determine the effects of incident wind shear and turbulence level on the flow around a building, *Journal of wind engineering and industrial aerodynamics*, vol.46-47, pp.129-134.

9. APPENDIX A

CALCULATING THE SUM OF MEAN AND BROAD BANDED VENTILATION

Consider the ventilation rate to be represented by a sinusoidal fluctuation of positive mean that becomes negative for the period shown in Figure A.1. Although there is a period where the ventilation rate becomes negative, in a two opening enclosure this still represents air exchange between the internal and external environment and hence is an addition to the total ventilation.

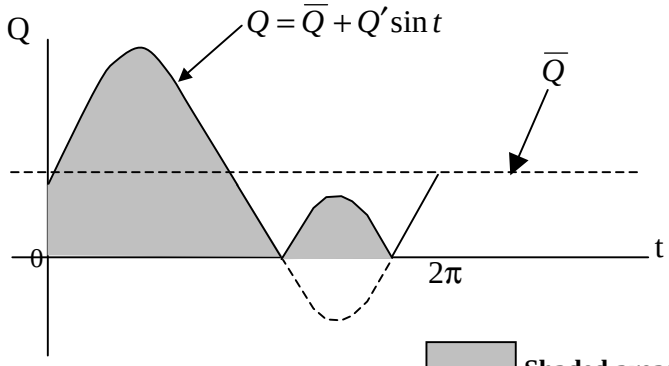

Figure A.1 Sinusoidally fluctuating ventilation due to mean and broad banded mechanisms

In order to calculate the total ventilation rate from Figure A.1 and to ensure the negative region adds to the ventilation, this section must be taken as a positive ventilation. Therefore the sum of the mean and broad banded ventilation, Q_B, is found through the following method.

$$Q = \overline{Q} + Q' \sin t \tag{A.1}$$

$$Q = 0 \quad when \quad t = \frac{3\pi}{2} \pm \tau$$

therefore,

$$\frac{-\overline{Q}}{Q'} = \sin\left(\frac{3\pi}{2} - \tau\right) \quad = -\cos\tau \tag{A.2}$$

$$\tau = \cos^{-1}\left(\frac{\overline{Q}}{Q'}\right) \tag{A.3}$$

and,

$$\frac{-\overline{Q}}{Q'} = \sin\left(\frac{3\pi}{2} + \tau\right) \quad = \sin\frac{3\pi}{2}\cos\tau = -\cos\tau \tag{A.4}$$

$$\tau = \cos^{-1}\left(\frac{\overline{Q}}{Q'}\right) \tag{A.5}$$

Thus the total ventilation Q_B is given by

$$2\pi.Q_B = \int_0^{\frac{3\pi}{2}-\tau}\left(\overline{Q} + Q'\sin t\right)dt + \int_{\frac{3\pi}{2}+\tau}^{2\pi}\left(\overline{Q} + Q'\sin t\right)dt - \int_{\frac{3\pi}{2}-\tau}^{\frac{3\pi}{2}+\tau}\left(\overline{Q} + Q'\sin t\right)dt \tag{A.6}$$

$$\begin{aligned} &= \left(\frac{3\pi}{2} - \tau\right)\overline{Q} - Q'\left(\cos\left(\frac{3\pi}{2} + \tau\right) - 1\right) + \left(2\pi - \frac{3\pi}{2} - \tau\right)\overline{Q} \\ &\quad - Q'\left(1 - \cos\left(\frac{3\pi}{2} + \tau\right)\right) - \left(\frac{3\pi}{2} + \tau - \frac{3\pi}{2} + \tau\right)\overline{Q} \\ &\quad + Q'\left(\cos\left(\frac{3\pi}{2} + \tau\right) - \cos\left(\frac{3\pi}{2} - \tau\right)\right) \end{aligned} \tag{A.7}$$

$$= \overline{Q}.2\pi + Q'\begin{pmatrix} -\cos\left(\frac{3\pi}{2}.\tau\right)+1-1+\left(\frac{3\pi}{2}+\tau\right)+\cos\left(\frac{3\pi}{2}+\tau\right) \\ -\cos\left(\frac{3\pi}{2}-\tau\right) \end{pmatrix} \quad \text{(A.8)}$$

$$= 2\pi\overline{Q} + 2Q'\left(\cos\left(\frac{3\pi}{2}+\tau\right)-\cos\left(\frac{3\pi}{2}-\tau\right)\right) \quad \text{(A.9)}$$

$$= 2\pi\overline{Q} + 2Q'\left(-\sin\frac{3\pi}{2}\sin\tau-\sin\frac{3\pi}{2}\sin\tau\right) \quad \text{(A.10)}$$

$$= 2\pi\overline{Q} + 4Q'\sin\tau \quad \text{(A.11)}$$

$$= 2\pi\overline{Q} + 4Q'\sqrt{1-\left(\frac{\overline{Q}}{Q'}\right)^2} \quad \text{(A.12)}$$

Thus

$$\begin{aligned} Q_B &= \overline{Q} + \frac{2Q'}{\pi}\sqrt{1-\left(\frac{\overline{Q}}{Q'}\right)^2} \\ &= \overline{Q}(1+\frac{2}{\pi}\frac{Q'}{\overline{Q}}\sqrt{1-\left(\frac{\overline{Q}}{Q'}\right)^2} \end{aligned} \quad \text{(A.13)}$$

Now the fluctuating ventilation, Q', is related to the standard deviation, σ_Q, by

$$Q' = \sqrt{2}\sigma_Q \quad \text{(A.14)}$$

Therefore the mean plus broad banded ventilation, Q_B, can be calculated from

$$Q_B = \overline{Q}\left(1+\frac{2\sqrt{2}}{\pi}\left(\frac{\sigma_Q}{\overline{Q}}\right)\sqrt{1-\frac{1}{2}\left(\frac{\overline{Q}}{\sigma_Q}\right)^2}\right) \quad \text{(A.15)}$$

10. APPENDIX B

MANIPULATION OF FLUCTUATING PRESSURE COEFFICIENT COVARIANCE

In POD (as in modal analysis) the fluctuating component of the pressure coefficient can be written as a sum of a series of dimensionless modal functions

$$C_p(x,t)' = T_1(t)P_1(x) + T_2(t)P_2(x)..... = \sum_{k=1,n} T_k(t)P_k(x) \tag{B.1}$$

where $P_1(x)$, $P_2(x)$ and $P_k(x)$ are modal pressure fields (individual distributions around the surface of the building), $T_1(t)$, $T_2(t)$ and $T_k(t)$ etc are modal time functions and the subscript k refers to mode numbers. Armitt (1968) assumed that

c) modal time functions are uncorrelated

$$\overline{T_j(t)T_k(t)} = 0, \ if \quad j \neq k \tag{B.2}$$

or

$$\overline{T_j(t)T_k(t)} = \overline{T_k(t)^2}, \ \ if \quad j = k \tag{B.3}$$

where the overbar denotes a time average and the subscripts j and k are individual mode numbers.

d) modal spatial functions are orthogonal

$$\int P_j(x)P_k(x)dx = 0, \ if \quad j \neq k \tag{B.4}$$

or

$$\int P_j(x)P_k(x)dx = 1, \ \ if \quad j = k \tag{B.5}$$

The covariance function $R(x_r, x_s)$ defined as

$$R(x_r, x_s) = \overline{C_p(x_r,t)' C_p(x_s,t)'} \tag{B.6}$$

From equation (B.1) this becomes

$$R(x_r, x_s) = \overline{\sum_{j=1,n} T_j(t) P_j(x_r) \quad \sum_{k=1,n} T_k(t) P_k(x_s)} \tag{B.7}$$

When expanding the right side of equation (B.7) and taking the time average, from equation (B.2) and (B.3) all the time varying quantities go to zero, except when $j=k$. Thus we obtain

$$R(x_r, x_s) = \sum_{j=1,n} \overline{T_j(t)^2} P_j(x_r) P_j(x_s) \tag{B.8}$$

Now multiplying equation (B.8) by an arbitrary mode shape $P_k(x_s)$ and integrating through space with respect to x_s

$$\begin{aligned}
&\int R(x_r, x_s)\, P_k(x_s)\, dx_s \\
&= \int \left(\sum_{j=1,n} \overline{T_j(t)^2} P_j(x_r) P_j(x_s) \right) P_k(x_s)\, dx_s \\
&= \sum_{j=1,n} \overline{T_j(t)^2} P_j(x_r) \int P_j(x_s)\, P_k(x_s)\, dx_r \\
&= \overline{T_k(t)^2} P_k(x_r)
\end{aligned} \tag{B.9}$$

The final step in equation (B.9) is due to the orthogonality condition of equations (B.4) and (B.5).

The integral on the left side of equation (B.9) can be expressed as a series and can be written in the matrix form as

$$[R(x_r, x_s)][P_k(x_r)] = \overline{T_k(t)^2} [P_k(x_r)] \tag{B.10}$$

APPENDIX C

SAMPLE COVARIANCES, EIGENVECTORS AND EIGENVALUES FROM PROPER ORTHOGONAL DECOMPOSITION

The following pages provide data produced through the evaluation of pulsating ventilation from the proper orthogonal decomposition of external surface pressures.

- Pressure coefficient covariance matrices for 0° and 90° wind angles
- Eigenvector matrices for 0° and 90° wind angles
- List of eigenvalues for 0° and 90° wind angles

Table C.1 Pressure coefficient covariance matrix for surface pressure taps around cubic structure for 0° wind direction

Tap No.	1	2	3	4	5	6	7	8	9	10	11	12	13	14	15	16
1	0.139	0.152	0.158	0.151	0.109	-0.133	-0.143	-0.108	-0.069	-0.035	-0.02	-0.025	-0.028	-0.03	-0.025	-0.023
2	0.152	0.176	0.185	0.175	0.125	-0.151	-0.165	-0.128	-0.083	-0.043	-0.025	-0.029	-0.032	-0.035	-0.03	-0.027
3	0.158	0.185	0.207	0.203	0.148	-0.167	-0.183	-0.141	-0.092	-0.048	-0.028	-0.032	-0.035	-0.038	-0.033	-0.03
4	0.151	0.175	0.203	0.213	0.166	-0.165	-0.179	-0.136	-0.088	-0.046	-0.027	-0.03	-0.033	-0.035	-0.03	-0.028
5	0.109	0.125	0.148	0.166	0.158	-0.107	-0.114	-0.088	-0.057	-0.028	-0.015	-0.016	-0.018	-0.019	-0.016	-0.014
6	-0.133	-0.151	-0.167	-0.165	-0.107	0.33	0.283	0.151	0.088	0.058	0.051	0.067	0.073	0.079	0.073	0.07
7	-0.143	-0.165	-0.183	-0.179	-0.114	0.283	0.363	0.176	0.095	0.064	0.055	0.067	0.072	0.077	0.071	0.068
8	-0.108	-0.128	-0.141	-0.136	-0.088	0.151	0.176	0.247	0.124	0.061	0.041	0.043	0.046	0.048	0.044	0.042
9	-0.069	-0.083	-0.092	-0.088	-0.057	0.088	0.095	0.124	0.171	0.075	0.034	0.03	0.032	0.033	0.031	0.029
10	-0.035	-0.043	-0.048	-0.046	-0.028	0.058	0.064	0.061	0.075	0.105	0.041	0.026	0.025	0.025	0.023	0.022
11	-0.02	-0.025	-0.028	-0.027	-0.015	0.051	0.055	0.041	0.034	0.041	0.066	0.03	0.026	0.025	0.023	0.022
12	-0.025	-0.029	-0.032	-0.03	-0.016	0.067	0.067	0.043	0.03	0.026	0.03	0.033	0.031	0.03	0.028	0.027
13	-0.028	-0.032	-0.035	-0.033	-0.018	0.073		0.046	0.032	0.025	0.026	0.031	0.033	0.033	0.031	0.029
14	-0.03	-0.035	-0.038	-0.035	-0.019	0.079	0.077	0.048	0.033	0.025	0.025	0.03	0.033	0.037	0.033	0.031
15	-0.025	-0.03	-0.033	-0.03	-0.016	0.073	0.071	0.044	0.031	0.023	0.023	0.028	0.031	0.033	0.034	0.031
16	-0.023	-0.027	-0.03	-0.028	-0.014	0.07	0.068	0.042	0.029	0.022	0.022	0.027	0.029	0.031	0.031	0.031

Table C.2 Pressure coefficient covariance matrix for surface pressure taps around cubic structure for 90° wind direction

Pressure Tap	1	2	3	4	5	6	7	8	9	10	11	12	13	14	15	16
1	0.152	0.126	0.11	0.113	0.107	0.068	0.077	0.069	0.066	0.057	0.057	0.051	0.051	0.05	0.046	0.043
2	0.126	0.158	0.126	0.125	0.115	0.072	0.082	0.073	0.068	0.06	0.059	0.053	0.052	0.05	0.046	0.044
3	0.11	0.126	0.145	0.13	0.117	0.071	0.082	0.072	0.066	0.058	0.056	0.051	0.05	0.048	0.044	0.043
4	0.113	0.125	0.13	0.167	0.138	0.084	0.092	0.08	0.073	0.063	0.062	0.056	0.056	0.054	0.049	0.047
5	0.107	0.115	0.117	0.138	0.18	0.097	0.094	0.079	0.073	0.063	0.061	0.056	0.056	0.054	0.05	0.047
6	0.068	0.072	0.071	0.084	0.097	0.154	0.097	0.085	0.08	0.071	0.068	0.059	0.058	0.057	0.053	0.051
7	0.077	0.082	0.082	0.092	0.094	0.097	0.14	0.099	0.087	0.076	0.072	0.062	0.06	0.059	0.055	0.053
8	0.069	0.073	0.072	0.08	0.079	0.085	0.099	0.13	0.1	0.086	0.08	0.068	0.067	0.066	0.062	0.059
9	0.066	0.068	0.066	0.073	0.073	0.08	0.087	0.1	0.132	0.099	0.087	0.077	0.074	0.072	0.068	0.064
10	0.057	0.06	0.058	0.063	0.063	0.071	0.076	0.086	0.099	0.136	0.098	0.084	0.079	0.076	0.072	0.068
11	0.057	0.059	0.056	0.062	0.061	0.068	0.072	0.08	0.087	0.098	0.141	0.09	0.078	0.072	0.068	0.066
12	0.051	0.053	0.051	0.056	0.056	0.059	0.062	0.068	0.077	0.084	0.09	0.141	0.108	0.096	0.087	0.084
13	0.051	0.052	0.05	0.056	0.056	0.058	0.06	0.067	0.074	0.079	0.078	0.108	0.128	0.106	0.096	0.087
14	0.05	0.05	0.048	0.054	0.054	0.057	0.059	0.066	0.072	0.076	0.072	0.096	0.106	0.12	0.101	0.09
15	0.046	0.046	0.044	0.049	0.05	0.053	0.055	0.062	0.068	0.072	0.068	0.087	0.096	0.101	0.12	0.097
16	0.043	0.044	0.043	0.047	0.047	0.051	0.053	0.059	0.064	0.068	0.066	0.084	0.087	0.09	0.097	0.116

Table C.3 Eigenvectors of pressure coefficient covariance matrix for 0° wind direction

	Pressure Tap															
Mode	**1**	**2**	**3**	**4**	**5**	**6**	**7**	**8**	**9**	**10**	**11**	**12**	**13**	**14**	**15**	**16**
1	-0.269	0.237	0.055	0.024	-0.009	0.026	-0.457	-0.024	-0.010	0.543	-0.146	0.524	0.009	0.040	-0.090	0.239
2	-0.310	0.269	0.032	0.026	-0.002	0.000	-0.472	-0.012	-0.012	0.111	0.196	-0.491	0.046	0.039	0.156	-0.535
3	-0.344	0.307	0.040	0.054	0.028	-0.018	-0.191	0.027	0.016	-0.496	0.057	-0.241	0.002	-0.200	-0.096	0.623
4	-0.340	0.342	0.068	0.097	0.081	-0.021	0.229	0.051	0.024	-0.468	-0.198	0.474	-0.047	0.179	0.018	-0.416
5	-0.242	0.376	0.089	0.154	0.162	-0.006	0.653	0.115	0.088	0.466	0.110	-0.225	0.023	-0.057	0.018	0.107
6	0.396	0.391	-0.333	-0.102	0.033	-0.602	-0.106	0.389	0.205	-0.002	0.004	0.032	-0.005	0.004	0.007	-0.004
7	0.426	0.373	-0.293	0.183	0.402	0.605	-0.094	-0.143	0.013	-0.047	-0.005	0.008	0.002	0.001	0.002	-0.003
8	0.307	0.066	0.475	0.723	-0.310	-0.005	-0.096	0.215	-0.012	-0.030	-0.004	-0.001	0.002	-0.003	0.003	-0.006
9	0.200	0.033	0.623	-0.167	0.562	-0.280	-0.080	-0.337	0.166	-0.026	0.011	0.001	0.002	-0.002	-0.004	-0.001
10	0.118	0.122	0.380	-0.498	0.001	0.324	-0.015	0.614	-0.311	-0.015	-0.002	-0.002	-0.001	-0.001	0.004	-0.002
11	0.082	0.173	0.152	-0.287	-0.457	0.255	0.033	-0.140	0.730	-0.007	-0.157	-0.059	0.028	0.028	0.015	-0.001
12	0.092	0.181	0.043	-0.113	-0.235	-0.003	0.056	-0.215	-0.096	-0.025	0.694	0.278	-0.295	-0.380	-0.163	-0.114
13	0.099	0.184	0.031	-0.090	-0.199	-0.052	0.059	-0.230	-0.221	-0.041	0.309	0.033	0.165	0.688	0.378	0.241
14	0.105	0.192	0.018	-0.083	-0.182	-0.079	0.075	-0.229	-0.273	-0.012	-0.135	-0.012	0.767	-0.211	-0.332	-0.107
15	0.095	0.192	0.021	-0.076	-0.169	-0.084	0.050	-0.240	-0.295	0.034	-0.413	-0.028	-0.219	-0.412	0.612	0.019
16	0.090	0.190	0.019	-0.067	-0.158	-0.077	0.037	-0.213	-0.268	0.053	-0.308	-0.259	-0.494	0.297	-0.551	-0.025

Table C.4 Eignvectors of pressure coefficient covariance matrix for 90° wind direction

	Pressure Tap															
Mode	**1**	**2**	**3**	**4**	**5**	**6**	**7**	**8**	**9**	**10**	**11**	**12**	**13**	**14**	**15**	**16**

1	-0.254	0.283	0.216	-0.240	-0.251	0.435	0.122	-0.141	-0.013	-0.008	0.499	-0.042	0.192	-0.047	-0.345	0.235
2	-0.268	0.320	0.220	-0.230	-0.173	0.254	0.021	-0.004	0.014	-0.013	-0.161	-0.020	-0.525	0.108	0.500	-0.257
3	-0.260	0.311	0.180	-0.113	-0.026	-0.087	-0.071	0.105	-0.001	0.028	-0.478	0.029	0.716	0.036	0.109	-0.100
4	-0.285	0.327	0.137	0.050	0.168	-0.310	-0.067	0.094	-0.014	0.017	-0.303	0.107	-0.407	-0.200	-0.534	0.239
5	-0.285	0.314	0.049	0.320	0.439	-0.374	0.139	-0.128	0.015	-0.016	0.494	-0.044	0.074	0.120	0.273	-0.083
6	-0.247	0.060	-0.402	0.544	0.144	0.556	0.229	-0.117	-0.008	0.011	-0.262	0.106	0.015	-0.022	-0.023	0.045
7	-0.260	0.073	-0.343	0.183	-0.278	-0.026	-0.453	0.387	-0.006	-0.010	0.153	-0.503	-0.016	0.032	-0.122	-0.224
8	-0.256	-0.032	-0.345	-0.047	-0.349	-0.212	-0.204	-0.013	-0.010	0.024	0.092	0.422	0.010	-0.093	0.358	0.528
9	-0.257	-0.106	-0.310	-0.198	-0.204	-0.224	0.108	-0.411	0.002	-0.023	0.011	0.300	-0.007	0.186	-0.302	-0.546
10	-0.247	-0.186	-0.246	-0.347	0.105	-0.144	0.362	-0.231	-0.008	-0.004	-0.185	-0.617	-0.015	-0.012	0.081	0.292
11	-0.241	-0.188	-0.201	-0.424	0.457	0.169	0.091	0.546	0.011	-0.026	0.149	0.251	0.023	-0.190	0.007	-0.143
12	-0.240	-0.298	0.166	-0.070	0.327	0.179	-0.520	-0.216	0.071	0.305	-0.033	0.013	-0.025	0.487	-0.056	0.157
13	-0.236	-0.298	0.236	0.086	0.069	0.052	-0.257	-0.233	-0.471	-0.546	-0.010	-0.032	0.029	-0.364	0.069	-0.078
14	-0.229	-0.290	0.238	0.150	-0.098	-0.020	-0.004	-0.087	0.748	0.075	0.015	-0.035	0.022	-0.432	0.048	-0.109
15	-0.217	-0.294	0.252	0.190	-0.209	-0.088	0.270	0.168	-0.446	0.629	0.038	0.004	-0.010	-0.106	0.020	-0.085
16	-0.206	-0.275	0.230	0.176	-0.197	-0.080	0.310	0.351	0.118	-0.453	-0.031	0.067	-0.023	0.531	-0.081	0.141

Table C.5 Eigenvalues of pressure coefficient covariance matrices for 0° and 90° wind direction cases

Mode No.	Eigenvalues 90° case	Eigenvalues 0° case
1	1.251	1.472
2	0.343	0.285
3	0.146	0.2
4	0.094	0.101
5	0.067	0.064
6	0.057	0.065
7	0.05	0.052
8	0.044	0.044
9	0.015	0.03
10	0.018	0.012
11	0.039	0.00608
12	0.034	0.00409
13	0.02	0.003
14	0.03	0.000663
15	0.027	0.00149
16	0.026	0.00113

11. APPENDIX D

12. CALCULATING RATIO OF NET OUTFLOW FROM RMS CALCULATED PULSATING VENTILATION

Consider the ventilation rate to be represented by a sinusoidal fluctuation of zero mean and rectified about zero as shown in Figure D.1 below.

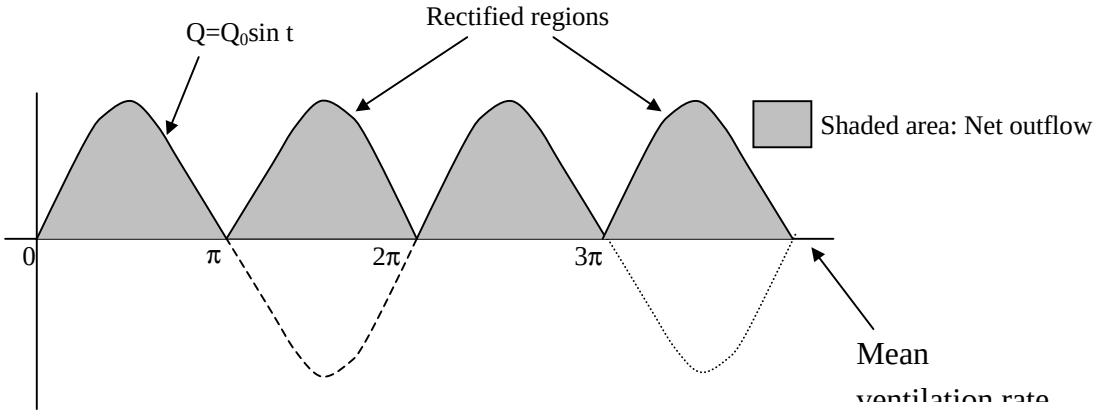

Figure D.1 Sinusoidally fluctuating ventilation rate

The ventilation rate over a cycle is given by the mean of the rectified signal

$$\overline{Q} = \frac{1}{\pi}\int_0^{\pi} Q_0 \sin t \quad = \frac{2Q_0}{\pi} \qquad \text{(D.1)}$$

The pulsating ventilation was defined in section 5.3.1.3 as the rms of the ventilation rate. This is given by

$$Q_{rms} = \left[\frac{1}{2\pi} \int_0^{2\pi} \left(Q_0 \sin t\right)^2 dt \right]^{1/2}$$

$$= \left[\frac{{Q_0}^2}{2\pi} \int_0^{2\pi} \frac{1-\cos 2t}{2} dt \right]^{1/2} \qquad \text{(D.2)}$$

$$= \frac{Q_0}{\sqrt{2}}$$

The ratio of the net outflow to the rms of the ventilation (pulsating ventilation) is

$$\frac{\textit{Net outflow}}{Q_{rms}} = \frac{2Q_0 / \pi}{Q_0 / \sqrt{2}} \qquad \text{(D.3)}$$

$$= \frac{\sqrt{2}}{\pi}$$

The product of the rms of the ventilation rate of the total ventilation rate provides the net turbulent outflow of air.